CARDIFF UNIVERSITY

Methodology platform for prediction of damage events for self-sensing aerospace panels subjected to real loading conditions

Ryan Andrew Marks

A thesis submitted in partial fulfilment for
the degree of Doctor of Philosophy

Mechanics, Materials and Advanced Manufacturing
School of Engineering

June 2016

Abstract

With the growing size of aircraft fleets and the complexity of aircraft structures it has been proposed that there are many cost and operational benefits of installing a structural health monitoring system to monitor the aircraft's structure throughout its in-service life. A method of achieving this is through monitoring the acoustic emission emitted during a damage event. One of the limiting factors to this however is having sufficient confidence in the placement of the sensors to ensure coverage while limiting the mass associated with the system.

A series of five studies were conducted which use both experimental and numerical approaches to investigate Lamb wave propagation and its interaction with damage in both metallic and composite materials. These studies have used some of this data and through the use of genetic algorithms sought to optimise the placement of sensors with the objective of achieving a high probability of damage detection.

The use of 3D scanning laser vibrometry has been harnessed along with the use of numerical reasoning using the local interaction simulation approach. This has enabled studies to be conducted which consider both the in-plane and out-of-plane components of the Lamb waves which is an important consideration when selected the appropriate sensing methods. In addition, a novel method of training sensor networks for AE location using the delta-t technique is also presented.

The results of these studies has led to the development of two separate methodologies; one for the placement of sensors in an acousto-ultrasonic system for the detection of adhesive disbonds and one for the placement of AE sensors to maximise the coverage of the sensor network on a structure with complex geometry. These methodologies have many advantages, particular in their prompt convergence which makes progress towards enabling a concurrent sensor network-structure development.

Declaration of Authorship

This work has not been submitted in substance for any other degree or award at this or any other university or place of learning, nor is being submitted concurrently in candidature for any degree or other award.

Signed ……………………………………………… (candidate) Date………………………………

STATEMENT 1

This thesis is being submitted in partial fulfilment of the requirements for the degree of PhD.

Signed ……………………………………………… (candidate) Date………………………………

STATEMENT 2

This thesis is the result of my own independent work / investigation, except where otherwise stated. Other sources are acknowledged by explicit references. The views expressed are my own.

Signed ……………………………………………… (candidate) Date………………………………

STATEMENT 3

I hereby give consent for my thesis, if accepted, to be available for photocopying and for inter-library loan, and for the title and summary to be made available to outside organisations.

Signed ……………………………………………… (candidate) Date………………………………

‘If you are looking for perfect safety, you will do well to sit on a fence and watch the birds; but if you really wish to learn, you must mount a machine and become acquainted with its tricks by actual trial.’

Wilbur Wright, Aviation Pioneer

Acknowledgments

There are many people that I owe a debt of gratitude for their support during my post graduate study. Without these people, none of this would be possible.

Firstly, I would like to thank my supervisors Dr Alastair Clarke, Dr Rhys Pullin and Professor Carol Featherston for all of their excellence guidance, advice and support. I would also like to thank them for supporting my professional development as a researcher through assisting me with conference attendance and writing of journal papers.

I would also like to thank Airbus especially Professor Christophe Paget for supporting this project financially, the supply of test components and industrial support. I would also like to that the EPSRC for also funding this project under the doctorial training grant (grant number EP/K502819/1).

I owe a massive amount of gratitude to all members of the CUSP team who have assisted me throughout this project. In particular I would like to thank Dr Mark Eaton, Dr Matthew Pearson and Dr Davide Crivelli for their additional guidance, support and interesting discussions. Without their advice on setup and best practice this project would have been a real struggle. I need to also make a special mention for Stephen Grigg and Clare Gillam who I supervised throughout their undergraduate projects. I feel that we learned a lot together and that we produced some good results.

I need to acknowledge the team at Polytec Ltd. particularly Roger Traynor, Matthew Archer and Niamh O’Meara who have offered exceptional technical support regarding laser vibrometry. I am really grateful for how they have gone out of their way to support with advice on best practices and allow me to trial new equipment.

An exceptional amount of thanks goes to all of my friends who have supported me and kept me sane when things were getting crazy. A few beers with you on a Friday night (and the occasional other days that end with a y), the walks in the Beacons and good times have been brilliant. There are so many to mention but all of the team members from Cardiff Racing deserve a special mention. I’ve had some of the best moments of my life with you guys and I hope the success continues.

Finally, to all of my close family. Mum, you were the one that put me in the backseat of an aircraft aged 17 months and Dad, you were the first person to take me into the skies where this obsession started. Thank you both for being the most amazingly supportive parents. You’ve kept me grounded while letting me soar. My brother Brett, you have always encouraged me and pushed me to do my best. Flying with you has kept my interest going and our flights together always seem to come at the time when we need it most. Lastly, my partner Rebecca, you’ve always been there for me. Through the highs and more importantly the lows which come with any advancement in science. You have allowed me to fly higher than I ever thought I could… and the view from up here with you is pretty good.

List of Abbreviations

AE	Acoustic Emission
AU	Acousto-ultrasonic
SHM	Structural health monitoring
NDT	Non-destructive testing
NDE	Non-destructive evaluation
GA	Genetic Algorithm
FFT	Fast Fourier Transform
SNR	Signal-to-noise ratio
FEA	Finite element analysis
LISA	Local interaction simulation approach
FD	Finite Difference
RMS	Root mean square
CUDA	Computer unified device architecture
GPU	Graphical processing unit
CPU	Central processing unit
CLoVER	Composite long-rang variable-direction emitting radar
CMAES	Covariance matrix adaptation evolutionary strategy
CSA	Clonal Selection Algorithm
RAF	Royal Air Force
SNOBFIT	Stable Noisy Optimisation by Branch and Fit
MA	Monkey Algorithm
FSSP	Firing squad synchronisation problem
SPEA2	Strength Pareto Evolutionary Algorithm
MGL	Mistras Group Ltd.
NPL	National Physical Laboratory
DLL	Dynamic Link Library
RAM	Random access memory
FOD	Foreign Object Damage
GSE	Ground service equipment
BVID	Barely visible impact damage
TOA	Time of Arrival

Contents

1. Introduction

Structural integrity of aircraft has long been a widely considered field of aerospace design. It could be argued that the earliest example of considerations of the structural integrity of an airframe stems back to ancient Greece with the myth of Icarus. In the myth the designer, Daedalus, had explained that operating Icarus' aircraft outside of the operating envelope would cause major structural damage. Icarus flew outside these limits causing delaminations of his wings and his own fatal demise. Though only a story set thousands of years before man successfully achieved flight, the moral of the story still stands today; know the structural limits and operate the aircraft within those limits.

Aerospace as an engineering field is still reasonably primitive. The first manned, powered flight by the Wright Brothers first took place in 1903; just over one hundred years ago. When compared with other fields of engineering such as ship building and bridge building, aerospace is an infant.

1.1. Lessons learned

The biggest challenged faced however, is knowing the structural limits of an airframe, unlike Daedalus. One of the earliest examples of this is the De Havilland Comet. The British-built De Havilland Comet was the world's first commercial jet airliner, first flown in 1949 leading the way in commercial jet transport. The Comet flew faster and higher than aircraft had previously. Prior to this, commercial aircraft did not commonly have pressurised cabins (the first commercial airliner to adopt a pressurised cabin was the propeller driven Boeing 307 which entered service in 1940) forcing them to fly at lower altitudes to enable their passengers to be able to breathe without breathing apparatus. This however was the downfall of the Comet. In 1954 two Comets unexplainably broke up at high altitude over Italy. Following this, the whole fleet was grounded whilst airframe pressurisation tests were conducted [1] by submerging the fuselage in a water tank. The conclusion from the tests and the recovery of the wreckage was that the rapid depressurization of the airframe was caused by fatigue cracks which grew from the 'square windows' on the fuselage. An example of this is shown on the recovered wreckage of *G-ALYP* in Figure 1.

Figure 1: Wreckage of G-ALYP, one of the Comets that exploded mid-air, showing the fatigue cracks growing from the square windows. Currently on display in the London Science Museum.[2]

Britain never regained its position as the world leader in commercial jet airliner production as, while the Comet investigation was being conducted and public opinion waivered, American based Boeing produced the hugely successful 707 enabling Boeing to establish itself as a world leading aerospace company, a position it still holds to this day. This said, an important lesson was learned. The designers of the Comet were not incompetent but rather had discovered a problem which had never been seen before. Since the Comet disasters, much has been studied about metal fatigue and how to design better aircraft, and for that matter structures in general, to ensure structural integrity. It is because of the Comet that today all commercial pressurised aircraft have oval windows.

In 1988, Boeing 737-200 Aloha flight 243 experienced significant structural failure at 24,000 feet. The failure resulted in the top of the forward section of the fuselage breaking away from the aircraft resulting in the death of a crew member and injury to seven passengers. Despite this major structural failure, the aircraft was still able to land, unlike the Comet incidents years earlier, as shown in Figure 2.

Figure 2: Boeing 737-200 Aloha Flight 243 showing significant structural failure.[3]

The National Transport Safety Board (USA) found that the probable cause of the disaster was due to deficiencies in the maintenance program which allowed fatigue induced disbonds to go undetected, leading to the failure of a lap joint [4]. The root cause of the failure was a bonded joint that used a cold bonding technique. This was found to lack the necessary robustness to survive the rigours of flight. Since then Boeing 737 has incorporated a hot bonding technique along with improved mechanical fastening which has resulted in lower stress concentrations [5] and hence more structurally robust airframes.

On 1st February 2003 Rockwell International space shuttle *Columbia* was returning to Earth from a sixteen day scientific research mission. On re-entry into the Earth's atmosphere the shuttle broke up killing all seven astronauts on board. An in-depth study was conducted by the Columbia Accident Investigation Board (CAIB), which was made up of industry leading experts. The debris recovered for the investigation is shown in Figure 3.

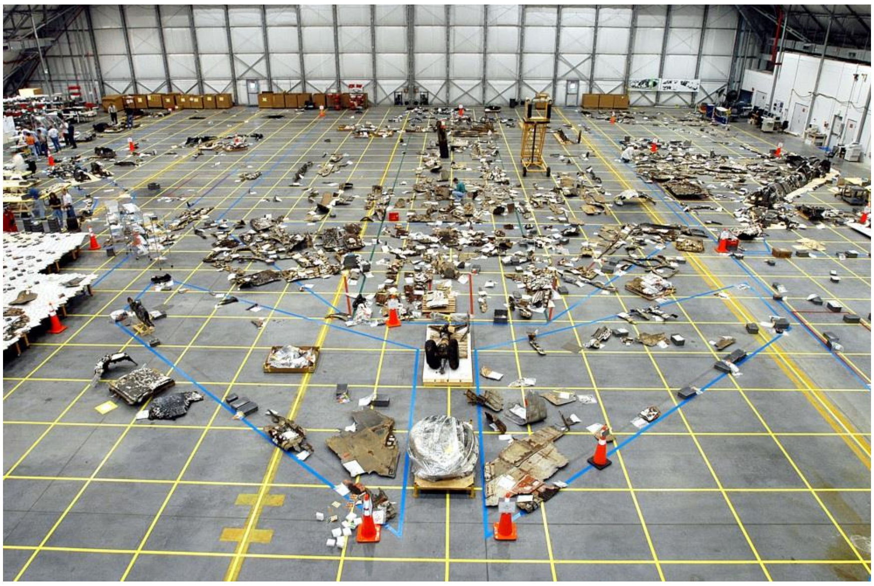

Figure 3: Debris gathered from the *Columbia* disaster [6].

The board ruled that the cause of the disaster was impact damage to the leading edge of the left wing being hit by a piece of insulating foam from the 'bipod ramp' (the structure that connected the shuttle to the external fuel tank). The impact caused significant structural damage that allowed superheated air to enter the internal wing structure during re-entry causing catastrophic structural damage under aerodynamic loading. The board also ruled that human error was also responsible as political and financial pressures developed a culture at NASA that lead to a series of decisions being made which allowed the damage to go unquantified. Though NASA knew of the impact they dismissed it as previous shuttle flights had experienced similar impacts and were found to be structurally sound [7].

There are numerous cases of aircraft structural failures throughout the years from which many engineering lessons have been learned which in turn have been applied to improve the safety of future aircraft designs. These lessons have typically promoted the design philosophy of increased safety factors and structural robustness to prevent catastrophic structural failure.

1.2.A new challenge

As history has demonstrated in the cases above, structural failure mechanisms are typically not identified until structural failure occurs (usually with catastrophic consequences). The De Havilland Comet, the Boeing 737-200 and the Space Shuttle *Columbia* were all certified to fly and deemed structurally sound. However all suffered significant structural failures due to failure to identify the initiation of the damage.

A common statistical failure analogy that was first discussed by Taleb [8] is that of the black swan. Taleb presents that it was once thought by Europeans that there could be no such thing as a black swan since all of the swans found in Europe were white. With the discovery by Europeans of Australia, this was found to be completely false as black swans did exist and were living on the other side of the world. This analogy has been widely applied to aircraft safety and in particular, structural safety.

Despite having developed advanced techniques for structural design and incorporating tools such as computer aided design and finite element modelling, it is still possible that structural weaknesses and areas of high stress concentration may go overlooked. This is particularly significant as aerostructure designers develop design solutions with ever increasing complexity using cutting edge materials. The case of the De Havilland Comet could indeed be regarded as a black swan event. The engineers who designed the aircraft were by no means incompetent and stress concentration calculations were conducted during design for the window that failed. It was the under-estimation of the loads experienced in the operational envelope combined with limited knowledge of the metal fatigue at the time that resulted in the failure. Since learning of this particular black swan, aircraft structural designers have considered it. The next question has to be however, “what is the next ‘black swan’ in terms of structural design and what can be done to reduce the impact that it has?”

As projected air travel is forecast to double in the next fifteen years [9], there are increasing environmental pressures to reduce the environmental impact of air travel [10]. The International Civil Aviation Organisation (ICAO) is working to address this by enforcing international aerospace polices which are directing the global aerospace industry to directly reduce their emissions [11]. This, combined with pressures from airline operators to reduce the costs of air transport, means that aircraft manufacturers have the continuing challenge of improving efficiency of aircraft operations. A method of achieving this that is being adopted by aircraft manufacturers is to reduce the weight of the structure of the aircraft whilst maintaining structural performance through the application of advanced composite technologies [12]. Modern commercial aircraft are using an increased amount of composite by weight such as the Airbus A380 (25%) the Airbus A350 (53%) and the Boeing 787 (50%) [13].

Though composites have been used in aircraft for many years (arguably since the very beginning with canvas and dope) it is only in recent years that they are being applied to the primary structure; the structure where the consequences of failure are catastrophic. Aircraft designers use many modelling and experimental techniques combined with many design practices based on past experience to verify that their designs will withstand the loading cycles that the aircraft will experience throughout its operational lifetime. However it is impossible to foresee the unexpected and hence there have been numerous accounts of structural failures in aircraft. The Comet, the Boeing 737-200 and the Space Shuttle all were pushing the limits of what was possible and the oversights in their design and operation ultimately led to their failures. The adoption of composite materials poses the next challenge in ensuring structural integrity of aircraft structures.

If a method of continually monitoring the structure for damage could be employed on an aircraft's structure, the initiation of damage could be detected early-on before it causes a catastrophic failure. If such a system had been employed on the Comet; the crack initiation would have been discovered early, the root cause investigated and a modification employed to the design without a single life being lost. If such a system was on Aloha flight 243, the disbonds would have been detected early and not missed using traditional non-destructive testing (NDT) methods in the maintenance intervals. The discussed issue would have been reported back to Boeing and again a modification to the design could have been implemented before any catastrophe had occurred. The impact to *Columbia's* wing could have been detected, located and quantified allowing the crew at NASA to make a decision on the best course of action. The accident report actually states that simulations carried out by NASA after the disaster state that a rescue mission with another shuttle could have been performed, albeit with difficulty. In addition, the recommendations to the continuation of the space shuttle program stated that a method of inspecting the shuttle's thermal protection system should be employed [7].

1.3.Structural Health Monitoring

The philosophy behind Structural Health Monitoring (SHM) is not to dissimilar to that of the human nervous system [14]. When the human body experiences damage, say a cut on the finger, the human does not need to routinely inspect the finger for cuts nor do they have to visit a physician for an inspection. The pain receptors in the finger almost instantly send a message to the brain where the message is processed. The brain interprets the message and the human instantly knows is the location and severity of the cut due to the amount of pain. From the pain and a visual inspection, a decision can be made as to the best course of action whether that is simple first aid or a hospital visit.

SHM aims to achieve the same goal. There are for main objectives of a SHM system [15];

1. **Detection** – The ability to detect the presence of damage on the structure as it occurs in real time.
2. **Location** – to locate the damage on the structure; this is particularly important for planning repair operations especially on large aircraft such as the Airbus A380

3. **Characterisation** – the ability for the system to determine the type of damage such as impact damage or fatigue crack growth.
4. **Evaluation** – the ability for the system to understand the significance of the damage and make recommendations to the aircraft operative on the best course of action such as perform an emergency landing.

Applying an SHM system to an aircraft has many benefits. As mentioned, the ability to detect damage early would significantly improve the safety of the aircraft through an increased assurance of structural integrity. Risk to the lives of the occupants (and indeed those on the ground) can be defined simplistically by the probability of the incident happening multiplied by the consequence of it happening. As the consequence of an air disaster happening is high, risk has to be reduced by reducing the probability of an air disaster happening. Hence, an SHM system could play a significant role in reducing the risk associated with air travel.

SHM systems on aircraft can also greatly improve the efficiency of aircraft maintenance operations particularly as the lifespan of a modern aircraft is greater than 30 years [16]. Aircraft are required by law to have periodic maintenance checks which are titled in increasing severity A-checks, B-checks, C-checks and D-checks [17]. A-checks and B-checks are not greatly invasive however C-checks and D-checks require the aircraft to be stripped back and individual components inspected. Due to the large amount of inspection it is believed that around 12% of an aircraft's total operating cost is attributed to the maintenance alone. It is also predicted that the cost to an airline for having an aircraft grounded for unplanned maintenance is estimated to be $23,000 per hour [18]. This cost is a combination of the lost revenue of the aircraft in addition to the cost of the maintenance operation. In addition to the direct maintenance cost of unplanned maintenance, other issues also arise such as scheduling problems and customer dissatisfaction [19]. Of all of the aircraft's Direct Operating Costs (DOCs) such as fuel, staffing fees and aircraft insurances, airline operators have identified that the DOC where the biggest cost savings can be made is in the aircraft's maintenance [14]. It is this customer demand that is forcing aircraft manufacturers to engineer aircraft with reduced maintenance costs.

A large amount of the costs from maintenance operations can be attributed to the inspection of the aircraft. Inspection is a time consuming operation especially as increasing global air travel demands have resulted in larger aircraft being introduced. Many inspection operations also require specialist equipment operated by technicians and as a result exposes the inspection to human error. It is estimated that up to 40% of identified areas of inspection are classed as ‘no fault found’ [20]. Due to having a human aspect in the inspection process, damage can go undetected [21].

Human error is a large cause of concern with respect to detecting aircraft structural damage. Arguably the pioneer of research into human error with application to aerospace medicine is James T. Reason. One of the most influential models for human error developed by Reason [22] is the ‘Swiss cheese model’. The Swiss cheese model considers human error mechanisms as a slice of holey Swiss cheese. Each slice is representative of a check or safeguard that may prevent something happening with the size of each hole in the model being representative of how likely a human operative is to cause an error. An example of this in a maintenance operation could be that the first slice represents the human error by a trainer in the operatives training, the second slice could be the human error by the operative in the use of the equipment, the third slice may be the human error by the operative in failing to report that they are not competent in using the equipment and the fourth maybe the sign off of the inspection by a supervisor without further inspection. Thus, despite all of the layers, the error propagates through. A graphical representation of this is presented in Figure 4. It is worth noting that the size of the holes in each layer of the Swiss cheese can vary over time due to human factors. The size of the hole may increase due to an operative’s tiredness and conversely may decrease after conducting some refresher training. It should be noted that although the Swiss cheese model was developed for modelling human error, it can also be adapted to model almost every type of error mechanism and therefore is very useful tool for the understanding and reduction of error.

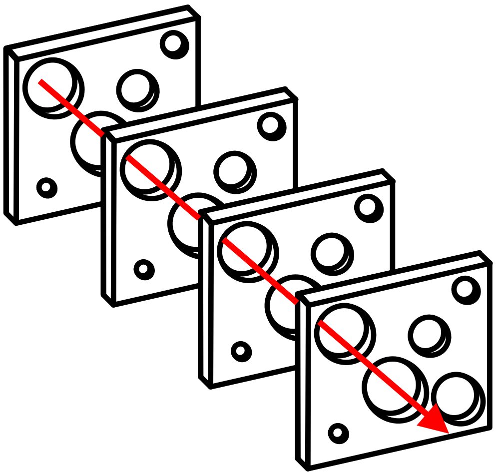

Figure 4. A graphical representation of a four-slice Swiss cheese model. Note that all of the holes are alligned enabling the Human error to propagate through, resulting in a failure

An alternative approach to understanding human error is the pathogen model [23]. This model states that a cause of human error may be embedded in a human’s psyche, like a pathogen, and lays dormant until it becomes active at an important moment. An example of this in an aircraft maintenance environment may be that the maintenance company has a blame culture. This culture could be regarded as a latent pathogen within an aircraft technician which at the point where they cause damage to a structure during maintenance (say a tool drop) causes them to not make the presence of the damage known and hence catastrophic structural failure may occur.

An example of failure to successfully identify the presence of damage as a result of a human error of judgement which had fatal consequences was the incident of the Pierre Robin DR400/180 G-DELS [24]. This incident in question was the case of a light aircraft where the pilot clipped a hay bale with the wing on approach when landing the aircraft. The pilot of the aircraft, realising the damage event had taken place inspected the external visible sections of the wing as well as tugged it in an attempt to assess the extent of the damage. Rather than perform a more thorough investigation, the pilot deemed the aircraft sound for flight where in fact the main wooden spar had experienced significant structural damage. As a result, this caused the wing to separate from the aircraft mid-flight. The decision to fly the aircraft based on visual inspection alone resulted in fatality.

Reducing the influence of human factors in aircraft maintenance operations can significantly improve the safety of the aircraft and reduce the likelihood of catastrophic failure. It is possible that this could be achieved by implementing an SHM system onto the aircraft. In the case of the Swiss cheese model, it could be thought of as adding an additional layer. However, a high level of detection is required to ensure that the damage does not go undetected. In addition, successful identification is required with type I (also known as a 'false positive'. In the case of an SHM system, a type I error is where the system appears to detect damage that in fact does not exist) and type II (also known as a 'false negative'. In the case of an SHM system this would be damage occurring and the system failing to detect it.) errors minimised to ensure that human confidence is built in using the SHM system.

If a SHM system could be installed onto an aircraft which enabled aircraft maintenance technicians to accurately locate and diagnose faults, maintenance operations can be pre-planned prior to the aircraft arriving at the Maintenance, Repair and Overhaul (MRO) facility. It is forecast that an SHM system installed on the aircraft could reduce maintenance costs by up to 75% at service bulletin level whilst also increasing the availability of the aircraft [25].This would reduce the requirement to inspect the entire aircraft for damage, reducing the time of maintenance operations and in-turn the cost of aircraft maintenance operations. It has to be stated that SHM is not to been seen as a substitute for traditional non-destructive testing

(NDT) inspection techniques. Instead it is envisaged that the two would work together. Just as when a patient visits a physician with a pain, the physician inspects the painful area to further diagnose the ailment and prescribe a course of action to remediate, SHM would enable aircraft maintenance technicians to locate the exact areas of the aerostructure that need inspection.

At present aerostructures are designed to account for these maintenance errors. In the case of composite components, manufacturing defects and processes such as drilling can lead to small delaminations [26] which can significantly reduce the structural performance. This has resulted in aerostructures being over engineered to ensure structural performance; resulting in heavier than required structures. It is predicted that by concurrently designing an SHM system with the structure, mass reductions of up to 15% can be made at component level [25]. Having a smart structure reduces the requirements for robustness whilst maintaining an acceptable risk for air travel.

1.4.Structural Health Monitoring techniques

There are many techniques that have been adopted to monitor structures for damage. Typically these techniques can be divided into two categories; active and passive. Active systems require some form of input and the response is then measured, such as ultrasound. Passive systems do not require an external input but instead acquire data from changes in the structure such as strain gauges.

Many of these techniques rely on measuring some physical aspect of the structure such as its thermal properties using environmental degradation monitoring systems, changes in strain under loading using strain gauges and its modal response using accelerometers. Though many techniques have been employed to monitor the health of a structure, many can only monitor a small area of the structure. An example of such a technique is comparative vacuum monitoring which measures pressure drops of a series of galleries bonded to the structure to monitor damage such as crack growth. Because of this, much of the structure goes unmonitored.

Other techniques such as modal analysis measure the frequency response of the healthy structure which is used as a baseline. When the structure is damaged there is a shift in the frequency response indicating the presence of damage. There has been some work into locating damage on a structure using this technique however this usually relies on prior knowledge of the structure from experimentation or computational modelling [27]. This technique can also be susceptible to noise when the aircraft is operating making the application of this technology challenging. For an in-depth overview of aerospace SHM techniques the reader is referred to Speckmann and Henrich [14].

The use of ultrasonic surface waves has shown great potential in recent years for SHM applications [28]. Primarily, there are two techniques that use ultrasonic surface waves; Acousto-Ultrasonics (AU) – an active technique, and Acoustic Emission (AE) – a passive technique.

AU in its simplest form requires two transducers to be attached to the structure. An electronic signal (usually in the form of a cyclic wave) is used to actuate one of the sensors which results in an ultrasonic surface wave being induced. The surface wave travels across the structure to the other transducer where it is converted back into an electrical signal. If damage occurs in the path of the two sensors, the surface wave is disrupted resulting in a change in the signal sensed by the transducer. This is demonstrated in Figure 5. An in-depth explanation and review of the technique is presented in chapter 2.

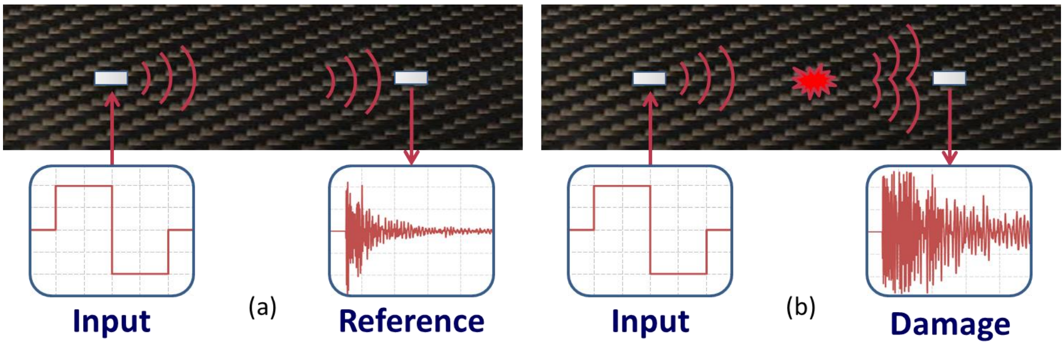

Figure 5: A schematic of an AU system. (a) Healthy structure. (b) Damage present in the path of the two sensors

AE, like the AU technique, detects ultrasonic surface waves using transducers mounted to the structure. These waves typically manifest as Rayleigh waves, Love waves or a Lamb waves in the case of the plate-like structure of an aircraft. Therefore, the focus of this work is mainly on that of Lamb waves. However, unlike the AU technique, there is no active element. Instead, the surface waves are generated from the elastic strain energy emitted during a damage event. AE as a technology offers many advantages as an SHM technique:

- It has been proven that AE can be used as a global monitoring technique on large structures such as bridges [29] whilst it has also been proven to be capable of detecting damage locally in complex, composite structures [30].
- Due to the passive nature of the technology, damage can be continually monitored not periodically monitored as is the case for an active system
- The passive nature of the technology requires less power and therefore makes it well suited to large structural monitoring particularly in cases where energy can be harvested to power the system [31].

- Using sensor arrays it is possible to locate the source of the AE event and hence the location of the damage [32].
- As different damage mechanisms emit different acoustic emission signals it is possible to characterise the damage [30].

However, there are also some disadvantages to AE. These include;

- The detection of false alarms which can occur from noise signals generated from sources such as fluid-structure interactions and engines.
- The high computational cost required in order to detect AE signals.
- Large amounts of data need to be collected and potentially stored creating data management issues.
- A high level of data transfer rate is required between the sensors and the processing unit.
- The improper location of sensors and system parameters can result in damage being undetected.

However, there are potential solutions to these disadvantages. For example, when considering the massive amounts of data, the data can be reduced by using 'sleeping' sensors that are only triggered when the AE signal received exceeds a certain frequency. The data storage requirement can be reduced also by only a statistical measure such as a Chebyshev descriptor rather than storing the entire sampled waveform.

1.5.Aims and objectives

With both of the SHM systems discussed, the probability of detecting damage and indeed the level of sensitivity achieved by the system is closely linked to the placement of the sensors. The failure to place sensors in suitable locations of the structure can result in the failure to detect the damage and indeed locate it. However, with the size of modern commercial aircraft the number of sensors is also a consideration. Minimal numbers of sensors need to be placed on the structure to reduce the implementation cost of the SHM system as well as the associated mass. Thus the optimisation problem, and therefore the aim of this work, is to develop a methodology for maximising the probability of damage detection whilst minimising the number of sensors on aircraft structures.

The key objectives of this work are:

- A thorough investigation into the Lamb wave propagation and interaction with adhesively bonded stiffeners and disbonds for what is regarded as a common structural defect.
- Develop a methodology for optimising the placement of sensors for an AU SHM system to maximise the probability of damage detection.
- Conduct an investigation into wave propagation and interaction with impact damage on a composite specimen with a view to highlighting areas for suitable sensor placement for an AU system.
- Use numerical modelling methods to model Lamb wave propagation and interaction with damage.
- Validate the numerical models with experimental studies.
- Use the numerical approach developed for the location of AE activity on an aerospace component under real loading conditions.
- From the numerical methodology developed, create an AE optimisation platform and generate optimal sensor solutions for a representative structure.

1.6.Novelty statement

This thesis investigates the optimisation of sensor locations for both AE and AU systems for aerospace applications. The novelty in this work is as follows;

- A thorough experimental investigation of both the out-of-plane and in-plane Lamb modes using 3D scanning laser vibrometry. The results of this investigation were visualised as well as the results of signal processing presented.
- A novel methodology for the optimal placement of sensors for an AU system using both 3D scanning laser vibrometry and numerical methods. Both in-plane and out-of-plane modes are considered.
- Visualisation of Lamb wave interaction with impact damage in a composite is presented using 3D scanning laser vibrometry. The interaction is quantified and visualised using a cross-correlation coefficient technique; highlighting suitable areas for sensor placement.
- A numerical method was used for the training of a physical sensor network. This was then used to successfully detect and locate the presence of AE as a result of fatigue damage on a complex structure.
- Numerical modelling was used for the mapping of a structure in terms of peak amplitude. This enabled an optimisation platform to be created for the placement of AE sensors for a given sensor network size.

1.7. Thesis organisation

This chapter has given an overview of the history of aircraft structural damage. This has outlined the motivation for the SHM of aircraft structures. Two SHM techniques are briefly discussed and the requirement for the optimisation of sensor placement has been stated.

Chapter two covers the background and theory associated with this work. An in-depth explanation of surface waves is presented from first principles. This is followed by the background of AE, the associated mechanisms and phenomena associated with surface waves and AE and a review of studies where AE has been applied to aircraft. Background is also presented on the use of AU to monitor structures. A comprehensive literature review is presented on the use of laser vibrometry to sense surface waves, the development and application of the local interaction simulation approach and the optimisation of sensor networks for SHM applications.

Chapter three contains full details of the experimental and simulation techniques and instrumentation used commonly throughout this body of work.

Chapter four presents a detailed experimental investigation into the interaction of AU Lamb waves with an adhesively bonded stiffener and disbond on a metallic structure representative of that of an aircraft. A corresponding numerical study is also presented. Signal processing techniques are used and plotted to visually demonstrate the Lamb wave interaction. The findings are supported by using traditional NDT techniques.

Chapter five presents an AU sensor location optimisation methodology based on both numerical and experimental results for the detection of an adhesive disbond on a stiffened panel. Different excitation locations are considered in order to investigate different excitation-disbond-sensor paths. Both the in-plane and out-of-plane components of the Lamb waves are investigated.

Chapter six investigated the Lamb wave interaction with impact damage on a composite wind turbine blade. This component was chosen for investigation as it is a representative structure that is subject to aerodynamic loading. Different signal processing techniques were used to identify the presence of the damage based on the Lamb wave data. A series of cross-correlation coefficient analyses were conducted to identify regions within the area of investigation which would be most suitable for the detection of damage. The extent of the damage was quantified using surface profilometry where it was found that the damage was less than that commonly regarded as Barely Visible Impact Damage (BVID); demonstrating the sensitivity of Lamb wave SHM systems.

Chapter seven covers an investigation into using delta-t training data created using numerical methods to locate experimental AE signals. The technique is first investigated on an aluminium plate in a linear location investigation. The technique is then adapted for the planar location of AE signals within a more complex geometry plate subjected to fatigue loading. The results show a significant performance gain over the traditional location technique as well as producing results that correlate well with the time consuming experimental training method.

Chapter eight presents a numerical investigation into the mapping of an aluminium structure using numerical methods in order to establish a multi-source, multi-sensor AE optimisation platform methodology. The peak amplitudes of different source locations for a large set of candidate sensor locations are considered. The technique is first applied to a flat aluminium plate with no features before being expanded to a plate with complex geometry.

Chapter nine summarise the findings of the different investigations in this thesis and discusses the potential of directions for future work.

1.8.Published outputs in support of this thesis

Marks, R., Clarke, A., Featherston, C., Paget, C., Pullin, R. "Sensor location studies for damage detection in Aerospace Structures using 3D scanning Laser Vibrometry". Proceedings of the 34th Conference and the 28th Symposium of the International Committee on Aeronautical Fatigue and Structural Integrity, Helsinki, Finland, 1–5 June 2015, ISBN 978-951-38-7442-1, pp808-818

Marks, R., Clarke, A., Featherston, Kawashita, L., C., Paget, C., Pullin, R. "Using genetic algorithms to optimize an active sensor network on a stiffened aerospace panel with 3D scanning laser vibrometry data". Journal of Physics: Conference Series – 11th International Conference on Damage Assessment of Structures - DAMAS 2015, Ghent, Belgium, 24th-26th August 2015,

Grigg, S., Pearson, M., Marks, R., Featherston, Pullin, R. "Assessment of Damage Detection in Composite Structures Using 3D Vibrometry". Journal of Physics: Conference Series – 11th International Conference on Damage Assessment of Structures - DAMAS 2015, Ghent, Belgium, 24th-26th August 2015,

Marks, R., Clarke, A., Featherston, C., Paget, C., Pullin, R., "Lamb wave interaction with adhesively bonded stiffeners and disbonds using 3D vibrometry", 2016 6(1), pp1-12 Applied Sciences

Work submitted for publication

Marks, R., Gillam, C., Clarke, A., Armstrong, J., Pullin, R., “Damage detection in a composite wind turbine blade using 3D scanning laser vibrometry”, Proceedings from the journal of the Institution of Mechanical Engineers: Part C *(Currently being corrected following peer review)*

R. Marks, A. Clarke, C. Featherston, C. Paget, R. Pullin “Optimising an acousto-ultrasonic sensor network using genetic algorithms with 3D scanning laser vibrometry and local interaction simulation approach data” – Journal of Non-Destructive Evaluation

Conferences

Marks R, Pullin R, Clarke A, Holford KM, Featherston CA, Kawashita L, Optimisation of acoustic emission sensor positioning on aerospace structures using 3D scanning laser vibrometry, *16th International Conference on Experimental Mechanics*, (2014)

Marks R, Clarke A, Featherston CA, Paget C, Pullin R, Sensor location studies for damage detection in aerospace structures using 3D scanning laser vibrometry, *ICAF 2015 Structural Integrity: Embracing the Future - respecting the past; supporting aging fleets with new technologies - Proc. 34th Conf. & 28th Symposium of the International Committee on Aeronautical Fatigue & Structural Integrity.* , (2015) 808-818 ISBN 9789513874421

Marks R, Clarke A, Featherston CA, Kawashita L, Paget C, Pullin R, Using genetic algorithms to optimize an active sensor network on a stiffened aerospace panel with 3D scanning laser vibrometry data, *Journal of Physics: Conference Series* , 628 (2015) ISSN 1742-6588 10.1088/1742-6596/628/1/012116

Marks R, Gillam C, Clarke A, Pullin R, Barely visible impact damage detection in a composite turbine blade using 3D Scanning Laser Vibrometry, *British Society for Strain Measurement Conference 2015*, (2015)

R. Marks, M Pearson, A. Clarke, C.A. Featherston, C. Paget, R. Pullin, Improved damage detection and location on aircraft structures using and inverted delta-t acoustic emission technique, Aerodays 2015, London, UK, 20th-22nd October 2015

R. Marks, M Pearson, A. Clarke, C.A. Featherston, C. Paget, R, Virtual delta-t mapping technique using a local interaction simulation approach for improved location of acoustic emission damage events for aerospace applications, British Society of Strain Measurement Postgraduate Conference of Experimental Mechanics, Southampton, UK,19th-20th November 2015.

1.9.Awards received for work submitted as part of this thesis

2016 – 3 Minute Thesis Cardiff Heat 2nd Place and ‘People’s Choice’ award

2016 – Institute of Engineering and Technology Present around the World competition, South East Wales local heat winner.

2016 – Institute of Materials, Minerals and Mining Technical outreach competition - Winner.

2016 – Institute of Materials, Minerals and Mining Young persons’ lecture competition, South East Wales winner, South West and South Wales winner and 2nd place at National Final.

2015 – British Society of Strain Measurement second prize in best paper competition at the postgraduate conference in experimental mechanics

2015 – CEAS Young Aerospace Researcher Competition (Aerodays2015) - Finalist

2015 – IMechE Western Aerospace Centre Communicating Engineering Excellence award

2015 – South Wales Institute of Engineers Education Trust David Douglas award

2. Background and Theory

2.1. Introduction

In this chapter, an overview is presented of the governing mechanics of Lamb waves which are used in both AE and AU systems and their derivation from first principles. This leads to a detailed explanation of the physical phenomena exhibited by Lamb waves and how these are important considerations when using Lamb waves for SHM considerations.

A detailed historical review of AE is then presented with a review of works where the phenomenon has been adapted for use as an SHM method. The source mechanisms of AE are also discussed. This is followed by a comprehensive review of studies that have used AE for monitoring the structural integrity of aircraft structures. This review highlights the challenges of applying AE to the monitoring of aircraft structures as well as the historical reluctance that has arisen as a result.

An in-depth review of location of AE sources is presented highlighting the wealth of different techniques that can be used to locate AE sources. The benefits and drawbacks of each location method are also discussed.

Previous studies and historical development of the AU technique is then presented. A particular focus was placed on reviewing studies where AU had been used for the monitoring of aircraft structures and materials. This leads to a thorough explanation of laser vibrometry and review of previous studies that have used laser vibrometry to sense Lamb wave propagation.

The modelling of Lamb waves using the local interaction simulation approach (LISA) is outlined with an in-depth review of the technique from its development in the early 1990s to recent developments and applications.

Lastly, different optimisation methods are discussed and brief explanation of the workings of a genetic algorithm is given. This is followed by a comprehensive review of the literature where sensor networks have been optimised for SHM applications.

2.2. Sound in solid media

Sound in solid matter has been the subject of study for many years. One of the earliest studies of waves propagating through solid media was conducted by Biot who measured the speed of sound in a 1000m iron rod; quantifying that the speed of sound through metal was vastly greater than that through air [33].

2.3.Bulk waves

As with many aspects of solid mechanics, there are many fluid mechanics techniques and methodologies that can be applied to understand solid mechanics problems. Considering wave propagation through a gas, the velocity of the wave can be directly related to its bulk modulus as shown in Equation (1). A full derivation from first principles is presented by Rienstra & Hirschberg [34].

$$c = \sqrt{\frac{B}{\rho}} \tag{1}$$

$where\ c\ is\ wave\ velocity, B\ is\ bulk\ modulus\ and\ \rho\ is\ density$

For the case of a solid material it is possible to substitute the bulk modulus for the Young's modulus as expressed in Equation (2). However, Equation (2) is only true for solids in the case where the waves propagate in a rod with circular cross-section and the wavelength is greater than that of the diameter of the rod [35].

$$c = \sqrt{\frac{E}{\rho}} \tag{2}$$

$where\ c\ is\ wave\ velocity, E\ is\ Elastic\ modulus\ and\ \rho\ is\ density$

Solids differ from gases however in that they are able to support both pressure (longitudinal) and shear (transverse) waves shown in Figure 6 (where it can be seen fundamentally shear waves can take the form of vertical shear waves (SV-wave) or horizontal shear waves (SH-wave)).

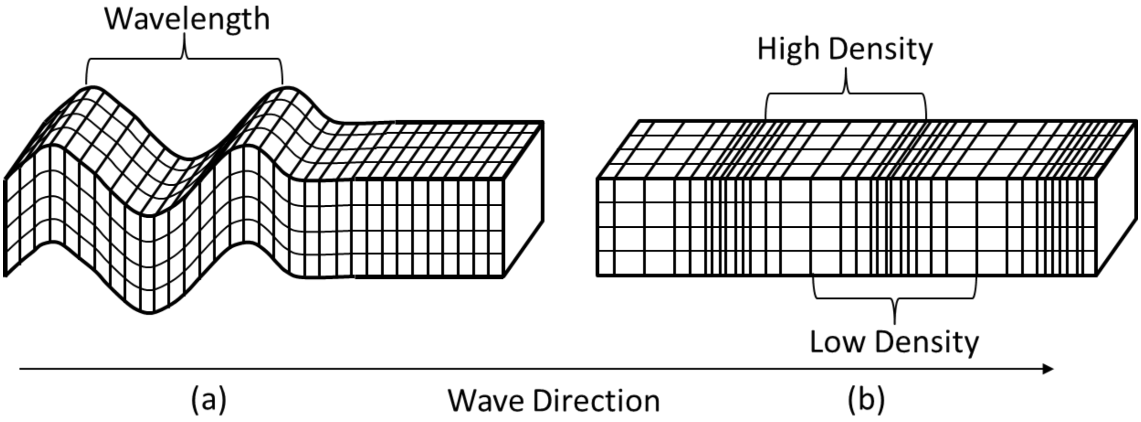

Figure 6. Two modes of bulk waves (a) Pressure wave, (b) Shear wave

To reason the two wave modes in terms of their velocities, a more appropriate substitution is Lame's constants given in Equations (3) and (4).

$$\lambda = \frac{Ev}{(1+v)(1-2v)} \quad \textbf{(3)}$$

$$\mu = \frac{E}{2(1+v)} \quad \textbf{(4)}$$

$Where\ E\ is\ Young's\ Modulus, v\ is\ Poisson's\ ratio\ and\ \lambda\ and\ \mu\ are\ Lame's\ constants$

Using Navier’s equations for displacement from fluid mechanics, a relationship for the displacement and Lame’s constants can be expressed as shown in Equation (5).

$$\mu \nabla \boldsymbol{u} + (\lambda + \mu)\nabla(\nabla \cdot \boldsymbol{u}) - \rho \frac{\partial^2 \boldsymbol{u}}{\partial t^2} = 0 \quad \textbf{(5)}$$

$where\ \boldsymbol{u}\ is\ the\ displacement\ vector\ of\ scalar\ components$

Assuming the bulk wave vectors for both the shear and pressure modes, Navier’s equation in Equation (5) can be rearranged and solved for each respective wave velocity. By substituting Equations (3) and (4) into Equation (5), velocities for the shear and pressure modes can be expressed as shown in Equations (6) and (7) respectively. A full derivation is presented by Schmerr and Song [36].

$$c_s = \sqrt{\frac{\mu}{\rho}} \quad \textbf{(6)}$$

$$c_p = \sqrt{\frac{\lambda + 2\mu}{\rho}} \quad \textbf{(7)}$$

It is evident from studying Equation (7) that the velocity of the pressure mode is significantly greater than that of the shear mode (over two times greater). By combining Equations (6) and (7) and substituting Lame’s constants it can be demonstrated that the ratio of the two mode velocities is proportional to the material’s Poisson’s ratio as demonstrated in Equation (8).

$$\frac{c_p}{c_s} = \sqrt{\frac{2(1-v)}{(1-2v)}} \quad \textbf{(8)}$$

It also can be seen that the defining equations do not consider the geometry of the material. Without imposing any boundary conditions it is therefore assumed that the material is infinitely thick. Hence, this type of wave is said to form in the bulk of the material and is known as a bulk wave or plane wave. With the assumption that the material is infinite, there are no considerations for reflections or refraction [37].

There are also no terms which define any characteristics of the wave such as frequency. It can therefore be stated that the velocity of the waves is independent of frequency; waves with such property are known as non-dispersive waves.

Since bulk waves form within thick materials, they are not typically used for SHM applications. However, the equations that define bulk waves can be expanded to derive wave solutions at the boundaries.

2.4.Rayleigh waves

With the introduction of a boundary, the pressure and shear bulk waves combine to form a Rayleigh wave as shown in Figure 7; first mathematically reasoned by Rayleigh in 1885 [38]. Considering the geometry of the material as a half space (in the sense that *x*, *y* and *z* dimensions are all vastly greater than zero) it is assumed that the surface of the material is at *z* = 0 and that the *z* dimension is 'semi-infinite' (meaning that the material is sufficiently thick that the wave does not form at the opposite boundary).

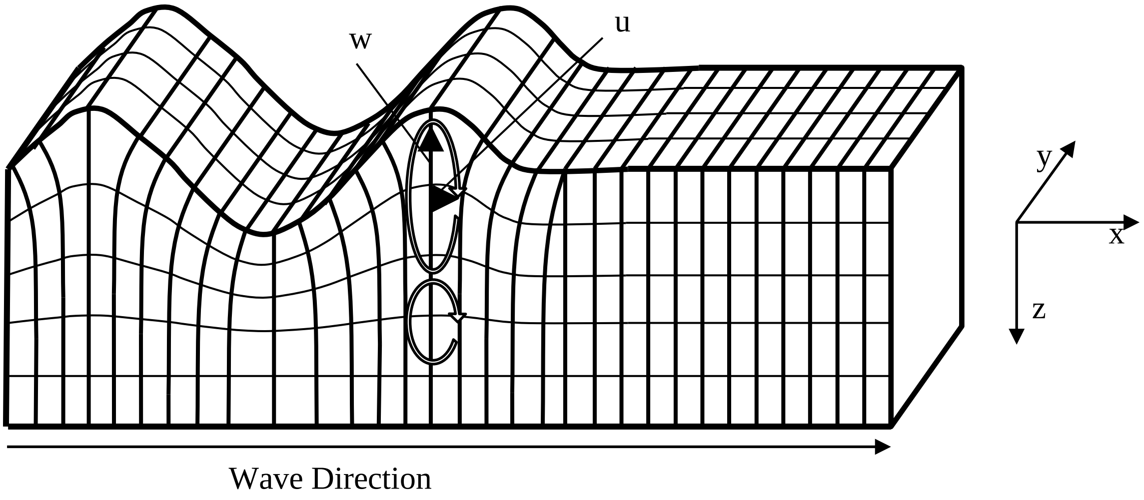

Figure 7. The schematic of a Rayleigh wave forming at that boundary of a semi-infinite solid.

Rayleigh waves can be visualised as the particles of the material rolling in an elliptical displacement path as the wave travels across the surface as depicted in Figure 7. As the depth of the material increases, the *z*-component of the ellipse decreases. Hence, the wave decays as *z* increases.

Considering a 2D Rayleigh wave (neglecting the *y*-dimension) with the wave propagating in the positive *x*-direction it is possible to derive the displacement of the pressure component (*u)*, shown in Equation (9) and shear component (*w)* shown in Equation (10). A full derivation is presented by Rose [37].

$$u = A(re^{-qz} - 2sqe^{-sz}) \cos k(x - ct) \tag{9}$$

$$w = Aq(re^{-qz} - 2e^{-sz}) \sin k(x - ct) \tag{10}$$

$$\text{where A is the amplitude,} \qquad \mathrm{k} = \frac{2\pi}{\lambda}; \tag{11}$$

where λ is wavenumber; and:

$$q = \sqrt{1 - \left(\frac{c}{c_p}\right)^2}, \qquad s = \sqrt{1 - \left(\frac{c}{c_s}\right)^2}, \tag{12), (13}$$

$$r = 2 - \left(\frac{c}{c_s}\right)^2 \tag{14}$$

In order to establish the velocity of a Rayleigh wave, a characteristic equation is imposed as shown in Equation (15). It can be demonstrated that there is only one real solution to the characteristic equation. This is known as the Rayleigh wave velocity. The full derivation of the characteristic equation is presented by Rose [37] and an in-depth discussion is presented by Worden [35].

$$\eta^6 - 8\eta^4 + 8\eta^2(3 - 2\zeta^2) + 16(\zeta^2 - 1) = 0 \tag{15}$$

where,

$$\eta = \frac{c}{c_s} \; and \; \zeta = c_s = c_p \tag{16), (17}$$

Rayleigh waves have an important role in SHM applications, particularly when monitoring structures such as concrete bridges and thick walled pressure vessels; however their use in monitoring of aircraft structures is somewhat limited. Though Rayleigh waves may be present in some aircraft components such as those used on landing gear linkages, they are not common. This is due to the aircraft structures typically being made up of thin skins with stiffeners attached to provide the required strength whilst minimising the mass of the structure [39]. In the case of thin geometries of the plate, Lamb waves form.

2.5.Lamb waves

Lamb waves (sometimes referred to as plate waves) are elastic guided traction free surface waves first mathematically reasoned by Horace Lamb in 1917 [40]. Though fundamentally different than bulk waves which occur in the bulk of the materials, Lamb waves are governed by the same set of differential equations [37]. Lamb waves are the result of bulk waves coupling at the surfaces.

To understand Lamb waves, the plate has to be considered as a 2D problem as shown in Figure 8 where the y-dimension is assumed to be infinite and the distance between the two surfaces is 2d.

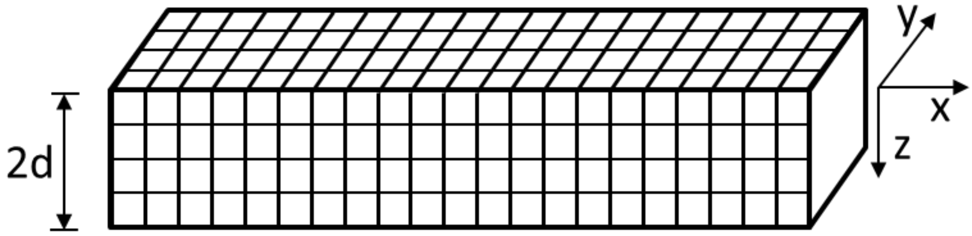

Figure 8. 2D representation of a plate where Lamb waves can form

Working through from first principles and applying Helmholtz decomposition [41] two solutions are found for the displacements; one symmetric shown in Equations (18) and (19), one antisymmetric shown in Equations (20) and (21).

For symmetric modes;

$$u = (ikA\cos(pz) + qBcos(qz))e^{ik(x-ct)} \tag{18}$$

$$w = (-qA\sin(pz) - ikBsin(qz))e^{ik(x-ct)} \tag{19}$$

For antisymmetric modes;

$$u = (ikC\sin(pz) - qDsin(qz))e^{ik(x-ct)} \tag{20}$$

$$w = (qC\cos(pz) - ikDcos(qz))e^{ik(x-ct)} \tag{21}$$

where;

$$p = \frac{\omega}{\sqrt{c_p^2 - c^2}};\ q = \frac{\omega}{\sqrt{c_s^2 - c^2}} \qquad \textbf{(22), (23)}$$

and A, B, C and D are arbitary constants

A diagrammatic representation of the symmetric and antisymmetric modes is presented in Figure 9.

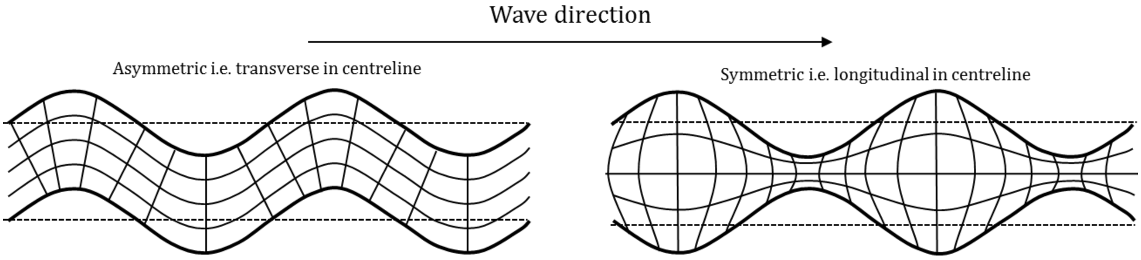

Figure 9: A representation of the two fundamental Lamb wave modes (a) Symmetrical Mode, S (b) Antisymmetric Mode, A [42]

By imposing the boundary conditions it can be assumed that the plain strain at the two surfaces is equal to zero [41]. This not only simplifies the analysis but defines Lamb waves as 'traction-free' surface waves. Applying this boundary condition to Equations (18) - (21), a matrix can be formed where for the arbitrary constants to be non-trivial the determinants of the two matrices must tend to zero. This leads to the Rayleigh-Lamb equations presented in Equation 24 for the symmetric modes and Equation 25 for antisymmetric modes. A full detailed derivation of these equations is presented by Rose [37] with further discussions by Raghavan [41] and Worden [35].

$$\frac{\tan(qd)}{\tan(pd)} = \frac{4k^2pq}{(q^2-k^2)^2} \tag{24}$$

$$\frac{\tan(qd)}{\tan(pd)} = -\frac{4k^2pq}{(q^2-k^2)^2} \tag{25}$$

The formation of Lamb waves occurs when internal modes combine to convert and reflect producing the different surface Lamb modes as shown in Figure 10 [36].

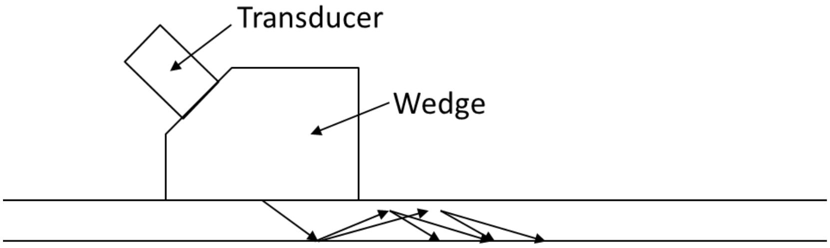

Figure 10: Coupling and conversion of internal modes to induce different Lamb wave modes

The use of a wedge in proportional to how much incident energy goes into generating a Lamb and how much energy goes into generating horizontal shear waves (SH waves). As the steepness of the angle of the wedge increases, the amount of shear energy increases and hence more shear waves are generated. The reader is referred to Rose [37] for detailed explanation.

2.5.1. Dispersion

Unlike bulk waves, it has been demonstrated that the velocity, *c*, of Lamb waves is related to the angular frequency, ω, presented in Equations (22), (23). This therefore means that the velocity of the wave is dependent on the frequency of the wave which can therefore be described as dispersive.

Considering Equations (24) and (25) it is also apparent that the thickness of the plate from the centreline, *d*, also influences the velocity of the propagating wave. This is known as the ‘frequency-thickness product’ [35]. Due to the presence of the tangential function in Equations (24) and (25), it is also possible for modes of higher order to be present and in theory, it is possible for an infinite number of modes to exist. In SHM applications however, only the two fundamental modes are usually excited (S_0 and A_0). If higher order modes are excited, their amplitude tends to be considerably less than that of the principle modes meaning that their use in SHM systems is limited [43]. Also, as higher modes tend to require higher frequencies (though they may be excited at lower frequencies in thicker plates) the constraints of the sensors (such as frequency response) and the acquisition system (such as sampling rate and available power) also have to be considered when assessing how practical their use is. Studies have however shown there are some advantages in using higher order modes, particularly for monitoring the microstructure of a material in a small region of a structure [44]. A representation of the calculated dispersion curves for a 3mm aluminium plate is presented in Figure 11.

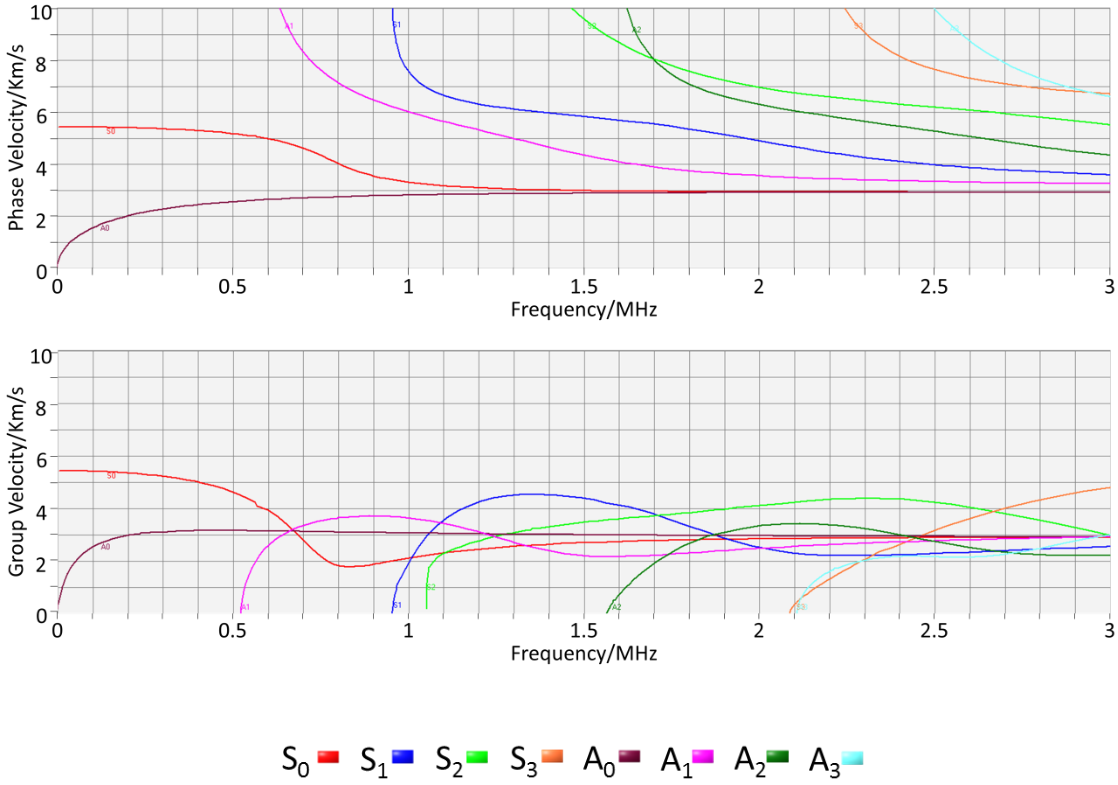

Figure 11. Example theoretical phase and group dispersion curves for the first four mode orders of a 3mm aluminium plate (calculated using Mistras Group Ltd (MGL). AE Win)

Figure 11 shows two dispersion curves; one for the phase velocity and one for the group velocity. From Equations (24) and (25), it is possible to derive the relationship for the phase velocity, c_{ph} which is defined as a function of the angular frequency and the wavenumber shown in Equation (26).

$$c_{ph} = \frac{\omega}{q} \qquad \textbf{(26)}$$

Group velocity, c_g, is defined as the derivative of the angular frequency with respect to the wavenumber as shown in Equation (27).

$$c_g = \frac{d\omega}{dq} \tag{27}$$

It is beneficial to represent phase and group velocity visually as shown in Figure 12. In this example, three wave packets are moving through the media with; phase velocity > group velocity. The red dot represents the phase velocity which moves along the dashed line. The group velocity is the velocity of the wave envelope which is represented by the green dot.

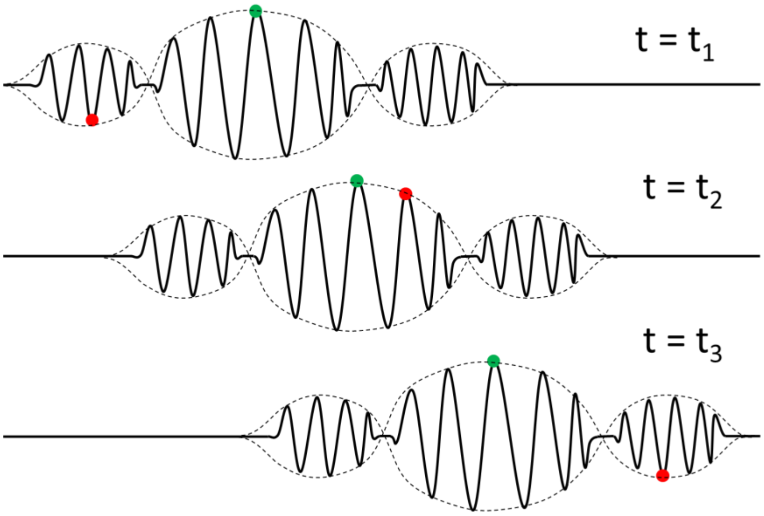

Figure 12. A visual representation of group (green) and phase (red) velocities in a dispersive media (note in this example, phase velocity is faster than the group velocity)

Though this example considers the situation where the phase velocity is greater than the group velocity, this is not always the case. This can been seen in Figure 11 for a 200kHz A_0 mode where the phase velocity and group velocity are approximately 2km/s and 3km/s respectively.

It is worth stating that these dispersion relationships are only true for isotropic media. In isotropic materials, the wave velocity is the same in all propagation directions. In anisotropic composite materials (as with fibre composites where the wave velocity is influenced by the wave direction), wave velocities can differ in differing directions (with the variation is typically dependant on the mode).

One solution for the case of dispersion in anisotropic materials is to produce dispersion curves for varying angles as presented by Rose [37]. Though this technique attempts to characterise the dispersive properties in an anisotropic material it is difficult to fully determine the dispersion in all directions. In addition, anisotropic materials exhibit a dispersion characteristic called beam-skewing where the vectors of the group and phase velocities are not parallel. A comprehensive review of studies investigating dispersion calculations for composites is presented by Eaton [43].

2.5.2. Attenuation

Attenuation is the phenomena of the loss of energy as a wave travels through a material. This is typically represented by a reduction in the amplitude of the wave. This can be attributed to five main causes [45];

- Geometric spreading – Geometric spreading can be defined as the loss of wave energy as a wave propagates. If a circular wave front is considered in an isotropic material, as the wave front travels away from the source, the circumference of the circle increases and hence the wave energy is spread over a larger region. Due to this, geometric spreading is the predominant mode of attenuation in the near-source field.
- Internal friction – Attenuation of the wave due to internal friction is the result of particle movement within the microstructure resulting in the generation of thermal energy. Internal friction contributes to the attenuation more in composites than in metals. This is due to the viscoelastic behaviour of the material, friction between surfaces and incompletely bonded fibres [43]. Internal friction causes the wave to attenuate exponentially and is more severe with higher frequency waves and is the biggest source of attenuation in the far-from-source field.
- Wave dispersion – Wave dispersion can cause the wave to attenuate as it propagates away from the source causing the amplitude to reduce. This is mostly dependent on the source length, and the gradient of the dispersion curve.
- Scattering – Scattering occurs within the microstructure; typically in metallic materials at grain boundaries or surface corrosion [46] and at changes in fibre directions in composites. Scattering can cause the wave energy to be partially reflected.
- Dissipation of the wave into adjacent media – As a wave comes into contact with adjacent media the wave energy can be partially absorbed. This attenuation is mainly concerned with solid-fluid interaction and is not something that has a strong influence on the studies presented in this work. However, this is a consideration that should be made particularly for the monitoring of space structures where the wave energy would not be absorbed by the surrounding layer of air.

2.5.3. Mode conversion of Lamb waves

Where there is a change in the material thickness, acoustic impedance or the presence of a defect or feature, it is possible for a Lamb mode to convert to another mode. This phenomena is known as mode conversion. Alleyne and Cawley [47] studied the interaction of Lamb waves with notches in a plate experimentally and identified mode conversion behaviour. Cho [48] investigated mode conversion at thickness changes of the material numerically using a boundary element method (BEM). Cho demonstrated that changes in thickness, particularly through a joint or a change in thickness due to a defect can result in different guided wave behaviours including reflection, transmission and mode conversion. The work presented was further supported by experimental validation. Lemistre and Balageas [49] also experimentally investigated the mode conversion phenomenon of Lamb waves interacting with a delamination in a composite panel based on a working hypothesis derived from the work of Han *et al.* [50]. The work demonstrated that the diffraction effect exhibited by interaction with the defect did indeed induce mode conversion. Changes in wave mode can cause issues with the detection of Lamb waves, in particular for systems that primarily detect one wave component.

2.6.Acoustic Emission

AE has been defined by Miller and McIntire [51] as 'The elastic energy spontaneously released when materials undergo deformation'. As a result, transient elastic waves are generated which in the case of plate-like structures (such as those that make up aerospace structures) manifest as ultrasonic Lamb waves. An AE signal is usually defined as any stress-wave signal resulting from deformation with frequency content within the range of 10kHz – 1MHz [21]. By mounting sensors on a structure it is possible to detect the AE signals and hence the presence of damage. AE is defined as a 'passive' monitoring technique as there is no requirement for an external input to assess the structural integrity.

One of the earliest accounts of AE in the audible range was from Cornish tin miners who heard what they described as 'knocking' sounds from the wooden props in the mine which gave an early indication of mine collapse. This was forged into Cornish folklore where it was believed that these sounds were made by small pixie-like creatures known as 'Knockers' and the miners were said to leave the crust of their Cornish pasties for the knockers as offerings to ensure the early warnings of mine collapse continued [52].

In the 1940s and 1950s, interest grew in understanding the 'knocking' in mines, particularly those related to rock bursts. The main bodies of this work were conducted in Canada by

Hodgson and Gibbs [53, 54] and in the United States by Obert and Duvall [55-58] who looked into using sub-audible ‘microseisms’ generated in the rocks to detect and predict the event of rock bursts.

What is regarded as modern AE technology was first studied by Kaiser [59] in 1950 when the AE of irreversible strain in metals was demonstrated. In this study, Kaiser demonstrated that AE was irreversible; when the specimen was unloaded and then reloaded no AE was generated until the material experienced a stress level higher than that previously experienced. This has come to be known as the ‘Kaiser-effect’. The term ‘Acoustic Emission’ was first used in the 1950s by Schofield [60] who in 1963 investigated AE in metals with oxide layers under an applied load. It was found that the source of the AE was not from the oxide layer but the presence of the layer did influence the AE propagation.

Schofield [60] and Tatro [61] are credited with making significant advancements in the late 1950s and 1960s to improve the instrumentation for detecting and locating AE generated during plastic deformation. During the 1960s, AE was applied for first time for assessing the integrity of structures. In 1963, Dunegan [62] used AE for the first time to monitor pressure vessels. It was during this series of studies that great advancements were made in the instrumentation, and as such, Dunegan founded the world’s first company to supply commercial AE equipment. In 1964, Green *et al*.[63] used AE in conjunction with the US Navy to assess the structural integrity of Polaris rocket motors; probably the first aerospace application of the technique.

By the 1970s, many working groups were formed to research and develop AE techniques, with a range of pioneering works conducted. However, the decline of heavy industry and the poor economic climate in the 1980s and 1990s saw a decline in the application of AE technologies as it was seen that the implantation of the technology would be more costly than traditional NDT techniques [64]. This, combined with the miss-selling of AE as a suitable SHM technique for complex materials and structures whilst the technology was still immature in the early 1980s, resulted in a distrust in AE monitoring [65]. A full historical review of breakthroughs in AE is presented by Drouillard [64, 66].

This historic distrust in AE has resulted in a lack of faith in the technology particularly in the aerospace community who choose over-engineered structural design solutions and traditional NDT techniques over AE monitoring. However, recent computational developments have enabled AE technologies to make great advancements with studies being conducted that are showing great potential for the monitoring of aircraft structures using AE [67, 68].

2.6.1. AE source mechanisms

There are many mechanisms associated with the generation of AE. As previously discussed, rock bursts are a naturally occurring mechanism of AE that formed one of the earliest set of AE studies. In the application of aerospace materials such as aluminium alloys and carbon fibre reinforced plastics (CFRP) there are a wide range of source mechanisms. Pao [69] attributed AE activity to microscopic activity such as dislocations, microcracks and phase transformations. Other sources of AE have been identified as including crack growth, twinning, grain boundary sliding and the fracture and decohesion of inclusions [51] and, for composites, fibre failure, fibre pull-out, fibre/matrix debonding, matrix microcracking, transverse matrix cracking, splitting parallel to fibres and delamination [43]. It is worth noting that these mechanisms are not independent. In complex scenarios it may be the case that two or more of these mechanisms combine to generate the AE source.

AE sources can be described as either transient waves (also known as burst waves) or continuous waves. Typically, only transient waves are used in SHM as they are generated by the source mechanisms previously mentioned. Transient signals have a start and end point and hence it is possible to determine the arrival of a wave. Continuous signals are typically used for the monitoring of gears, bearings and hydraulics where the signal continues for as long as the machine is in operation.

In terms of AE source mechanisms in aerostructures in-service, AE can be generated by a range of damage events including bird strikes, hail damage, lightning strikes and various mechanical failures.

2.6.2. Applications of AE for monitoring aircraft structures

There have been many applications using AE to monitor aircraft structures during in-flight testing and lab based testing. The first in-flight test that used AE was conducted by Lewis Jr. *et al.* [70] in the 1970s. The test was conducted on a Lockheed C-5A where AE noise was monitored at nine locations which included the wing, empennage and landing gear over four flight tests at three different altitudes to establish the signal-to-noise ratio and assess AE as a technique for in-flight monitoring of aircraft structures. The tests used off-the-shelf, commercially available AE equipment with 40dB preamplifiers and a Lockheed designed spectrum analyser. In addition, the tests aimed to detect the presence of crack growth during flight. It was found that the structure-borne noise did not prevent the use of AE for in-flight testing providing that the system operated within the 0.5MHz-1MHz range. The highest level of noise was found at the landing gear though it was stated that it was still possible to achieve a signal-to-noise ratio of 2:1. From the results of the noise study, it was concluded that AE could be used to detect the crack growth. However, the authors state that the laboratory equipment could be improved upon to consider the in-flight environment (i.e. power requirements, electromagnetic interference and temperature changes).

Further in-flight testing of AE was conducted on a Boeing KC-135 tanker aircraft by Mizell and Lundy [71]. This study built upon the work previously conducted by Lewis Jr. *et al*. [70]. This study used a bespoke thirty-two channel narrow band AE system which operated around a central frequency of 250kHz. The area of the aircraft that was focused upon was the lower central wing panels which were made from 7178-T6 aluminium alloy. The brittle nature of the material was a cause for concern at the time as it was reported that cracks up to seven-feet long had been found on this aircraft type. The parameters of the AE system were carefully selected to detect AE bursts with the characteristics associated with crack growth in this particular grade of aluminium. Compensation for other parameters such as cable impedance and temperature were also considered. Due to the narrow band considered it was found that crack growth less than two inches long could not be detected. The study concluded however, that the early detection was sufficient to prevent failure of the structure and that, at the time of the publication, the technology was being rolled out to the US Air Force KC-135 fleet. A publication by Carlyle *et al.* [72] however, stated that the application of AE technology to the KC-135 had had a negative impact on the widespread adoption of the technology. This is because the signal processing techniques did not eliminate the noise and false alarms were being triggered, alerting pilots to damage that was non-existent. Carlyle also states that AE was used to monitor a bulkhead that was thought likely to fail on a Grumman F-14 Tomcat during a full scale fatigue test. The AE system and setup failed to detect the presence of damage even after catastrophic failure. This was observed by a high ranking Admiral of the US Navy which prevented the roll out of the technology within the US Navy. Instances such as this, Carlyle suggests, have caused poor impressions at high management levels which has resulted in a widespread reluctance to the development of AE technologies within the aerospace community. However, this reluctance has been built on the experience of a few poorly executed projects.

A Canadian study was conducted by McBride [73] investigating the monitoring of crack growth in the wing of an Avro Canada CF-100 during sixty hours of flight. The AE system used in this study was a single channel system which measured transient AE in the frequency range of 0.1MHz to 1MHz. The test aircraft had a known 3mm crack in the wing trunnion which from previous NDE had been found to grow at a rate of approximately 5μm per flying hour. Due to high levels of noise, it was not possible to distinguish AE from the crack growth based on amplitude methods alone. However, through using frequency analysis McBride was successful in distinguishing the AE from the crack growth. With supporting evidence from laboratory testing, it was found that the detection of AE from the crack growth related to approximately 1mm^2 of new fracture surface. It was also established when comparing the data with flight data recordings that the crack growth took place during the high loading conditions experienced during take-off. The drawback to this approach was the massive amounts of data that were required to be recorded for successful detection and the computation requirements particularly considering the computational technologies of the time of publication (1979).

In-flight AE testing of the centre wing section tension member of a Macchi MB326 was conducted by Hutton and Skorpik [74]. From the experiences of the operators of this aircraft type, fatigue cracks were known to originate from the holes in the tension member and to demonstrate the aircraft's airworthiness, inspection intervals of one hundred hours were required using traditional NDE techniques. A bespoke two-channel AE system was designed with 400kHz transducers to monitor a hole where many surface cracks totalling 7mm in length were present. High levels of AE resulting from crack growth were observed when the aircraft was conducting low-level flying and aerobatics (due to high loads experienced during the high-energy manoeuvres). It was found that the crack grew at an approximate rate of 0.16μm per AE event. The effects of noise were successfully mitigated by measuring AE at a separate location which acted as a noise compensator.

An aircraft that has been the subject of many full scale AE investigations is the Vickers VC-10 [75-77]. Though primarily designed as a commercial airliner, the VC-10 was converted to a tanker-transporter for use by the Royal Air Force (RAF). Work by Hoyle [78] states that the VC10 was a subject of interest as it was an aging aircraft where, in extreme cases, individual aircraft had experienced in excess of 45,000 flying hours and 16,000 flight cycles. The motivation for the investigation came from the discovery of fatigue cracking on the aircraft's main spar which was not in-line with the expected fatigue damage which was in-turn based on questionable engineering data.

To investigate damage in the fuselage, proof-pressure testing was conducted on a VC10 fuselage. During the proof-pressure testing, the fuselage was monitored for the onset of damage. The main goal was to prevent catastrophic failure of the fuselage. In this case AE was not used to supplement the traditional NDT inspections but to act as a fail-safe. Skinner [79] expanded on the use of AE during the proof-pressure testing using piezo-ceramic sensors mounted on the outside of the structure, placed in a pattern to allow damage triangulation. The sensors were located around areas of interest such as the pressure bulkheads and were calibrated while the aircraft was under static load. The study concluded that AE was a useful tool in the assessment of the structure while also saving time, cost and the human error associated with traditional NDT methods.

One of the most recent studies was conducted by Hill and Rovik [68] who monitored fatigue crack growth in-flight using AE on a Cessna T-303 Crusader. In this study, a 7075-T6 aluminium alloy channel section was notched and cyclically loaded in the laboratory with AE captured throughout. The AE data captured was characterised into three groups; fatigue cracking, plastic deformation and rubbing noise. Using this data, a neural network was trained to identify the AE signals from the respective damage mechanisms. A similar channel section was installed as a 'redundant' member in the vertical stabiliser and was instrumented with transducers to monitor the onset of damage (in this study the installed member was referred to as 'redundant' in the sense that that it was additional structure. This does not mean that it did not undergo loading as the load was distributed between the 'redundant' member and the neighbouring members which resulted in the structure having a higher stiffness than required). AE signals were recorded for different aspects of flight including taxiing, take off, straight and level flight and a series of Dutch rolls (a manoeuvre where the aircraft oscillates in yaw). It was found that plastic deformation occurred throughout all aspects of the flight but was most prevalent during taxiing. A high level of fatigue signals were measured when the Dutch rolls were carried out and low levels of rubbing noise were present during the flight. The effects of background noise were reduced by using a high pass filter. The authors claimed that the flight testing was a great success. However, it is questionable, based on the experiences with noise from previous in-flight testing, whether background noise was miss-classified as a damage mechanism.

2.6.3. Acoustic Emission Source Location

By installing a network of sensors on a structure, it is possible for AE events to be located. Traditionally this has been achieved by using a 'time-of-arrival' (TOA) method. The TOA location method uses an estimate of the damage location which it then compares with the measured data. By an iterative procedure, the TOA algorithm converges onto a solution for the AE source location. This has been proven to be successful in studies on flat plates made of isotropic materials [51]. However, the algorithm is not capable of being able to take into consideration the complexities introduced when considering anisotropic materials where wave velocities are different in different directions [80] as in the case for a fibre composite material. In addition, the algorithm does not take into account features on the structure such as holes, thickness changes, mechanical fasteners and stringers which all influence the propagation and attenuation of the waves [81]. This, combined with errors due to premature triggering and dispersion effects [82], typically causes the TOA algorithm to locate AE events (and hence damage) at incorrect locations on the structure leading to a 'false positive'. The low success of location by the TOA algorithm has been one of the main inhibitors to the wide scale adoption of AE systems on in-service aircraft.

There have been many studies conducted to improve the accuracy of location of AE sources for applications on complex structures. One method is the signal sensor modal analysis location (SSMAL). This method uses information on the dispersive characteristics of the component being monitored. By post-processing the signal received by a single broadband sensor it is possible to separate the different Lamb wave modes based on their frequency content. As the symmetrical component travels faster, and therefore is first to arrive at the sensor, it is then possible to locate the source by interrogating the dispersion curves. Dungan [83] used this technique to locate AE sources within an 700mm x 600mm aluminium plate and it was found that the location of the sources at best were found to be within 3.2mm of the actual location however minimal results were presented. Maji *et al*. [84] used the SSMAL technique to evaluate steel beams and plates. This was successful in terms of linear location and in the case of a steel beam could identify two potential locations for the source. As with the TOA method, this technique assumes a completely continuous structure whilst also requiring prior knowledge of the structure's dispersive characteristics; something that is not easy to establish particularly in composite structures. In addition, the size of the source-sensor distance has to be large enough to ensure that the Lamb wave modes are fully formed which leaves a 'black area' surrounding the sensor where sources cannot be accurately located.

The idea of using the dispersive characteristics of Lamb waves was expanded by Mostafapour *et al*. [85] to enable planar location of AE sources using multiple sensors. Through the use of wavelet transforms and cross-time frequency spectrum (CTFS) the location of AE sources on a 3mm thick steel plate was determined using four sensors. The location of the sources were found to have a percentage error between 1.3% and 3.5% which was significantly lower than the error found when using a cross-correlation technique previously used for AE source location by [86]. Though a high level of location accuracy was achieved in this study, prior knowledge of the structure is still required and the presence of features on the structure were not considered which may have significantly affected the location accuracy.

Paget *et al*. [87] made attempts to address the problem of locating AE signals in composite materials where the wave velocity is related to the fibre direction. Their method assumed an elliptical wave front with differing wave velocities in two directions. The results presented demonstrated good potential however, the method still required longitudinal and transverse group velocities to be known and also assumed that the monitored structure was continuous with no features present.

Work has also been conducted to use an array of three sensors to locate AE sources. Aljets *et al*. [88] coupled a triangular array of three sensors to a carbon fibre reinforced plastic (CFRP) plate. AE sources were created at the nodes of a grid on the plate and a Gabor wavelet transform was used to separate the arrival of the S_0 and A_0 modes based on their frequency content. By comparing the difference in arrival times between the three sensors for known locations, the angle and distance (by adapting the SSMAL method) of the AE source from the triangular array could be determined with a good degree of accuracy. This study showed great potential for monitoring composite materials without the requirement of prior knowledge of the dispersive characteristics. In addition, the small sensor array has many benefits for SHM applications on aircraft as it reduces cable routing. However, it has not been proven that this method would be as accurate when features are present on the structure.

Delta-T, first developed by Baxter *et al*. for source location in aircraft landing gear components under verification testing [65], has shown a lot of potential particularly for complex aerospace components for improved AE source location [30, 89]. The technique involves drawing a grid onto a structure which serves as a layout for training the sensor network. The sensor network is then trained by creating representative AE sources (called ‘Hsu-Neilson’ (H-N) sources) by breaking pencil leads at each node on the grid. By calculating the difference in the time of arrival of the H-N source between a sensor pair it is possible to create a dataset of difference in time of arrival for each node on the grid for each sensor pair. Once training is complete, these datasets can be interrogated to locate the source of AE events on a structure. A process diagram for the Delta-T technique is presented in Figure 13.

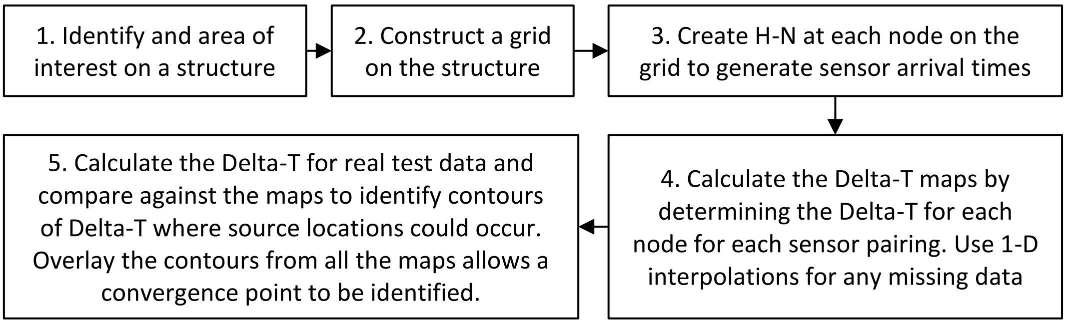

Figure 13. Delta-T Mapping Technique

The findings by Baxter *et al.* showed a reduction in location error from 4.81% to 1.77% for locating H-N sources at random locations across a component when compared to that of the TOA method.

A drawback to the Delta-T technique is the determination of the arrival time of a wave; a similar problem to that of the TOA technique, as a thresholding technique was used. This was a source of error particularly for low amplitude AE signals where the time of arrival can be falsely identified as the arrival of the A_0 mode and not the S_0 mode. Similarly, with high amplitude signals, error can arise in that the point at which the wave crosses the threshold is actually after the wave arriving. Pearson *et al.* [90] improved upon this technique by incorporating the Akaike Information Criteria (AIC) for determining the arrival of the AE signal. By using AIC improvements to AE source location of 75% were seen over the tradition delta-T technique locating the damage to within 3mm of the actual location.

2.7.Acousto-Ultrasonics

AU, also known as guided waves, is an SHM technique where a Lamb wave is excited using an actuator (usually a piezo transducer) at a site using some form of electronic signal. This Lamb wave travels across the surface of the structure and is then detected by a sensor (or sensors) mounted at other locations on the structure. If damage occurs in the actuator-sensor path it is likely that the Lamb wave will interact with the damage and thus a different signal will be received by the sensors. In many cases, the transducers need to have the ability to both actuate and sense. In addition, some transducers have the ability to sense AE signals as well, making some setups dual purpose. Unlike AE, AU is an ‘active’ monitoring technique since an external input is required in order to assess structural integrity. This also means that the power requirements for AU systems are vastly greater than those of an AE system. A drawback of AU is that it can only periodically monitor the structure unlike AE where the monitoring is continuous. However, AU has the ability to conduct inspection of large areas quickly at relatively low cost (particularly in areas which are difficult to inspect with traditional NDT techniques).

Though it could be argued that the concept of using acoustic waves to detect defects is a technique used throughout the ages by tapping a component and listening to its response, excited ultrasonic waves have only been used for the last forty years. This technique (commonly called ultrasonic-acoustic or stress wave factor at the time) was first studied at the NASA Lewis research centre by Vary and Bowles [91] and Vary and Lark [92] in the late 1970s. These initial studies were conducted to investigate whether materials and defects could be characterised and this proved to be successful. The technique saw many advances throughout the 1980s [93-96] particularly in the reproducibility of signals and the coupling of actuators and sensors. As the 1980s drew to a close the technique was being adopted globally for material characterisation.

The first application of AU for assessing adhesively bonded joints in aircraft structures was conducted in Canada by Fahr *et al.* [97-99] in the early 1990s and such joints have been the subject of many AU investigations since. The use of AU for in-situ monitoring was first published in work by Tiwari *et al.* [100]. The work used AE as well as AU to assess the onset of micro-cracking in composites subjected to mechanical testing. A comprehensive historical review of AU technologies is presented by Drouillard and Vary [101].

Within the aerospace industry AU has been heavily investigated for the Non-Destructive Evaluation (NDE) of aircraft structures and components. Rose and Soley [102] presented a summary of various studies which used AU for the detection of defects in aircraft components (including cracks in helicopter blades, corrosion and cracks in multilayer media and skin de-bonding of honeycomb sandwich panels). Lamb wave interaction with fuselage wall thinning was also investigated. By comparing the frequency content of the received signals of a thinned section and a section of the fuselage where thinning was not present using a Fast Fourier Transform (FFT), it was found that there were significant changes in frequency content indicating the presence of mode conversion.

The integrity of lap splice joints was also investigated using AU techniques [103]. The importance of excitation frequency was discussed as well as the transmission of Lamb waves through the bonds. An actuator was positioned on one side of the joints with a sensor on the other. By comparing the amplitude of the signals received from good and poor adhesive bonds it was possible to determine the integrity of the bond based on the amount of Lamb wave energy transmitted.

A study on inspection of adhesively bonded tear straps from a Boeing 747 was also presented by Rose *et al.* [102, 104]. This study used the aircraft's skin as a wave guide and used a pulse-echo technique to inspect the integrity of the bond. Results from the echo showed a difference in the reflected wave packet as the integrity of the bond reduced. When the bond had failed, no echo from the tear strap was received.

In recent years, there have been many advances and further applications of AU technologies. An exciting application of AU for the detection, location and monitoring of defects on an aircraft wing was presented in work by Zhao *et al.* [105]. In this study a circular network of eight actuator/sensor transducers (approximately 30mm in diameter) were mounted on the inner surface of a section a Northrop Grumman E-2 wing. Within the circular network many structural features were present including rivets and stiffeners as well as structural defects. Using a correlation analysis based on a probabilistic approach the received signals were processed and an estimation of the defect size and location was successfully calculated.

Successful use of AU Lamb waves to detect the presence of impact damage on a scale carbon fibre wing structure was reported by Pullin *et al*. [106]. Measurements of Lamb waves were taken pre and post impact using macro-fibre composite (MFC) transducers. By using the pre-impact measurements as a baseline, a quantitative comparison of the received waveforms was made using a cross-correlation technique. The analysis showed a significant change in the wave form by a reduction in the cross-correlation coefficient as well as demonstrating the potential for energy harvesting using acousto-ultrasonic Lamb waves.

A comprehensive review of AU technologies and their used for damage detection in composite structures is presented by Su *et al.* [107].

2.8.Lamb wave measurement using laser vibrometry

Laser vibrometry (also known as laser doppler vibrometry or a laser velocimetry) is a technique that compares the doppler shift between a reference laser beam and that of the backscatter of a laser beam focused on the component under investigation. Figure 14 shows the internal layout of a scanning laser vibrometer. The light from a heterodyne laser is split with part of the laser passing through a Bragg cell (which provides a stable carrier frequency) and into the detector which acts as the reference signal. The other half of the beam is aimed at the component under investigation (the steering mirror enables the beam to be easily aimed at many areas of the component during one measurement). As a component vibrates the wavelength of the laser light changes with the wavelength increasing as the material moves away from the vibrometer and the wavelength decreasing as the material moves towards the vibrometer. This is known as the doppler effect. The light that is backscattered toward the vibrometer is guided through the vibrometer to the detector. A comparison of the wavelengths of the reference beam and the backscattered light can then be made which is directly proportional to the velocity of the vibration.

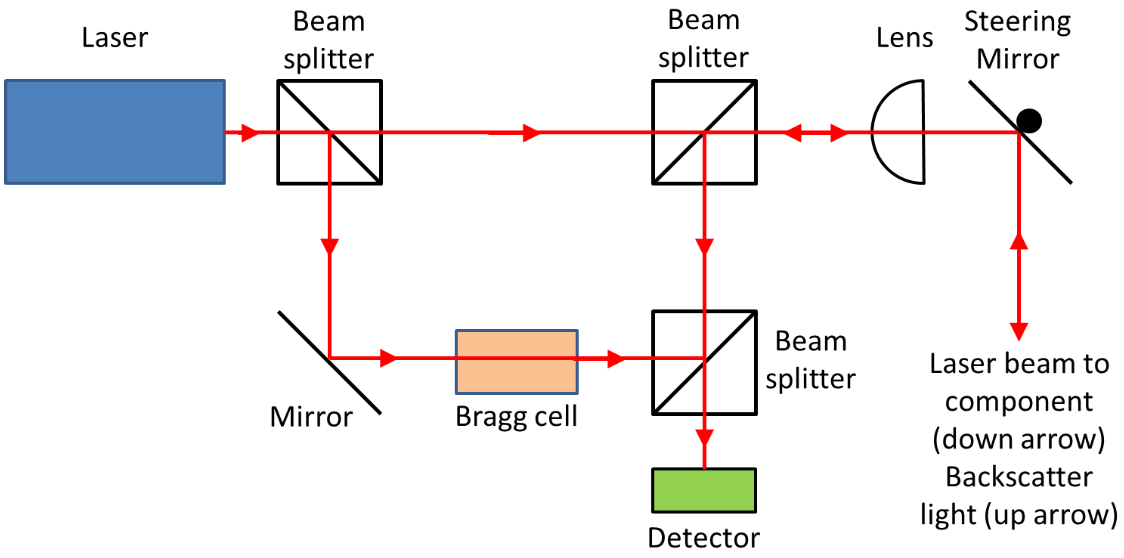

Figure 14. The internal layout of scanning vibrometer

Through the use of the scanning mirror, many measurements can be taken over a component. By using false colour imaging and vector mathematics it is then possible to combine these measurements to construct a visual representation.

A comprehensive and detailed explanation of the theory of laser vibrometry is presented by Polytec [108]. An explanation on the physics associated with laser vibrometry including mathematical reasoning is presented by Halkon [109].

The AU technique requires an actuator/sensor network typically coupled to the surface of the structure or, as in the case of MFCs, embedded into the material. It is possible to substitute the receiving sensor for a laser vibrometer to measure the Lamb wave signal. This has many advantages over the use of mounted sensors to receive the signal which include;

- No mass damping – as no sensors are attached to the structure, there is not any influence due to mass damping which can affect wave propagation.
- Broadband/wideband frequency response – mounted sensors have a designed frequency response. As the bandwidth of light can be assumed infinite (for this application at least) laser vibrometers have a broad frequency response.
- Transfer function of unity – Mounted sensors have a transfer function as the Lamb wave energy is converted to an electronic signal. This means that the signal measured is not necessarily the signal that was present on the structure. As a vibrometer measures doppler shift, it can be said that the transfer function is unity.

Laser vibrometers were first developed as a measurement tool in the 1980s. Early vibrometers had limited sensitivity and low signal-to-noise ratio (SNR) which meant that their application was limited. It was not until the 1990s with substantial advances in computation that the instrumentation became mature enough for widespread use [110]. Laser vibrometry has been used in a wide range of applications from measuring the speed of sound in spider silks [111] to measuring the motion of inlet valves on a motorcycle cylinder head [112].

As vibrometry technology advanced further towards the end of the last century it reached a level of maturity that made it possible to measure ultrasonic elastic waves. The first study of the use of laser vibrometry to measure ultrasonic elastic waves was conducted by Nishizawa *et al.*[113] who used a laser vibrometer to measure shear waves in a steel block.

The out-of-plane component of Rayleigh waves was measured in steel and aluminium alloy by He and Kobayashi [114] using laser vibrometry. The measurements were taken at two points on the materials 40mm apart and recorded using a digital oscilloscope. From the measurements recorded, the stress-acoustic coefficients were calculated and were found to be consistent with values calculated from measurements using surface mounted piezo transducers.

One of the first studies to measure Lamb waves with a scanning laser vibrometer was conducted by Kehlenbach *et al.* [115]. The study focused on constructing a finite element model (FEA) using the commercially available software ANSYS to investigate Lamb wave interaction with defects in an aluminium plate. The motivation for this study was to improve the damage localisation and characterisation capabilities of AU sensor networks. To validate the computational models, a scanning laser vibrometer was used which measured the out-of-plane component of the Lamb wave. It was noted by the authors that the A_0 mode was more dominant, having a much greater amplitude than the S_0 mode in the laser vibrometer results. This was justified as the A_0 mode has a greater out-of-plane component. The numerical results showed good correlation with the experimental results.

One of the earliest studies to use scanning laser vibrometry to investigate Lamb waves in composites was conducted by Maslov and Kinra [116]. The study investigated the use of laser vibrometry as a long-rang ultrasonic technique for the non-destructive evaluation of glass/epoxy composite tubes with Lamb wave excited by a dry contact piezoelectric transducer. The authors identified that the sensitivity of the vibrometer was a factor to ensure that meaningful results were obtained and that at 140kHz (the peak frequency used) the signal-to-noise ratio became unacceptably small. As a result, a maximum distance of around 1m from the transmitter to the receiver was found. Signal processing techniques such as Fourier transforms in the space domain established a high-speed technique of determining the presence of damage.

The first fully comprehensive study of the use of Lamb waves for damage detection was conducted by Staszewski *et al*.[117]. The study sensed the out-of-plane component of relatively low frequency Lamb waves using a commercially available single point laser vibrometer. The measurements taken with the vibrometer were validated with transducers bonded to the structure and were verified using a finite difference (FD) simulation. It was found that the signal measured with the vibrometer could be refined by post-processing the signals using Kaiser-Bessel filters, Savitzky-Golay filters and wavelet-based de-noising. The study concluded that laser vibrometry was a suitable method for measuring Lamb waves.

A further study into the measurement of Lamb waves for damage detection using laser vibrometry was conducted by Mallet *et al.* [118]. The focus of this study was to use laser vibrometry to investigate the out-of-plane component of Lamb wave interaction with notches in an aluminium plate. As with the previous study, numerical simulation was conducted using a FD package to support the experimental results. Several measurements were taken over the surface of the aluminium plate and the peak-to-peak values were plotted. These plots highlighted the location of the notches and demonstrated how the Lamb wave propagation path is influenced by the presence of damage.

Lamb wave fatigue crack growth was evaluated using Lamb waves and sensed using a laser vibrometer by Leong [119]. In this study an aluminium plate with a spark eroded notch was subjected to cyclic loading to induce a fatigue crack. Lamb waves were induced using a commercially available transducer bonded to the surface of the plate and the out-of-plane component of the Lamb wave was measured at points across the plate. Measurements of the Lamb waves were taken prior to the cyclic loading and at three intervals in the cyclic loading as the fatigue crack grew. Peak-to-peak amplitude values for the measured waves were calculated and plotted to demonstrate the effect of the fatigue crack on the Lamb wave propagation and hence to determine the location of the crack. The study concluded that through the use of laser vibrometry, local amplitude and time of flight variations could be calculated for the near field that would be difficult to achieve with traditional mounted transducers. A closing remark was made suggesting that the sensitivity of the Lamb waves to the damage could be achieved by increasing the excitation frequency.

The out-of-plane component of a Lamb wave was sensed and analysed using scanning laser Doppler vibrometry by Radzieński *et al.*[120] to successfully detect damage in a stiffened panel. Experimental work was carried out to detect the voids left by the absence of rivets used to attach a t-shaped aluminium stiffener to a flat aluminium plate. The plate was excited by a lead zirconate titanate (PZT) transducer with a 5-cycle sine wave multiplied by a Hann-window at frequencies of 5 kHz, 35 kHz, 100 kHz and random noise. By calculating the root mean square (RMS) of the signal received at each measurement point it was possible to generate a visualisation that clearly showed the absence of the rivets. The best visualisations were found to be obtained from results taken at higher frequencies.

Out-of-plane measurements of Lamb wave interaction with delaminations in a composite plate as a result of impact damage and disbonds of a composite spar were sensed using a laser vibrometer by Sohn *et al*. [121]. In this work, frequency-wavenumber domain and Laplacian image filters were placed over the wave field images to enhance imaging of the defect. This successfully located and sized the presence of the damage. This highlighted the potential for image-based techniques for use in SHM applications where laser vibrometry can be used as an effective NDE tool.

Both the in-plane and out of plane components of Lamb waves were measured in a thin aluminium plate using a 3D scanning laser vibrometer by Olson *et al* [122]. The purpose of this study was to investigate the viability of using 3D laser vibrometry (which has the ability to measure both the in-plane and out-of-plane components) to validate results from finite element analyses. This study made a comparison of the results of a 1D vibrometer (that can only measure the out-of-plane component) with a 3D vibrometer. It was found that the 3D vibrometer had many advantages over the 1D system particularly for validating the S_0 component in FEA simulations. The study concluded that through the use of 3D vibrometry FEA models can be qualitatively and quantitatively more accurately validated.

A study by Lee *et al*. [123] investigated the viability of using a pylon mounted laser vibrometer with integrated transducers to initiate a Lamb wave as a non-contact method which can inspect the full length of a wind turbine blade. The focus of the study was the development of a cost-effective, portable laser vibrometer for in-service monitoring of turbine fleets. Image processing techniques were used to quantitatively compare baseline images with images that showed the presence of damage. The result of the analysis gave a visual representation of the damage and its location. The main focus of this study was not the interaction of Lamb waves with damage for the development of an SHM system comprised of a network of sensors but rather the development of a laser vibrometer for in-service use.

Staszewski *et al.* [124] used 3D laser vibrometry to measure Lamb waves generated by a piezo-ceramic transducer bonded to the surface of an aluminium plate. A fatigue crack was grown in the aluminium specimen from a spark eroded notch. The interaction of Lamb waves excited at 75, 190 and 325 kHz with the fatigue crack was investigated. A peak-to-peak amplitude was conducted on all three components of the Lamb waves which identified the location of the fatigue crack and how its presence influenced the waves. The capability of the 3D vibrometer was exploited allowing an in-depth study of the interaction of both S_0 and A_0 modes with the damage to be conducted. It was also confirmed in this study that the S_0 mode attenuated less than the A_0 mode.

Schubert *et al.* [125] investigated Lamb wave interaction with impact damage in carbon fibre reinforced plastics using 3D scanning laser vibrometry. It was found that the A_0 mode showed the strongest interaction with the damage. Phase-based techniques were used to evaluate the time signal difference before and after damage. The ratio of Lamb wave energy before and after damage of the out-of-plane component was also obtained. The study concluded that phase based signal processing was more sensitive to impact damage than amplitude based methods.

A study by Grigg *et al.* [126] investigated Lamb wave interaction of both the S_0 and A_0 mode with impact damage in a flat carbon fibre panel using 3D scanning laser vibrometry. Three excitation frequencies of 100kHz, 300kHz and 500kHz were used to investigate how different frequencies interact with impact damage. The results of this study highlighted the influence of the fibre direction on the S_0 mode as an elliptical wave front was observed. This was particularly evident in the in-plane component plots where the S_0 mode was more dominant. As the wave fronts reached the damage there was little interaction of the S_0 mode with the impact damage but a significant disruption to the propagation of the A_0 mode. It was found that the presence of the impact damage had a greater effect on Lamb waves of higher frequencies.

2.9.Local Interaction Simulation Approach

Modelling of Lamb waves has long been the subject of much research particularly with the application of structural health monitoring. There have been numerous studies conducted to simulate AE mechanisms and their propagation using FEA [127]. Examples of such work are the studies conducted by Sause and Horn [128, 129] into accurately modelling the Lamb waves excited in an AE event.

A technique that has shown great promise for the modelling of Lamb waves over the past twenty years is a FD method called LISA. The technique was first developed and published by Delsanto *et al.* [130] in 1992. The focus of this study was to develop a one-dimensional Lamb wave simulation technique (as in the case of a uniform wave form propagating through a plate, normal to its surface) that harnessed the emerging parallel computational technologies of the time (connection machines). The aim of this approach was to harness the technology to develop a simulation technique that efficiently converged. Using a series of cells and the theory of Lamb waves, a model was constructed for an arbitrary material and was found to show good results. The benefit of this approach was that the values were calculated for each cell meaning that there were no explicit requirements for boundary conditions. When this was combined with a parallel processing approach the time to compute the solutions was fast (0.4s for a 100 time step model on a cutting edge research supercomputer of the time).

This work was expanded on by Delsanto *et al.* [131] in 1994 to investigate adapting LISA modelling to a two-dimensional case. In this study, the modelling environment was considered as a one-cell-thick plate. Aluminium material properties were used for this investigation which enabled displacement results to be plotted for both the longitudinal and shear components of the waves. Different excitation pulses and shapes were also used. The results were compared with traditional theoretical approaches and were found to correlate well. The 2D LISA model was also compared to modelled solutions derived using traditional FD approaches and was found to have a higher level of accuracy due to traditional FD methods requiring a degree of smoothing. To demonstrate the potential of LISA, the authors conducted studies investigating wave interaction with defects and reported that the results correlated well with the results of experimental ultrasonic pulse photoelastic visualisation experiments.

The LISA technique was further expanded by Delsanto *et al.* [132] in 1997 to investigate wave propagation in a three-dimensional case. This work investigated wave propagation in a cube of steel with an aluminium sphere embedded inside. A Gaussian pulse was excited on the surface and the displacements of the internal material were plotted for sequential time steps. LISA was found to produce good results for the wave interaction and the interfaces. The technique was found to have good computational performance though the graphical capabilities of the time limited the presentation of the results.

The first reported use of LISA as an analytical tool was an investigation by Iordache *et al.* [133] who used a one-dimensional LISA model to investigate pulse distortions in elastic wave propagation. In this study both a numerical and analytical approach were taken to study the distortions. It was found that both approaches were in good agreement with each other. A depth study altering the Courant number was conducted and distortions in the pulses were observed which, after a suitable number of iterations, stabilised in amplitude.

The accuracy, stability and validity of LISA modelling has been the subject of many investigations. Ruffino *et al.* [134] investigated the problems of accuracy and reliability in two dimensional simulations, considering the case of the ‘ladder’ problem where an oblique (to the imposed co-ordinate system) boundary was approximated. It was found that by ensuring a small cell size in the model, the effect of the approximated ‘ladder’ edge becomes negligible in two-dimensional simulations. However, it was highlighted that considerations would still need to be made for increased time steps. The study concluded that considerations in terms of cell size were important for ensuring accuracy particularly for the shear components of the waves at oblique angles. However, it was demonstrated that LISA is an accurate and computationally efficient modelling technique particularly when compared with traditional FD methods, FEA methods and the Trefftz spectral method.

An in-depth study into the accuracy and convergence of one, two and three-dimensional LISA models was conducted by Sundarararman and Adams [135]. Like the work of Iordache, this study investigated distortions in amplitude in both one dimension and three dimensions using the Courant-Friedrich-Lewy criterion. With respect to the way in which LISA iterates, the Courant criterion was investigated in relation to the size of the time-step, the cell size and the accuracy of the model. It was found that by altering the size of the cells, and the time-step (and hence the sampling frequency) there was a significant change in amplitude in the one dimensional model. It was also found that there were significant differences regarding the distortion of the wave as the time-step and cell size was altered. Convergence was also a subject studied with respect to decreasing cell size. It was found that smaller cell sizes produced a higher peak response of the first wave packet. Using the data from the LISA simulation and a two dimensional FFT, dispersion curves for the waves were calculated. Results from the simulations were validated using a commercially available accelerometer bonded to the surface of a plate in an experimental setup. It was found that there was a good correlation between the experimental and simulation data particularly in the first wave packet to arrive. The study concluded that LISA produced good results though considerations for spatial and temporal samples needed to be made to reduce distortional effects.

The LISA technique was used by Lee and Staszewski [136] to investigate Lamb wave propagation for damage detection. This study focused on the modelling of a commercially available piezo-ceramic SONOX-P5 sensor actuator and couplant (oil grease). A one dimensional multi-layer model was created and diffusion of the wave through each layer was considered. It was found that there was very little dispersion (though the wave speed did change due to the different material properties) and attenuation through the thickness of the material though partial reflections were observed. The partial reflections with absorption phenomena resulted in a reduction in amplitude through the layers. The investigation was then expanded to investigating the multi-layer model in two dimensions. In this setup, the sensor/actuator was considered to be coupled to an aluminium plate. This enabled a visualisation of the propagating wave to be produced. Measurements were taken using the model of the sensor and couplant at various locations on the plate which enable a power spectra to be calculated and hence the frequency content of the two excited modes to be derived. The simulations were experimentally validated using two SONOX-P5s (one acting as an actuator, and one as the sensor) coupled to plates to represent the parameters of the models. A high level of correlation was found between the experimental and simulation results. The study concluded that the LISA method showed good potential for modelling Lamb wave propagation in aluminium structures.

This study was further expanded to investigate Lamb wave interaction with damage by Lee and Staszewski [137]. In this simulation two SONOX-P5 sensor/actuators were coupled at the edges of a 400mm x 150mm aluminium plate with a 10mm damage slot of varying width located at the centre. A 325kHz 5-cycle cosine wave with a Hanning window was used to investigate the Lamb wave interaction with the damage. The results plots at incremental time steps presented clearly showed the wave interacting with damage slots of both 1mm and 5mm thicknesses. The simulated results were validated experimentally using sensors bonded to the surface of a representative aluminium plate. A high level of correlation was found between the two sets of results verifying LISA as suitable tool for modelling Lamb wave interaction with damage.

Lee and Staszewski [138] used LISA to model Lamb wave interaction with a damage slot and a fatigue crack in aluminium plates to investigate suitable sensor locations. The first part of this study used the model setup from the previous study. The results for an aluminium plate with a notch present were processed using a peak-to-peak amplitude analysis and incremental time windows. The results showed both the S_0 mode and the A_0 mode interacting with the damage and highlighted the area on the structure where low amplitudes of the Lamb wave were sensed. The results of a simulated sensor in the model were validated experimentally using a laser vibrometer. It was found that the two results sets correlated well though a low level of noise was present in the experimental measurement. A similar analysis was conducted on an aluminium plate where a fatigue crack had been grown. Two actuator locations were used for the Lamb wave excitation and the peak-to-peak analysis was conducted for incremental time windows. The interaction of the Lamb wave with the fatigue damage was highlighted as well as an area of low amplitude and hence poor sensing locations. As with the notch, the results were found to correlate well with the experimental results from a laser vibrometer. The study concluded that, in the case of the crack, the best sensing locations were found to be in in the sensor-damage path.

A great advancement in LISA technology came in 2012 which was presented in work by Paćko *et al.* [139]. The focus of this study was to adapt LISA so that it could harness the massively parallel computational technology of the Computer Unified Device Architecture (CUDA) Graphical Processing Units (GPUs). This enabled LISA models to be computed at a much faster rate due to the hundreds of cores which are capable of running thousands of threads in parallel. The study demonstrated the performance advantages of CUDA GPUs over the traditional Central Processing Unit (CPU) approach. This parallel approach (known as cuLISA3D) was demonstrated by predicting dispersion curves for an aluminium plate which agreed well with dispersion curve solutions derived from traditional analytical and FEA approaches. The parallel approach was then applied to modelling an interdigital grated transducer and the Lamb wave interaction with an approximated crack damage. The results in terms of waveforms and propagation plots agreed well with those produced by FEA. The study concluded that the parallel approach produced solutions that corresponded well with those from FEA. The main advantage of the parallel approach however was its computational efficiency; out-performing the FEA approach – taking minutes instead of hours to compute.

One of the most exciting applications of LISA is the modelling of Lamb wave propagation in fibre composite laminates. In a study presented by Nadella and Cesnik [140] a LISA technique was written in FORTRAN95 and adapted to incorporate fibre directionality. A fibre composite plate (most likely carbon although it is not explicitly stated in the paper) was modelled in this study, with Lamb waves induced by two different designs of Composite Long-range Variable-direction Emitting Radar (CLoVER) actuators. The out-of-plane results produced by the LISA model were validated using a one dimensional laser vibrometer. The LISA results plots correlated well with those of the laser vibrometer particularly for directionality when only parts of the CLoVER were used for Lamb wave actuation. However, no waveforms were presented for a more quantitative comparison.

2.10. Sensor placement for damage detection optimisation

Optimisation is the study of making something the best it can be within a defined set of parameters (known as the search space). This is usually expressed mathematically as minimising (or inversely maximising) a function known as the 'objective function' (also known as the fitness function or cost function). In its simplest form, optimisation can be conducted by a technique known as an exhaustive search. This technique requires every possible solution within the search space to be considered and the best one chosen (known as the fitness). Naturally, this is very time consuming and not computationally efficient though it will always find the best solution. Because of the inefficiency, an exhaustive search is not typically used as an optimisation tool for complex, multi-variable engineering problems (however it is worth stating that for simple problems, an exhaustive search may be considered a suitable method).

Iterative optimisation techniques, such as the Newton-Raphson method or the random walk optimisation method, have many computational performance advantages over exhaustive search methods. In these cases, a random point is taken within the search space and the fitness for that point is assessed. The fitness of another point is then considered and compared with that of the first point. This continues until an optimal solution is converged upon. Though these types of methods are suitable in a wide range of applications, they do have drawbacks especially when considering more complex problems. The key drawback to this type of algorithm is that it can converge on a local minima rather than the global minima. A local minima is a minimum solution within a certain region of the search space that the optimiser converges on but is not the optimal solution within the whole search space. A graphical demonstration of the minima is given in Figure 15.

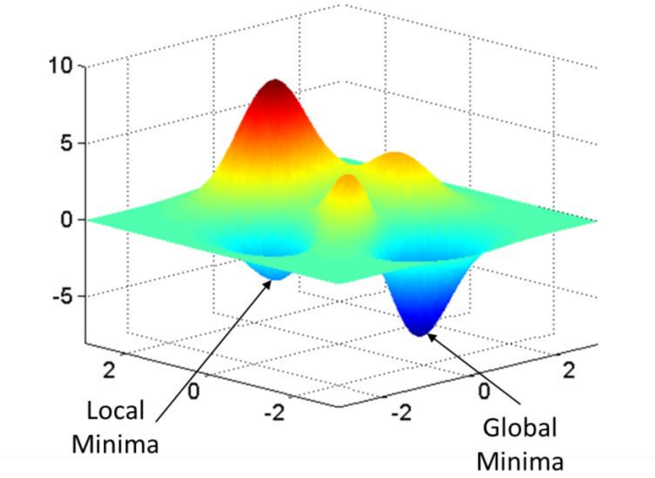

Figure 15. A 3D surface plot demonstrating local and global minima

Therefore, in the case where there are many minimal solutions, it is beneficial for the optimisation algorithm to be computationally efficient whilst converging on the global minima. An extensive overview of traditional optimisation techniques is presented by Venkataraman [141]. A comprehensive explanation of different optimisation techniques with their advantages and disadvantages is presented by Venter [142].

One type of optimisation methods that have shown great performance in converging on global minima with good computational efficiency are those that attempt to simulate nature. These algorithms are usually grouped under the umbrella term of ‘Evolutionary algorithms’. Examples of these include simulated annealing, ant colony optimisation and genetic algorithms. A comprehensive history and comparison of different minimum-seeking algorithms is presented in work by Khan *et al.* [143].

2.10.1. Genetic Algorithms

One algorithm that has shown a lot of potential and has been the subject of many sensor optimisation studies are Genetic Aalgorithms (GAs). Though it could be argued that the concept of a GA stems back to the work of Turing [144] in the 1950s, GAs in their modern form were first developed by Holland [145]. GAs attempt to mimic Darwinian evolution where each 'generation' (iteration) produces better solutions with only the best solutions being taken forward and less suitable solutions being discarded ('the survival of the fittest' (N.B. Darwin did not make this statement but it was remarked by Spencer [146] on reading Darwin's work and drew parallels with his economic study)).

GAs have advantages over other optimisation techniques as they have the ability to 'mutate', allowing the algorithm to interrogate the whole solution space to find the global minimum or maximum rather than converging on local minima or maxima without fully exploring the solution space. The way that the algorithm interrogates a relatively low proportion of the total solution space is also not as computationally expensive as other techniques [147]. Figure 16 shows the schematic representation of a GA[148].

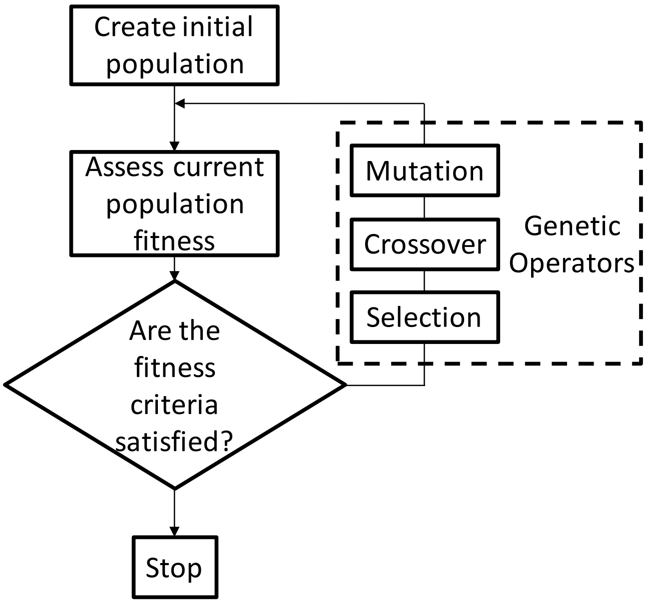

Figure 16. Schematic representation of a GA (recreated from Clarke *et al*.[148])

There are many ways of encoding a search space so that it can be optimised by a GA but the most common method is binary encoding. This is demonstrated in Figure 17. Another common method is continuous encoding.

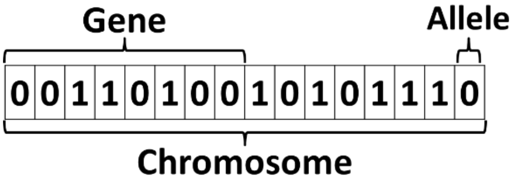

Figure 17. Definition of the terms used in binary encoded genetic algorithms

With binary encoding, each part of the solution is encoded as either a one or a zero. This can be explained by considering trying to find the global optima shown in Figure 15. Every point on the surface can be defined by two co-ordinates, the x-co-ordinate and the y-co-ordinate. Values for both of the co-ordinates can be defined by as a binary number. Each binary string that relates to a respective co-ordinate is known as a ‘gene’. Each gene is made up of binary digits which are called ‘alleles’. When two genes are put together, which in this case would reference a location on the surface; it is known as a ‘chromosome’.

A GA starts with a small, random selection of possible solutions (known as the ‘initial population’). The fitness of possible solutions in the initial population is assessed and they are then usually arranged in descending order of fitness.

The algorithm then determines whether the fitness criterion has been satisfied. There are many ways of achieving this - the fitness criteria may be to find a solution with a value below a threshold for instance. A common fitness criterion is to determine whether the optimal fitness has been achieved by letting the algorithm run and assessing whether the fittest solution has been improved upon. If the solution has not been improved upon for a certain number of generations the algorithm is told to stop. When designing a GA this is an important consideration as allowing the algorithm to run for too many generations can be computationally inefficient whereas not allowing it to run for long enough will result in a sub-optimal solution being found.

Where the fitness criteria are not satisfied, the population is taken through to the genetic operators. In this part of the algorithm, a sub-set of the good solutions (known as the ‘mating pool’) of the population is selected and hence the poor solutions are discarded. The next stage is the cross-over or ‘mating’ process. In this process the solutions from the mating pool are paired up to ‘mate’ with other good solutions from the mating pool (known as the ‘parents’). The concept behind this is to take the good attributes from one solution and the good attributes from another to produce a better solution.

There are many methods for pairing the solutions for mating. A few of the common methods are;

- Pairing from top to bottom – In this instance, the best solution is paired with the second best; the third is paired with the fourth and so on.
- Random pairing – A random number generator is used to pair the solutions (also known as the ‘Keys-in-the-bowl’ method of pairing).
- Weighted random pairing or roulette wheel pairing – The solutions are allocated a probability of mating proportional to their fitness. Two random numbers are generated and the respective solutions are paired (like spinning a ‘roulette wheel’ with proportional sized segments).
- Tournament selection – a random sub-set of the mating pool is selected to ‘compete in a tournament’. The fittest solution is carried forward for mating and the process is repeated until all solutions are mated.

Once the entire mating pool has been paired up the new solutions are created by splitting the attributes from each parent to make two ‘children’. The way in which it is decided which attributes go to which child is determined by what is known as the ‘cross-over’. In the case of binary encoding, the chromosome is split at one or more arbitrary locations.

With the children added to the population the final genetic operator known as the ‘mutation’ can take place. As in nature, parts of the solution can be changed which allows the algorithm to sample areas of the entire search space, meaning that the algorithm can converge on a global optima rather than a local optima. To determine which parts of a solution are mutated, if any, a probability of mutation is assigned. This may be a varying probability (particularly useful where it is desirable to investigate a lot of the search space in early generations whilst focusing on convergence in later generations) or a fixed probability. In the case of binary encoding, mutation is commonly executed by mutating alleles so that a ‘1’ becomes a ‘0’ and vice-versa. In many cases, the best solutions in the population are immune to mutation to prevent a good solution being mutated into a poorer solution.

With the genetic operations complete, the population is placed back into the loop for the fitness to be assessed, with this process repeated until the fitness criterion is achieved. There are many variables associated with GAs such as the population size, cross-over points and mutation probability. Important considerations need to be made regarding these variables to ensure computational efficiency of the algorithm. Particularly in the case of a GA that will be heavily used it has been suggested that a further GA may be used to optimise the parameters of a GA [149]. For further explanation of GAs the reader is referred to Haupt and Haupt [147].

2.11. Sensor location optimisation studies

The placement of sensors for SHM applications has long been the subject of much study. Poor consideration of AE sensor placement has historically been a large contributor to the failure to detect damage [150] and as a result there has been a lack of faith in the technology to locate damage.

There are two main objectives of optimising sensor placement. The first is to ensure that there are enough sensors to detect damage on structure whilst also minimising the number of sensors. The second is to ensure that the locations the sensors are placed in produces a high probability of damage detection. To achieve this, many studies have been conducted using different mathematical optimisation methods and fitness techniques. Although many of the studies conducted consider the optimisation of sensors and locations for modal responses, these methodologies can be adapted for optimising AE and AU sensor networks.

One of the earliest studies to consider sensor placement for a SHM application was conducted by Kammer [151] who considered the placement of modal sensors on large space structures. The motivation for this work stemmed from the requirement to monitor large space structures when in orbit whilst minimising the mass caused by a sub-optimal sensor network which would have significant financial cost penalties, particularly in terms of launching the additional mass. The study considered a large number of ‘candidate’ sensor locations based on the modal kinetic energy distribution and determined the optimal locations within this set. The fitness of the candidate sensor locations was determined by the location’s contribution to the linear impedance of the corresponding target modal partitions. Using an iterative method known as effective impedance which maximises the determinants of a Fischer information matrix, an optimal solution for sensor placement on Phase I of the space station could be achieved (note that ‘the space station’ is most likely in reference to the NASA project *Space Station Freedom* which ultimately developed into the international space station [152]). The study concluded that this optimisation method was particularly computationally non-intensive especially when compared with exhaustive search techniques.

Kammer [153] expanded on this work to consider noise within the sensor network and how that influenced the sensor placement. This work draws on the findings and experience of Kammer’s previous study but with noise considered by using a covariance intensity matrix - the candidate sensor locations were effectively given a weighting. This had a significant influence on the sensor placement due to the target modes that were being considered. In addition to the consideration of the effects of noise on the monitoring of desirable mode shapes, a criterion was also introduced which enabled the sensor network designer to determine the required amount of sensors for a desired signal-to-noise ratio. This was demonstrated through the use of examples derived from FEA. Kammer again comments that the use of this optimisation technique delivered a computational efficiency though further study would be required to determine the actual efficiency when compared to other methods.

Using GAs for optimising sensor placement was investigated by Yao *et al*. [154] for monitoring modal shapes on large space structures. In this work a set of candidate sensor locations was considered. The fitness of the location was assessed based on the determinant of the Fischer information matrix which related to the location's modal response. The study gives a detailed overview of the algorithm including the setup and parameters used. The algorithm was applied to a numerical model of a photovoltaic solar array and a truss section of an early design of the space station. It was found that the genetic algorithm technique was successful in producing an optimal solution for sensor placement. It was noted that forced mutation had to be applied, enabling the algorithm to interrogate a much wider area of the search space which significantly improved the convergence. The results from the GA optimisation were compared with the results found by Kammer [151] using the effective impedance method. It was found that the solutions derived by the GA were better at determining the modal response. The study concluded that the GA produced better solutions than the effective impedance technique as well as being quicker to converge. However, the author does state that the parameters of the GA have to be carefully considered to ensure good computational performance. In addition, the GA had no indication of convergence. This was overcome in this study by applying a 'no-improvement' tolerance (i.e. the GA was allowed to run and only stopped after the maximum fitness had not been improved upon for a set amount of iterations). The authors warn however that if the tolerance is set too low then the optimal solution will not be achieved and if it is set too high then the GA will be computationally inefficient.

Genetic algorithms were used for the placement of piezoelectric sensors and actuators for modal analysis in a composite plate by Han and Lee [155]. The objective of this study was to find efficient locations of sensors and actuators for a cantilever composite plate using modal data obtained from FEA. The main novelty in this study lies with the multi-input multi-output approach considered for the actuator/sensor pairing. The composite plate was divided up into an 11 x 9 grid which acted as the candidate locations for the sensors and actuators. The fitness of the sensor location solutions was determined by controllability, observability and spill-over prevention based on the modal energy eigenvalues. The GA converged on a solution though some recommendations were made by the authors on adjusting the GA parameters in order to improve the computational efficiency of the algorithm. The GA found optimal solutions for both the sensors and the actuators to be near the built-in end of the composite plate. These locations were then investigated experimentally and were found to have significant vibrational control particularly for the first three modes.

Sensor placement optimisation for modal response was investigated by Manson and Worden [156]. The objective of this work was to develop a methodology for the detection of damage using novelty (or anomaly) detection. This involves determining a baseline (or healthy) condition of the structure so that when damage occurs, the condition can be statistically compared to that of the baseline to determine the presence of damage. A FEA of a 1 m x 0.5 m x 3 mm aluminium plate was used as the data source for the optimisation study with a section of the plate removed to alter the modal response and transmissivity. Twenty-two candidate locations for the sensor-actuators were allocated around the edge of the plate. A GA was used to optimise the locations based on the statistical novelty index derived from the simulations performed with and without damage. It was found that with six transmissivity paths, the damage could be identified and located to one of the eighteen 0.17 m x 0.17 m regions of the plate. It was found however that by increasing the number of sensors on the plate, the probability of the correct location of the damage increased.

An review of the optimal sensor location methods for structural damage detection was presented by Staszewski and Worden [157], mainly focusing on modal techniques. One of the studies of particular interest presented is the case of an aluminium plate modelled in FEA with clamped edges with loading conditions applied. The damage in this case was simulated by reducing the Young's modulus for a set of elements. Twenty-five strain sensors arranged in a uniform grid on the plate were used to train a multi-layer perception network. The fitness was determined by the number of misclassifications of the damage achieved by the suggested network against that of a neural network training set. A genetic algorithm was used to optimise the number of sensors on the plate. Of the optimal results presented, the probability of misclassification of the damage was found to reduce exponentially as the number of sensors increased.

An approach for optimising sensor networks using supervised learning (neural networks) with genetic algorithms and simulated annealing for damage detection with modal techniques was presented by Worden and Burrows [158]. Like previous studies, the FEA model was used to simulate the modal characteristics of a cantilever plate. Damage was simulated by applying a Young's modulus of zero to different areas of elements of the model. Twenty candidate sensor locations were arranged in a uniform grid on the plate. The neural network was trained using the modal shapes and their curvatures to respond to differing amounts of damage on the plate (i.e. as the severity of the damage increased the target for the neural network increased). The optimisation of the sensor network was first approached by using a measure of fitness technique called iterative insertion/deletion. The measure of fitness was established using a mean squared error between the desired responses and the estimated responses of the network. All sensor locations were assumed to be occupied and then one was removed. This gave twenty possible sensor network solutions for a nineteen-sensor network. This process works by assessing all twenty solutions by calculating their respective fitness. The sensor location which contributes the least is then removed and the process is continued with an eighteen-sensor network. The authors commented that this process was time consuming. The performance of the networks was assessed on their ability to classify the presence of differing severities of damage and cored using statistical methods. Using this method it was found that a ten-sensor network was the 'best' network in terms of performance and maximum error. However, the authors infer that a requirement for the level of the damage detection is required to fully determine the network size. A GA using binary encoding was then used to optimise the network. It was found that the sensor network solution using the GA for a ten-sensor network placed eight sensors in common with the iterative insertion/deletion technique. The authors commented that the GA outperformed the previous method and found a five-sensor solution that had a 99% probability of locating the damage. A simulated annealing technique was then used to optimise the sensor network. The size of the sensor network to optimise was set before running the algorithm and was first used to find a suitable ten-sensor network. The simulated approach converged on a ten-sensor network solution that was found to out-perform the solution found by the GA. The simulated annealing approach also found good solutions for four and three-sensor networks. An exhaustive search was conducted on the three-sensor network distribution and was found to be in agreement with the solution found by simulated annealing.

An investigation to optimise a strain gauge sensor network for SHM on a truss-structure using an improved genetic algorithm was conducted in a study by Guo *et al.*[159]. Detecting changes in localised stiffness when modal vibration was present in an FEA model caused by the presence of damage was the objective of this study. The fitness of the sensor network was established by using the determinant of a Fischer information matrix which allowed for the best estimate of the damage coefficients to be predicted. The novelty in terms of algorithm development involved the introduction of an efficient penalty function mechanism for solutions that fell outside of the constraints. In addition, an improved crossover technique which ensured only the best attributes of a solution were carried forwards was also introduced. This optimisation technique was applied to the design of the sensor network on a truss which had thirty-one candidate sensor locations. The convergence criterion in this study was determined by two attributes; when the absolute value of the average fitness subtracted from the maximum fitness was less than a specified value, and, when the maximum fitness value has not been found after a set number of iterations. It was found that the GA exhibited excellent convergence performance though the authors suggested that altering the mutation probability may improve convergence. The technique demonstrated advantages in convergence and the efficiency of the improved genetic algorithm over penalty function and forced mutation methods particularly for the application of placing sensors for damage detection.

An interesting approach to a sensor placement problem using an ant colony metaphor was taken by Overton and Worden [160]. This method uses natural optimisation observed in nature by ants. Ants naturally find the shortest path between their nest and their food by following the path which has the most pheromones left by other ants. The shortest path will take the shortest time to follow and therefore more ants will follow it. It was commented that this technique is particularly useful for the 'travelling salesman problem' (i.e. finding the shortest path between various locations). The algorithm used in this study also considered variables such as 'evaporation' (meaning that a solution became less favourable the less it was used) and 'visibility' which is the same solution ordered differently (i.e. a two-sensor network with sensors 2 and 7 is the same as one with sensors 7 and 2 which improves convergence on favourable solutions. The optimisation technique was applied to a sensor network for experimentally detecting an impact in a composite panel. Seventeen piezo-ceramic sensors were placed on the surface of panel at candidate locations to sense changes in strain due to impact. The sensor network was trained with a neural network using all candidate sensors to establish the minimum error. The parameters used were; time after impact of maximum response, magnitude of maximum response, peak-to-trough range of response and real and imaginary parts of the frequency response spectrum. The case of a three-sensor distribution was first considered. For comparison, a solution was found by an exhaustive search using different starting conditions which yielded a location error of 1.99%. The distribution was remarked to be 'intuitive'. In addition, a GA was found to find an optimal solution which converged on the of 1.99% error. Applying the ant algorithm to the problem found a solution for a three-sensor network with an error of 1.89%. The authors remark that the solution was found quicker than the exhaustive search and the GA. Larger sensor distributions were considered and the performance of both the sensor distribution and convergence was compared with that of a GA. It was concluded that the ant colony algorithm produced promising results that provided effective solutions for the placement of sensors. However, the authors commented that the use of a neural network to train the sensor distributions leaves a degree of uncertainty in establishing the fitness values.

In a study by Gao and Rose [161], covariance matrix adaptation evolutionary strategy (CMAES) was used for optimising the placement of acousto-ultrasonic sensors for SHM. In this study, the fitness of the sensor locations is based on ultrasonic wave mechanics. In an isotropic material the ultrasonic signal is said to be radially emitted from an actuation site. The strength of this signal decreases with radial distance until a point where the signal strength has reduced so much that the signal cannot be distinguished from the background noise. This formed a probability distribution of areas where the signal was most likely to be detected from a source. As such, the objective of the optimiser was to determine locations where the miss-detection probability (MDP) was minimal. The authors applied the CMAES optimiser to interrogate these probability distributions to find the areas of high signal strength and hence the optimum sensor locations. This was first applied to a sample problem where a probability mask was applied to the structure for areas of high likelihood of damage. The optimiser was stopped once the decision variable (i.e. the fitness) was smaller than 0.25 (0.25 being a fitness that was deemed a suitable enough solution). The results from this initial study produced a sensor network that had an 11% improvement in performance compared to the initial sensor distribution that the authors had originally tried. Performance of the optimisation algorithm was also assessed and was found to be reliable and repeatable at finding optimal solutions in an efficient manner. A second investigation was conducted on a Northrop Grumman E2 aircraft wing. In this investigation the number of sensors in the network was also considered and the resultant values of MDP against number of sensors were presented. The optimisation of the sensor network for the E2 wing panel presented was a more realistic problem. The problem was constrained so as to not allow sensors to be placed on areas of the structure where stiffeners were present. The results from the study identified the areas of high probability of damage to be around the rivet holes. A sensor network was presented that provided a suitable trade-off between MDP, number of sensors and sensor performance.

The use of an immune system metaphor to optimise a damage detection sensor distribution was presented by Zhang *et al.* [162]. This study uses an algorithm that simulates the processes of the biological immune system to converge on an optimal solution. This particular algorithm works on the mechanics of the adaptive immune system which in the body optimise the response to microbes by modifying certain cells. In doing so, they are able to maximise their recognition ability. The algorithm used for the sensor location study is known as the Clonal Selection Algorithm (CSA) and is similar to that of a genetic algorithm without the ability to cross-over. The manuscript gives a detailed description of the workings of the algorithm. The composite panel setup previously used in the study by Overton and Worden [160] along with the neural network training method, objective, and fitness criteria, was used for the optimisation. The mutation probability for the optimiser was determined by trial-and-error and good results were found to be achieved with a 0.01 probability. For a three sensor distribution, the CSA was found to converge on the solutions achieved with the exhaustive search and less iterations were required for convergence than were required for the GA. However, to achieve this, more functions were considered per iteration than by the GA. Nevertheless, the study presented concluded that the CSA approach demonstrated good potential for optimising sensor network distributions for damage detection.

An optimisation study was conducted for the placement of actuators and sensors of an acoustic based SHM system for monitoring composites by Das *et al*.[163]. In this study, the design of a sensor pair was considered for a 4kHz excitation. The objective in this study was to maximise sensing certainty while minimising sensor density. Fitness was assessed on three criteria; the sensor spacing provided sufficient spatial coverage of the component under investigation, the sensing density was sufficient to satisfy the requirements of damage detection and location and the detection of damage had to be achieved even with the presence of noise. This was based on the two-dimensional spatial characteristics of the acoustic signals. To achieve this, the composite plate was divided up into a grid of candidate sensor/actuator locations. From experimental investigation, the sensing radius of a sensor was determined (i.e. regions where the placement of an actuator was identified). This allowed regions of overlapping of neighbouring sensor/actuators to be identified based on a minimal overlap criterion. By applying this to the composite plate a network was designed that had a 76% coverage of the plate with 22% overlap. This design of sensor network was tested to determine its ability to detect damage by artificially creating delaminations in the composite plate which were compared to measurements taken on a healthy composite panel. It was found that the sensor network was successful in detecting the damage present. It should be noted that the approach taken in this study was not one of traditional optimisation as no mathematical algorithm was used but rather sensors were placed using a more heuristic approach. The approach taken in this study was similar to a technique known as 'radio planning' used for the placement of mobile phone antennae [164].

A Bayesian approach to the placement of sensors and actuators for active ultrasonic guided waves was present by Flynn and Todd [165] using genetic algorithm optimisation. This study formulated a global optimality criterion from Bayes risk which minimised the probability of a type I or type II (false positive or false negative) error. In turn, this effectively maximised the global detection rate. This technique was applied to the placement of sensors and actuators for simplistic structures including a flat plate and a stress-mapped gusset plate in a theoretical environment. A genetic algorithm was used with a time-varying mutation rate, which enabled a large area of the global optimality criterion search space to be sampled in the early generations while allowing efficient convergence in later generations. These examples considered two sensing methods; pitch-echo (where the actuator pulses and then acts as a sensor to sense the reflected signal) and pitch-catch (where the signal is induced by an actuator and sensed by a sensor at a separate location). For these cases both sensor and actuator locations were considered relative to the performance constraints. The novelty in this work came from the application of Bayes risk to establish the fitness metric and, as such, it was demonstrated that this approach had many performance gains in maximising the probability of the detection while minimising the probability of false alarm over other techniques, particularly studies where the objective is to maximise the determinant of the Fischer information matrix.

This work was expanded upon by Flynn and Todd [166] who used this Bayesian optimisation approach for the placement of actuators and sensors in an ultrasonic guided wave sensor network. Though many parallels can be drawn with the first study, the approach was applied to an experimental test on two 1.1mm thick steel plates of irregular shape. The results from the experimental investigations were compared with those achieved in the theoretical investigations for varying sizes of sensor networks. Damage was simulated on the plates and the respective Bayes risk for a false alarm was calculated as a measure of the sensor network performance. The study concluded that the sensor locations presented were likely to be near optimal though performance gains could be achieved with further experimental investigation.

GAs were used for the optimisation of a passive sensor network on fibre-composite panels by Markmiller and Chang [167]. The objective of this study was to minimise the number of passive sensors (strain gauges) whilst maximising the probability of detecting impact damage. To achieve this, the impact forces and location were estimated with a modal-based approach using an FEA model. The process for this investigation used impacts at multiple locations with the response measured at multiple candidate sensor locations within the FEA model. The locations of the sensors were then optimised based on the probability of detection using a GA for a particular sensor network size. It was noted that the size of the area of the probability of detection for different impact locations altered dramatically depending on the location of the impact. This was due to the presence of the stiffeners and the layup of the composite. It was found that the GA was effective in converging on a solution. Unsurprisingly, as the size of the sensor network increased, the probability of detection also increased. Only sensor networks up to twenty-five sensors were considered. The trend between the number of sensors and the probability of detection suggest that there are no performance gains above a twenty-five sensor-network. Different impact loads were also considered. The results from the higher impact loads show that the higher the load the fewer the number of sensors required to maintain the same level of probability of detection. The same approach was applied to a second composite panel of more complex geometry. It was found that many more sensors were required in order to achieve the same probability of detection as the first panel even when substantially higher loads were applied. Nevertheless, a novel methodology for the sensor placement problem was presented in this work.

A methodology for the arrangement of sensor arrays for SHM systems under uncertainty was presented by Guratzsch and Mahadeven [168]. The authors of this study used FEA models to simulate modal responses as a means of monitoring the structure. The approach was taken to experimentally validate the modal responses of an aluminium plate modelled in the FEA software package. Once the model had been successfully validated, a probabilistic analysis was conducted using the FEA model by modifying the material properties. The simulations were run multiple times for various scenarios, with and without damage. The site of the actuation was fixed with the sensors allowed to move to various locations on the plate. To classify and locate the presence of the damage a combination of Bayes decision theory and Malhalanobis distance was used. As such, the probability of type I and type II error was established. The optimisation approach taken in this study was to use a SNOBFIT (Stable Noisy Optimisation by Branch and Fit) algorithm which does not require a set of candidate locations for optimisation but rather considers the problem using a set of continuous variables whilst also having the benefit of being able to search for the global minima. For a detailed explanation of the SNOBFIT algorithm, the reader is referred to Huyer and Neumaier [169]. The problem was considered for a four-sensor network (where ‘sensor’ one acted as the actuator and remained fixed). It was found that by making adjustments to the objective function, different distributions of sensors were achieved which gave different probabilities of type I and type II error. The authors concluded that additional investigation was required to determine the optimal number of sensors though they did state the addition of sensors has a weight penalty which is not ideal for aerospace applications.

The use of a modified monkey algorithm for optimal sensor placement was investigated by Ting-Hua *et al.* [170]. This study used modal analysis as a means of monitoring the health of a structure with the novel implementation of the monkey algorithm (MA). MAs attempt to simulate the mountain climbing processes exhibited by monkeys in nature. The concept behind the algorithm is that monkeys naturally find the shortest route to the top of a mountain. The algorithm uses three main operators;

Climb – the algorithm ‘climbs’ towards the local maxima

Watch-jump – the algorithm searches for areas of the local search space that exceed the current values which speeds up convergence

Somersault – the algorithm ‘somersaults’ to other regions of the search space to search for other promising maxima and in-turn the other two operators are executed.

An MA is a form of evolutionary algorithm that is reasonably similar to GAs. A full description of MAs is presented in work by Zhao and Tang [171].

The objective function in this study was formulated from structural dynamic principles. This involved maximising the off-diagonal elements in the modal assurance criterion matrix and also maximising the average of the off-diagonal modal assurance criterion. The algorithm was terminated once a specified number of iterations had run. The structure used to demonstrate the optimisation methodology was an FEA model of the Dalian world trade building in China. The number of sensors considered for the optimisation ranged from five to fifty sensors and the results from the MA were compared to those of solutions derived using a firing squad synchronisation problem (FSSP) algorithm. It was found that that by modifying the MA performance gains of 66.42% over the original MA and 77.93% over the FSSP could be achieved. It was also found that the optimal solution found by the modified MA was found at twenty-four sensors whereas the optimal solution found with the FSSP required thirty-one sensors. The authors concluded that it was possible to achieve a much higher performance through using the modified MA over the FSSP algorithm.

Gao *et al.* [172] conducted a study to design a sensor network for monitoring the health of a full-scale horizontal tail using ultrasonic Lamb waves. The tail section used in this study was not from any particular aircraft but was manufactured for the purpose of the study with a representative internal structure. The tail was supported at the centre (as to represent the attachment to a fuselage) with representative in-flight static loads applied at seven locations along the length of each side of the tail fin. It was stated that the most common failure mode in this loading condition is delamination at the skin-stiffener interface. Based on sensor-actuator paths, a set of candidate sensor locations was established. The presence of damage was determined using a correlation coefficient calculated from baseline wave measurements. For optimising the sensor network, an objective function was established based on the probability of detection of the damage. This probability was determined from preliminary tests of cross-stiffener and along-stiffener wave propagation measurements. The ability to detect damage was also established in a preliminary test by inducing a delamination in a composite t-section using a tensile test. The sensor network was optimised by using a coverage rate method where solutions with less than 95% coverage of the tail fin were disregarded. The results showed that this could only be achieved with a six-sensor network where a 98.1% coverage was obtained. Despite this the authors decided to use a seven-sensor network that had a coverage of 98.5%. Coverage results for sensor networks with more than seven sensors were not presented. Different loading conditions were applied to the tail fin and the damage induced was plotted. It should be noted that the optimisation method used in this study could be seen as somewhat questionable particularly as it could be argued that the data on which the optimisation study was based is not representative of an actual tail fin.

A novel approach for the optimal placement of sensors to detect impact damage in a composite panel was presented by De Stefano *et al.* [173]. This study develops the methodology used by Worden and Staszewski [174] where a sensor network was trained using a neural network and optimised using a GA to detect and locate impact damage in a composite plate based on strain caused by the impact. This was then tested and proven experimentally. This study builds upon this work to use a trilateration-based approach to replace the requirement for a neural network; reducing the need for training and hence significantly reducing time and effort. Trilateration is a method commonly used in global positioning systems and for locating earthquakes. The method uses the distances between three sensors to determine the location of the impact. A quasi-isotropic composite plate, representative of a skin panel of an aircraft, was restrained along its edges and was instrumented with twenty piezo-electric sensors in a regular square grid which acted as the candidate sensor locations. Impacts were performed experimentally using a commercially available instrumented impact hammer at one hundred and fifty four nodes on a regular square grid to produce training data. Features were extracted which included time after impact of maximum response, magnitude of maximum response and time at which the signal is received by the sensor. The first two features were used to train a neural network to conduct the optimisation study using the original approach and the third feature was used for the trilateration approach.

A GA was used to optimise the sensor network (particularly the Strength Pareto Evolutionary Algorithm (SPEA2). More information on this algorithm is presented by Zitzler *et al.* [175].) with an objective of fail-safe location and detection (i.e. redundancy in the network is present so that location and detection is still possible despite a proportion of sensors breaking down). In this study, this was achieved with a four-sensor network (as only three sensors were required). The two techniques investigated (the traditional approach and trilateration) produced sensor networks with only two sensors in common with each other. It was concluded that the trilateration approach achieved results that were comparable to that of the traditional approach though it achieves them in one tenth of the time.

2.12. Summary

The theory outlined has demonstrated the numerical reasoning for the AE and AU induced Lamb waves. In addition, the physical phenomena such as dispersion and attenuation have been discussed and reasoned.

The reviewed literature has given a detailed overview of previous studies that have used both AE and AU for SHM applications. The benefits and drawbacks of such systems have been discussed in particular historical experiences which have resulted in reluctance to apply systems for in-service applications.

Uses of laser vibrometry have been reviewed and it has been noted that advances in Lamb wave sensing have only been made in recent years with the development of higher performance computational ability. It is because of this that there are limited published works on the subject and even fewer works that consider in-plane wave components.

Similarly, the LISA modelling method has only come to the fore with the adaptation of the method to the massively parallel processing ability supplied by NVIDIA CUDA GPU architecture. There have been many studies conducted using this technique and it shows great potential for the modelling of Lamb waves. However, its widespread adoption is somewhat limited.

A wide range of sensor location optimisation studies for SHM applications has been presented. It has been demonstrated that there have been many studies conducted for the placement of sensors based on the numerical models for modal variations. There is some limited works on the placement of AU sensor but minimal works on the placement of sensors for AE systems. Some promising attempts have been made using probability density functions to predict the likelihood of damage to 'weight' specific areas of the search space.

Within industry, the requirement to ensure airworthiness of large aircraft to EASA standard CS 25 [176] while also optimising maintenance operations is a key driver. Critical areas of the aircraft are mapped in terms of probability based on the probability of damage occurrence and the effect on the strength of airframe should damage occur. This allows maintenance inspections to be conducted more regularly on more critical areas of the structure. However, this is a challenging task as metallic and composite structures are prone to different damage mechanisms. To ensure airworthiness, a large focus is put on creating damage tolerant structures which allow for a level of damage to be present which lowers the risk of the strength of the airframe being compromised [177]. There is some potential to use these probability maps as a ‘mask’ for optimising SHM sensor networks.

Due to the experimental and numerical overheads, there have been few studies that consider a multi-source, multi-sensor approach. This therefore indicates a promising and novel avenue to explore.

3. Experimental and numerical techniques

This section gives an overview of the different equipment, software and techniques used in the studies presented within this thesis. Details of both experimental and numerical techniques are presented.

3.1.Transducers

The transducers outlined in this section have been used for laser vibrometry and AE investigations. A transducer is defined in the Oxford English dictionary as ‘Any device by which variations in one physical quantity (e.g. pressure, brightness) are quantitatively converted into variations in another (e.g. voltage, position)’ [178]. In these studies the term transducer is used to describe a device that converts energy from surface waves into an electrical signal. Typically, the type of transducer used for sensing surface waves is a piezo-electric transducer that uses the piezo-electric effect to convert the surface wave into an electrical alternating current. A diagram of a typical piezo-electric transducer is presented in Figure 18.

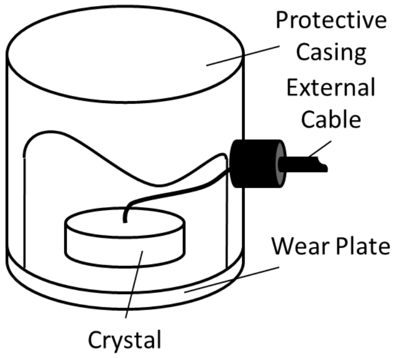

Figure 18. Diagram of a Piezo-electric transducer

The electric signal from the transducer is typically passed through a pre-amplifier that adds a gain to the signal (usually 40dB). The signal is also usually filtered using a high-pass filter which removes any low frequency mechanical noise. Coaxial cables are used for the transfer of the signal which reduces the electro-magnetic noise. Once filtered, the signal is then received by an AE system for acquisition.

There are a range of different transducers available for different applications. Three types of transducer are typically used in research for sensing surface waves; broadband, resonant and wideband.

Broadband transducers are said to have a flat frequency response meaning that, in theory, their transfer function is the same regardless of the frequency although in practice there is a small variation over the frequency range. For the measurement of AE signals, this is typically in the range of 10kHz – 1MHz. Broadband transducers are particularly useful where frequency analysis is used. However, their reduced sensitivity and inability to distinguish signals from background noise means that they are not commonly used in commercial applications.

Resonant transducers are tuned to have a frequency response for a specific frequency. Because of this they have a greater transfer function for the tuned frequency when compared to a broadband transducer. If the frequency content of AE signals is known it may be beneficial to pair a resonant transducer to that frequency which will improve the sensitivity to detection. Due to this, resonant transducers typically have a better signal-to-noise ratio however they are not suitable for frequency analysis.

Wideband transducers are something of a compromise between broadband and resonant sensors. The wideband transducer has a flatter frequency response than a resonant sensor but produces a higher fidelity signal with a greater sensitivity than a broadband sensor.

In addition to generating an electrical current from surface waves, it also possible to drive a transducer with an electrical alternating current to induce surface waves. The resultant wave is a function of the excitation signal, the sensor transfer function and the frequency response.

(Note: the term ‘transducer’ and ‘sensor’ have the same meaning in the context of the studies presented.)

Throughout the course of these studies three transducers have been used for both excitation and sensing; PANCOM Pico-Z, National Physical Laboratory (NPL) conical transducer and MGL Nano30.

3.1.1. PANCOM Pico-Z

The PANCOM Pico-Z (approximately costs £500) is a wideband transducer with an operational frequency range of 200kHz-500kHz. As the name suggests, it is a physically small transducer with a small sensor face (6mm). When used as a receiver, it is particularly useful for reducing the time-of-arrival error as this is directly proportional to the diameter of the sensor face [65]. In addition, the smaller transducer size minimises the effects of mass damping. Throughout these studies, Pico-Z transducers have been used for inducing surface waves. The small sensor face diameter is beneficial and has been shown to produce better results for the excitation of surface waves [179].

3.1.2. National Physical Laboratory conical transducer

The National Physical Laboratory (NPL) conical transducer is a broadband transducer that was developed by Theobald *et al.* [179, 180] to generate a self-calibrating repeatable reference signal for the characterisation of AE systems as an alternative to H-N sources. A cross-section of the conical transducer is presented in Figure 19.

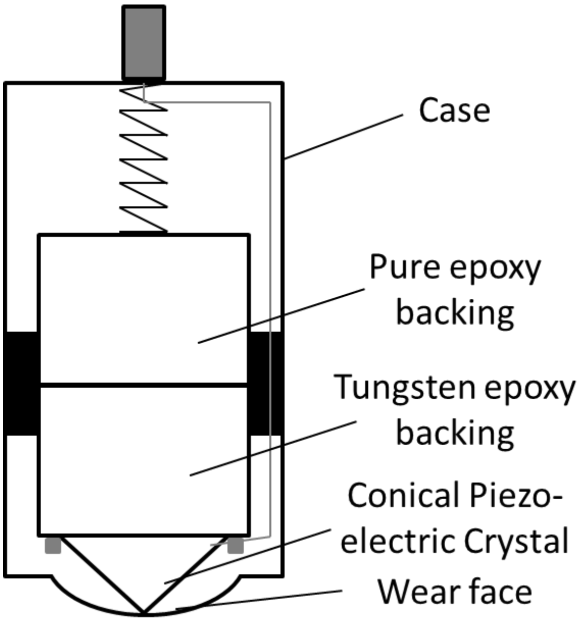

Figure 19. Cross-section of the NPL conical transducer

The piezo-electric crystal in the transducer is conically shaped, 3mm thick, and reduces from 10mm to 1mm in diameter. The small contact area of the tip makes the transducer akin to a point source when it is used to excite surface waves. The size and expense of this type of transducer means that it is not typically used outside of research environments. The conical transducer is only used for excitation in these studies.

3.1.3. Mistras Group Limited Nano30

The Nano30 sensor (approximately costs £300) is a commercially produced sensor widely used in industrial applications. The sensor is reasonably broadband with a resonance range, according to the manufacturers, of 150kHz – 750kHz [181] although it is resonant at 300kHz. Though larger than the Pico-Z, the Nano30 is still a relatively small sensor with a face diameter of 8mm. The small dimensions of the sensor make it ideal for monitoring areas where space is limited. Therefore the Nano30 sensor is an ideal choice for aerospace applications. Nano30 sensors are used within these studies for the sensing of AE signals.

(It should be noted that the high costs of the sensors used is due to their robust, wideband performance. For application on an aircraft structure it is suggested that lower cost, narrow-band sensors are used based on laboratory investigation)

3.1.4. Mounting of transducers

The mounting of transducers is an important consideration to ensure consistent and repeatable acquisition of AE signals and excitation of surface waves. Traditionally effective mounting of sensors to structures requires clamping or coupling.

Clamping methods ensure a good contact is made and maintained between the transducer and the structure. There are two main key points that must be adhered to [182];

- Adequate pressure must be applied to the transducer to ensure that contact with the structure is maintained.
- The transducer must not be able to move to ensure that errors do not occur in the location of AE signals.

There are numerous traditional clamping methods. Electrical tape has been used for the clamping of transducers. This works well where the tape can be wrapped around the structure and the transducer (for example, in the case of monitoring a small concrete beam) however it is not suitable for larger test specimens. Changes in temperature, high loads or long acquisition periods can lead to degradation of the tape and therefore this is an unsuitable clamping method for tests under these conditions.

Similar to electrical tape, self-adhesive tabs and zip ties can be used to clamp sensors to the surface of the structure. These have the advantage over electrical tape that they can be applied to most structures. However the presence of the adhesive tabs may affect wave propagation.

Magnetic clamping has also been used with some success. This method uses two magnets with a clamp in the middle which holds the sensor in place. It is ideal for quick application and removal of sensors to/from a structure particularly within the research environment. However, the material needs to be ferrous or thin enough to enable a ferrous backing plate to be placed on the underside. The presence of the clamp also adds additional mass damping.

Probably the simplest method of clamping sensors is to apply a mass to the back of the sensor to weight it down. This method is only applicable to flat surfaces where it is unlikely that the test will result in the movement of the sensors (i.e. failure of the structure). The addition of mass however also results in additional mass damping which may affect the frequency response characteristics of the transducer.

Baxter [65] conducted a thorough investigation into different clamping methods and found that magnetic clamps provided a good clamping solution for Nano30 transducers. However a small change in the frequency response of the sensor was observed.

In terms of coupling, it is recommended in ASTM E650 [182] that a couplant should be used to couple to the transducer to the structure. The presence of a couplant layer removes any air between the transducer and the structure which has a significantly lower acoustic impedance than the structure and transducer and therefore can reduce the quality of the signal received. The standard doesn’t recommend a suitable couplant though it does recommend that the couplant should be of sufficiently high viscosity to support shear forces, not corrode the structure and be carefully selected for the environment in which the transducer will operate.

A range of different couplants are typically used including, grease, silicone and ultrasonic gels. Many studies have been conducted to assess the usefulness of different couplants. Dugmore *et al.* [183] considered different couplants for monitoring AE on composite structures. It was found that most couplants needed at least three minutes to stabilise before useful results could be obtained. Colombo *et al.* [184] conducted a comprehensive investigation into the frequency response of transducers with different couplants. Signal parameters such as signal quality and repeatability performance of the different couplants was considered. It was found that cyanoacrylate adhesive produced the best results though complications can arise when the transducer is required to be removed. Beck [185] investigated the degradation of different couplants over time with respect to their transmissivity on concrete. It was found that couplants that were absorbed into the concrete suffered the biggest losses. Hensman *et al.* [186] investigated the reproducibility of transducer couplings for AE monitoring. Various commonly used couplants were used for coupling and recoupling of transducers. Cross-correlation analysis was used to assess the reproducibility of the different coupling methods. It was found that water-based ultrasound gels produced the best results though it was recommend that these couplants should only be used for short periods due to evaporation. Grease produced the best long-term results with silicone grease performing the worst; contradicting the findings presented by [187]. Baxter [65] investigated different couplants for monitoring AE on landing gear steels using Nano30 transducers. In this study, two transducers were coupled ‘face-to-face’ with one being excited by an electronic signal and the other receiving. Sensors were also coupled to steel plates and the degradation of the couplants was monitored over twenty-seven days. Finally, sensors were coupled to a steel plate to measure the transmission of a surface wave through a plate. It was concluded by Baxter that the most suitable couplant was silicone grease for the purpose of his studies.

An important consideration for selecting the appropriate coupling is the construction of the transducer. Some coupling methods may chemically damage the transducers or cause damage on removal. The Pico-Z transducer is metallic with a metallic wear plate. This makes the transducer reasonably resistant to damage caused by the coupling. Therefore, based on the findings of Colombo *et al.* [184] a cyanoacrylate adhesive (Loctite Ethyl-2- cyanoacrylate) was used throughout these studies for the coupling of the Pico-Z transducers. This coupling method acted as its own clamping method once set, although masses were placed on top of the transducers whilst the adhesive cured. To remove the Pico-Z transducers, acetone was used to soften the cyanoacrylate adhesive. A localised shear load was applied to the side of the transducer case with great care taken to ensure that it was not damaged. The sensor face was then cleaned using acetone to remove any remaining cyanoacrylate adhesive before re-coupling.

The NPL conical transducer has a plastic wear plate. Cyanoacrylate adhesives can cause degradation of plastics as well as causing damage during sensor removal. Considering the size and shape of the conical transducer, it was decided to use grease, based on the experiences of Hensman *et al.* [186], to couple the transducer with a brass backing mass which ensured a tight coupling of the conical tip with the structure.

Nano30 transducers similarly have a plastic wear plate which rules out the use of cyanoacrylate adhesives for coupling. Due to the small size and mass of the Nano30 transducers additional clamping methods would be required if grease were to be used. This was not suitable for the applications in which the Nano30 transducers are used in these studies. Therefore, based on the experiences of Baxter [65], it was decided to use a silicone based couplant that once set would also act as an integral clamping method.

3.2.Acousto-Ultrasonic signal generation

In the experimental investigations where acousto-ultrasonic (AU) Lamb waves have been generated, a Mistras Group Ltd. (MGL) µdisp/NB-8 combined acoustic emission system and wave generator was used. The µdisp/NB-8 contains a MGL WaveGen1410 arbitrary waveform generator subsystem. The WaveGen 1410 has two output ports for the wave generator; a low voltage port with a maximum peak voltage of 10V and a proportional high voltage port with a maximum peak voltage of 160V. A block diagram for the WaveGen 1410 is presented in Figure

20. In all cases the low voltage port has been used as a reference signal with the high voltage port used for exciting the mounted transducer. The µdisp/NB-8 was connected to a laptop computer via a card bus which enabled it to be controlled by the MGL WaveGen function generator software. The software has the capability to generate sine, square and saw tooth waves with or without a window function. In addition, there is a capability to generate frequency modulated waves as well as user-defined wave functions.

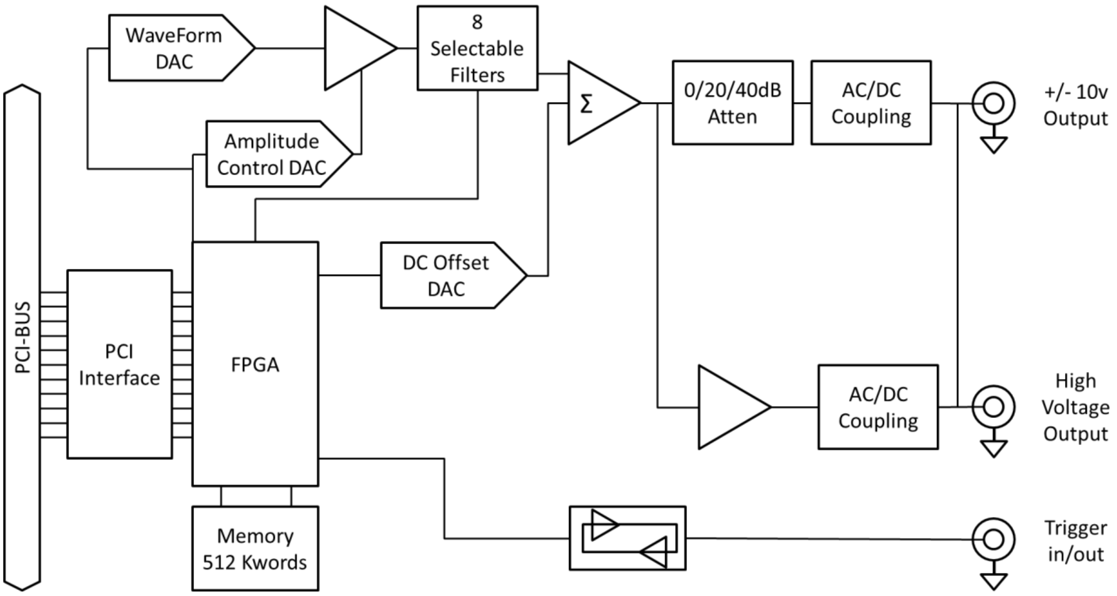

Figure 20. ARB1410 arbitrary waveform generator board block diagram (recreated from [188])

3.3.Laser vibrometry

The laser vibrometer used throughout these studies was the Polytec PSV-500-3D-M shown in Figure 21. This vibrometer is a three-dimensional scanning vibrometer which uses three laser heads. Through the use of scanning mirrors, this vibrometer can sample many points over the surface of a structure. This is achieved by tracking the locations of these points within images captured by a video camera mounted in the top scanning head. After training the movement of all three laser heads and conducting alignment, the lasers are then able to align at each scan point. The measurements recorded by each laser head can then be used to calculate both the in-plane and out-of-plane velocities using trigonometry. Since measurements are taken from three heads it is less important for the lasers to be perpendicular to the structure under test with a 3D scanning system than it is with a 1D system.

Figure 21. Polytec PSV-500-3D- M ([189])

The ‘M’ in the model identifier of the vibrometer is in relation to its sampling frequency (megahertz). The vibrometer used has the ability to sample up to a maximum frequency of 2.56MHz. Although this gives a Nyquist frequency (i.e. the maximum frequency that can be sampled without aliasing) of 1.28MHz, it is generally good practice to have a sampling frequency ten times that of the measured wave to ensure high fidelity in the reconstructed wave. Therefore only excitation frequencies of 300kHz and below have been considered in these studies.

A drawback of the vibrometry system used however is that at this sampling frequency, the lowest sensitivity range is 200 mm/s. This is not ideal as the amplitude of the measured velocities was of the order of 1 mm/s and thus the measured signal had a low signal to noise ratio. This was overcome by taking multiple measurements (two hundred unless otherwise stated) at each scan point and averaging the signals.

Measurements from the vibrometer were captured using the Polytec PSV 9.0 acquisition software. The acquisition of the vibrometer was triggered using a rising threshold of 15% from the 10v reference signal from the WaveGen. This ensured that that the acquisition was triggered by the reference waveform and not by any noise. A 10% pre-trigger was set on the acquisition to ensure that the start of the wave was captured. Nominally, (unless otherwise stated) a low-pass frequency filter was applied to the acquisition channels at 50kHz above the excitation frequency to filter out high frequency noise.

Results were analysed using the Polytec PSV 9.0 presentation software. This enabled the extraction of waveforms whilst also generating a visual representation of wave propagation.

3.3.1. Retroreflective glass micro-beads

The backscatter of light to the vibrometer head, and hence the signal received, is dependent on the surface finish and colour of the component under investigation. To improve the backscattering of the light to the vibrometer head, components were coated with a layer of retroreflective micro-beads which have a diameter of the order of 10μm.

Initial investigations were conducted to assess a number of different mounting methods. Grease was found to reduce the backscatter of light and hence the performance of the retroreflective micro-beads. Contact adhesive also had a negative influence on the performance of the beads. Spray adhesive was found to achieve the best results in applying a one-bead thick layer to the surface of a component. It appeared that this method gave the best backscatter and hence a high signal level with minimal influence on the wave being measured.

The recommendation from the Polytec for the mounting of beads is the use of steam which adheres the beads to the surface through the capillary action. This method was trialled however it was difficult to achieve consistent results over a large area. Additionally, the adhesion of the beads to the surface was weak meaning that beads were susceptible to falling off when specimens were being moved.

3.4.Acoustic Emission

This subsection outlines the techniques and equipment used for the study of acoustic emission.

3.4.1. Acoustic Emission data acquisition and storage

Two AE acquisition systems were used in these studies. Both were manufactured by MGL specifically for the acquisition of AE signals.

The PCI-2 system uses bespoke PCI-2 boards each of which provides two low-noise channels for the acquisition of AE signals. Though four boards were mounted in parallel (offering up to eight channels), no more than four channels were used at once throughout these studies. Each channel can be used to conduct full waveform acquisition and feature extraction. The PCI-2 features an 18 bit analogue-to-digital converter with a 40MHz sample rate. This gives the system a high-speed and high-resolution acquisition ability. The system also offers a wide bandwidth of 1Khz to 3MHz as well as programmable hardware filters. Though not used in these studies, the PCI-2 system also has the ability to continuously record raw signals (referred to as 'wavestreaming') [190].

The express-8 system is essentially an updated version of the PCI-2 system, offering much the same capability in a much smaller package, with the ability to simultaneously acquire on eight channels. There is a small compromise in the system specification for the smaller unit however. The express-8 offers 16 bit analogue-to-digital conversion and a reduced sampling rate of 10MHz but still maintains the ability to record and store waveforms [191]. For the AE signals recorded in these studies, this reduction in system specification is not detrimental.

Both AE systems use MGL AEWin software for setup, acquisition and post-test analysis. The software enables many test parameters to be set such as the values for pre-triggers, sample rates, sample lengths and filter settings. This gives the ability to fully tailor the acquisition of AE signals to the test that is being conducted. Regarding post-test analysis, the software offers the ability to easily replay AE tests and view their waveforms and energy content whilst also enabling on-the-fly source location using the time-of-arrival location method. Waveforms can easily be extracted in common plain-text formats for post processing.

3.4.2. Hsu-Neilson source

The Hsu-Neilson (H-N) source was first developed by Hsu *et al*. [192] as a method of calibrating AE sensors bonded to a structure. It was found that breaking pencil leads on the surface of a component induced an elastic wave that was representative of an AE signal. This method was developed to produce a repeatable signal for which a standard was written [193]. The standard states that a 0.5mm or 0.3mm dimeter, 2H grade lead must be used. To ensure repeatability of the source, the lead must be 2mm to 3mm in length and broken at an angle of 30°. In order the make the breaking of pencil leads readily repeatable, a Hsu-Neilson shoe was developed as shown in Figure 22.

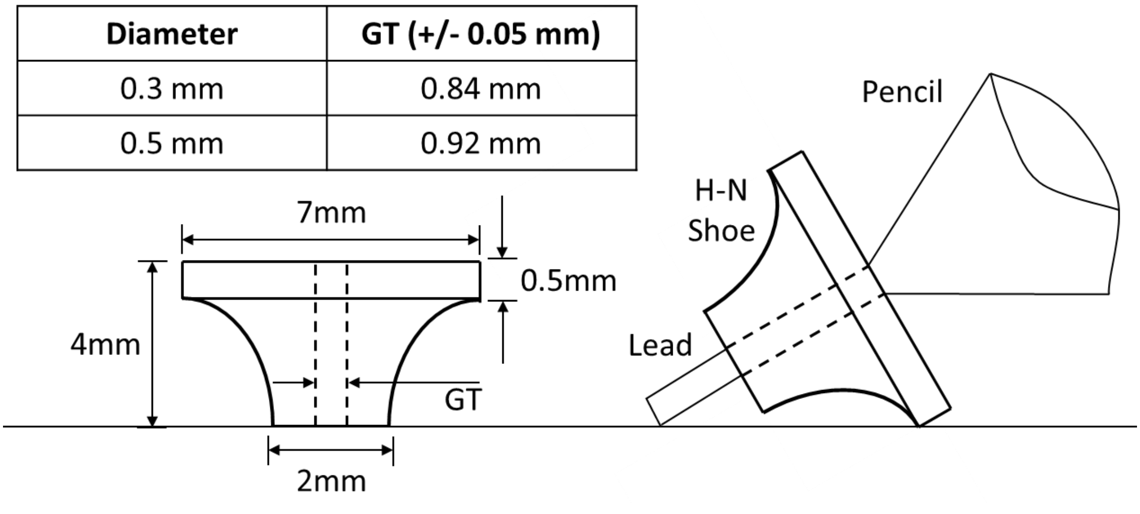

Diameter	GT (+/- 0.05 mm)
0.3 mm	0.84 mm
0.5 mm	0.92 mm

Figure 22. Dimensions and operation of an H-N shoe (recreated from [193])

The cost effectiveness and repeatability of H-N sources achieved has resulted in these being widely used in industry to represent AE events. In recent years they have been used in studies where it has been beneficial to map components' AE responses [32, 89, 194].

3.5.Ultrasonic inspection (C-Scans)

In order to characterise damage, a traditional ultrasonic NDT method known as a C-scan was conducted as part of these studies. The apparatus used for this was a MIDAS NDT ultrasonic C-scanner with a 10MHz transducer probe. The specimen under investigation is placed in a water tank which acts as a couplant for the transducer. The transducer is driven on rails which enable it to move in both the x and y-directions to inspect the entire specimen. It is excited with an alternating electrical current which induces an ultrasonic wave in the water towards the specimen. When the wave comes into contact with the specimen, some of the energy is reflected with the remainder transmitting through the specimen before making contact with a glass block where it is reflected back towards the transmitter. To receive the reflected signal, the transducer is electronically switched to act as a receiver. This is known as a 'pitch-catch' method.

A parameter of the received wave is then calculated (usually peak amplitude) which is then stored which corresponds to an x/y location. The transducer is then moved to the next location where the process is repeated.

Once complete, a false-colour image plot for the entire specimen is produced. Differences in peak amplitude denote changes in the structure and can be used to identify the location and shape of damage on a structure.

3.6.Dispersion curve calculation

Theoretical dispersion curves were calculated for particular metallic test specimens to aid understanding. This is particularly useful when discussing the interaction of different frequencies (and hence their wavelengths) with differing sizes of damage. Dispersion curves were calculated using the MGL AEWin software. This software has an integrated tool box for the calculation of dispersion curves for isotropic materials where material thickness, shear wave velocity and pressure wave velocity are specified.

3.7.Local Interaction Simulation Approach (LISA)

Two versions of the LISA software package cuLISA3D developed by Packo *et al.* [139] were used throughout these studies. The first version used was a pre-release version of v0.8.4 of the software which was acquired from Packo. The second version used was the full-release version of v0.8.4 (published by MONIT SHM) which featured minor upgrades to the management of the GPUs and hence a slightly better convergence performance than the pre-release version. There was no difference in the results obtained from the two versions.

cuLISA3D is a software package that is based on LISA (the reader is referred to the user manual published by AGH University, Poland for full details of the theory and programming [195]). The software take full advantage of the parallel processing power of nVidia CUDA architecture on modern GPUs for rapid solving and convergence of Lamb wave simulations. The software uses a MATLAB interface enabling a reasonably high degree of user-friendliness.

The parameters of the model are defined in a text file (or a tree of linked text files) which defines the parameters of the model. These parameters include the Cartesian co-ordinates for each cube, materials and environmental properties, actuator locations and details of the excitation and sensor locations. From a MATLAB script, a series of MATLAB MEX (binary encoded files) are called which take their inputs from the parameters outlined in the text files. These in-turn call a series of dynamic link library (DLL) files which allocate the processing within the GPU.

This software package produces results quickly which have been proven to be consistent with experimental results in published literature [135-137, 139, 196]. LISA has many advantages over other techniques such as FEA and analytical models. These include relatively quick production of results due to the efficient CUDA computation, the user-friendliness of the interface and accuracy in modelling of the boundary reflection and interaction with damage. It is because of these features that cuLISA3D was selected for numerical modelling in these studies presented.

This software package however does have some drawbacks. This commercially available package does not enable the user to define irregular cube sizes (i.e. cuboids – the reader is referred to the work of Sundarararman *et al.* [135]) or finer or coarser cube sizes for different areas of the model (a global cube size is defined by the user) and anisotropic materials cannot be modelled (pressure and shear wave velocity are not defined with respect to propagation direction). This means that composite materials cannot be modelled using this package (though a degree of heterogeneity can be achieved by allocating different material properties to adjacent cubes – the reader is referred to the work of Delsanto *et al* [132]).

Another drawback of this particular package is that because the GPU architecture is used, this requires the on-board graphics card random access memory (RAM) to be used which is typically an order of magnitude less than the RAM of the computer. This can result in larger models not being able to be computed as all of cube co-ordinates need to be pre-loaded on to the GPU RAM. Hence, it would be beneficial to have variable cube size to reduce the number of co-ordinates required.

The software package also includes a ‘cube viewer’. This enables the user to view all of the cubes in the model which is particularly useful for ensuring that the model is correct and that the correct material properties have been allocated to the correct areas of the model. It is also possible to use the cube viewer function to ‘dump’ the values for each cube at a particular time-step to give a visual representation of the wave propagation. By dumping data at sequential time-steps it is possible to animate the propagating wave. However, this does slow down the performance of the software.

3.8.Summary

This chapter has presented the experimental and numerical techniques used throughout this thesis. The techniques, methods and equipment presented here are common to these studies. Where possible, the best practices have been followed as stated within the published literature. However, some studies presented, such as those which use laser vibrometry, have required best practices to be developed.

4. Lamb Wave Interaction with Adhesively Bonded Stiffeners and Disbonds Using 3D Vibrometry

4.1. Introduction

Aircraft structures are typically constructed from thin load bearing skins with stiffeners attached to provide the structure with the required amount of rigidity [39]. There are two predominant methods of attaching the stiffeners to the skin; mechanical fasteners such as rivets, or bonding with an adhesive. Traditionally, mechanical fasteners have been used in the primary structure of the aircraft (i.e., the structure in which failure would be catastrophic) because of their ability to transfer loads between components with predictable performance. However mechanical fasteners create high stress concentrations which can lead to crack initiation [197, 198].

A significant contribution to mass reduction can be achieved by using adhesive bonding techniques in place of these traditional mechanical fastening methods. Bonding techniques have increased strength to mass ratios whilst having improved structural performance and more resistance to fatigue loading than mechanically fastened joints [199-201]. Adhesively bonded metallic joints have been used in the secondary structure of aircraft for the past fifty years [202]. Adhesively bonding stiffeners is also less labour intensive and more cost effective than using mechanical fasteners as it does not require repetitive drilling operations [203]. Adhesive bonding is particularly suited to composite structures where the use of mechanical fasteners presents additional difficulties. Due to the hardness, high tensile strengths and abrasive nature of some composites, drilling can cause rapid deterioration of the drill bits [204] resulting in high machining costs and thus skilled operatives are required to carry out the operation. Drilling can also cause damage to the composite such as interlaminar crack propagation, micro cracking, fibre breakage, fibre pull-out, matrix cracking, thermal damage and delaminations. The presence of the hole also forms a reduction in the strength of the material due to the fibres no longer being continuous.

Despite the mass saving, cost reduction and manufacturing benefits of adhesively bonded joints [203] there is a reluctance from aircraft design engineers to use them in the aircraft's primary structure due to a poor understanding of their failure mechanisms and lack of engineering confidence in their use [205], particularly in the hostile environments that the bond will experience (i.e. varying temperatures, water ingress and high levels of humidity) [206, 207]. From the experience of the Royal Australian Air Force (RAAF) 53% of defects detected in aircraft structures such as the F-111 were found to be bond failures [201]. In the case of the Boeing 737, Aloha flight 243, adhesive bond failure resulted in catastrophic failure of the fuselage [4]. Many cases of adhesive bond failure have been found to be the result of improper application of the adhesive or insufficient surface preparation [208] i.e., human error in the manufacture of the joint. In addition, there is little understanding of the in-service degradation of adhesively bonded joints that can be directly attributed to harsh environments that an aircraft experiences [209]. This has led to over engineered, heavy design solutions being created [210], typically using adhesives combined with arrestment fasteners [208].

The uncertainty in the condition of adhesive bonds throughout the aircraft's in-service life requires monitoring using non-destructive techniques to ensure airworthiness. Traditional non-destructive (NDT) techniques can be used to inspect the structural integrity of bonds on aircraft structures. However with the increasing size of commercial aircraft, the influence of human error and pressures from aircraft operators to reduce maintenance times [20], alternative solutions to traditional NDT techniques have to be found to enable the application of airworthy adhesively bonded stiffeners. If a sensor network could be installed to monitor damage and degradation of the bonded joint an "as required" inspection program could be used.

Adhesive bond defects are often complex, for example kissing bonds, where a bond fails but still retains close contact between the bond faces hence appearing to still be bonded. These are notoriously difficult to detect [211]. To enable complex defects be detected using techniques such as acousto-ultrasonics, sensor networks need a high probability of detection. In the case of acousto-ultrasonics an understanding of Lamb wave interaction with stiffeners and associated defects will enable better sensor network design whilst also driving towards minimizing the weight penalty the sensors add to the overall structure.

This chapter describes a study to investigate Lamb wave interaction with a stiffener and disbonds using 3D scanning laser vibrometry in order to visualise the wave propagation and interaction. Three excitation frequencies were used to investigate the different sensitivities of the different wavelengths to the disbond damage. A windowed root-mean-squared technique was developed to quantify the reflection, attenuation and transmission of Lamb wave energy across the structure, enabling the size and shape of the defect to be visualised. The technique was verified by traditional ultrasonic inspection techniques. This is further supported with an ultrasonic C-scan and a swept sine wave excitation vibrometry study.

A computational study using the software LISA was carried out for comparison with the experimental results. The objective of the simulation was to determine its viability as a tool for simulating wave interaction with disbonds for damage detection sensor network design. This approach enabled the Lamb wave interaction to be investigated numerically with a view to its potential use as a design tool for the optimisation of sensor locations.

4.2.Panel manufacture and geometry

A 3 mm thick 6082-T6 aluminium plate was bonded to a 6082-T6 aluminium unequal angle stiffener to construct a stiffened panel with the dimensions shown in Figure 23. The dimensions of the panel were chosen to reduce the effects of edge reflections. The stiffener was bonded to the plate using commercially available Araldite® 420 (Huntsman) adhesive. The film thickness of the adhesive was regulated using 0.1 mm copper wire gauges to achieve the optimal shear strength [36].

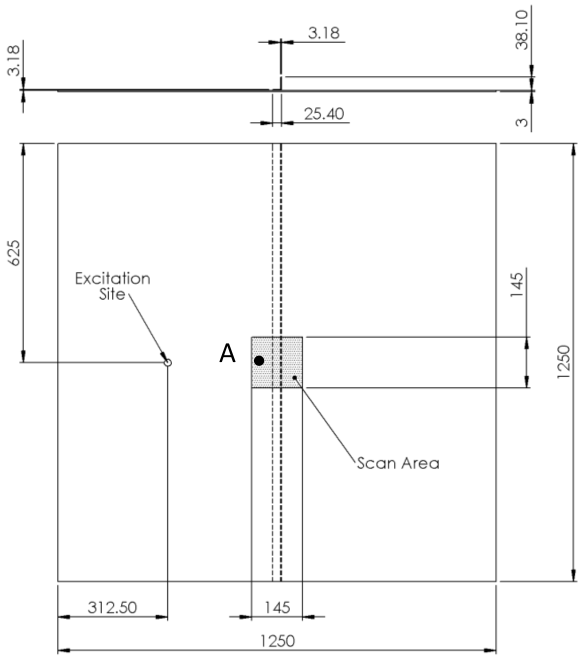

Figure 23. Dimensions of the stiffened panel (all dimensions in mm).

A geometrically similar second panel was also manufactured with an induced disbonded region of 25.4 mm length across the width of the stiffener. The disbonded region was induced by installing PTFE tape prior to applying the adhesive. This was then removed once the adhesive had cured.

A commercially available PANCOM Pico-Z transducer was acoustically coupled to the panel using Loctite® Ethyl-2-Cyanoacrylate adhesive. This transducer was selected because of its flat broadband frequency response in the frequency range under investigation and its relatively small face (5 mm), as previous studies have shown that sources that are more representative of a point source produce best results [179]. The transducer was located at the mid-point between the panel edge and the stiffener centreline to reduce the effects of edge reflections on the transmitted wave. This also was sufficient distance from the scan area to ensure that that the Lamb waves had fully formed by the time that they reached the scan area.

4.3.Experimental Setup

A 10-cycle sine wave was generated by the MGL WaveGen function generator software which was connected to the MGL µdisp/NB-8 hardware. This allowed the transducer to input sufficient energy into the structure. The peak-to-peak amplitude of the excitation signal was 160V. Three frequencies were selected for this experiment; 100 kHz, 250 kHz and 300 kHz. The frequencies investigated primarily excited the two fundamental modes as shown in the calculated dispersion curves for a 3mm aluminium plate in Figure 24.

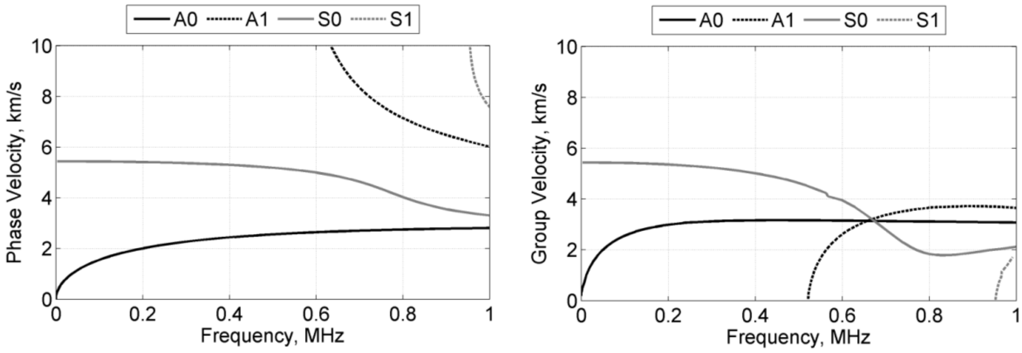

(a) (b)

Figure 24. Calculated dispersion curves for a 3 mm aluminium plate, (a) Phase Velocity (b) Group Velocity

100 kHz was chosen to investigate the interaction of a longer wavelength with the stiffener and disbonded region. The wavelengths of the A_0 and S_0 modes were calculated to be 15 mm and 55 mm respectively. Though this frequency fell outside the operating resonance window of the chosen transducer, the calibration certificate for the transducer showed that it would function at this frequency albeit at a reduced amplitude. Frequencies of 250 kHz and 300 kHz were selected to investigate the interaction of shorter wavelengths. The wavelengths of the A_0 and S_0 modes were calculated to be 9 mm and 22 mm respectively for the 250 kHz excitation and 8 mm and 18 mm respectively for the 300 kHz excitation. Frequencies above 300 kHz were not considered due to the constraint of the sampling frequency of the acquisition card in the laser vibrometer used. This was not seen to be an issue as the calculated wavelengths indicated that interaction would be observed considering the size of the disbond. A 10 V peak-to-peak wave was also generated and used as a reference signal for triggering the acquisition of the vibrometer. A repetitive trigger rate of 20 Hz was used as this gave sufficient time for the induced wave energy to fully dissipate before the next measurement was taken.

A sampling frequency of 2.56 MHz was used for the acquisition by the vibrometer, which gave sufficient resolution for reconstructing the wave. A drawback of the vibrometry system used however was that at this sampling frequency, the lowest sensitivity range is 200 mm/s. This is not ideal as the amplitude of the measured velocities was of the order of 1 mm/s and thus the measured signal had a low signal to noise ratio due to it being within the noise floor. This was overcome by using an averaging technique within the vibrometer software. This involved taking 200 repetitive measurements at each point. The 200 measurements were then averaged resulting in a waveform with improved fidelity as the random noise on the signal reduced to approximately zero. A scan area of 145 mm × 145 mm was measured which comprised of 5329 measurement points. The area was coated with retro-reflective glass beads to improve the level of backscattered light.

4.4.LISA model

A LISA model was designed to simulate the Lamb wave interaction with the stiffener and disbond in the metallic panel, which could be validated with the 3D vibrometry measurements.

4.4.1. Global cube edge length

As previously discussed, a major drawback of the LISA modelling package is that it uses a global cube edge length and hence the smallest component dimension drives the global cube edge length, as opposed to finite element techniques where the mesh can easily be refined in regions of interest whilst adopting a coarser mesh elsewhere. For the panels used in the experimental study, the smallest dimension was the adhesive film thickness of 0.1mm.

Using a 0.1mm global cube edge length generated a very large set of cube geometry data which was not possible to process using the CUDA graphics card due to insufficient memory (2GB). Therefore, the model was simplified to reduce the memory required.

4.4.2. Model setup

The simulation was performed on a PC fitted with an NVIDIA GTX690 CUDA graphics card (2 Kepler GPUs with 256 cores running at 995MHz, 2GB of RAM).

The inner 625mm x 625mm region of the plate stiffened aluminium plate was modelled with an ultrasonic actuator positioned on the edge to reduce the effects of edge reflections; a common ultrasonic modelling technique. The smaller geometry also reduced the computational costs and model processing time.

A global cube edge length of 0.5mm was used for the model. This introduced complexities in the modelling of the much thinner adhesive film. Attempts were made to model the adhesive layer by reducing the global cube edge length to 0.1mm however this was not possible to successfully model due to insufficient RAM on the graphics card used. A model with a 0.5mm adhesive film layer was also produced however the results from this model showed a high level of transmission through the stiffener with limited reflections which were not representative of experimental results. Therefore, the effects of the adhesive film were assumed to be negligible for the purpose of creating a simplistic model. In reality, the adhesive film layer would have an influence on the wave interaction as the density and Young's modulus of the adhesive is substantially lower than that of the aluminium (approximately 1200kg/m^3 and 1.5MPa respectively [212]). Due to the global cube edge length, a stiffener width of 25.4mm could not be modelled. This was rounded to the nearest cube integer of 25.5mm but is not thought to have any significant affect.

In the case of modelling the disbond, a group of cubes 25.5mm x 25.5mm x 0.5mm was removed from the underside of the stiffener to simulate the reduction in stiffness as shown in Figure 25.

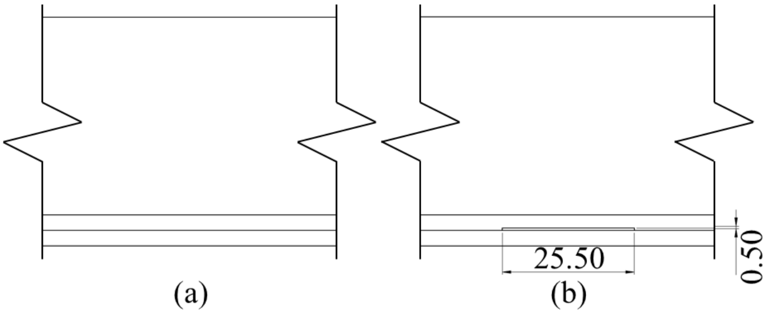

Figure 25. Side elevation of the LISA geometry for (a) the healthy panel and (b) the disbonded panel

A 10-cycle sine wave with a Hanning window was used for the excitation. As with the experimental setup, three frequencies of 100kHz, 250kHz and 300kHz were used for the excitation.

4.5.Results

The velocity measurements from the laser vibrometer were integrated using Polytec PSV software to obtain the displacement values. This was carried out to be representative of the signal that a sensor bonded to the structure would measure. The magnitude of each of the displacement components for each excitation frequency is presented in turn. For each set of results a 0µs datum point was taken immediately before the S_0 mode reached the measurement field. In each plot presented. The arrival of the S_0 mode was determined by studying the waveforms from the measurement point on the left-hand boundary in-line with transducer. The location of the stiffener is denoted by the dotted lines.

4.5.1. 100kHz results

The results from the healthy panel and the panel with the disbonded region are shown in Figure 26 and Figure 27 respectively.

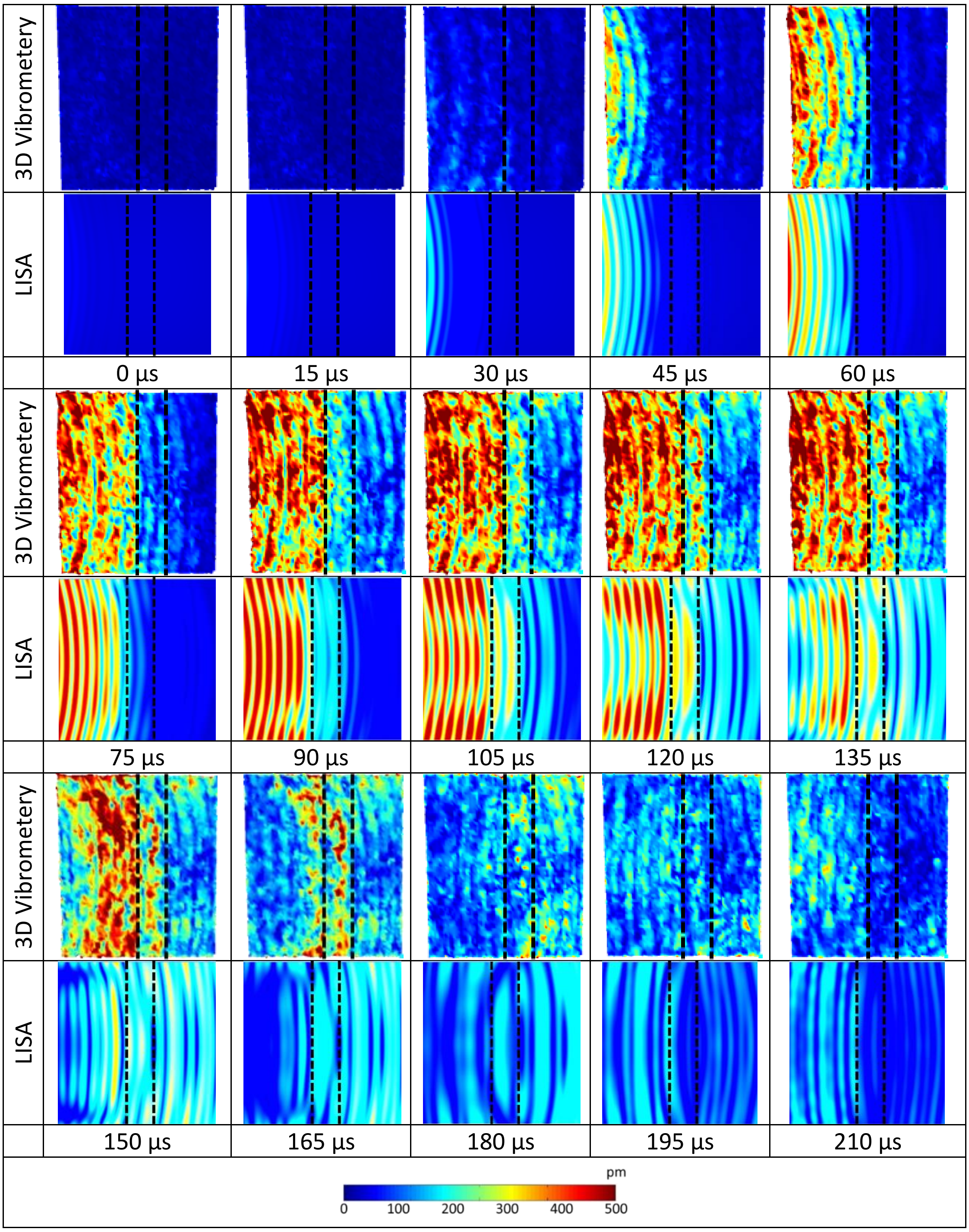

Figure 26. 100 kHz three-component resultant displacement magnitude showing Lamb wave interaction with the healthy stiffened panel.

The experimental results from the healthy panel show that the higher wave velocity S_0 Lamb mode is relatively unaffected by the presence of the stiffener and is mostly transmitted straight through. The slower wave velocity A_0 mode however is greatly affected. At 105µs in Figure 26 the A_0 mode interacts with the stiffener resulting in a reduction in amplitude of approximately 50% on the other side, demonstrating that the majority of the wave energy is being either attenuated or reflected by the stiffener rather than transmitted past it.

The results from the LISA model correspond well with the experimental results from the 3D vibrometry. In both sets of results shown in Figure 26, the amplitude of the displacements is seen to significantly decrease as the Lamb wave passes through the stiffener. This can be attributed to the significant localised change in stiffness as well as a proportion of the wave energy being reflected back towards the source.

The experimental results presented in Figure 27 from the panel with the disbond show that in this case the S_0 Lamb mode interacts with the disbonded region of the stiffener. This is seen in Figure 27 at 30µs as an area of higher amplitude in the disbonded region. Similarly, a higher level of wave amplitude is observed as the A_0 mode also interacts with the disbonded region shown at 75µs. As the A_0 mode continues to interact with the disbonded region, transmitted (right of the stiffener) and reflected (left of the stiffener) conical diffraction fringes are observed clearly from 105µs onwards. The behaviour of the Lamb wave outside the disbonded region is similar to that of the healthy panel.

Comparing the experimental results with the model, it is possible to see from the 3D vibrometry that at 30µs the S_0 interaction with the disbond produced a significant increase in the amplitude which is not reflected in the results from the LISA model. However from 60µs - 90 µs, the wave interaction with the disbond in both the results from LISA and the 3D vibrometry are very similar and in particular, the A_0 interaction with the stiffener shows a similar increase in amplitude when the two displacement plots at 75µs are compared. As the wave continues to interact, there is again a difference between the results from the model and the 3D vibrometry. In the LISA model, there is a fringe pattern of high amplitude on the right hand side of the stiffener as the wave is transmitted through the disbond. The fringe pattern observed on the 3D vibrometry is of lower amplitude with a higher amplitude fringe being observed to the left of the stiffener. Considering only the fringe patterns however it can be seen that there were similarities in the shape of the conical fringes on both sides of the stiffener.

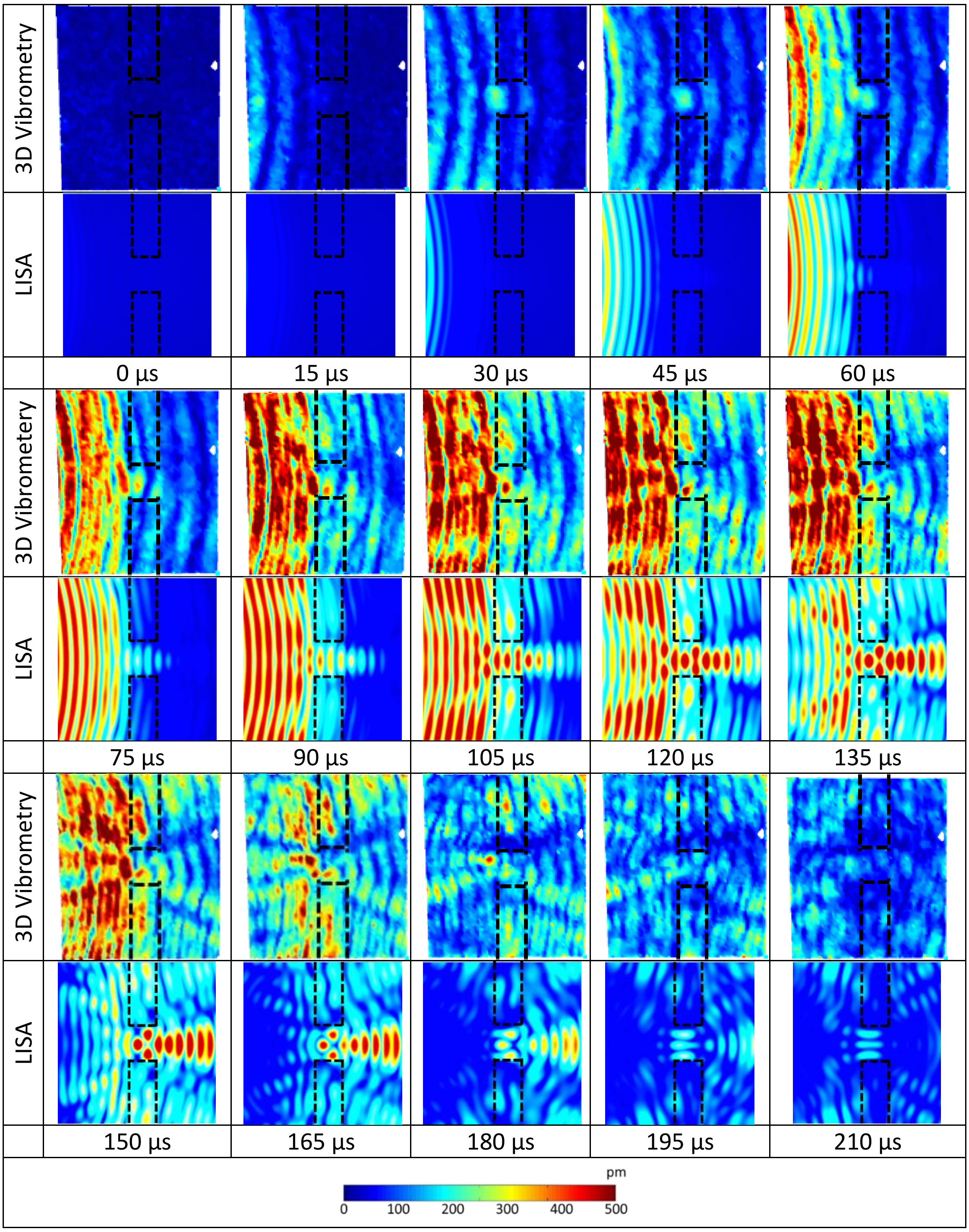

Figure 27. 100 kHz three-component displacement magnitude showing Lamb wave interaction with the healthy stiffened panel.

4.5.2. 100kHz windowed cross-correlation analysis of experimental data

Example waveforms of the out-of-plane component from the corresponding measurement points in the area of investigation are plotted in Figure 28 for the healthy and disbonded panel respectively from the experimental study. The measurements presented were at the left hand boundary on the centreline denoted by point A in Figure 23. This measurement point lay equidistant between the excitation site and the stiffener.

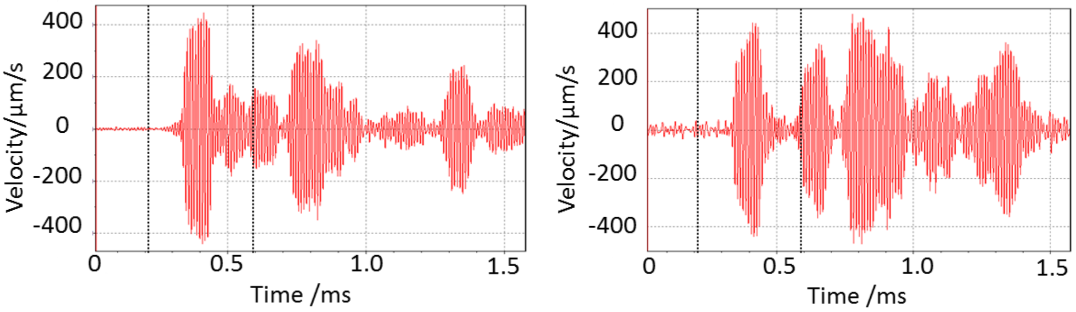

(a)

(b)

Figure 28. Waveforms from the left hand boundary of the area of investigation in-line with the disbonded region for each panel—(a) Healthy (b) Disbonded. The dashed lines denote the section of waveforms that was used for time windowing.

From visual comparison, it is evident that there is a significant difference between the two waveforms. The signal measured from the disbonded panel had a higher level of noise than the signal measured from the healthy panel. This is mostly likely due to a difference in the level of backscattered light received. Even by simple visual comparison, the incoming wave is similar. However, by 0.45ms there is a significant change in the waveforms. The healthy panel shows the reflected wave-packet from the stiffener whereas this is not present in the waveform from the disbonded panel as the wave is transmitted through the disbond.

To quantify this difference in the measured waves, a windowed cross-correlation analysis was conducted. Starting at 0.21ms, both waveforms were windowed into respective 100μs time windows and the cross-correlation coefficient was calculated. The windows were transposed by 20μs forward and the cross-correlation coefficient was once again calculated. The cross-correlation coefficients from this analysis are plotted in Figure 29.

The first two time windows show a low value for the cross-correlation coefficient. This is due to random noise mostly being present in these windows. As the wave arrives in the 0.25ms–0.35ms time window, the value of the cross-correlation coefficient significantly increases to 0.93 and continues to increase until it peaks in the 0.31ms–0.41ms time window at 0.97. It is worth noting that in an installed acousto-ultrasonic system, when comparing signals before and after damage for the same structure, the cross-correlation coefficient may be higher than this. However, due to two similar panels being used (particularly with two different sensor couplings) in this experiment and small differences in experimental setup this indicates a good correlation of the two wave forms. If this analysis was conducted on two results sets from the same plate, identical waveforms would be expected to be seen and therefore values of unity across at each time window after the wave arrives.

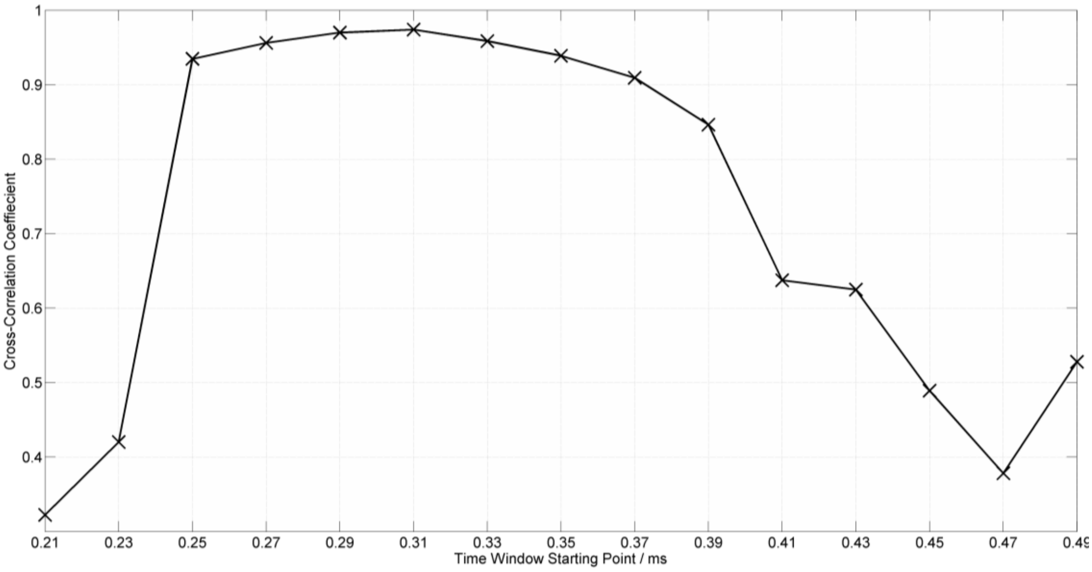

Figure 29. Moving window cross-correlation coefficient plot.

As the waveforms start to differ due to the reflections, the cross-correlation coefficient starts to reduce significantly. In the 0.47ms–0.57ms time window the cross-correlation coefficient was found to be 0.38 indicating a large difference in the waveforms and hence, the presence of the disbonded region.

This analysis demonstrates that the wave transmitted from the excitation site was comparable on both panels during this experiment. For an installed SHM system this technique demonstrates that reflected waves from the stiffener can be used to identify the presence of disbonds.

4.5.3. 250kHz results

The results from the experimental and LISA studies for the healthy panel and the panel with the disbonded region are shown in Figure 30 and Figure 31 respectively.

As with the 100 kHz results, there is a significant reduction in wave amplitude as the A_0 mode interacts with the stiffener. As with the results from the 100 kHz excitation, the S_0 mode interacts with the disbonded region, illustrated at 30µs in Figure 30 by the increase in wave amplitude. The S_0 mode wave energy transmitted through the disbonded region is also shown by a fringe of increased amplitude to the right of the disbonded region. The presence of the stiffener is clearly seen in Figure 30 at 60µs.

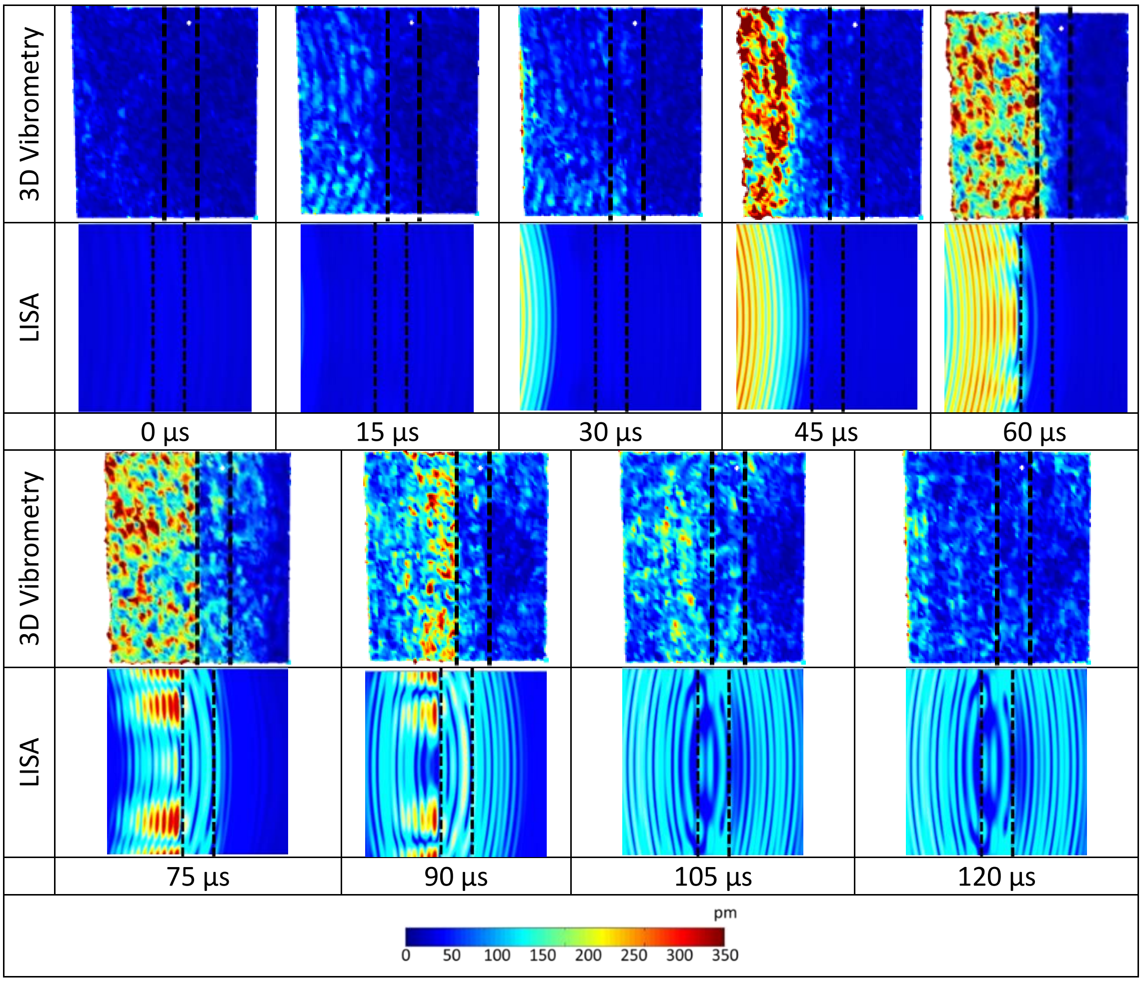

Figure 30. 250kHz three-component displacement magnitude showing Lamb wave interaction with the healthy stiffened panel.

The A_0 mode is transmitted through the disbonded region with a lower reduction in amplitude than for the bonded regions of the stiffener. This has led to a fringe of high amplitude to the right of the stiffener.

Observing both the experimental and LISA results in Figure 30 it is possible to see that the wave velocity of the 250kHz excitation is greater than that of the 100kHz excitation results presented in Figure 26. This is due to the dispersive phenomena of Lamb Waves. LISA was derived from the fundamental wave equation for particle displacement which can be developed from Green's approach [138].It is demonstrated that there is good agreement in terms of the dispersive wave velocity between the LISA model and the experimental results.

The high amplitude fringes that are observed in the LISA model as the incoming wave is guided along the length of the stiffener are present in the 3D vibrometry plots but to a lesser extent, as seen at 75µs and 90µs. This is due to the amplitudes of the waves reflected off the stiffener being of significantly higher amplitude experimentally than those that were observed in the model. However, this wave energy rapidly attenuated producing a good similarity between the model and the experimental results.

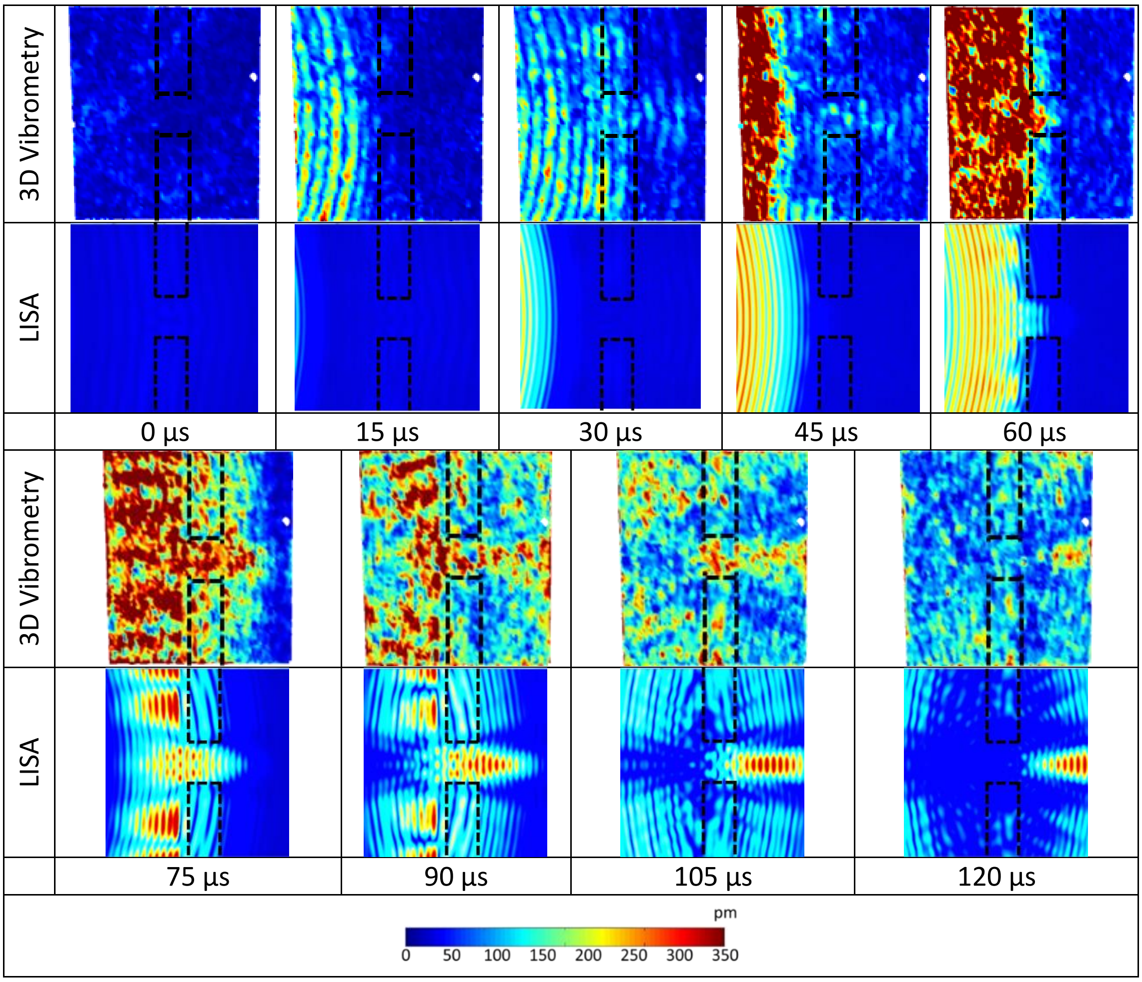

Figure 31.250kHz three-component displacement magnitude showing Lamb wave interaction with the disbonded stiffened panel.

The 250kHz LISA disbonded stiffened panel results shown in Figure 31 are qualitatively similar to the 3D vibrometry results. At 30µs the S_0 wave interaction with the disbond is apparent in both sets of results. However, the wave interaction in the LISA model displays significantly smaller amplitudes than those observed in the 3D vibrometry results

The interaction with the A_0 mode observed from 60µs onward shows great similarity. At 60µs there is high amplitude observed in the disbonded region in both the LISA model and the 3D vibrometry. As time progresses, there are high amplitudes of the Lamb wave displacement transmitted through the disbonded region. In the LISA model there is a more pronounced conical fringe pattern observed that is not as easily identifiable in the 3D vibrometry results.

4.5.4. 300kHz results

The results from the experimental and LISA studies for the healthy panel and the panel with the disbonded region are shown in Figure 32 and Figure 33 respectively. As with the other two excitation frequencies, the presence of the stiffener significantly reduces the amplitude of the A_0 mode as it interacts with it as shown at 60µs in Figure 32.

There is what appears to be a mode conversion in the LISA model as the A_0 mode interacts with the stiffener shown by a longer wavelength. This was also present in the 250kHz study but was not clearly observed in the results from the 3D vibrometry. Mode conversion in the presence of stiffeners has been treated theoretically by Reusser [213] which supports these findings.

It is also possible to observe once again similarities in the fringe patterns as the wave is guided along the length of the stiffener at 60µs and 75µs.

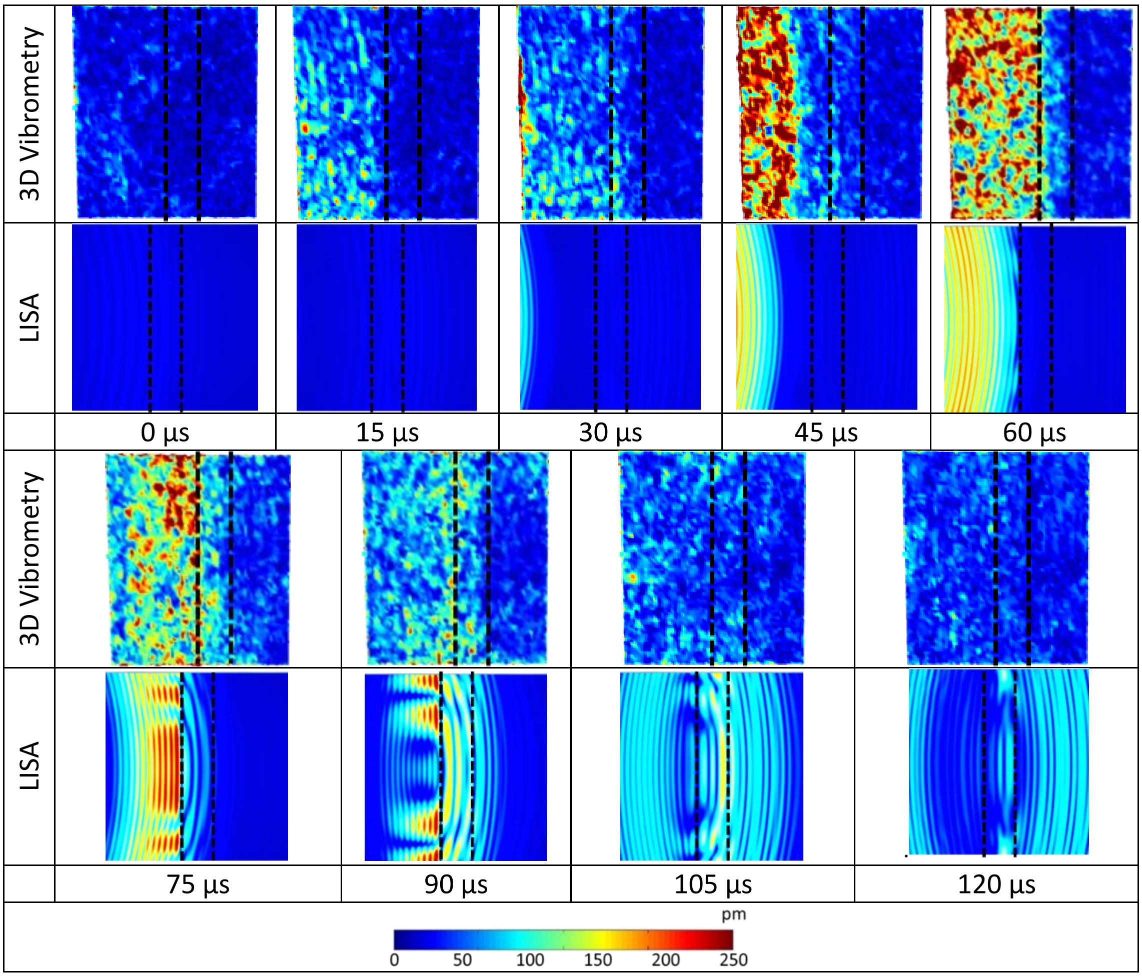

Figure 32. 300 kHz three-component displacement magnitude showing Lamb wave interaction with the healthy stiffened panel.

Again, as with the other two excitation frequencies, the S_0 wave transmits through the disbonded region more effectively than through the regions that are adhesively bonded as shown at 30µs in Figure 33.

As found in the 250kHz study, similar wave interaction fringes are observed between the LISA model and the 3D vibrometry. There is a similar interaction fringe with the S_0 mode observed at 30µs though the amplitude of the fringe observed in the 3D vibrometry results is significantly higher than those observed in the LISA model.

At 60 µs the A_0 mode also interacts with the disbonded region. This interaction results in a transmitted conical fringe pattern to the right hand side of the stiffener as the wave energy transmits through the disbonded region. It is observed from the 3D Vibrometry results however that the wave that is transmitted through the disbonded region appeared to attenuate more than the wave that is observed in the LISA model.

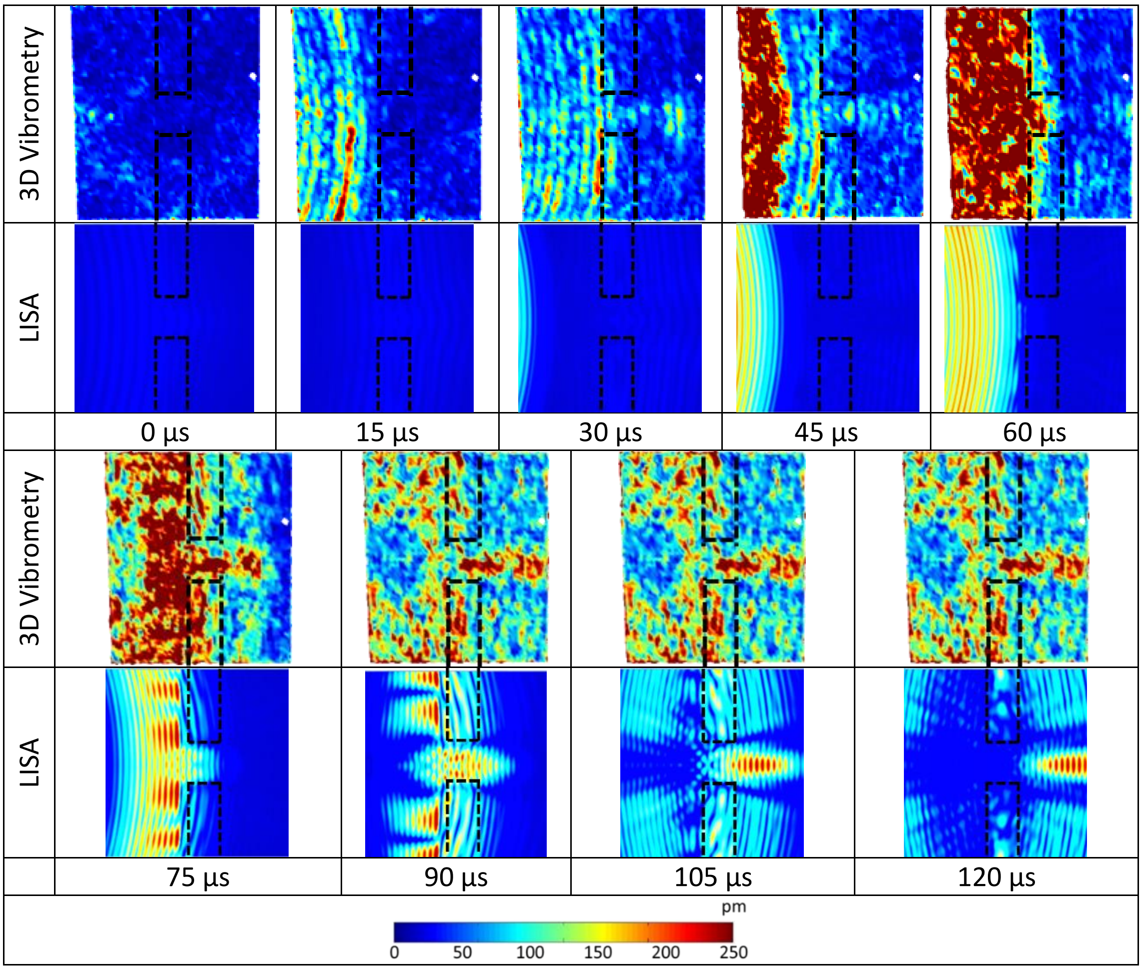

Figure 33. 300 kHz three-component displacement magnitude showing Lamb wave interaction with the disbonded stiffened panel.

4.5.5. Comparative discussion

When comparing these results sets, particularly the 100 kHz and 250 kHz results, dispersion was observed as the higher frequency waves can be seen to travel further in a shorter space of time. It was also observed in both the results from the LISA model and the 3D vibrometry that the amplitudes of the Lamb waves reduce at a higher rate for the higher excitation frequencies as they move across the area of investigation; therefore demonstrating that the higher frequencies attenuate more.

Comparing the experimental results from the two different panels, the S_0 mode is seen to have a greater amplitude in the disbonded panel results. This increase in wave amplitude can be attributed to a difference in sensor coupling. Despite using the same method to couple the sensor to each panel, it is very difficult to achieve a consistent and repeatable sensor coupling.

The differences seen in the LISA results compared to the 3D vibrometry could be due to several factors. It is important to note that assumption of the adhesive film layer being negligible may have resulted in the differences seen. The adhesive film had different material properties to the aluminium. This would result in a change in acoustic impedance which would influence the wave interaction. The extent to which this is significant requires further study. This may explain the higher reduction of the wave amplitude as the waves were transmitted through the stiffener in the LISA model.

One assumption that was made with the LISA model was that the source was a point source that was mostly acting out-of-plane. In reality however, the transducer was not a true point source as the transducer had a face diameter of 6mm. This would have some influence on the excitation as this is much larger than a point. Also, although the primary excitation would be out-of-plane, due to Poission's ratio, there would be some in-plane exciation. Another aspect of 'real' transducer is that it has a transfer function and although excitation frequencies were specified it may be possible that the frequency of the induced Lamb waves were different.

It was also assumed in the model that the aluminum used was perfectly ansiotropic. Although this is a fair assumption, production processes such as rolling direction may have had some influences on the wave velocities. Similarly, it was assumed that the thickness of the plate was 3mm throughout although it may have been possible that their may be small changes in thickness due to the production process.

One significant difference between the three experimental results sets at different frequencies is the transmitted conical fringe patterns produced by the Lamb wave interaction with the disbonded region. The results from the 100 kHz excitation show a reduction in wave amplitude to the right of the disbonded region. This differs greatly to what is observed in the results from the 250 kHz and 300 kHz excitations where an increased amplitude is seen to the right of the disbonded region. It has been suggested that this may be a function of the difference in the resultant wavelengths of the different excitation frequencies [38]. This is due to the shorter wavelengths of the higher frequencies being more sensitive to interacting with damage. In terms of the design of a damage detection system however there is a trade-off between the minimum damage size detectable and the global coverage required due to the greater attenuation of the higher frequency Lamb waves.

It may also be noted that the shape of the reflected conical fringe pattern to the left of the stiffener in the 100kHz excitation experimental results appears to diffract from the entire width of the disbonded region whereas in the other two sets of results the fringe pattern appears to diffract from a much smaller area. It is worth noting that this problem cannot be simply approximated in a similar manner to that of a fluid mechanics problem due to the transmission of the wave through the stiffener and the added complexity of differing wave modes.

During manufacture, PTFE tape was used to induce the disbond. Though every effort was made to achieve a perfect disbond, it was possible that the disbond was not geometrically perfect as modelled in the LISA simulation. This could explain some of the differences in the interaction fringes particularly those observed in the 100kHz study.

The results from the LISA simulation generally exhibited similar wave interaction to the results observed from the 3D vibrometry. There was however a reduction in the quality of the 250kHz and 300kHz plots compared to 100kHz plot. This could be attributed to the spatial resolution of the scan points. The number of scan points was kept consistent throughout the study in order to obtain results that were comparable and to allow the study to be completed in a timely fashion. By increasing the number of scan points, more detailed 3D vibrometry fringe plots could be achieved allowing a better comparison to be made between the experimental and simulated results.

The amplitude of the S_0 mode in the vibrometry results is much greater than that observed in the LISA results. A possible explanation for this is that the excitaton used in the LISA model had no in-plane component. This excitation was used to represent the excitation used in the experimental study which was predominantly out-of-plane. However, in reality it is likely that there is a small in-plane component to the excitation due to the Poission’s ratio of the piezo-ceramic crystal. This would differ from crystal to crystal and therefore to determine how much in-plane component it would be necessary to add to the excitation of the model would be the subject of another study.

The high amplitude of the waves transmitted through the disbond gives an indication that disbonds have a significant effect on wave interaction. The presence of high amplitude waves directly behind the disbond region and the surrounding low amplitude fringes compared to the low amplitude observed in the healthy bonds suggests that wave energy could be used to detect the presence of the damage.

4.6. Windowed RMS Analysis of experimental results

An understanding of the effects of wave interaction is fundamental in designing sensor networks to monitor stiffener disbonds in aerospace structures. It therefore is advantageous to obtain an understanding of the amplitude of the Lamb wave modes as they interact with defects.

It has been demonstrated by Lee and Staszewski that windowing the time signal and calculating a quantitative measure of the wave amplitude can provide a useful insight for sensor positioning [39]. This is particularly important for developing SHM systems with a high probability of detection.

A root mean-squared (RMS) value for a 10 µs time window of the magnitude of the three displacement signals was calculated for each measurement point of the experimental dataset. For each data set three plots of the time windows have been produced which show three stages of the interaction: the S_0 mode interacting prior to the A_0 mode interacting with the stiffener, the first interaction of the A_0 mode and the subsequent transmission and reflection of the A_0 mode. Due to dispersion, the higher frequency Lamb waves have higher wave velocities meaning that they interact with the stiffener earlier. Therefore, for each frequency, the three stages of Lamb wave interaction occur at different times, dependant on the wave velocity. 10 µs intervals between each time window plot are not presented for simplicity.

4.6.1. 100kHz RMS plots and discussion

The RMS plots for the healthy and disbonded panels with a 100 kHz excitation are presented in Figure 34. The time window of 10 µs–20 µs shows the wave packet starting to interact with the stiffeners. In this time window, the only mode present is the S_0 mode. The healthy panel shows clearly the presence of the stiffener as very little energy is transmitted through the stiffener. The panel with the disbonded region however shows an indication of a defect but it is not as clear or definitive as the later time windows. There is evidence of wave energy “bleeding” into the disbonded region which is initiating a low energy transmitted conical pattern. This is most likely a result of the S_0 mode interacting with the defect.

As the wave continues to interact with the stiffener it is apparent for both the healthy panel and the panel with the disbonded region that some of the energy is reflected back from the stiffener towards the source. This is shown in Figure 34 by the “tiger-stripe” interference fringes on the left of the stiffener. In the results from the panel with the disbonded region, this interference pattern is disrupted. This is clearly shown in the 50 µs–60 µs window by the circular shape of the reflection pattern to the left of the disbonded region. This reflected conical pattern to the left of the disbonded region has higher RMS values than both the neighbouring reflected signal and the reflected signal on the healthy panel. Conversely, as with the plots presented in Figure 26 Figure 27 there is an area of low energy to the right of the disbonded region. This area of low energy is shown by a transmitted conical region of low RMS values as the A_0 mode interacts with the stiffener. This transmitted conical fringe pattern suggests that at this excitation frequency a greater amount of the Lamb wave energy is reflected back towards the source than is transmitted through the disbonded region. The shape of the defect is also more prominent as the shorter wavelength A_0 mode interacts.

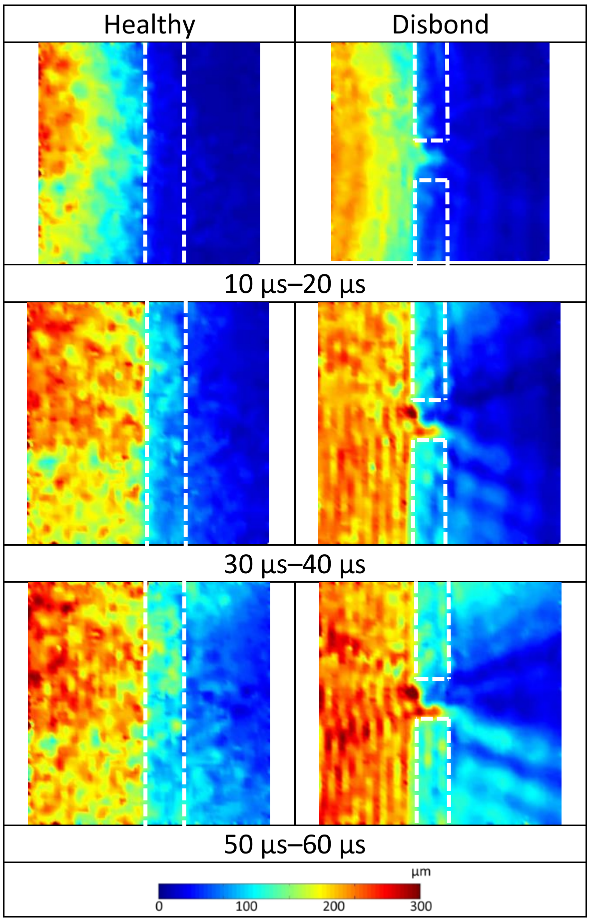

Figure 34.Windowed root mean-squared (RMS) plots of the three-component displacement magnitude for 100 kHz excitation.

4.6.2. 250kHz RMS plots and discussion

The RMS plots for the healthy and disbonded panels with a 250 kHz excitation are presented in Figure 35.

As with the 100 kHz excitation, as time continues the presence of the stiffener in the healthy panel reduces Lamb wave transmission. This demonstrates that significantly more wave energy is reflected back towards the source and attenuated by the stiffener than is transmitted through it. The 20 µs–30 µs window clearly shows the presence of the disbonded region as the short wavelength of the A_0 mode interacts however, the high RMS values observed in the disbonded region do not coincide with the supposed shape of the disbonded region. Instead only a small percentage of the 25.4 mm length of the disbonded region has a high RMS across the whole width of the stiffener. This is seen in the 40 µs–50 µs window to be the source of the transmitted conical fringe pattern. In this window a transmitted conical fringe pattern of higher Lamb wave energy is seen to be "leaking" through this part of the disbonded region. As a result of this there is a significant decrease in RMS values to the left of the disbonded region demonstrating that at this part of the stiffener more wave energy is being transmitted through the stiffener.

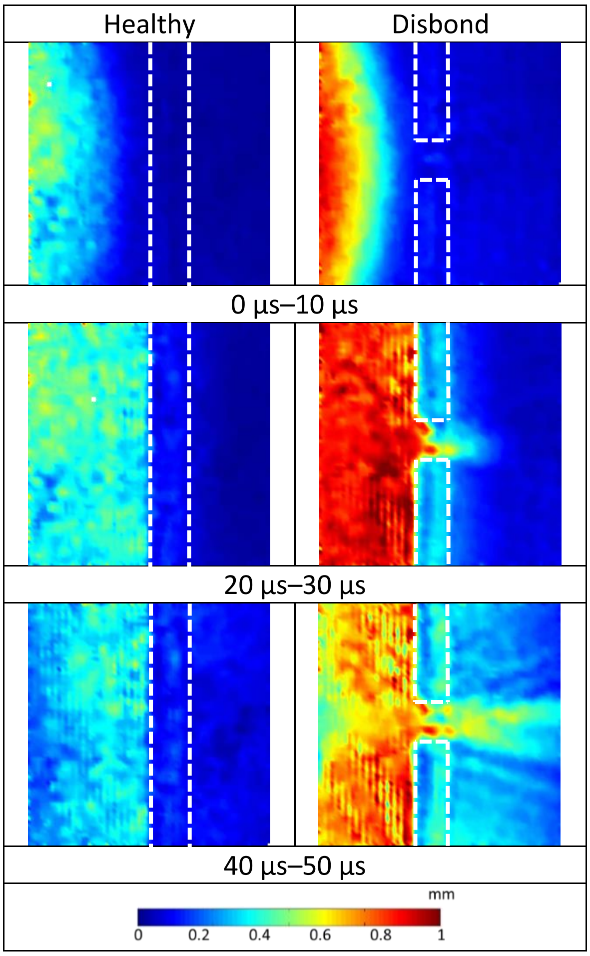

Figure 35.Windowed RMS plots of the three-component displacement magnitude for 250 kHz excitation.

The difference in amplitudes of the two datasets, as with the results presented in the time domain, can be attributed to a difference in sensor coupling. Despite of this, the results can still be compared qualitatively.

4.6.3. 300kHz RMS plots and discussion

The RMS plots for the healthy and disbonded panel with a 300 kHz excitation are presented in Figure 36. As with the 250 kHz excitation, a small amount of S_0 Lamb wave energy is seen to be interacting with the disbonded region in the 0 µs–10 µs window. This is shown by a small disruption in the low level RMS values in the disbonded region which are not present in the healthy plot. By adjusting the colour scales it may be possible to improve the clarity of this low energy interaction. However, this low level energy lies in the noise floor of the signal and thus the clarity of the rest of the image may be compromised.

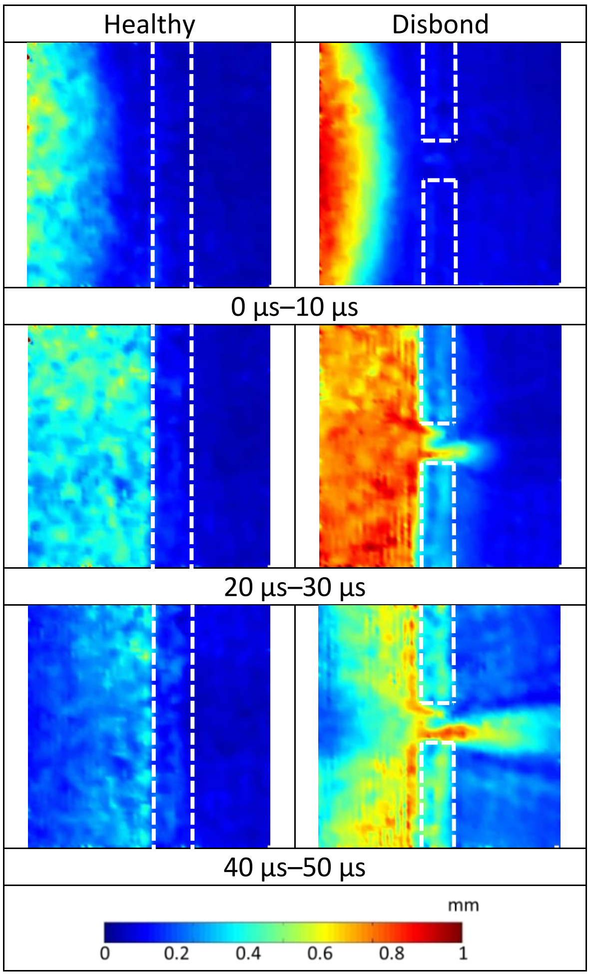

Figure 36. Windowed RMS of the three-component displacement magnitude plots for 300 kHz excitation.

As time progresses again, the influence of the stiffener on the Lamb wave transmission is apparent. In the 20 µs–30 µs time window, a clear division of energy is again observed as the A_0 mode interacts. The plot of the disbonded panel of the RMS values in this time window again shows the Lamb wave clearly interacting with the induced defect in the disbonded region. As with the 250 kHz excitation, the indication does not appear to be as expected as the values of high RMS are not formed in a square. There is again a line of high RMS values which appear to transmit across the entire width of the stiffener to the bottom of the disbonded region. There is also a smaller region of the high RMS values at the top of the disbonded region.

Studying the 40 µs–50 µs time window, the transmitted conical fringe pattern appears to initiate from the line of high RMS values. This is similar to what was observed with the 250 kHz excitation. A secondary fringe also appears to initiate from the top of the disbonded region. This is can be observed when studying the front of the conical fringes where there are two distinct cones of high RMS values.

As with the 250 kHz excitation, there is a reflected conical fringe of low RMS values to the left of the disbonded region. This indicates that again more Lamb wave energy is being transmitted through the stiffener at this point than is being reflected and attenuated.

4.6.4. Comparative discussion

There are distinct differences in the windowed-RMS results from the three excitation frequencies. The longer wavelength of the 100 kHz excitation interacts differently with the defect when compared with the shorter wavelengths of the 250 kHz and 300 kHz excitations. The primary difference is that the 100 kHz Lamb wave does not transmit through the disbonded region like the higher frequency excitations. This is demonstrated by the low RMS values to the right of the disbonded region and the higher values to the left indicating that the wave is reflected instead of being transmitted through the disbonded region.

All three sets of RMS plots indicate that the defect in the disbonded region is not a perfect square as was intended. Results at all three excitation frequencies suggest that there is a discrepancy in the defect allowing the Lamb wave to transmit better through the lower part of the disbonded region. This is seen in the RMS plots for the 100 kHz excitation however it is clearer on the higher frequency plots which also suggest that there are other inconsistencies present in the disbonded region.

There is a difference in the amplitudes between the 100 kHz vibrometry data and the higher frequencies shown by the differing values of the colour bars. This can be attributed to the higher frequencies attenuating more, thus the Lamb wave energy decreases significantly in the higher frequency plots.

4.7.Ultrasonic inspection of the disbonded region

As discussed, on reviewing the vibrometry results it was noted that the conical diffraction fringes were not as expected. From the displacement results, particularly the higher frequency excitation, the transmitted conical fringe appeared to originate from a smaller area at the bottom of the disbonded region. To investigate the condition of the induced disbonded region an ultrasonic C-scan was conducted.

4.7.1. Experimental setup

The panel with the induced disbonded was cut down to 465 mm × 626 mm to enable it to be positioned in the C-scan apparatus while ensuring that the cutting operation would not affect the disbonded region. A 10MHz scanning probe was used for the C-scan. A large enough area of the panel section scanned to ensure that the whole disbonded region was captured.

4.7.2. Results and discussion

The results from the C-scan are plotted in Figure 37. It is apparent that there is something present in the disbonded region which has had an effect on the interaction of the Lamb wave, shown in Figure 37 as a light grey area in the disbond region.

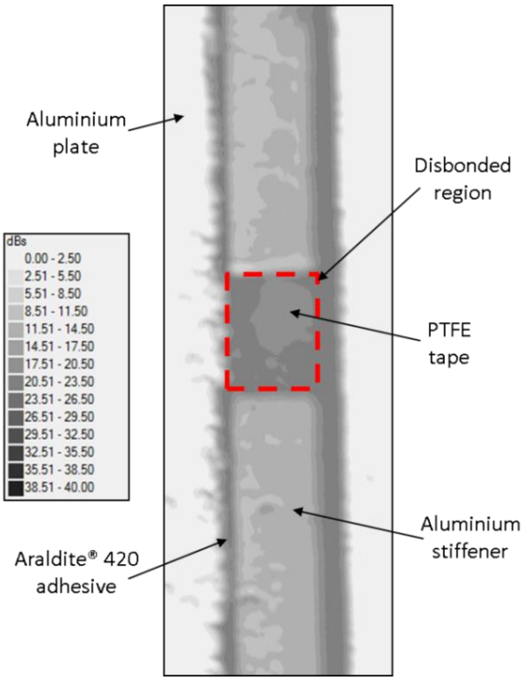

Figure 37. C-Scan results of the panel with the disbonded region. Note the region with the induced disbond containing what appear to be remnants of PTFE tape.

It was suspected that this defect occurred during the manufacturing process when the intentional disbond was being created. The disbonded region was induced by using PTFE tape.

When the adhesive was cured the PTFE tape was removed however it was possible that some tape was left inside the bond due to the difficulty of removing it. Therefore it is believed that the conical fringe patterns were caused by the Lamb wave interaction with this PTFE tape.

With that stated, it is highly unlikely that a disbond that occurs on an aircraft during its in-service life or its manufacture would be perfectly square and is more likely to be irregular in shape. Therefore, it is fair to state that the disbonded region that has been produced in this study is serendipitously more representative of what is likely to be found on a real aircraft structure.

The C-scan results also show that there is a small discontinuity in the adhesive film thickness of the healthy region of the stiffener. This is shown by a difference in the amplitude of the frequency response. This highlights the issue of the inconsistency of adhesive bonds.

4.7.3. Experimental swept sine wave excitation investigation

The RMS results presented in Figure 34, Figure 35 and Figure 36 demonstrated that the excitation frequency of a Lamb wave has a significant influence on its interaction with defects due to the difference in its wavelength. An additional experiment was undertaken using a swept sine wave excitation to further investigate the Lamb wave interaction.

4.7.4. Experimental setup

The NPL conical transducer was acoustically coupled in line with the disbonded region at a distance of 312.5 mm from the midpoint. The same excitation hardware was used for this investigation as previously. A swept sine wave ranging from 100 kHz to 500 kHz over a 200 µs duration was used for the excitation signal. This time window allowed the entire frequency sweep to be excited whilst reducing the effect of reflections.

The same vibrometry setup was used for this investigation although the area of investigation was changed to 250 mm × 90 mm with 5805 velocity measurement points. This not only improved the spatial resolution required for the higher frequency waves but also allowed the focus to be solely on the wave interaction with the disbonded region.

A sample of duration of 800 µs was used for this investigation as it allowed the whole transmitted wave to be captured at all measurement points while minimising the recording of edge reflections.

4.7.5. Results and discussion

The RMS value of each of the 5805 velocity measurement points was calculated and plotted as shown in Figure 38. Though measurements were taken for all three planes, the out-of-plane measurements most clearly show the interaction (most likely due to the source primarily exciting out-of-plane modes).

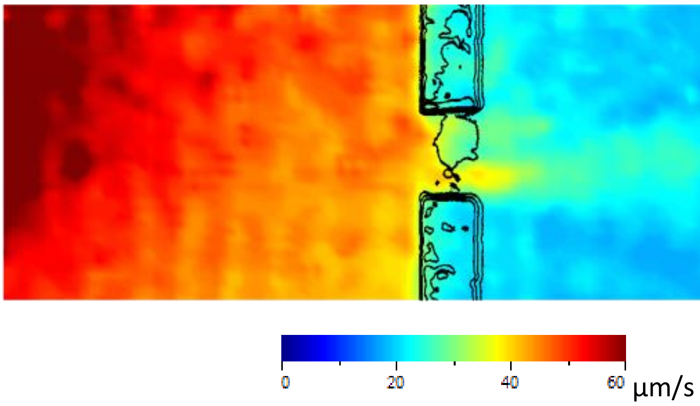

Figure 38. 100 kHz–500 kHz swept sine wave excitation out-of-plane RMS plot with an outline of the C-Scan over laid. Note the reduction in wave energy surrounding the PTFE tape region causing an amplitude reduction in the wave transmitted through the disbonded region.

It is apparent that the presence of the stiffener has a significant effect on the amplitude of the Lamb wave. On the left side of the stiffener, RMS amplitudes in excess of 60 µm/s were observed. As the Lamb wave is transmitted through the stiffener the RMS amplitude reduces to less than 15 µm/s; an approximate decrease of 75%.

As observed with the time domain results, a conical transmitted diffraction fringe is present to the right of the disbonded region. This is seen in Figure 38 as a region of higher amplitude (light blue).

As with the time domain results, particularly at 90 µs in Figure 33 the transmitted conical fringe pattern originates from the lower part of the disbonded region. This is particularly highlighted in Figure 38 where in the disbonded region the areas of highest amplitude (yellows) are observed in the lower part of the disbonded region.

When the results from the C-scan are superimposed onto this RMS plot it is evident that the region suspected of being remnants of PTFE tape has a significant influence on the propagation of the wave as the amplitude significantly reduces in this region.

As with the 300 kHz plots in Figure 36, areas of high RMS values are observed at the top and the bottom of the disbonded region. When comparing this to the results of the C-Scan it is evident that no or very little PTFE tape (or other obstruction) is present across the width of the stiffener in these areas.

4.8.Discussion

It is apparent that the induced Lamb waves in both the experimental and LISA studies all interacted with the disbonded region of the stiffener. There was a quantifiable difference in the Lamb wave interaction for panels containing a disbond when compared with the results for the healthy panel. This demonstrates that by using a statistical measure of the difference of the received Lamb wave such as the cross-correlation technique it would be possible to use an acousto-ultrasonic system to routinely inspect the condition of bonded stiffeners. By combining this technique with a statistical measure of the received energy, such as calculating the RMS value as demonstrated in this study, the location and characterisation of the damage could also be potentially assessed as well as its severity.

The results presented also demonstrate that the excitation frequency of an ultrasonic system is an important consideration for inspecting adhesively bonded stiffeners for disbonds. The 100 kHz excitation did not transmit through the disbonded region in the experimental study (though it was observed to do so in the LISA study) whereas the higher frequencies did. For damage detection systems, particularly those which are triggered on an amplitude threshold, this is particularly significant to fully ensure a high probability of detection.

A common observation that was made throughout all three frequency studies was the conical fringe pattern observed from the wave interaction with the disbond compared to the wave interaction with the healthy stiffener. By gaining a better understanding of this type of fringe pattern it a may be possible to design a sensor network that could not only detect the damage but also locate and quantify the size of the defect.

This study only considered a bond which had areas where the disbond spanned the whole width of the stiffener. In the case of real aircraft structure, this may not be the case. It would be beneficial to also be able to detect this type of disbond. The experimental results from the 100 kHz excitation suggest that this could be possible by considering the response of the reflected signal. Therefore an acousto-ultrasonic system capable of pulsing and receiving at different frequencies would be beneficial. Conversely, the LISA results suggest that where a disbond spans the width of a stiffener, the lack of a reflected signal in a ‘pitch-catch’ setup could be used to evaluate the condition of the adhesive bond.

All three excitation frequencies used in this study demonstrated that a low amount of the induced Lamb wave energy was transmitted through the healthy stiffener in both the experimental and LISA results. This is clearly a consideration for acousto-ultrasonic SHM systems but should also be considered important for passive SHM systems such as AE. AE induced Lamb wave propagation will be affected by the presence of adhesively bonded stiffeners on a structure. AE events occurring on one side of a stiffener may not be detected by sensors on the other side due to the decrease in Lamb wave amplitude. In addition to this, signals reflected from the stiffener may be interpreted incorrectly leading to added complications when locating and characterising damage using passive techniques. Therefore, the geometry of a structure is an important consideration for the design of a passive AE sensor network.

The results from the RMS plots demonstrate that laser vibrometry is not only a powerful tool in increasing understanding of Lamb wave interaction but can also be used to indicate the size and shape of a defect. The RMS plots serve as a useful aid in considering optimal sensor locations for an active sensor network by highlighting areas of high Lamb wave energy.

The transmission of the S_0 mode through the disbonded region in the experimental results seems mostly unaffected by the presence of the PTFE tape regardless of excitation frequency. The S_0 mode is mostly constructed of in-plane components which gives reason to suggest that in-plane modes maybe less influenced by the presence of kissing bonds. Further investigation using in-plane excitation would be beneficial in increasing our understanding of in-plane Lamb wave interaction with stiffeners.

LISA has been shown to be a useful tool for performing studies investigating wave interaction with defects for sensor network design. LISA's ability to run on the CUDA parallel computing architecture has the advantage over traditional FEA methods of being able to run multiple simulations in a relatively short space of time. This enables the exciting prospect of being able to model many different damage scenarios which could serve as an input to a sensor network optimisation tool.

The use of LISA also has cost and time advantages over experimental methods such as 3D vibrometry. Experimental methods require damage to be induced into structures in order for wave interaction studies to be performed. This typically requires the manufacture of many test specimens. However, it is important to validate models with experimental testing. It would be possible, with careful consideration given to experimental design, to perform a series of tests that would validate LISA's modelling of wave propagation and interaction with damage. It would then be possible to have a high confidence level in the validity of the model's results when simulating wave interaction with other damage scenarios.

The commercially available LISA software package does have drawbacks particularly regarding the modelling of composite materials at present. However, there have been studies conducted that have shown significant advances in adapting LISA to the modelling of composite materials [19] The ability to model composite materials will be of substantial benefit in the design of sensor networks for damage detection in advanced aerospace materials.

4.9.Conclusion

This chapter has demonstrated how 3D scanning laser vibrometry and LISA can be used to conduct a thorough investigation of Lamb wave interaction with adhesively bonded stiffeners and adhesive disbonds. Novelty can be found in the work from investigating Lamb wave interaction with stiffeners and disbonds visually where many previous studies use point measurements. In addition, both in-plane and out-of-plane components have considered in this investigation. The work presented has demonstrated that the way in which Lamb waves interact with disbonds is dependent on their excitation frequencies. It can be concluded that there is a good similarity of wave interaction between the 3D vibrometry and LISA model. This study has demonstrated that LISA is a very powerful tool in the simulation of wave interaction with stiffeners and disbonds and is representative of experimental observations.

It has been demonstrated that LISA is capable of modelling the wave interaction of both the S_0 and the A_0 modes which are the most common Lamb wave modes used in structural health monitoring of plate-like structures.

Analysis performed on the experimental results using a novel windowed RMS technique has revealed areas of high and low Lamb wave energy. This has revealed that, dependent on excitation frequency, conical fringes with high levels of Lamb wave energy can be found to be either reflected or transmitted through an adhesive disbond.

RMS plots are also beneficial in revealing optimal structural areas for locating sensors to ensure a high probability of damage detection using Lamb waves. These plots demonstrate the complexity of sensor network design and show that considerations such as amplitude threshold are important for use in active sensing systems.

The C-scan inspection revealed the suspected presence of PTFE tape within the disbonded region of the experimental investigation which had a significant influence on the interaction of the induced Lamb wave. By inducing a frequency swept Lamb wave and plotting the RMS of the velocity measurements taken using the 3D scanning vibrometer, it was possible to clearly observe the Lamb wave interaction. This revealed the shape of the PTFE tape which correlated well with the results from the C-scan. This novel aspect highlights the usefulness of non-contact full field Lamb wave measurement and visualisation for identifying flaws and defects within adhesive layers which mount stiffeners. This also provides an indication of regions on the structure for sensor placement which will maximise the probability of damage detection.

This study has only considered the wave interaction when the actuator is in line with disbond. In reality, this may not be the case. Therefore, it would be beneficial to investigate the effect of the actuator being at different angles and distances relative to the disbond. Other considerations could also be taken into account, including defect size, in order to work towards achieving an optimisation platform for sensor network design. By using the 3D scanning laser vibrometer as a validation tool, it is possible to validate computational models of a Lamb wave interaction. Therefore it would be of significant benefit to be able to model several damage scenarios which would then allow a platform for sensor location optimisation to be produced. The potential of modelling tools such as LISA to provide information for the design of damage detection sensor networks has been clearly demonstrated.

The work presented has shown that acousto-ultrasonically induced Lamb waves are a suitable method for the in-service monitoring of adhesively bonded structures for SHM applications. Careful consideration must be taken however when planning sensor location due to the complexity of the interaction with adhesive disbonds, in particular disbonds with irregular shapes.

5. Optimising an acousto-ultrasonic sensor network using genetic algorithms with 3D scanning laser vibrometry and local interaction simulation approach data

5.1. Introduction

The design of an AU sensor network is an important consideration for ensuring a high probability of damage detection. If damage occurs outside the path of the pulsing-receiving sensors then damage may go undetected and hence the structural integrity will be significantly compromised. Conversely, installing many sensors on the structure to ensure full coverage will result in additional weight penalties, power demands and computational requirements. Therefore an optimisation methodology is required to ensure a high probability of detecting damage whilst minimising the number of sensors on the structure.

In this chapter an experimental investigation into the effect of AU sensor location for the monitoring of an adhesively bonded stiffener with and without a disbond is presented. The results of an optimisation study based on the use of a genetic algorithm (GA) are then presented with consideration of both the out-of-plane and in-plane components of the Lamb waves. With a view to developing a network design technique to be used as part of the component design process, a computational study representative of the experimental investigation conducted using a local interaction simulation approach (LISA) is discussed. The results from this optimisation using the modelled data are then presented and explored, drawing comparisons between the experimental and computational investigations. Finally a series of recommendations are made on how the methodology presented could be used for the concurrent design of a structure and sensor network.

5.2. Experimental setup

An experimental investigation was conducted using 3D scanning laser vibrometry to investigate optimal acousto-ultrasonic sensor locations for detecting disbonds in an adhesively bonded stiffener using the stiffened same panels used in Section 4.2, one with a disbond and one without.

The excitation and vibrometer setup used in this study was the same as used previously (see Section 4.3). The entire area of investigation was coated with retroreflective glass beads to ensure high levels of backscattered light and hence improve the signal-to-noise ratio.

During testing each panel was laid on ‘bubble wrap’ packaging material to acoustically uncouple it from the floor. A series of markers were laid within the laboratory and on the panels to ensure that each panel was positioned in the same position relative to the laser heads. A low pass front end filter was applied to the measurements with the filter frequency set at 20kHz above the excitation frequency to filter out high frequency noise.

5.2.1. Geometry of the area of investigation

An area of investigation was designated on the face with the stiffener as shown in Figure 39. In the central square region of 625mm x 625mm 825 measurement points were located within as shown in Figure 40. Five excitation sites were used all located along the left hand boundary of the investigation area. Due to constraints on the availability of transducers, a single transducer was used. This required the transducer to be removed and re-coupled at each excitation location. For each excitation site and frequency, the transducer was excited and measurements were taken at each of the 825 measurement points. By having multiple excitation sites the effectiveness of the transducer-disbond path could be investigated; in effect simulating different disbond positions relative to a single transducer site. The distance from the left-hand boundary to the stiffener was selected to reduce the effects of edge reflections on the transmitted wave. This was also a sufficient distance from the measurement to ensure that that the Lamb waves had fully formed [37].

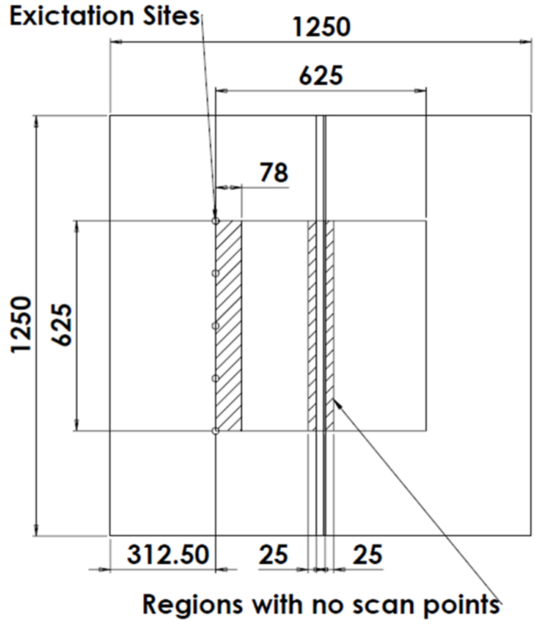

Figure 39. Dimensions of the Stiffened panel, excitations sites and scan area (all dimensions in mm)

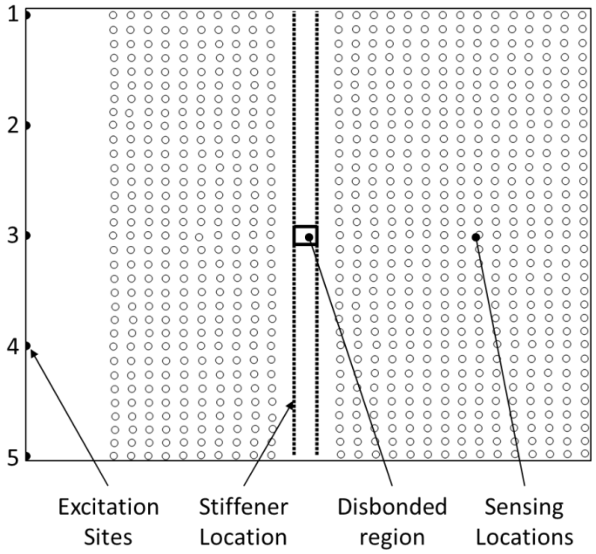

Figure 40. Layout of the area of investigation

No measurement points were positioned within a 25mm wide region on either side of the stiffener. This was due to the positioning of the laser heads which resulted in the stiffener casting a ‘shadow’ where it was impossible for all three lasers to align. There were also no measurement points positioned within a 78mm wide region to the right of the excitation sites as shown in Figure 39. This was in order to save acquisition time as preliminary tests had demonstrated insignificant findings in this region.

As with the previous study, a PANCOM Pico-Z transducer was acoustically coupled to the panel using Loctite® Ethyl-2-Cyanoacrylate adhesive. This transducer was selected because of its flat, broadband response in the frequency range under investigation and its relatively small face; making it more representative of a point source.

5.3.Signal processing

In order to determine the presence of damage, and hence develop a metric to establish the optimal sensor positions, the signals measured by the vibrometer were post-processed using a comparative technique details of which are discussed in the following sections.

5.3.1. Integration

The laser vibrometer measures the velocity of the wave whereas sensors bonded to the structure typically measure the displacement of the wave. In order to make this optimisation study more representative of the input received by a sensor bonded to the structure; velocity signals were integrated to obtain displacement signals. The displacement signals were then used for the optimisation study.

5.3.2. Cross correlation

The cross-correlation technique has been proven to be a successful statistical method for determining the differences between two waveforms quantitatively. Because of this, it is well suited to identifying the presence of damage in an AU system [106]. Typically a value of unity for the cross-correlation coefficient indicates that the received wave is identical to that of a baseline (i.e. when the structure is in an undamaged state) and hence there is no damage present. A value less than unity identifies that the waves are different and thus the presence of damage is detected.

By calculating the cross-correlation coefficient for the out-of-plane component of the Lamb wave for each measurement pair (with and without the induced disbonded region) it was possible to produce five data sets (one for each excitation site) with an assigned cross-correlation coefficient for each measurement point. A plot of the cross-correlation values of the 100kHz excitation for excitation site three is presented in Figure 41 to demonstrate areas of high and low cross-correlation coefficient. The out-of-plane component of the Lamb wave was initially considered as it is the principle component being excited by the bonded transducer. In addition, it is typical that bonded receiving sensors on a structure are primarily responsive to the out-of-plane component of the Lamb wave.

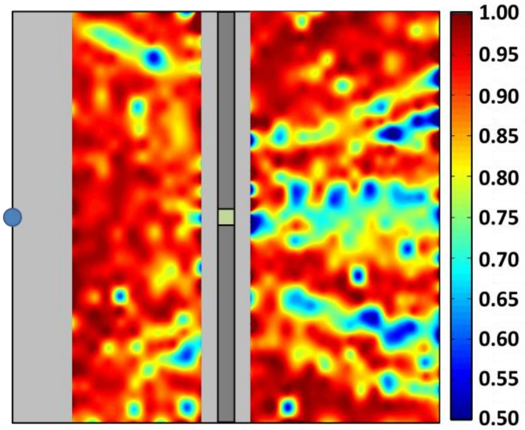

Figure 41. Cross-correlation coefficient plot for excitation site three (100kHz excitation). The location of the excitation is denoted by the blue circle

5.3.3. Three component cross correlation

Although the out-of-plane component of the wave was of primary interest, the 3D scanning laser vibrometer has the ability to measure the x, y and z components of the wave at each measurement point and therefore in-plane components could also be considered. In order to enable the optimiser to consider all three components, the vector sum of the cross-correlation of all three wave components was also calculated and divided by √3 to make the results comparable with the out of plane results.

5.3.4. Time window

The datasets (with and without the induced disbonded region) were originally correlated for the entire sample length of the measurements (1.6ms). This however produced low cross-correlation coefficient values at all of the measurement points due to reflections and refraction patterns caused by the disbond which had a significant influence on the edge reflections which were also measured within the entire sample length. To improve the correlation between the two data sets, a 200µs time window was used for the cross-correlation, reducing the edge reflection effects. To determine the start of the 200µs time window a threshold crossing method was used. The threshold value was set at 40% of the maximum amplitude value in the first 700µs of the entire sample length for each respective measurement point of the healthy data set. This ensured that the first wave received triggered the acquisition while also ensuring that the presence of noise did not exceed the threshold. A pre-trigger value was determined by a series of trial-and-error in order to ensure that the start of the wave was captured. Through this process a value of 14% was found to be suitable and was applied to the point at which the wave crossed the threshold to determine the start of the 200µs window as demonstrated in Figure 42.

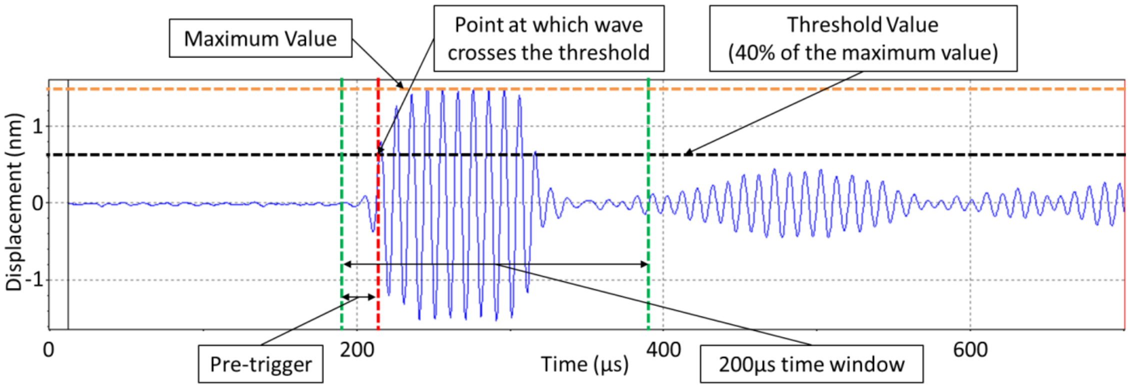

Figure 42. Example waveform to demonstrate how the time window was determined.

5.4.Optimisation

From cross-correlation dataset for each excitation site it was now possible to form a methodology for the optimisation of the sensor locations.

One of the biggest issues with any optimisation problem, is defining the fitness (also known as a cost function, or objective function) to interrogate. It is fundamentally important to consider the design of the objective function to be optimised. In this case the fitness function needed to indicate the ability of a sensor placed at a particular location to detect damage from a range of sources.

5.4.1. Fitness function

Each sensing location had five cross-correlation coefficient values (one for each excitation site). A fitness function needed to be devised that produced the best solution regardless of excitation site. If this was not considered a low cross-correlation for one excitation site may skew the fitness despite the other four cross-correlation values being high. This is demonstrated in Figure 43 where a sensor with a high deviation and cross-correlation for across the excitation sites is regarded as poor (red). Statistical measures such as averaging were considered but could result in skewing the fitness of the sensor network. Therefore the measure of spread needed to be assessed as well as the effectiveness.

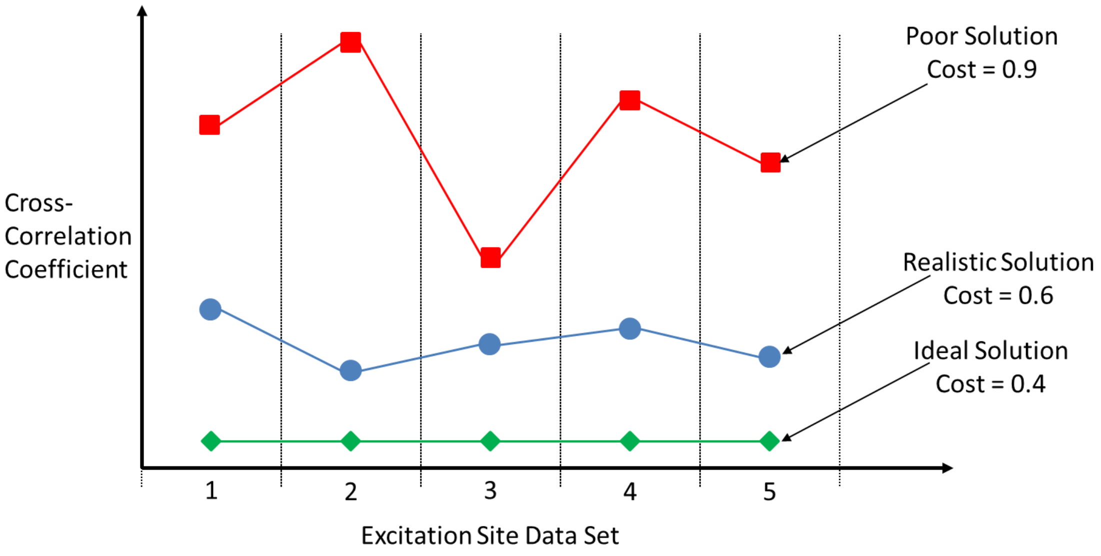

Figure 43. Demonstration of different sensor network solutions

This was achieved by assessing the spread of the five values calculating the standard deviation which was used to measure the spread of cross-correlation coefficient between the excitation sites and assessing the overall effectiveness by calculating the square-root of the mean of the squares which assessed the values of the cross-correlation coefficients. As the values for both the standard deviation and the square-root of the mean of the squares were of similar magnitude, they had similar weighting for calculating the fitness. In the case of a one sensor network it was therefore possible to calculate the fitness of that sensor by using the fitness function shown in Equation (28).

$$Fitness = 1 - \left(\sigma + \sqrt{\frac{1}{5} \sum_{i=1}^{5} x_i^2} \right) \tag{28}$$

Where σ is the standard deviation and x is the cross-correlation coefficient.

In order to allow for sensor networks with multiple sensors a 'pseudo-sensor' was created. This was achieved by selecting the lowest cross -correlation values from the sensors in a proposed network for each excitation site and then combining them to create a 'pseudo-sensor'. This pseudo-sensor was then used to calculate the fitness for that particular sensor network. This is demonstrated in the case of a two sensor network in Table 1.

Table 1. Cross-Correlation coefficient for a two sensor network

	Excitation Sites				
	1	2	3	4	5
Sensor A	0.8087	0.6007	0.7355	0.6502	0.8791
Sensor B	0.6412	0.9576	0.6435	0.8222	0.5681
Pseudo Sensor	0.6412	0.6007	0.6435	0.6502	0.5681

To avoid redundant sensors (i.e. sensors that do not contribute any cross-correlation values to the pseudo sensor due to them being higher than those for the other sensors for all excitation sites), a check was put in place to ensure that all sensors in the network were used. If the solution was found to have redundant sensors, an artificially low fitness was assigned to that sensor network to ensure it would not be identified by the optimisation algorithm.

5.4.2. Optimisation problem

The number of possible sensor network combinations increases with the number of sensors by a multiple of the respective binomial coefficient. In this study, the number of possible sensor locations was 825, arranged in a regular square grid within the areas of investigation shown in Figure 40. Layout of the area of investigation

The massive computational expense of evaluating the effectiveness of every possible solution as the number of sensors in the network increases ruled out simple techniques such as an exhaustive search leading to the selection of an evolutionary algorithm based technique which is well suited to this type of problem. A list of the maximum number of sensor combinations is shown in Table 2 for networks of up to 5 sensors. This demonstrates the reason for choosing a GA, which does not exhaustively sample the search space.

Table 2. The number of sensor network combinations for a given number of sensors in the network

Number of Sensors in network, N_s	Number of possible sensor network combinations
1	825
2	339900
3	93245900
4	1.92×10^{10}
5	3.15×10^{12}

5.4.3. Genetic algorithm configuration

For this study, the genetic algorithm used binary encoding. This involved each candidate sensor location being assigned a numerical value (i.e. locations 1-825) which was described by a binary string (a 'gene'). The number of sensors in the network defined how many genes made up the full binary string ('chromosome'). Each chromosome described one candidate sensor network within the population of solutions. These chromosomes were used by the algorithm for mating and mutation.

As the total number of measurement points was 825, a 10 digit binary string was required for each gene. As 825 is not the maximum 10 digit binary number it was possible for the GA to create a solution outside of this constraint. To resolve this, artificially high cross-correlation penalties were assigned to binary values representing locations greater than 825 hence giving solutions containing these genes poor fitness thereby ensuring that they were discarded by the GA. However, it is worth noting that this could be deemed inefficient as the size of the search space is larger than required. The initial population used was 40 times the number of sensors in the network, N_s. This ensured that a suitable amount of the population was considered whilst not having a detrimental effect on the optimiser's performance, and was based on prior experience. The size of the initial population was increased as the size of the search space increased in order to ensure sufficient sampling of the search space.

The selection method used for mating the chromosomes was a simple pairing technique where the best two solutions in the population were selected for mating, and then the next best two until the whole mating pool had been paired up. A randomly assigned cross-over point at chromosome level was used for each mating pair. This gave the algorithm a good ability to carry forward the best attributes of the solution without continuously producing poor solutions which can be a drawback of fixed point cross-over schemes.

An allele mutation was adopted for this GA as it allowed the algorithm to explore the search space preventing it from converging on a local maxima. A uniform probability of mutation of 0.1 was used for this problem as it had been found to yield good results in a previous, preliminary study in exploring the search space while allowing the algorithm to converge on a result [214]. The fittest 10% of solutions were made immune from allele mutation which prevented good solutions being mutated into poorer solutions, and hence being discarded.

As with all genetic algorithms, convergence can prove to be an issue as it is not always clear that the optimal solution has been reached. This is a drawback of GAs as every possible solution is not exhaustively considered. In this study, a solution was deemed to be optimal when the maximum fitness had not been improved upon for 2000 generations. This approach has previously been found to be successful by Clarke and Miles [148].

To ensure consistency in the results of the GA, each GA was run five times. In most cases, identical solutions were converged upon. However, for the larger search spaces, a few different solutions were found. These solutions had marginally worse fitness than the fittest solutions. In these cases, typically all sensors from the fittest solution were used bar one which was either found to be in a location next to the fittest solution or in a location that was a mirror image around the central horizontal axis. Convergence of the GA on the optimal solution was also confirmed on the low search space problems using an exhaustive search.

5.5.Optimisation results from experimental data

5.5.1. Out-of-plane Lamb wave component

The optimal calculated fitness for the out-of-plane component of the wave as the sensor network size increases for each excitation frequency is presented in Figure 44.

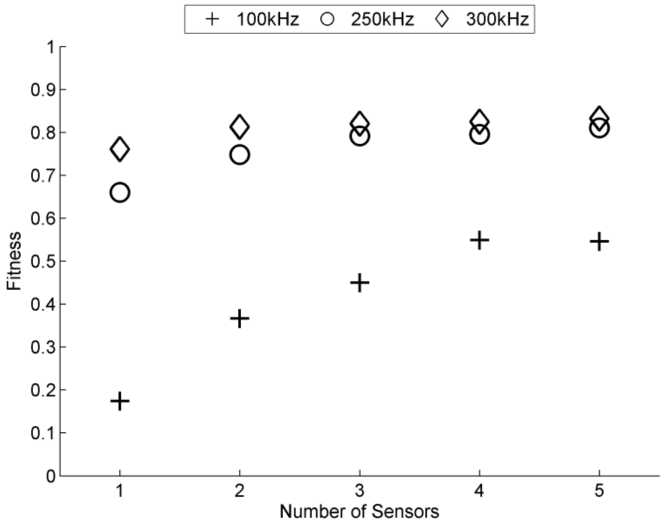

Figure 44. Calculated fitness for each number of sensors in a sensor network at the three excitation frequencies for the out-of-plane component of the Lamb wave

It is apparent that as the excitation frequency increases, there is a significant increase in fitness. This demonstrates the greater sensitivity of the higher frequency to the damage due to the shorter wavelengths involved. It is evident from the wavelengths calculated for the previous study (section 4.3) that as the frequency increases the wavelengths of both modes reduce. At 300kHz, the wavelength of the S_0 mode is of a similar size to that of the A_0 mode of the 100kHz excitation. Therefore at the higher frequencies, the interaction with the disbond has a more significant effect for both modes. This is supported by the findings reported by NASA[215] and is the visual representations of the previous study (section 4.5). However as the excitation frequency increases, the signal is more susceptible to noise due to the material's microstructure scattering the wave [215]. The presence of random noise would reduce the cross-correlation coefficient though not to the extent of the results presented here. It is worth noting that the attenuation of the wave increases with excitation frequency resulting in a greater reduction of amplitude as the wave propagates. Thus, signals that are measured further from the source can be said to have a lower signal-to-noise ratio. This is an important consideration for the design of sensor networks.

The results from this experimental study also demonstrate that fitness increases as the number of sensors in the sensor network increases, indicating that an increased number of sensors produces a network with a better ability to detect damage as would be expected.

The fitness of the 100kHz excitation sensor network increases by over 100% as the size of the sensor network increases from one sensor to two. There is a constant increase in fitness as the number of sensors in the network increases from two sensors to four where the maximum fitness is achieved. With the addition of a fifth sensor there is a small reduction in fitness. This is due to the optimiser being forced to use five independent sensors which does not achieve any significant improvement on the four sensor network.

The results from the 250kHz excitation demonstrate a large increase in fitness over that of the 100kHz excitation. The 250kHz excitation one-sensor sensor network shows an increase in fitness to more than double that of the 100kHz excitation one-sensor sensor network. As the size of the sensor network grows from one sensor to three a significant increase in fitness is observed. Increasing the size of the sensor network beyond three sensors however shows an insignificant improvement in fitness.

The 300kHz excitation demonstrates the best fitness of all three excitation frequencies. There is a minor increase in fitness between the single-sensor network and the two-sensor network however as more sensors are added to the network there are significant performance gains in terms of fitness.

5.5.2. Sensor location results

The locations for each optimal sensor network are presented in Figure 45. The locations of each excitation location, (denoted by the black dots on the left-hand side) the stiffener (denoted by the dashed line) and disbonded region (denoted by the thick black square) are included for completeness.

The optimal location for the sensor in the one-sensor network is to the right of the stiffener either above or below the disbond for each excitation frequency. From the results of the previous study (Section 4.5), it can be seen that the Lamb wave interaction with the disbonded region produces a diffraction pattern which results in low cross-correlation coefficients above and below the disbonded region as demonstrated in Figure 41.

The optimal locations for the two-sensor network are in line with the disbonded region. One of the sensors for the 100kHz excitation is positioned in the lower right-hand corner of the area of investigation. It is possible that again this is a function of the resultant diffraction pattern. This is also observed to a lesser extent with the location of one of the sensors for the 250kHz excitation. Interestingly, one of the sensors for the 300kHz excitation is positioned to the left-hand side of the disbond at the edge of the stiffener. This is most likely to be due to the differences in reflected signal from the disbonded region.

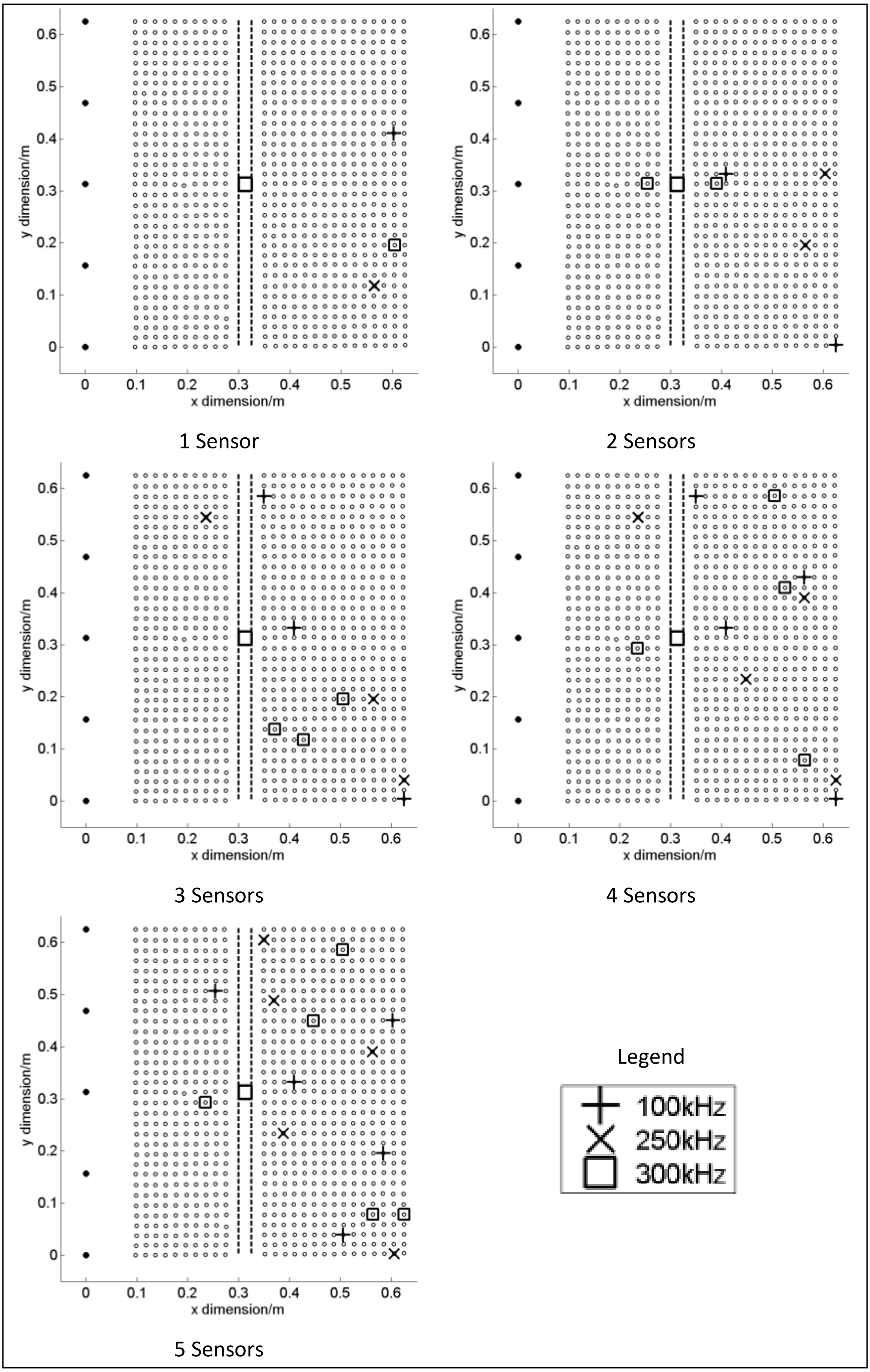

1 Sensor

2 Sensors

3 Sensors

4 Sensors

5 Sensors

Figure 45. Optimised sensor locations based on the out-of-plane component for all three excitation frequencies

There is a much wider spread in the distribution of sensors with the optimal locations for the three-sensor sensor networks. The 100kHz excitation results show a distribution of the three sensors along the length of the stiffener. This is logical as it would account for the different angles of the excitation site to the disbonded region.

Similarly, the sensor locations for the 250kHz excitation see a distribution of sensors along the length of the stiffener. However, two of the sensors are located to the lower right-hand side of the stiffener with the third located to the upper left-hand side. This is likely to have been the result of the presence of a reflection fringe caused by the presence of the disbond (demonstrated in the cross-correlation coefficient plot in Figure 41). This demonstrates that damage detection can be achieved on the same side of the stiffener as the Lamb wave excitation.

The locations for the 300kHz excitation prove to be more unconventional, clustered together in the lower right-hand quadrant of candidate sensing locations. This is most likely to be the result of reduced cross-correlation coefficients caused by the diffraction fringes as the Lamb waves interacted with the disbonded region.

The sensor location results for the four-sensor sensor network gives a distribution of sensors that again span the length of the stiffener. The 100kHz excitation locates two sensors in the upper right-hand quadrant, one in the centre and one in the lower far right-hand corner (this location appears to be a strong sensing location for this frequency). Though only demonstrated by one excitation site in Figure 41, it is evident that these sensor locations are areas of low cross-correlation coefficient due to the presence of the disbond. The 250kHz shows a similar distribution with two sensors above and below the disbonded region on the right hand side. As with the 100kHz excitation, one sensor is located in the lower right hand corner of the candidate sensor locations and one sensor is found located above the disbonded region to the left of the stiffener.

The 300kHz excitation results have a near uniform distribution of sensors in terms of their vertical positioning. As with the other two excitation frequencies, a sensor is located in the lower right-hand corner of the area of investigation. It is evident that this particular region of sensor locations is strong for detecting damage in this scenario. Two sensors are located on the right hand side of the stiffener above the disbonded region. However the fourth sensor in the network is located on the left of the disbonded region; once again demonstrating the detection capability of sensing locations on the excitation side of the stiffener.

The five-sensor network results mostly in distributing the sensors on the right hand side of the stiffener. The 100kHz excitation distributes three sensors in a triangular array mimicking the diffraction pattern presented in the previous study (section 4.5). An additional sensor is located below this with the fifth sensor located on the left-hand side of the stiffener. This location is in the same region as the sensor location for the three and four-sensor sensor networks for the 250kHz excitation. This again indicates that this is a strong region for sensing.

The 250kHz excitation positions three sensors in a triangular array however, unlike the results for 100kHz, the triangle is rotated so that two of the sensors are closest to the stiffener with the third is to the right. The other two sensors are located along the diagonal with one above the disbond region close to the stiffener and one located in the lower right corner; albeit in a different location than used in previous sensor networks.

The location results for 300kHz positions two sensors on the right hand side of the stiffener in the lower corner. This once again demonstrates the heightened sensitivity in this area. This area may be of heightened sensitivity due to the imperfect nature of the disbond discussed in Section 4.7. Two sensors are located above the disbonded region on the right hand side of the stiffener with the fifth sensor being located centrally on the left-hand side of the stiffener.

It is worth stating that a high level of confidence was obtained from the results of the GA by running it multiple times. Each time that the GA was run, the algorithm consistently converged on the same results. In addition, the results for the single-sensor network were also double checked using an exhaustive search which was suitable due to the small sample size.

5.5.3. Three component magnitude of the Lamb wave

When the three components of the wave were considered, the optimal fitness values calculated from the three component magnitudes were divided by $\sqrt{3}$ to normalise them and make them comparable to the out-of-plane results.

The optimal calculated fitness values for the three component magnitude as the sensor network size increases for each excitation frequency are presented in Figure 46.

As with the results where only the out-of-plane component of the wave was considered, an increase in excitation frequency significantly improves the fitness for each sensor network size. As previously stated, this is most likely to be a function of the smaller wavelength of the higher frequency excitation being more sensitive to the damage.

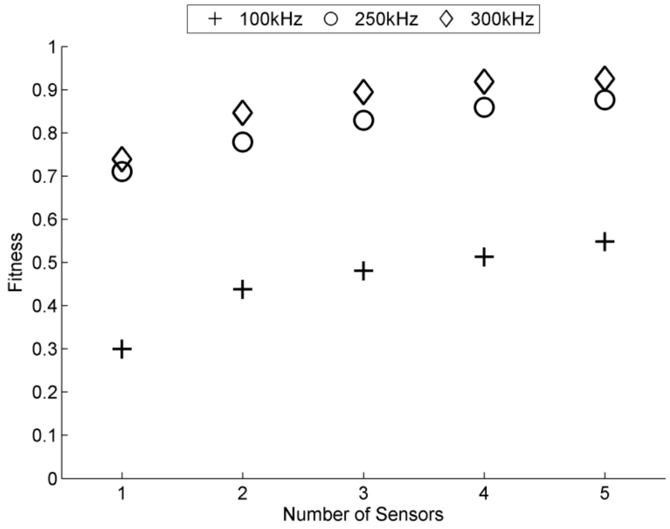

Figure 46. Calculated fitness for each number of sensors in a sensor network at the three excitation frequencies for the three component magnitudes of the Lamb waves

When considering the results at 100kHz as before there is an evident trend that as more sensors are added to the sensor network, the fitness improves as would be expected. As the size of the sensor network is increased from one sensor to two sensors there is an increase in fitness of around 64%. As the size of the sensor network increases from two to five sensors there is a constant, linear increase in fitness. However, the increase in fitness between two and five sensors is less than that between one and two indicating a good performance from the two sensor network. It is likely that if the size of the sensor network was further increased, at some size there would be no significant increase in fitness as additional sensors deliver ever diminishing improvements in performance.

With the 250kHz excitation there is a 9% increase in fitness as the size of the sensor network is increased from one sensor to two sensors. The fitness of the single sensor solution is further improved upon with a fitness increase of 16% as the network size increases to three sensors. The rate of the increase in fitness is reduced as the sensor network grows larger than three sensors. The highest fitness is achieved by a network size of five sensors with an increase in fitness of 23% over the one sensor network.

The fitness increase observed for the 300kHz excitation shows that the rate of increase reduces as the sensor network grows. Increasing the size of the sensor network from one sensor to two sensors sees an increase in fitness of 15%. This increase in fitness is improved by the three sensor network which gives an increase of 21% over the one sensor network. The maximum fitness is achieved by the five sensor network with an increase in fitness of 25% over that of the one sensor network. However it is worth noting that the performance gains to be achieved by a sensor network of this size over say a three sensor network are not significant.

5.5.4. Sensor location results

The locations for each optimal sensor network for the three component magnitude are presented in Figure 47. The locations of each excitation location, (denoted by the black dots on the left-hand side), the stiffener (denoted by the dashed line), and disbonded region (denoted by the thick black square) are included for completeness.

The optimal placement for the one-sensor network places all sensors regardless of excitation frequency below the disbond on the right-hand side of the stiffener. This corresponds well with the diffraction pattern observed in the previous study (Section 4.5) and the cross correlation pattern seen in Figure 41. This location was also shown to be a particularly strong sensing location in the out-of-plane optimisation results for the one-sensor network shown in Figure 45.

When a second sensor is considered in the network, the placement of the sensors changes depending on excitation frequency. The placement for the 100kHz excitation puts sensors above and below the disbond region. Again, it is possible to explain this with the diffraction interaction previously observed. These placements differ somewhat to those observed for the out-of-plane results though a similarity could be drawn in the sense that both sensor placements were placed along a line of low cross-correlation coefficient leading out from the disbonded region.

The 250kHz excitation for the two-sensor network, places one sensor in-line with the disbonded region to the left of the stiffener and one sensor below the disbonded region on the right of the stiffener. The placement of the sensor on the right of the stiffener agrees well with the placement of sensors for the one-sensor network and also is in agreement with the out-of-plane placement. This indicates that this region is a particularly strong region for sensor placement. The placement of the sensor to the left of the stiffener however was not consistent with placement of the sensor when only the out-of-plane component was considered with a 250kHz excitation although it was consistent with the 300kHz excitation. This highlights a difference in the reflected waveform and hence a reduction of the cross-correlation coefficient. This may also be due to the fact that when the three components of the wave are considered the S_0 mode will have had a more significant influence on the cross-correlation coefficient.

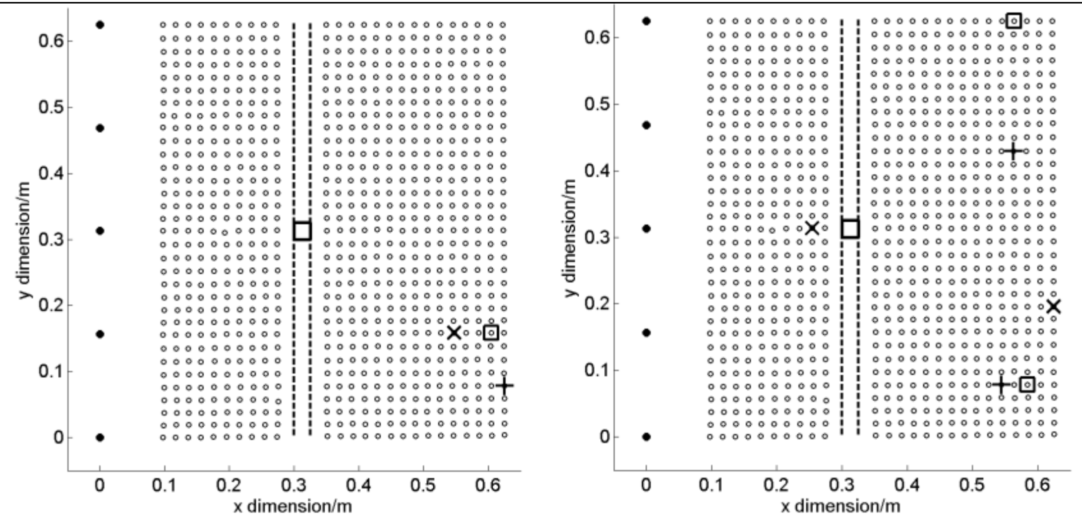

1 Sensor

2 Sensors

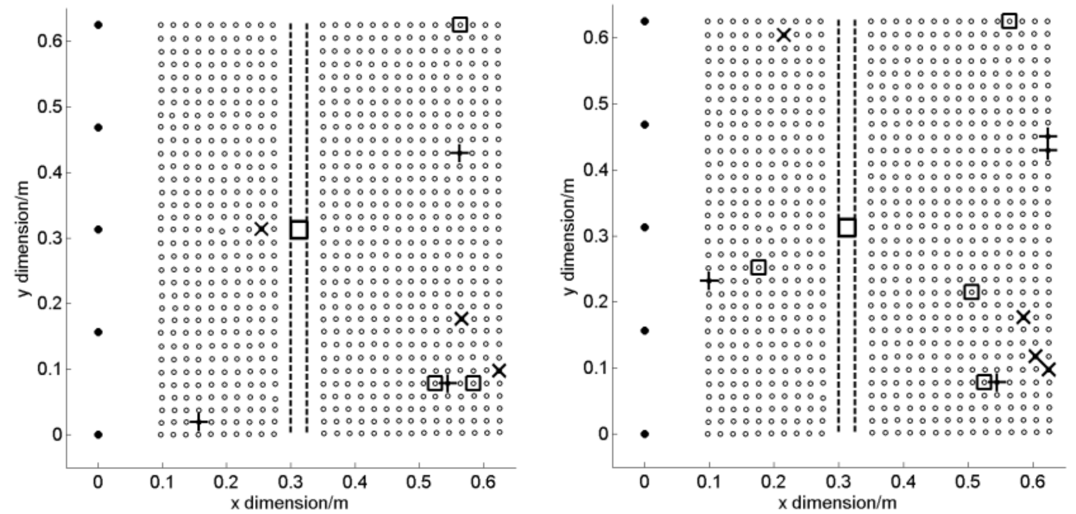

3 Sensors

4 Sensors

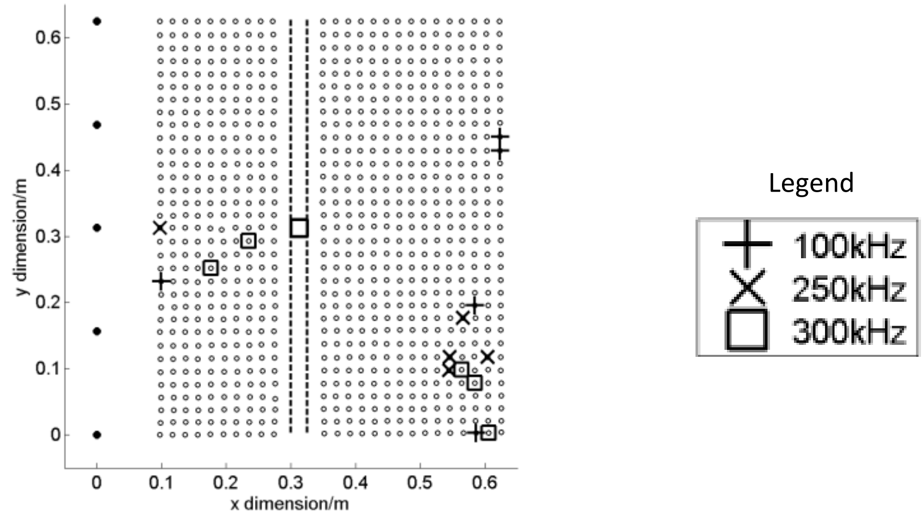

5 Sensors

Figure 47. Optimised sensor locations based on the three component magnitude for all three excitation frequencies

The placement of the two-sensor network for the 300kHz excitation puts both sensors at the top and bottom of the panel on the right of the stiffener. This is inconsistent with what was observed when only the out-of-plane component was considered which suggests that the in-plane components of the wave experience a high degree of scattering when interacting with the disbonded region.

The placement of sensors for the three-sensor network for the 100kHz excitation repeats the locations from the two-sensor network whilst adding an additional location on the left of the stiffener below the disbonded region to improve sensitivity to damage. This sensor location is consistent with the reflected diffraction patterns previously observed. However, the placement of these sensors is different to the placement of the sensors when only the out-of-plane components are considered. This is most likely due to the influence of the in-plane components of the wave.

With the 250kHz excitation, two sensors are placed to the right of the sensor below the disbond region further demonstrating the high-level of sensitivity to the damage in this region. The third sensor is retained from the two-sensor network and placed in-line with the disbond to the left of the stiffener. Similarly to the 100kHz excitation, the three sensor network for the 300kHz excitation retains the two sensors from the two sensor network whilst adding an additional sensor to the right of the stiffener, below the disbonded region further reinforcing the high level of sensitivity to the damage in this region.

With the placement of sensors for a four-sensor network the 100kHz excitation retains one sensor to the right of the stiffener, below the disbonded region in a location retained from the two-sensor and three-sensor networks. Two sensors are placed above the disbonded region to the right of the stiffener which again infers the placement of a sensor along a transmitted diffraction pattern. The fourth sensor in the network is placed to the left of the stiffener, below the disbonded region. This demonstrates that the reflection of the Lamb waves (or indeed, the lack of reflection) has a significant influence on the cross-correlation coefficient. Some similarity can be seen with placement of the sensors when only the out-of-plane component is considered as sensors are placed both above and below the disbonded region to the right of the stiffener. However, no sensors are placed to the left of the stiffener for the 100kHz excitation.

Considering the 250kHz excitation, three of the four sensors in the four-sensor network are placed together to the right of the stiffener below the disbonded region. The fourth sensor is placed on the left of the stiffener above the disbonded region. The placement of this sensor is consistent with the placement when only the out-of-plane component is considered. However, the other three sensors are more logically distributed along the length of the stiffener on the right-hand side.

The placement of the four-sensor network for the 300kHz excitation could be regarded as more logical. Two of the three sensors are retained from the three sensor network at the top and bottom of the panel to the right of the stiffener. A third sensor is placed just below the disbonded region to the right of the stiffener with the fourth being placed in a similar location to the left of the stiffener. This is very consistent with placement of sensors when only the out-of-plane component is considered albeit a mirror image (if a line of symmetry was placed horizontally across the centre of the disbonded region).

The placement of the sensors for the 100kHz excitation for the five-sensor network positions four of the sensors along the right hand boundary with two of the sensors placed close together just above the disbonded region. The fifth sensor is placed on the left hand boundary below the disbonded region. This gives similar positioning for three of the five sensors to that found when only the out-of-plane component is considered.

When a 250kHz excitation, four of the five sensors in the network are positioned to the right of the stiffener below the disbonded region with the fifth sensor being placed on the left hand boundary in line with the disbonded region. The 300kHz excitation places three of the five sensors in similar locations to the 250kHz excitations to the right of the stiffener. The other two sensors are also placed on the left of the stiffener in similar locations to those determined using the 100kHz and 250kHz excitations. The placement of these sensors is much more grouped when compared to the results where only the out-of-plane components are considered.

A common observation when comparing the out-of-plane results with the three component magnitude results, more sensors are placed on the left of the stiffener. This indicates that the interaction of the S_0 mode which has a large in-plane component reflected by the disbond causes a significant reduction in cross-correlation coefficient of the in-plane components in this area.

The results also indicate an area of high sensitivity to the damage in the lower, right hand quadrant of the area of investigation. Arguably, this area of sensitivity was identified in the out-of-plane results however, the consideration of the in-plane results demonstrate that the in-plane components of the Lamb waves are also significantly influenced (more so than can be observed in section 4.5) by the presence of the disbonded region. As a result, this region experiences a significant reduction in cross-correlation coefficient.

5.6.Discussion

From both the out-of-plane and three-component magnitude results presented, it is evident that increasing the excitation frequency significantly improves the performance of the sensor network. The best performance is achieved by the 300kHz excitation. Due to experimental constraints excitation frequencies above 300kHz were not considered and therefore it is not possible to state whether increasing the excitation frequency further would improve the performance. It is evident that there are significant performance gains in using a 250kHz excitation frequency rather than 100kHz however the increase in performance from 250kHz to 300kHz is less significant (but then so is the jump in frequency and hence the change in A_0 and S_0 mode wavelengths).

Although the higher excitation frequencies show performance gains, the attenuation performance of the chosen Lamb wave frequency is an important consideration. As the excitation frequency increases, the attenuation of the wave also increases. In this study a relatively small area of investigation was considered which ensured that attenuation effects did not significantly influence the results. Expanding the area of investigation may prove to favour the lower excitation frequencies due to the larger area over which the waves can propagate, however lower frequencies may be more susceptible to noise from other sources and less effective at detecting smaller defects.

In the case of a damage detection system installed on an aircraft, excitation frequency is an important consideration in terms of computational overheads. Increasing the excitation frequency requires a higher sampling rate from the system and hence increases data transfer and processing overheads. Though these considerations fall outside the scope of this study, they are important when implementing a damage detection system; particularly for a self-powered system.

Another consideration for the selection of excitation frequency is the size of the defect that is required to be detected by the system. Though any defect on an aircraft can be a cause for concern, it may be acceptable for less critical areas of the structure to have a small level of damage present during in-service operation – known as a damage tolerant structure. This may reduce the requirements of the installed SHM system thus adding an extra objective to the optimiser. However, designing aircraft structures with a level of damage tolerance typically requires additional material, adding mass to the structure. Therefore, when designing an SHM system and an aircraft structure concurrently, considerations have to be made for optimising acceptable damage tolerance and the minimum detectable defect size.

Comparing the two results sets it is apparent that consideration of the in-plane components of the wave improves the performance of the sensor network. The 100kHz excitation saw a maximum fitness increase when the in-plane components of the wave were considered of 72% on the one sensor network over that of the out-of-plane component alone. Lower fitness increases were observed with the higher frequency excitations. Fitness increases of 8% and 11% for the 250kHz and 300kHz excitations respectively were seen for the five-sensor networks.

Although there are significant performance gains to be achieved by considering the in-plane wave components it is actually difficult to achieve this from a single sensor in practice, as sensors usually primarily detect either in or out of plane motion, but rarely both (although, it is theoretically impossible for a Lamb mode to be solely in or out-of-plane due to Poisson's ratio effects). However the results presented do demonstrate that network performance could be improved by sensing the in-plane and out-of-plane components at the same locations. This may be an important consideration to take into account for the design of a sensor network where it may be advantageous to reduce the number of sensors whilst maintaining the same level of damage detection capability for reasons such as reducing the mass from cabling. In addition, this study has only considered the damage scenario of a disbond. In service aircraft are prone to a range of damage events such as fatigue, impacts and corrosion. Therefore it may also be beneficial to consider the type of damage likely to be present in the monitored area of the aircraft and to select an appropriate sensing methodology to detect that damage. For example; it may be possible that in-plane components of Lamb waves are more sensitive to particular damage scenarios than out-of-plane components of the wave.

Studying both sets of results it is clear that there are sensor network sizes beyond which increasing the number of sensors does not lead to significant increases in fitness. In the case of the out-of-plane component this is four, three and two sensors for 100kHz, 250kHz and 300kHz excitations respectively. Although a one sensor network did detect the presence of the disbond, improved sensitivity was observed by adding additional sensors. It could therefore be recommended that a three sensor network may prove to yield sufficient detection capability regardless of excitation frequency, for this particular example.

When using all three components of the magnitude, adding more sensors to the network for the 100kHz excitation continuously increases the fitness (although the biggest increase is observed when the network size increased from a one sensor network to a two sensor network). Whilst this is also true for the 250kHz and 300kHz excitations, minimal fitness increases were observed with sensor networks larger than three.

For this study the size of the time-window sample used in calculating the cross-correlation coefficient was kept constant in order to reduce the effects of reflections whilst still having a suitably long time window to calculate a useful cross-correlation coefficient. However, it may be beneficial to tailor the size of the time window to the frequency in order to further reduce any effects of reflections. For this however, locations of features on the structure would need also to be considered which could be achieved using some form of mapping technique.

The start of the time window was determined by using a simple thresholding technique. Other techniques such as the Akaike information criterion (AIC) have been proven to exhibit better performance in determining the arrival of a wave [216]. Adopting this technique for determining the start of the time window may have an influence on the cross-correlation coefficient calculated for each candidate sensor location.

5.7.LISA optimisation study

The experimental study described above has only considered one disbond scenario (although different excitation site-disbond paths and angles were considered by having multiple excitation sites). On real aircraft structures however it is possible for a disbonded region to vary in both shape and size. The shape and size of the disbonded region will influence how the Lamb wave interacts with it and therefore how the sensors are placed. To carry out such extensive experimental programmes for each scenario would be both time consuming and costly as in reality many different materials, complex geometries and loading scenarios would need to be considered, therefore it would be advantageous from a design perspective to have a simulation tool which would enable sensor network designers to model different damage scenarios in order to determine the optimal locations in which to place their sensors on the structure. Therefore the remainder of this chapter focuses on modelling the damage scenario investigated in the experimental study with a view to developing a suitable design tool using LISA.

5.7.1. Model setup

In order to reduce computational overheads, only the area of investigation (outlined in Figure 40) was modelled. The excitation sites were modelled on the left-hand boundary which reduced the effects of edge reflection. The same excitation frequencies were used in the model as in the experimental study.

To ensure continuity of the sensor locations from the experimental vibrometry study, the co-ordinates of the sensor locations were exported from the vibrometry software. These were then rounded to the nearest 0.5mm and assigned to the corresponding cube on the model. The sensing locations were modelled as points representing the point measurements in the laser vibrometer study. In the case of an installed sensor this would not be the case as the face of the sensor covers an area. This varies for different sensors and was not considered in this study.

A sampling frequency of 20MHz was used for the model as this had been shown to produce representative results in the previous study (Section 4.4.2). To be consistent with the experimental study, a sample length of a 1.6ms was recorded at each sensor location. As with the laser vibrometry data, the x, y and z components of the Lamb wave were recorded.

The plate and the stiffener were both given the properties of 6062-T6 aluminium alloy (density = 2710kg/m^3, longitudinal velocity = 6.32 x 10^6 mm/s, transverse velocity = 3.04 x 10^6 mm/s). Due to the global cube edge length being 0.5mm, the adhesive layer was not modelled. Instead the interface between the stiffener and plate was modelled as a continuous structure as previously (Section 4.4.1).

5.7.2. Modelling the disbond region

As previously demonstrated, the disbond used in the experimental study was not 'perfect' (section 4.4.1). As a result, three approaches were taken to modelling the disbond;

- The disbond was modelled as a missing section (as previously modelled in section 4.4) to approximate the reduction in stiffness
- Using the data from the C-scan (section 4.7) the shape and size of the residue material in the disbonded region was modelled approximately using cubes and given the material properties of aluminium 6062-T6
- The same as above but the residue material in the disbonded region being given the properties of PTFE as it was believed that the shape of the residue material in the disbonded region was the result of PTFE tape inside of the bond.

It is worth noting that as a global cube edge length of 0.5mm was used again, the dimensions of the disbond were rounded to 25.5mm x 25.5mm. This did however mean that the disbond was 0.5mm thick instead of >0.1mm as it was in the experimental study. The PTFE shaped disbond model is presented with the results in from the C-scan (for details see section 4.7) in Figure 48.

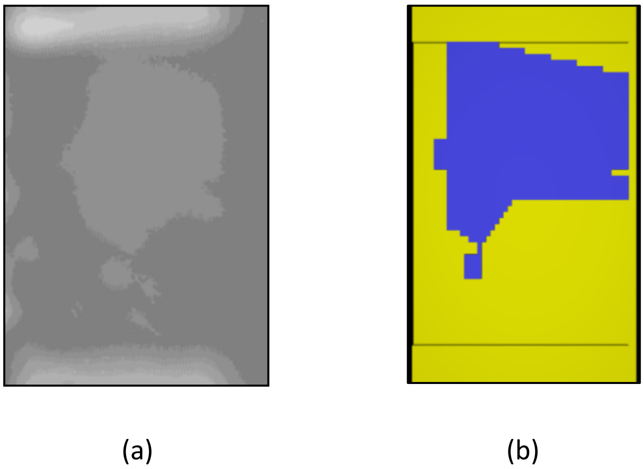
(a) (b)

Figure 48. (a) C-scan of the disbonded region (b) LISA model PTFE shaped approach. Stiffener (yellow), PTFE (Blue).

5.8.Optimisation results from modelled data

5.8.1. Out-of-plane component of the Lamb wave

The results for all three approaches of modelling the disbond for both the out-of-plane component and the three-component magnitudes are presented.

5.8.2. Missing Section Disbond

The optimal calculated fitness based on the out-of-plane component of the wave as the sensor network size increases for each excitation frequency is presented in Figure 49 for the missing section disbond.

As with the experimental results, the excitation frequency has a significant influence on the maximum fitness. However, unlike in the experimental setup the excitation which results in the highest fitness for the one and two sensor networks is the 250kHz excitation and not the 300kHz.

In addition to this there is not as significant an increase in fitness between the 100kHz excitation sensor networks and the higher frequency excitation sensor networks as was found in the experimental results.

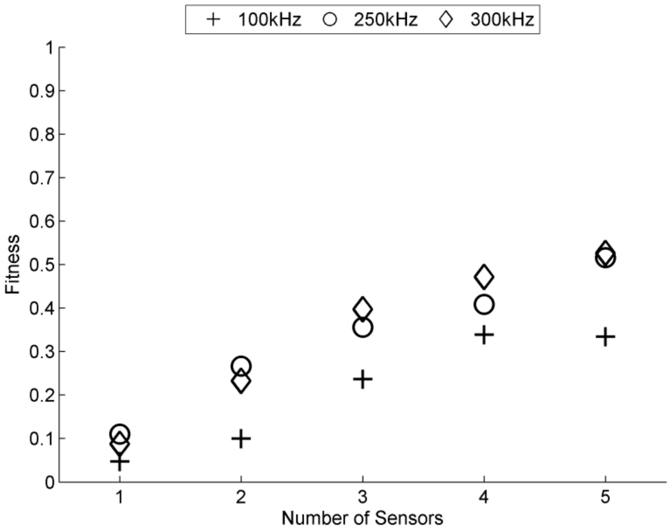

Figure 49. Fitness against the optimal network configurations for a given number of sensors using the out-of-plane data from the LISA model (missing section disbond)

With all three frequencies it was demonstrated that the poorest performance is achieved from a single sensor network as expected. The best performance with the 100kHz excitation was observed with a four sensor network with a small reduction in fitness as the sensor network grew to five sensors as observed in the experimental study. This can be explained by having a particular strong sensing position in the four sensor network that had low cross-correlation for more than one excitation site. When a five sensor network is considered, the GA is forced to use five individual sensors which do not have cross-correlations as low as the strong sensing location used in the four sensor network. As such, forcing the algorithm to adhere to these conditions can produce results which are poorer than can be achieved with a smaller network. There was also a similar rate of increase of fitness observed between two and four sensor networks to that of the experimental study, albeit at a lower overall fitness.

The 250kHz and 300kHz results achieved their best performance with a five sensor network which differs greatly from what was observed in the experimental study. The performance of the 250kHz excitation networks saw a significant increase in fitness as the size of the network grew from one sensor to two sensors. The rate of the fitness increase reduced as the network grew from two to three and reduced again as the network grew from three to four sensors. However as the network grew from four sensors to five the fitness increased dramatically indicating a significant improvement in performance.

The 300kHz excitation showed an almost linear increase in fitness as the size of the network grew from one sensor to three sensors at which point the 300kHz excitation out-performed the 250kHz excitation. The network size increase from three sensors to five again caused an almost linear increase in fitness but a reduced rate.

5.8.3. Residue material in the disbonded region modelled as Aluminium

The optimal calculated fitness for the out-of-plane component as the sensor network size increases for each excitation frequency is presented in Figure 50 for the residue material in the disbonded region modelled as aluminium.

Though there is a relationship between excitation frequency and fitness, when the disbond is modelled using this approach the influence of the excitation frequency is less significant. Unlike the results for the missing section disbond and the experimental results, the excitation frequency with the best fitness is not 300kHz but 250kHz. This is most likely to be due to the 250kHz Lamb wave having a short enough wavelength to significantly interact with the damage while not being as attenuative as the 300kHz wave.

It is evident that the fitness achieved by this approach to modelling the disbond achieved a much lower respective fitness than that found in the experimental results and in the missing section approach. It could be inferred that this is due to the smaller effective disbond size and hence the sensor network needs an increased level of sensitivity to achieve a more suitable fitness.

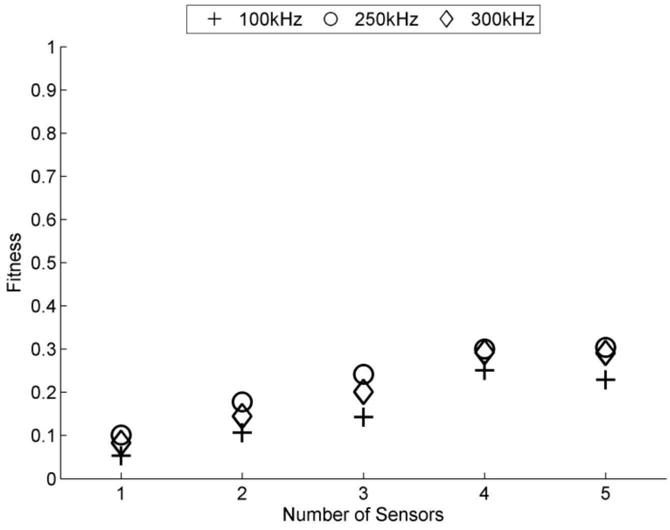

Figure 50. Fitness against the optimal network configurations for a given number of sensors using the out-of-plane data from the LISA model (the residue material in the disbonded region modelled as aluminium.)

As the sensor network size increased, the fitness improved which was in agreement with the results for the missing section disbond. A small reduction in fitness was observed with the five sensor network which suggests that the four sensor network offered the best performance. As previously discussed this is due to the GA being forced to select five individual sensors.

The fitness characteristic demonstrated by this method of modelling the disbond did not improve upon the performance of the missing section disbond and was not consistent with that observed in the experimental study.

5.8.4. Residue material in the disbonded region modelled as PTFE.

The optimal calculated fitness for the out-of-plane component of-the-wave as the sensor network size increased for each excitation frequency is presented in Figure 51 for the residue material in the disbonded region modelled as PTFE.

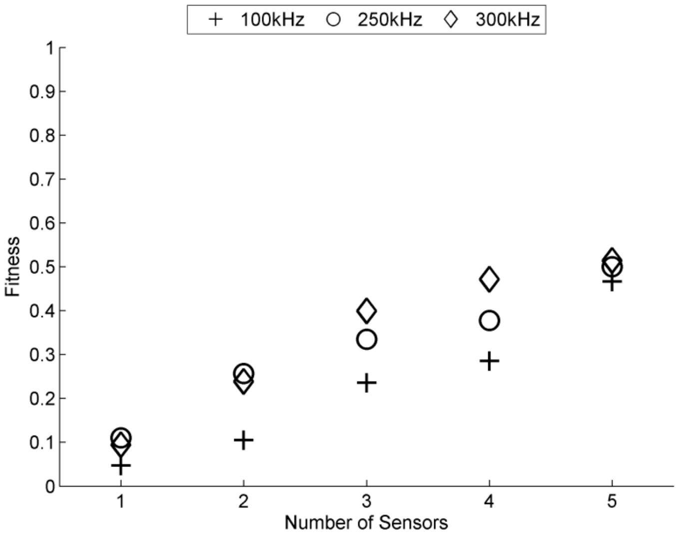

Figure 51. Fitness against the optimal network configurations for a given number of sensors using the out-of-plane data from the LISA model (the residue material in the disbonded region modelled as PTFE.)

As with the experimental results and the results from the missing section disbond, nominally an improvement in fitness was observed as the excitation frequency was increased. Additionally, as the size of the sensor network increased, performance gains were achieved. It is worth noting that there were no cases of performance decrease as the size of the sensor network increased.

The best performance achieved with a one-sensor network was with a 250kHz excitation though there was a minimal decrease in fitness when a 300kHz excitation was used. A clear performance increase was observed when using the higher frequency excitations over the 100kHz as the size of the sensor network grew to two. This trend continued as the sensor network size grew to three and four sensors. For these sensor network sizes, the 300kHz excitation demonstrated the best performance with a more significant performance gain over the two other excitation frequencies.

An unusual effect on performance was observed as the size of the sensor network grew to five sensors. The five-sensor network demonstrated a similar performance regardless of excitation frequency. A significant improvement in performance was achieved by the 100kHz excitation. This performance was not experienced by the five sensor networks of the experimental nor the missing section disbond model.

A better performance was observed with the PTFE shaped disbond than the aluminium shaped disbond with better fitness values achieved; more consistent with those observed in the experimental results. However, the overall performance of this approach to modelling the disbond was still substantially lower than the experimental results.

5.8.5. Three component magnitude of the Lamb Wave

The optimal calculated fitness for the three component magnitude as the sensor network size increases for each excitation frequency for the missing section disbond is presented in Figure 52.

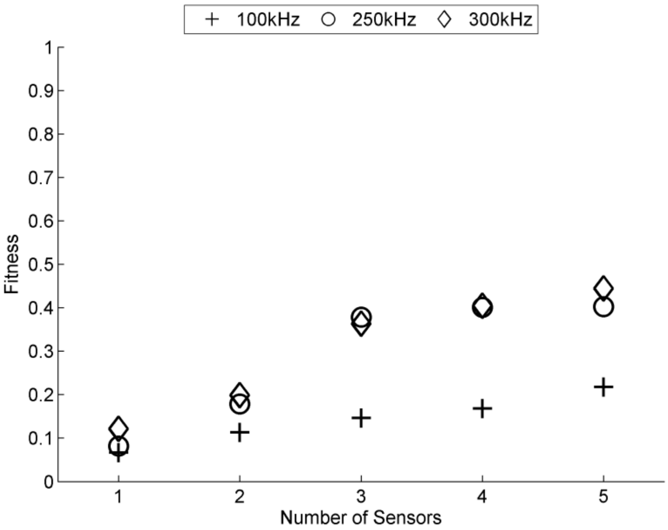

Figure 52. Fitness against the optimal network configurations for a given number of sensors using the three component magnitude data from the LISA model (missing section disbond)

As with the out-of-plane results, the higher frequency excitations out-performed the 100kHz excitation. The results from the 100kHz excitation showed a near linear, gradual increase in fitness of 150% for a four sensor network over a one sensor network. Increasing the size of the network to five sensors saw a further increase in fitness of only 29% compared to the four sensor network. The near linearity of these results does not aid in suggesting an optimal sensor network size.

The 250kHz and 300kHz excitations showed similar increases in fitness as the size of the sensor network grew. From one sensor to three sensors there was a progressive increase in fitness for both excitation frequencies. However sensor networks larger than three sensors showed minimal increase in fitness. This reduced rate of increases in fitness demonstrates that there are minimal performance gains to be achieved with sensor networks greater than three sensors; thus suggesting that a three sensor network is optimal when considering the three component magnitude.

5.8.6. Residue material in the disbonded region modelled as Aluminium

The optimal calculated fitness for the three component magnitude as the sensor network size increases for each excitation frequency for the aluminium shaped disbond is presented in Figure 53.

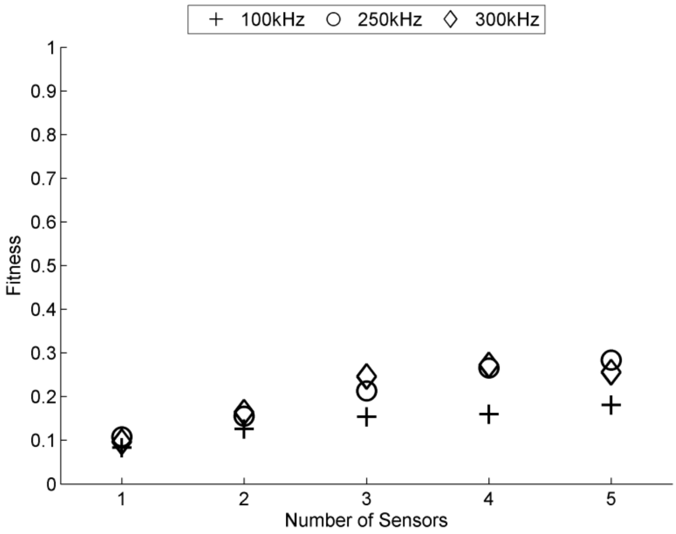

Figure 53. Fitness against the optimal network configurations for a given number of sensors using the three component magnitude data from the LISA model (the residue material in the disbonded region modelled as aluminium.)

As with the results from the out-of-plane aluminium shaped disbond, the performance from the three-component magnitude was substantially lower than the performance observed in the results of the experimental study and the missing section disbond model.

Consistent trends for the 250kHz and 300kHz excitation were observed with an increase in performance as the size of the sensor network grew. However, this cannot be said to be true of the 100kHz excitation. For sensor networks larger than three sensors, marginal gains in performance were observed. With the higher frequency excitations, minimal performance gains were observed between 250kHz and 300kHz.

5.8.7. Residue material in the disbonded region modelled as PTFE

The optimal calculated fitness for the three component magnitude as the sensor network size increases for each excitation frequency in Figure 54 for the residue material in the disbonded region modelled as PTFE.

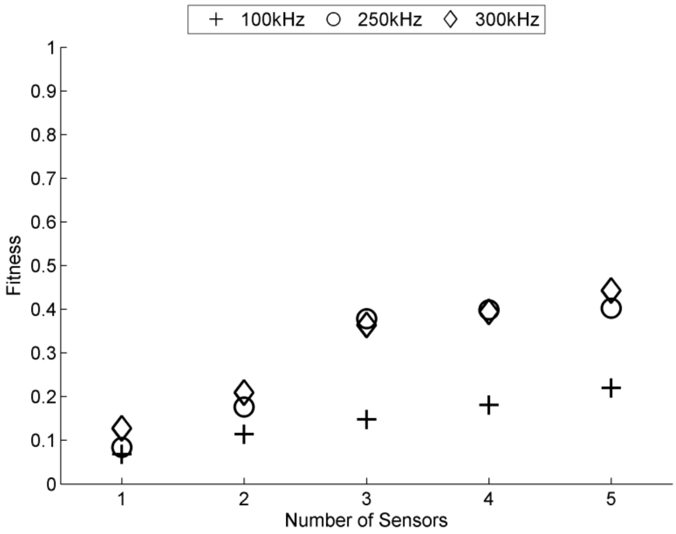

Figure 54. Fitness against the optimal network configurations for a given number of sensors using the three component magnitude data from the LISA model (the residue material in the disbonded region modelled as PTFE.)

As with the experimental results, an increase in performance was observed as the excitation frequency was increased. In addition, performance gains were also achieved as the size of the sensor network was increased.

Marginal increases in performance were observed between the three different excitation frequencies with the one-sensor network although the best performing excitation frequency was 300kHz. This is consistent with the missing section disbond.

As the sensor network size increased, significant performance gains were observed by the higher excitation i.e. frequencies over the 100kHz excitation. The three-sensor and four-sensor networks demonstrated that there were marginal differences in performance between the 250kHz and 300kHz excitations. This was not found to be the case in the experimental results.

The rate at which the fitness increases as the size of the sensor network increases is marginal with the 100kHz excitation. In addition, the performance gains are almost linear which does not aid in suggesting a suitable sensor network size. With the 250kHz and 300kHz excitations, there are minimal increases in fitness between the three-sensor and five-sensor networks. This suggests that a three sensor network size is suitable.

The results of the PTFE shaped disbond demonstrated were found to be more consistent with the results observed with the missing section disbond approach because the elastic modulus is significantly lower than that of Aluminium. However, it is worth noting that the performance was still significantly lower than what was observed in the experimental studies and not as representative of the experimental study as the missing section disbond.

5.9.Discussion on different disbond modelling approaches

Assessing the performance of the three modelling approaches, it is evident that none of the approaches resulted in producing sensor networks that had similar performance characteristics to those observed in the experimental results.

The least successful of the approaches was the aluminium shaped disbond. This technique produced networks with low performance which were not consistent with the experimental results in terms of trends. This is most likely due to the effective size of the disbond being significantly reduced. Although a reduction in the disbonded region was observed in the result from the C-scan (Section 4.7) the residue was likely to be PTFE tape not aluminium and of a smaller thickness which would affect the stiffness of the structure. As a result the reduction in cross-correlation coefficient being less significant as well as only affecting a smaller number of sensing locations.

Similar performances were observed with both the missing section disbond and the PTFE shaped disbond approach. This is due to the similarity in the reductions in structural stiffness exhibited by both models. However, it could be argued that a better performance was exhibited by the missing section disbond particularly when only the out-of-plane component was considered. Therefore the missing section disbond was chosen for further investigation.

5.10. Experimental and optimal location results

The sensor locations for the out-of-plane component of the Lamb waves for the missing section modelling approach are presented in this section.

5.10.1. Missing section disbond

Regardless of the differences between the fitness results from the experimental and computational studies, it is important to compare the optimal locations that have been produced by each study. To achieve this, the optimised sensor locations for the out-of-plane component for 100kHz, 250khz and 300kHz excitations are presented in Figure 55, Figure 56 and Figure 57 respectively.

With the one-sensor network for the 100kHz excitation, the sensor is placed in different locations. However some similarities can be drawn. Both the experimental data and the model placed the sensors slightly above and below the disbonded region. Again, the positioning is consistent with diffraction patterns previously observed and diffraction patterns of cross-correlation shown in Figure 41.

As the size of the sensor network size increases to two sensors there is more commonality between the two datasets. Sensors from both the experimental and LISA model place a sensor in-line with the disbonded region on the right of the stiffener. The distance from the stiffener is also similar for the placement of both of these sensors. The second sensor was however placed in two different places. The sensor positioned based on the experimental data was placed at the bottom right hand corner of the area of investigation which has been shown to be a strong sensing location. However, the second sensor was placed to the left side of the stiffener above the disbonded region.

The three-sensor network showed the modelled solution to distribute the sensors almost uniformly along the length of the stiffener at a similar distance from the stiffener. The placement of the sensor based on the experimental results similarly positioned the three sensors along the length of the stiffener. However, two of three sensors were placed much closer to the stiffener than for the modelled locations. In particular one of the sensors was positioned very close to the stiffener as previously discussed.

The placement of the sensors in the four-sensor network showed good agreement between the solutions derived from the experimental and modelled data. Interestingly, the experimental data placed a sensor in the lower right corner of the area of investigation where a sensor was also placed next based on the modelled data. This therefore indicated a good agreement. Similarly, both data sets placed a sensor reasonably in-line with the disbond at a similar distance; again showing a good agreement between the two datasets. A third sensor was also placed on the right of the stiffener above the disbonded region. Though there was a larger discrepancy between the placement of this sensor based on the two datasets, the area in which they are placed is highlighted as being a strong sensing region.

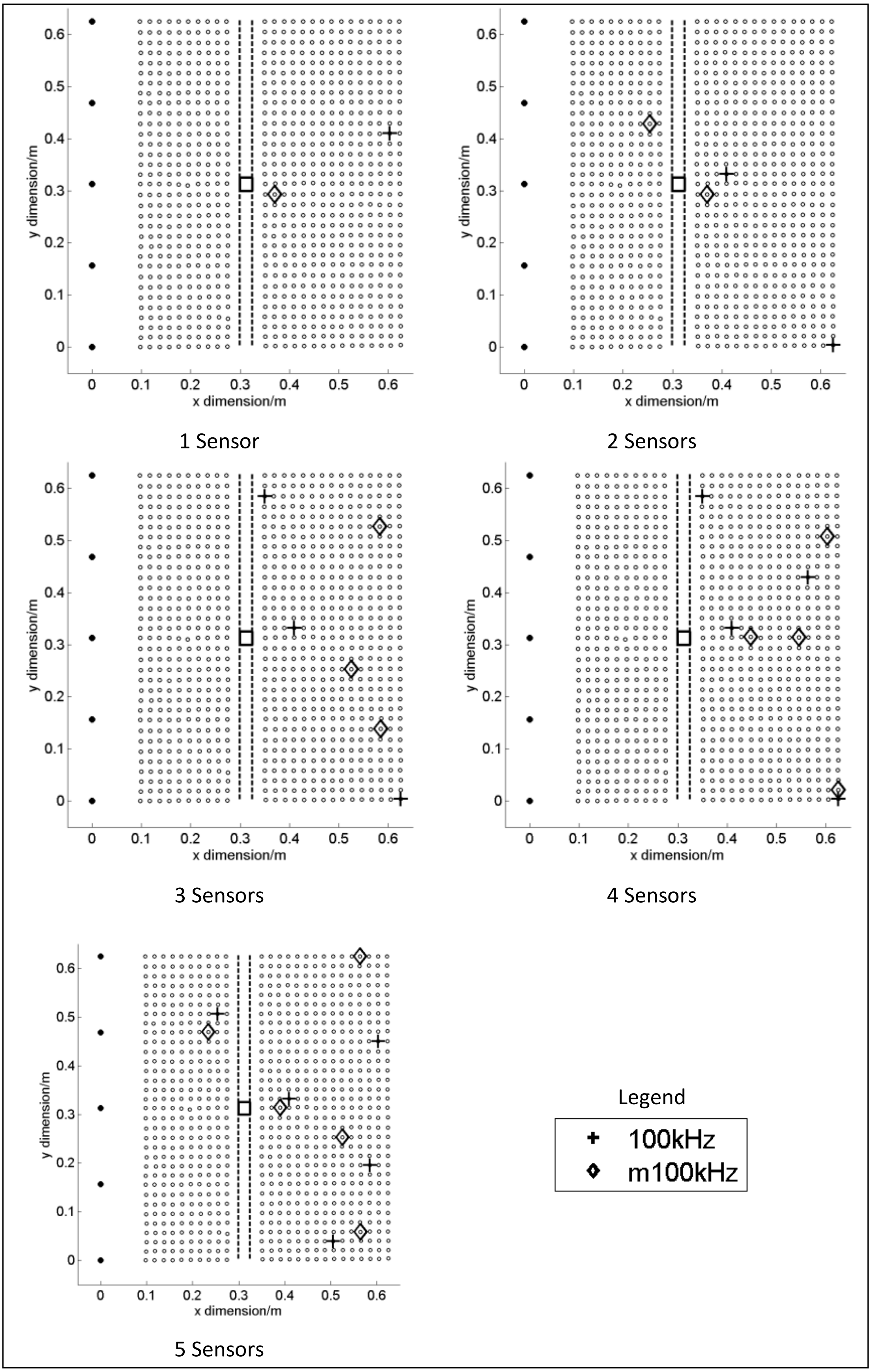

1 Sensor

2 Sensors

3 Sensors

4 Sensors

5 Sensors

Figure 55. Optimised sensor locations based on the out-of-plane component for the 100kHz excitation. The locations from the LISA model are denoted by ‘m100kHz’.

A difference in sensing location was shown with the placement of the fourth sensor. The sensor placed based on the experimental data was placed in the same position as in the three-sensor network; demonstrating that the location was a strong sensing location. The sensor positioned based on the modelled data however was placed to the right of the stiffener, in-line with the disbonded region. This is perhaps a more intuitive placement of the sensor however the differences between the modelled and experimental disbonded regions may be the reasoning for this difference in sensor placement.

When considering the five-sensor network, the placement of the sensors based on the experimental data and the modelled data correlates well. Both datasets place a sensor in the bottom right hand corner of the area of investigation. Similarly, sensors are also placed by both datasets to the right of the stiffer below the disbonded region. A high level of consistency in the placement of sensors is achieved by the third sensor where both datasets placed a sensor in-line with the disbonded region using candidate locations next to each other. Similarly, both datasets placed a sensor on the left of the stiffener above the disbonded region. These sensor placements were next to each other, again demonstrating a high level of agreement between the two data sets.

A small difference in sensor placement was observed with the placement of the fifth sensor. The fifth sensor was placed on the top boundary to the right of the stiffener based on the modelled data. However, the fifth sensor was not placed as high up in the area of investigation and at a further distance away from the stiffener. Nevertheless, the placement of the two sensors is within the same quadrant of the area of investigation.

The sensor placements for the 250kHz excitation are presented in Figure 56. When a one-sensor network is considered, the placement of the sensors based on the data from the laser vibrometry and the LISA model is to the right of the stiffener below the disbond. Although there is a difference in the placement of the sensors this may be justified by the differences between the physical disbond and the model. Nevertheless, the fact that both datasets place the sensors within the same region is promising.

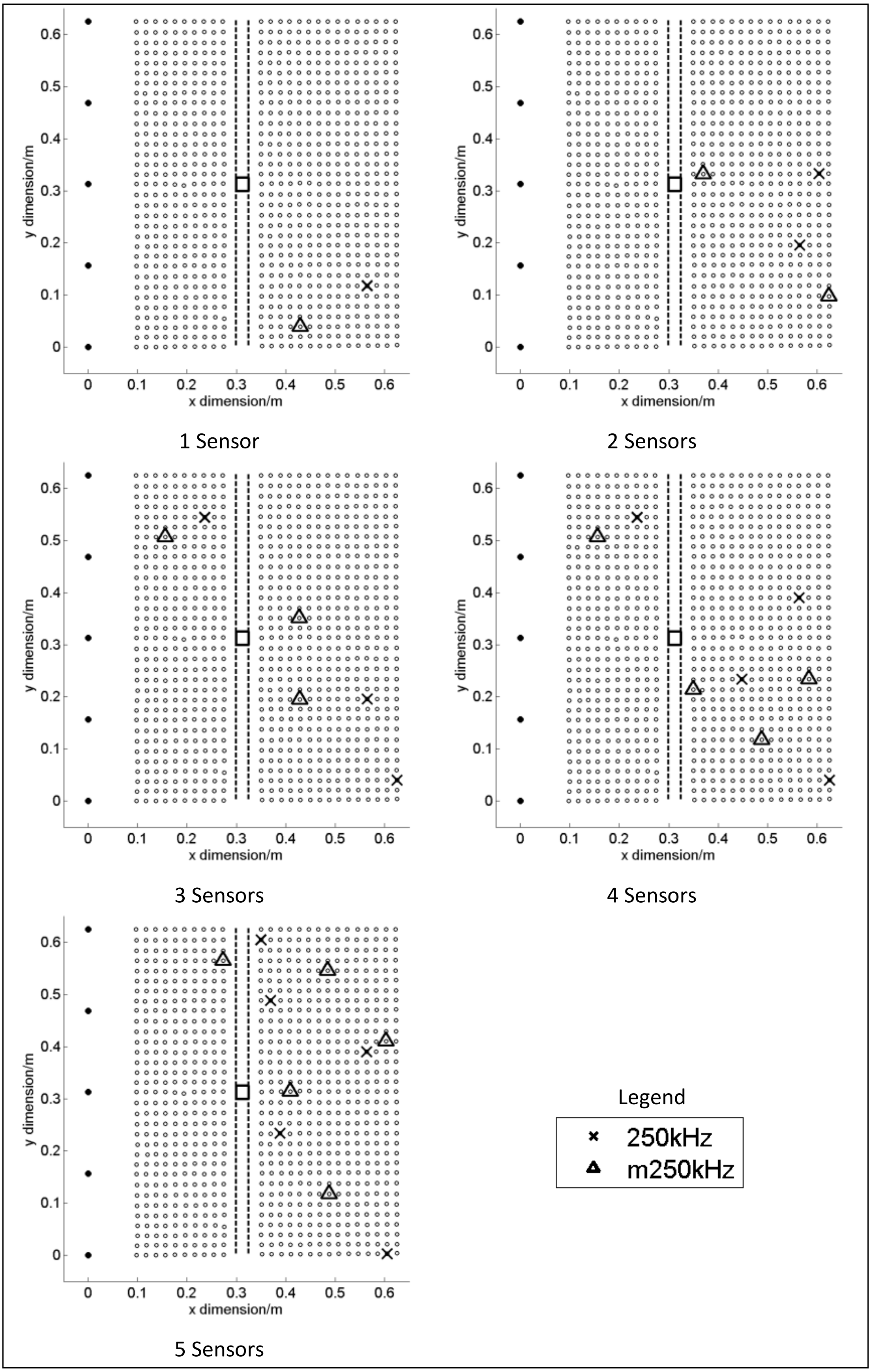

1 Sensor

2 Sensors

3 Sensors

4 Sensors

5 Sensors

Figure 56. Optimised sensor locations based on the out-of-plane component for the 250kHz excitation. The locations from the LISA model are denoted by 'm250kHz'.

When a two sensor-network is considered the placement of the sensors based on the two datasets differs somewhat. The first sensor for both datasets is placed to the right of the stiffener, below the disbond. However the position of the sensor based on physical data is above the sensor placed based on the LISA model. Both sensors appear to be placed on a line of the diffraction pattern as observed previously. The placement of the second sensor for both datasets is in-line with the disbonded region to the right of the stiffener. The second sensor placed based on the LISA model however is close to the stiffener whereas the sensor placed based on the experimental data is further from it. Though a difference in actual placement location, it was previously shown in Figure 55 for the 100kHz that this region has a high level of sensitivity for a two-sensor network.

The placement of the sensors for a three-sensor network shows some similarity between the two datasets. The first sensor is positioned to the left of the stiffener above the disbonded region for both datasets. Although there is a small difference in the placement of the sensors they are both located in the same region demonstrating good correlation between the experimental and model results.

When the placements of the second and third sensors are considered there are some differences. The modelled data places both sensors to the right of the stiffener; one sensor just above the disbonded region and one below. The experimental data however places the both sensors below the disbond and at a position further away from the stiffener on the right-hand side. Similarities can be drawn when considering the vertical spacing of the sensors based on their respective datasets.

When the size of the sensor-network grows to four sensors, the placement of the first sensor to the left of the stiffener is retained for both datasets from the three-sensor network. This highlights the suitability of these locations regardless of the dataset considered. The placement of the remaining three sensors is on the right of the stiffener for both datasets. The sensors based on the modelled data are placed in a triangular array below the disbonded region. One of the sensors placed based on the experimental data is located below the disbonded region close to the stiffener which is also close to one of the locations found using the modelled data. The third sensor location is placed on the right-hand boundary and is retained from the three-sensor network. Drawing a line between this location and the disbonded region it is worth noting that the placement of one of the sensors based on the modelled data lies on this line indicating that this is likely to be a line of diffraction. At first glance, the fourth sensor based on the experimental data appears not to correlate with the sensor location found using the modelled data. However, when the problem is considered as a symmetrical problem with a line of symmetry drawn horizontally through the centre of the disbonded region, it is apparent that the two placements are practically symmetrical solutions of one another.

Considering a five-sensor network, there is a good level of correlation between the experimental data and the modelled data. The first sensor is placed to the right of the stiffener below the disbonded region for both datasets. The placement of each of these sensors from their respective dataset has a similar diagonal spacing to the disbonded region as observed previously in the three and four-sensor networks. However, it should be noted that although the placement of this sensor based on the modelled data was retained from the four-sensor network, a new solution is found for the placement based on the experimental data.

The placement of the second sensor indicates an optimal location close to the stiffener on its right-hand side for both datasets. The modelled data places the sensor in-line with the disbonded region whereas the experimental data places the sensor below the disbonded region.

There is a high level of correlation between the experimental and modelled datasets with the placement of the third sensor. Both sensors are placed above the disbonded region to the right of the stiffener close to the right-hand boundary. Both placements based on the respective datasets derive solutions which are on the same diagonal. This is also diagonally in-line with the disbonded region. With all of the placements of the first three sensors it could be argued that they align with a diffraction pattern similar to that presented in Figure 41.

The placement of the fourth sensor is above the disbond and to the right of the stiffener. The placement of the sensor based on the experimental data is closer to the stiffener whereas the sensor positioned based on the modelled data is further from the stiffener. Even so, this region is highlighted as a region with a suitable degree of sensitivity especially as the fifth sensor based on the experimental data is also placed within this vicinity. The placement of the fifth sensor based on the modelled data is in a similar location albeit on the left of the stiffener. Although these sensors are places on opposing sides of the stiffener, they are at a sufficient vertical distance from the disbond which means that the reduction in cross-correlation coefficient is likely to be the result of the waves being guided along the length of the stiffener as previously observed (section 4.5).

The placement of sensors for the 300kHz excitation for both the modelled and experimental datasets is presented in Figure 57. Considering the one sensor network, there is a difference in the location of the sensor. As previously demonstrated in Figure 45, sensors from the experimental study were placed either above or below the disbonded region. The optimal location for both the experimental and modelled data positioned the sensor below the disbonded region although the modelled solution was positioned closer to the disbonded region. As previously discussed, the Lamb wave interacting with the disbonded region results in a diffraction pattern. Drawing a line between the two solutions and the disbonded region it is clear that both of these solutions have been placed along the path of a diffraction pattern (as presented in Figure 41) and therefore a region of significant difference in waveform.

The two sensor network showed similarity between the experimental and modelled data for the placement of one of the sensors in the network. Both datasets positioned a sensor directly to right of the disbonded region. However, there was a significant difference in the placement of the second sensor. The results from the experimental data placed the second sensor to the left of stiffener, in line with the disbonded region. The modelled data positioned the second sensor above the disbonded region on the right of the stiffener. The reasoning for this is most likely to be due to the modelling of the disbonded region not capturing the reality of the disbond used in the experiment.

When studying the three sensor network at first it appears that there is a significant difference in the placement of the sensors. However, when the problem is viewed as a symmetrical problem with a line of symmetry at y = 312.5mm (the centreline running horizontally through the centre of the disbonded region) it becomes apparent that similar solutions have been produced by both the experimental and computational studies. The experimental study positions three sensors below the disbonded region in a triangular array. The modelled solution positions three sensors above the disbonded region in in a triangular array, though the network was more sparsely distributed compared to that of the experimental solution. Like that of the two sensor network this can be attributed to the modelling of the disbonded region. The disbonded region in the experimental study not being as ‘perfect’ as it was modelled in the LISA would have a significant influence on the Lamb wave interaction; thus influencing the diffraction pattern and the sensor positioning.

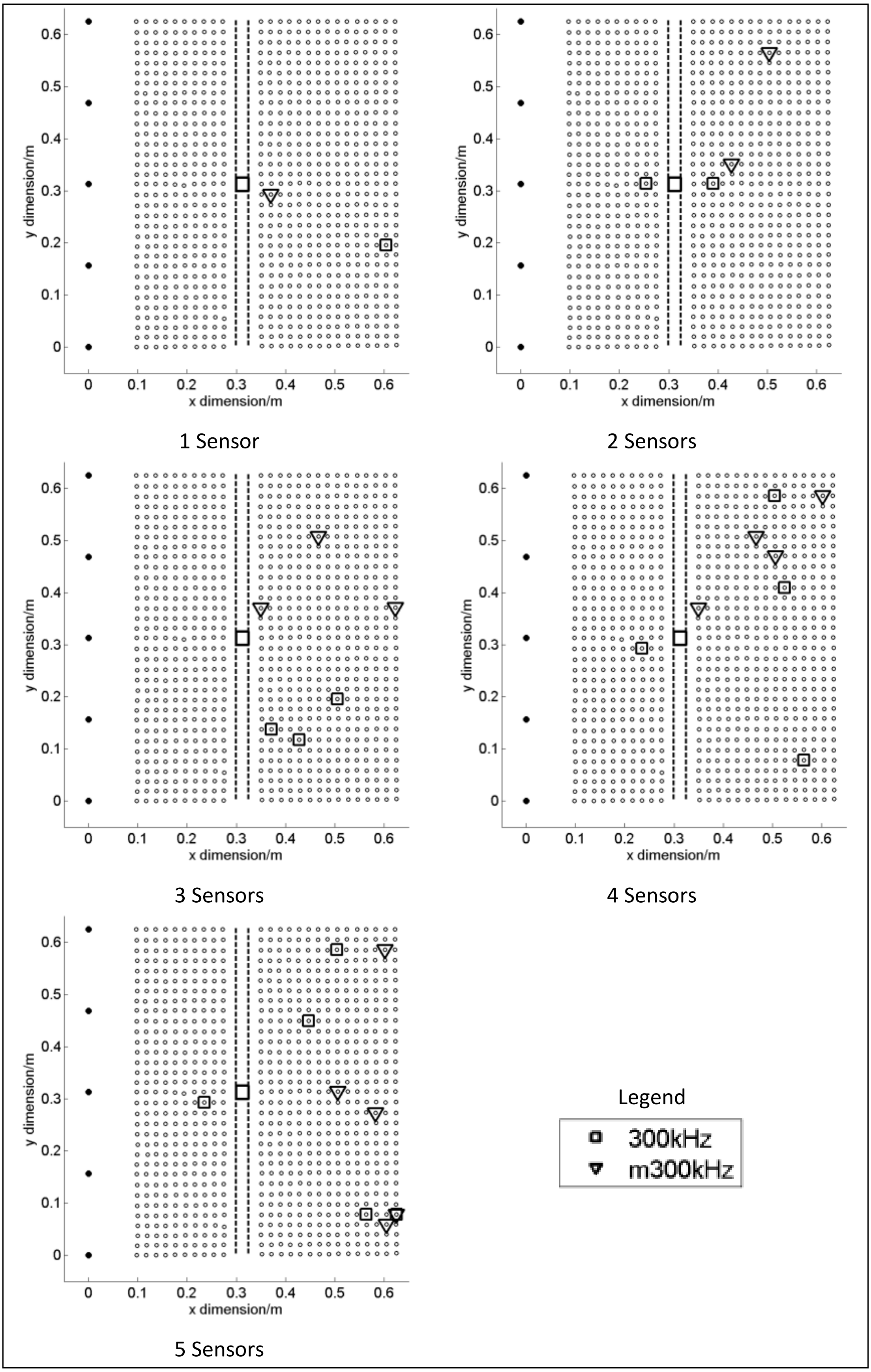

1 Sensor

2 Sensors

3 Sensors

4 Sensors

5 Sensors

Figure 57. Optimised sensor locations based on the out-of-plane component for the 300kHz excitation. The locations from the LISA model are denoted by 'm300kHz'.

There is good agreement for the location of three of the sensors in the four sensor network. The modelled data positioned three of the sensors above the disbonded region. Of those placed using the experimental data only two sensors were located in close proximity to the modelled solutions with the third sensor being positioned below the disbonded region. However if, as with like the three sensor network, the problem is treated as symmetrical, this third sensor is positioned in a similar location to that of the modelled solutions. Like the solution generated for the two sensor network, there is a difference with the placement of the fourth sensor. The experimental solution positions the sensor to the left and below the disbonded region whilst the modelled solution positions the sensor to the right and above the disbonded region. The positioning of the sensor based on the experimental data most likely results from the reflected diffraction pattern caused by the Lamb wave interaction with the disbonded region.

Again the five sensor network sees both similarities and differences in the positioning of the sensors. Two sensors are positioned by both the modelled and experimental solutions below the disbonded region at the right-hand edge of the area of investigation. For one of the sensor locations, both datasets select the same location. A third sensor is positioned above the disbonded region by both datasets however these solutions are much more sparsely spaced than those of the first two sensor locations. The fourth sensor was placed above the disbonded region for the experimental data. However, the modelled data positioned the fourth sensor in line with the disbond. The biggest difference in sensor location was with the fifth sensor. The experimental solution positioned the sensor to the left of the stiffener below the disbonded region whilst the modelled solution positioned the sensor to the right of the stiffener. This indicates a difference in the model to that of the experiment.

Only the results for the out-of-plane components for the three excitation frequencies have been presented as the out-of-plane component has been the main focus of this study. Although there are some differences in the placements of the sensors, overall there is a general agreement between the experimental and modelled solutions with sensors being placed at similar locations on the structure.

5.11. Comparative discussion

It is apparent that whilst there are differences in the solutions derived from the experimental study and the computational study, there are many plausible reasons for these differences.

The adhesive layer being omitted from the model would have an influence on the Lamb wave interaction with the stiffener due to the difference in acoustic impedance and hence this is an influencing factor on the results. It is difficult to quantify the influence of including the adhesive layer on the model results. Comparing the placements of the sensors, there is a general agreement with the majority of the locations. By modelling the adhesive layer, the location of the sensors may become more representative of the experimental solutions.

The biggest contributing factor to the difference in results is most likely the method used to model the disbonded region. As mentioned, the adhesive layer was not modelled and as a result the disbonded region was approximated by removing cubes in the disbonded region hence generating a reduction in stiffness. In addition, the reduction of stiffness modelled removed a section of 0.5mm thickness whereas in the experimental study this was approximately 0.1mm thick. This is likely to have had considerable effect.

The results from the ultrasonic C-scan found that there appeared to be a small amount of PTFE tape left inside the disbonded region which would have significantly influenced the Lamb wave interaction meaning that the disbonded region was more representative of a real ‘imperfect’ disbond rather than the ‘perfect’ artificial disbond that it was intended to create. Improved LISA models were created in an attempt to be more representative using the shape of the defect from the C-scan results. However due to the geometry of the imperfect disbond it was not possible to model it with sufficient fidelity using a 0.5mm cube edge length. This was demonstrated by being unable to improve upon the fitness results from the missing section disbond approach. The cause of this is mostly associated with a deficiency in computational hardware. Improving the hardware should allow for a more representative model to be created through reducing the global cube edge length. However, a similar level of fidelity maybe achieved if different cube edge lengths could be applied to different areas of the model. This is achievable within the software however reducing the global cube edge length increases the number of cubes in the model and thus the amount of on-board GPU memory required.

The sensor location solutions from the LISA model used a simple point source actuation composed entirely from an out-of-plane component as the input. In the experimental study however a transducer was used at the excitation sites which had a face larger than that of a point. Due to Poisson’s ratio, although the excitation would have mainly been out-of-plane there would have been an additional in-plane component. To determine the magnitude of this in-plane excitation, a separate study would need to be conducted.

In addition, the transducer was excited using an electrical signal which was set to the required frequency. Due to the transducer having a transfer function as it converts the electrical signal to motion it is possible for the frequency and the envelope of the wave to change resulting in a different wave being excited to the one specified. Both of these factors would have had an influence on the positioning of the sensors particularly when all three wave components were considered.

The experimental study saw fitness values that were substantially higher than those calculated from the LISA data. There are a number of possible reasons for this. The fitness is calculated from the values of the cross-correlation coefficients. This means that the metric by which the two waveforms are being compared is sensitive to noise. With the experimental data, despite taking the average of two hundred measurements and improving the signal quality by coating the surface there was still some noise present on the received signal. The data from the LISA model did not have any noise which may have contributed to lower fitness being calculated from the modelled data.

The cross-correlation coefficient proved to be successful as a statistical method for determining the presence of damage as well as being relatively computationally efficient. However, other statistical methods, such as the Mahalanobis distance which has been used previously by Sheppard *et al.* [217] for determining the presence of damage on aerospace structures using Lamb waves, may offer gains in performance. This maybe an improvement in computational efficiency or offering a higher sensitivity to damage detection.

The setup of the experimental study required two panels to be manufactured. This resulted in a new transducer coupling for each excitation site on each panel. Though the coupling technique used had shown in previous studies to produce repeatable results [184], and each coupling was tested prior to use, a consistent coupling cannot be guaranteed. Small inconsistencies in coupling the transducer such as not being perpendicular to the surface of the panel or inconsistencies in the surface preparation may have resulted in reduced repeatability of the signal.

An additional source of error from using two separate panels is the inconsistency of the measurement points. Though every effort was made during the experimental study to ensure that representative points were measured on each panel, it is possible that there was a small amount of error in the location of the measurement points. This would in-turn lead to differences in the waveforms being measured and hence increase the calculated fitness. A method of reducing this would be to conduct the test on one panel and induce a delamination on the panel by subjecting it to some form of mechanical loading. The vibrometry measurements could then be taken in-situ. However this also has other risks such as inducing additional unwanted damage to the panel. In addition, a longer test period with more testing machinery is required. The study presented here however demonstrates a methodology that could be used for such a study.

This study has considered only the positioning of sensors for the detection of damage. Though it would be possible to locate the damage to a region of the structure by looking at the change in waveform of a particular pulse-receive path it would not definitively locate the damage and further NDT processes would be required. Applying a location technique to the optimisation scenario may influence the positioning of the sensors and thus a different sensor network may need to be designed to accommodate this.

This study considered eight hundred and twenty five candidate sensor locations with five excitation locations. Through the use of candidate locations, the solution has to be discrete (i.e. only the candidate sensor locations can be selected). This can result in sensor network solutions being created being sub-optimal although it is feasible to have a large set of candidate locations but this is less than ideal. Therefore, statistical interpolative methods could be employed to project the fitness of a sensor location between the candidate sensor locations. This would produce cross-correlation values for each region on the panel in a similar fashion to interpolation employed in Figure 41. In addition, through the use of LISA multiple excitation locations could be considered and similar interpolative methods could be applied to optimise the excitation location.

Though this study considered three excitation frequencies it may be beneficial to optimise the sensor locations regardless of excitation frequency especially as different excitation frequencies produced different sensor network solutions. This would produce sensor networks that were capable of detecting the presence of damage regardless of excitation frequency offering the ability to ‘tune’ the network’s operation in order to be able to detect different defect sizes. A multi-objective function could be used to achieve this and to optimise the placement of sensors and the excitation frequency used.

The application of LISA has shown great potential for the design of sensor networks. The ease of use, quick setup and fast computation make it suitable for running models that cover a wide range of scenarios. The adoption of such a strategy to the design and optimisation of active sensor networks would enable designers to consider a wide range of damage types and defect sizes which would not be possible to feasibly achieve experimentally. This approach would also enable the design of sensor networks concurrent with the design of the structure and would be particularly useful for the design and development of sensor networks on complex structures.

5.12. Conclusion

This study has demonstrated a methodology for optimising an active sensor network for monitoring the structural integrity of adhesively bonded stiffeners for aerospace applications. The methodology presented was applied to two datasets; one experimental and one computationally modelled.

Ultrasonic Lamb waves were excited at three different frequencies from five excitation sites on two stiffened panels; one panel with no defects and one with an intentional disbonded region. The response at 825 candidate sensing locations was measured using a 3D scanning laser vibrometer enabling both the in-plane and out-of-plane components of the wave to be measured.

A cross-correlation coefficient was calculated for each candidate sensing location for the out-of-plane component of the lamb wave and used as a metric for comparing the received waveforms. A statistical technique was applied to create a fitness surface which was then interrogated using a genetic algorithm to produce optimal sensor locations for different sensor network sizes.

It was found that the excitation frequency had a significant influence on the placement of the sensors and also the performance of the sensor network with higher frequencies offering the best performance. The benefits and drawbacks of using higher excitation frequencies were discussed for use in an in-service damage detection system.

All three components of the Lamb wave were considered using a three component cross-correlation coefficient magnitude technique. It was found that it was possible to achieve performance gains by considering all three components of the wave. The complications of measuring all three components on a real sensor network were discussed.

The experimental setup was simulated using a LISA model. The data was used to locate the optimal sensor locations on the structure using the same optimisation technique. It was found that the sensor networks generated were not as effective as the experimental study. Factors such as noise and the constraints of the model were discussed as potential reasons for this result.

The optimal locations for the all excitation frequencies and sites based on the out-of-plane component of the wave were presented for both the experimental and computational datasets. There were many similarities in locations on the structure where sensors were placed. It was found that the presence of PTFE tape remaining in the disbonded region on the experimental setup may have influenced some of the sensor positioning results. It was concluded that this was the most probable cause for some of the differences in sensor locations for the two datasets. The drawback of not being able to model the adhesive layer was also discussed.

The use of LISA as a design tool was demonstrated, showing great potential for modelling Lamb wave interaction with several different damage scenarios. The potential to treat problems such as the one presented as a symmetrical problem which may be useful for improving the computational efficiency should be considered. This would have many benefits to the design of aerostructures and SHM sensor networks as well and enable a more thorough optimisation study to be conducted.

The results suggested that a three sensor network would be suitable for successfully detecting damage for the structure and damage scenario presented whilst delivering an acceptable level of sensitivity. Other considerations in the design of an active SHM system still required to be considered include power and mass constraints. Therefore this optimisation methodology should not be considered a design solution but more of a design tool for assessing sensor network performance.

This study has presented an in-depth investigation into the optimisation of sensor locations based on experimental and computationally modelled data. It has been demonstrated that genetic algorithms have the ability to produce optimal solutions efficiently and the ability to model damage scenarios has many benefits for optimal sensor network design.

6. Damage detection in a composite wind turbine blade using 3D scanning laser vibrometry

6.1. Introduction

Impact damage is regarded as one of the most prominent sources of damage to aircraft and can occur both in-flight and whilst on the ground. Impact damage can be caused by a number of sources. The primary source of impact damage, according to a study at the University of California at San Diego, is impacts on the ground from ground service equipment (GSE) [218]. This includes refuelling vehicles, air stairs, baggage trolleys and cargo loaders. This type of impact can typically result in high amounts of damage due to the large mass of GSEs. As such, impact damage caused by GSEs has been historically the largest source of impact damage and this is expected to continue to be the case [219].

Another source of impact damage is foreign object damage (FOD) at airports which can cause catastrophic damage to aircraft. It is predicated that the extent of FOD costs the aerospace industry around $4 billion a year [220]. Though this value considers damage to other components of the aircraft (such as FOD to engines and landing gear), FOD in the case of impact damage is a major source of damage to aircraft structures. An example of this impact damage is presented in Figure 58 which shows damage caused by a lost access panel impacting the fuselage of an Airbus A330. The presence of the damage is not immediately apparent from the outside resulting in the extent of the damage not being realised until an internal inspection is conducted.

Figure 58. FOD caused by a lost access panel to an Airbus A330. Not that the extent of the damage is not apparent when viewed from the outside (reproduced from Kim [221]).

Sources of damage from impacts can also be the result of what are classed as 'high velocity impacts'. These impacts are usually in excess of 1000J of energy and occur when the aircraft is in flight and hence, the aircraft's relative speed to the object increases the impact energy. Commonly this type of damage is the result of hail impacts although it can also be attributed to impact with other bodies such as birds (or projectiles in the case of military aircraft). This type of impact can cause significant structural damage.

Alternatively impacts can be defined as ‘low velocity impacts’. This source of damage can be caused by hail (while the aircraft is stationary), insect impact and small stones while the aircraft is in operation. Damage can also occur while the aircraft is in maintenance. The common example of this is a tool being dropped onto the structure by a maintenance technician. The result of such impacts is usually barely visible impact damage (BVID). As the name suggests, the damage is not instantly identifiable by visual inspection alone.

Although impact damage threatens the structural integrity of metallic structures, it poses a more significant threat to composite structures [222]. When an impact occurs in a composite material it can result in the cracking of the brittle matrix while the fibres remain intact. This results in a delamination. In more severe cases, as demonstrated in Figure 58, the instantaneous bending load can result in matrix cracking and fibre breakages on the opposing side of the structure leaving the structure to appear visibly intact from the outside. If undetected, this damage can result in catastrophic failure of the structure.

One example of this catastrophic failure due to undetected impact damage is the case of the Delta II rocket explosion in 1997 which is presented by Gunn [223]. The Delta II rocket was used in this instance for the launch of a GPS satellite. After 12.5 seconds of flight, the graphite-epoxy rocket motor failed causing in excess of \$22 million in damage and the loss of a \$40 million satellite as well as creating numerous safety and environmental issues. On studying the photographic and video footage of the launch it was concluded by the air accident investigation board that the failure of the pressure vessel was consistent with a crack resulting from impact damage that occurred sometime after the proof pressure test had been conducted. However, the root cause of the impact damage was never discovered.

Composite wind turbine blades experience similar damage cases to that of aerospace structures. As such, conducting Lamb wave damage interaction studies on wind turbine blades can be beneficial for developing optimal sensor networks on composite aerospace components. Using the information from wind turbines which currently have sensor networks, a study was conducted on composite wind turbine blades. This showed that 51% of blade damage was attributed to manufacturing defects whereas 49% of damage was as a result of in-service operation. Of all damage events, 16% are attributed to foreign object damage while the turbine blade is in-service (with lightning strikes (20%) and the tips deflecting causing them to hit the tower (13%) making up the rest of the 49%)[123]. In optimum wind conditions, large wind turbine blade tips can move through the air at relative speeds of up to 320 km/h (200 mph)[224] making impacts from even small objects significant. Damage to both the leading edge and blade surface (from rain, hail, ice, sand, salt, UV rays and insects)[225] is detrimental to aerodynamic efficiency and as a result power generation is compromised. Serious structural damage can also be caused by lightning and bird strikes. A detailed discussion of turbine blade damage is presented in a study conducted at Risø National Laboratory [226].

Small impacts can create BVID which, if allowed to grow under aerodynamic loading, could necessitate significant repair works or result in catastrophic failure of the blade structure. The level of damage which can be seen easily depends on many factors such as the colour of the structure, illumination and angle of viewing [25] although it has been suggested that BVID usually lies within the range of 0.25 - 0.5 mm deep [227] however it has also been stated that BVID lies within the range of 1.27mm – 2.54mm deep [228]. Non-destructive testing (NDT) methods are therefore needed to detect this damage, with the process often requiring blade removal. Maintaining the structural performance of the blades is therefore vital to the turbine's efficiency [229]. Like aircraft structural components, wind turbine blades are also subjected to aerodynamic loading making them a suitable component as the subject for this investigation.

This chapter presents the results of an experimental study into the interaction of Lamb waves with impact damage on a composite wind turbine blade using 3D scanning laser vibrometry. Visualisations of both the out-of-plane and in-plane components, and the magnitude of all three components of the Lamb wave interaction with impact on a real structure are presented. Results showing Lamb wave interaction along with post-processing of the vibrometry data using RMS baseline subtraction techniques are presented and discussed. Novelty is found within this study with the consideration of both Lamb wave components (particularly the in-plane) and the visual and signal processing methods used to present the interaction with the impact damage. This advances understanding of the interaction of the different fundamental Lamb modes as well as highlighting areas suitable for the placement of sensors for an acousto-ultrasonic system. The results are further compared to surface profilometry and white light interferometry measurements of the impact site. The extent of the impact damage is considered to be 'barely visible'. The surface measurements are shown to correlate with the interaction of the Lamb waves shown in the laser vibrometry results, demonstrating the sensitivity of Lamb wave-based SHM systems to detect impact damage.

6.2. Experimental study

A commercial 1.8m composite wind turbine blade constructed from a short glass fibre chopped strand mat with a black epoxy matrix was used for this study, as shown in Figure 59.

The placement of the fibres was random and hence the direction of the fibre placement was inhomogeneous (N.B. this is not in reference to the material properties being inhomogeneous). The structure of the blade was hollow, made from two 3mm thick matched halves bonded together.

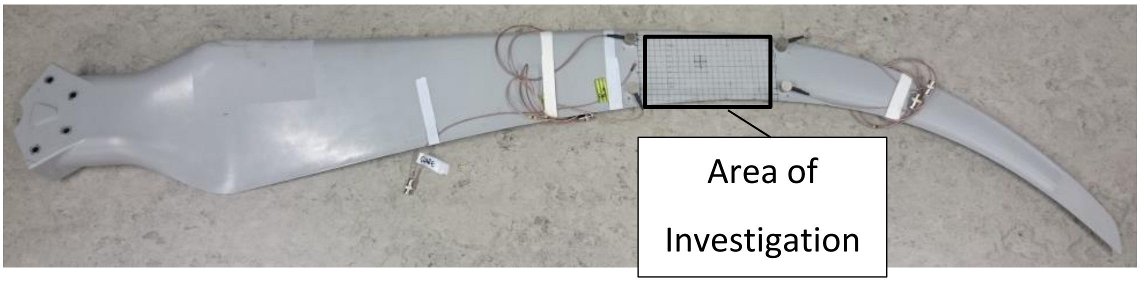

Figure 59. Composite wind turbine blade used throughout the experiments, demonstrating the location of the area of investigation.

An area of investigation of dimensions 50mm x 120mm was located on the low pressure face 1.17m from the root of the blade as shown in Figure 60.

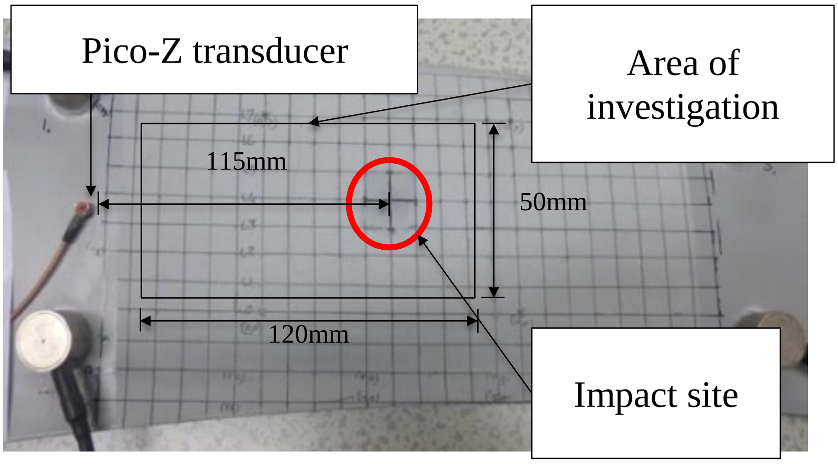

Figure 60. Dimensions of the area of investigation and location of the impact

6.2.1. Lamb wave excitation and 3D scanning laser vibrometer setup

A commercially available PANCOM Pico-Z transducer (200kHz – 500kHz) was acoustically coupled to the blade using Loctite® Ethyl-2-Cyanoacrylate, at a distance of 115mm from the impact site. This was sufficient distance to ensure that that the Lamb waves had fully formed before interacting with the impact damage [37].

Three transducer excitation frequencies 100kHz, 200kHz and 300kHz were selected to investigate the sensitivity of different wavelengths to the presence of impact damage. Although 100kHz lies outside of the published operating resonance of the transducer it has been shown to produce useful results in previous studies [126, 214, 230]. Due to the maximum sampling frequency of the vibrometer being 2.56MHz, frequencies above 300kHz were not considered due to insufficient temporal resolution.

A 150V, 5-cycle sine burst was generated by the MGL software and hardware previously used (section 4.3) with the same repetitive rates and reference signals. A Polytec PSV-500-3D-M Scanning Vibrometer was once again used for this study. The area of investigation, which was coated with retroreflective glass beads, comprised of 2514 measurement points which gave sufficient spatial resolution for wave reconstruction. The vibrometer parameters were as previously used (section 4.3).

A purpose built steel stanchion was used to support the turbine blade while the laser vibrometry measurements were taken. This allowed the blade to be removed for impacting and replaced in the same position relative to the laser heads.

6.3.Impact damage

The blade was secured at its base to a steel stanchion and supported on both sides of the area of investigation. The blade was impacted using a 20mm radius impactor with an impact energy of 10 J in an INSTRON dynatup 9250HV impact test machine. The impact caused BVID on the surface as shown in Figure 61. The impact was representative of a hail stone impact.

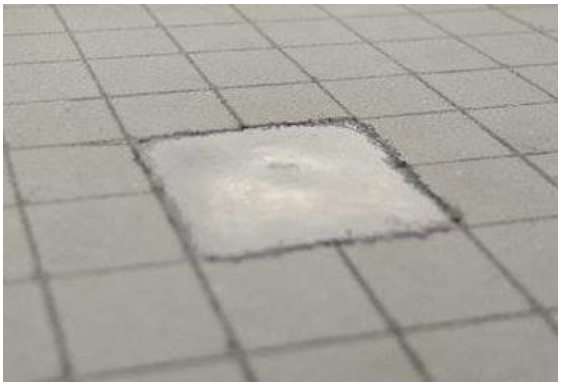

Figure 61. BVID on the turbine blade after being impacted. The retro-reflective beads have been removed around the impact site for clarity.

6.4.Laser vibrometry results and discussion

For each set of results, a 0µs datum point was taken at the point when the S_0 mode reached the measurement field. A selection of images are presented which illustrate the propagation of the Lamb waves through the area of investigation. For consistency, the time windows for each excitation frequency have been kept the same. As wave velocity increases with frequency due to dispersion, fewer images are presented for the higher frequency excitations. For each set of post-impact measurements, the white dashed line denotes the impact site.

6.4.1. 100kHz Results

The results of the resultant magnitudes (the magnitude calculated from the three components measured by the vibrometer) from the pre and post impact scans are shown in Figure 62.

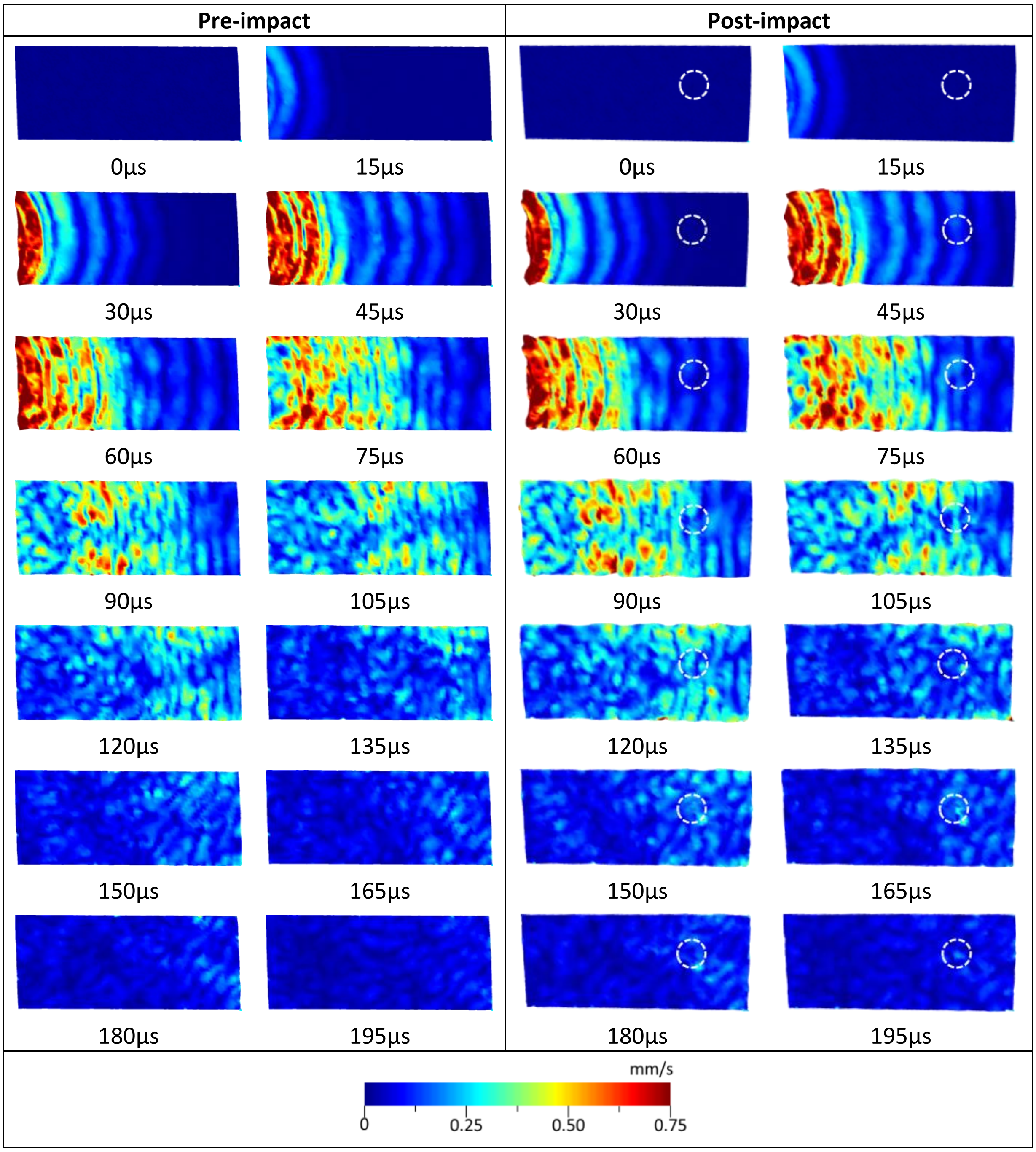

Figure 62. Resultant magnitudes from of the 100kHz excitation vibrometry scan of the blade pre and post-impact

Studying the pre-impact results, it is apparent that the S_0 mode propagates away from the source and appears either not to reflect off the edges of the turbine blade or has dissipated by that point, or by the time any reflections have reached the area of investigation.

The A_0 mode however appears to be significantly disrupted as it propagates through the area of investigation. There are two possible explanations for this. The first is that the edge reflections interact with the propagating wave. However it is also likely that the scattering of the A_0 mode observed is the result of the fibre distribution in the material. The random distribution of the fibres results in a inhomogeneous microstructure [231]. This could be causing scattering of the Lamb waves resulting in a high level of noise in the propagating wave [232]. This is observed from 90µs onwards.

Comparing the two sets of results pre and post impacts, the S_0 mode appears to be mostly unaffected by the presence of the impact damage. This concurs with the findings of Grigg *et al.*[126]. The A_0 Lamb mode does appear however to be affected by the presence of the impact damage. This can be seen in the results at 90µs - 120µs although it is not very clear when the resultant magnitude is plotted.

As the A_0 Lamb mode is mostly out-of-plane, this component was isolated and plotted separately for clarity as shown in Figure 63. It is evident that the out-of-plane component of the Lamb wave interacts with the damage causing a disruption in the wave front. This suggests that the unintelligibility of the interaction of the A_0 mode with the damage in the resultant magnitude plots in Figure 62 is mostly caused by noise from the in-plane components.

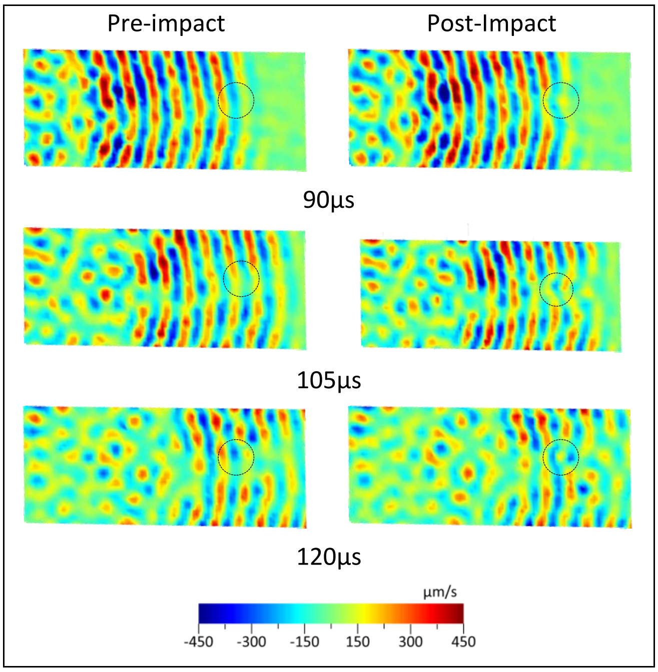

Figure 63. 100kHz excitation out-of-plane component highlighting the Lamb wave interaction with the impact damage

6.4.2. 200kHz Results

The resultant magnitudes from the pre and post impact scans for the 200kHz excitation are shown in Figure 64.

Comparing these results to those from the 100kHz excitation there is an increase in the amplitude of the measured Lamb wave. This can be attributed to 200kHz being inside the transducer's operating resonance.

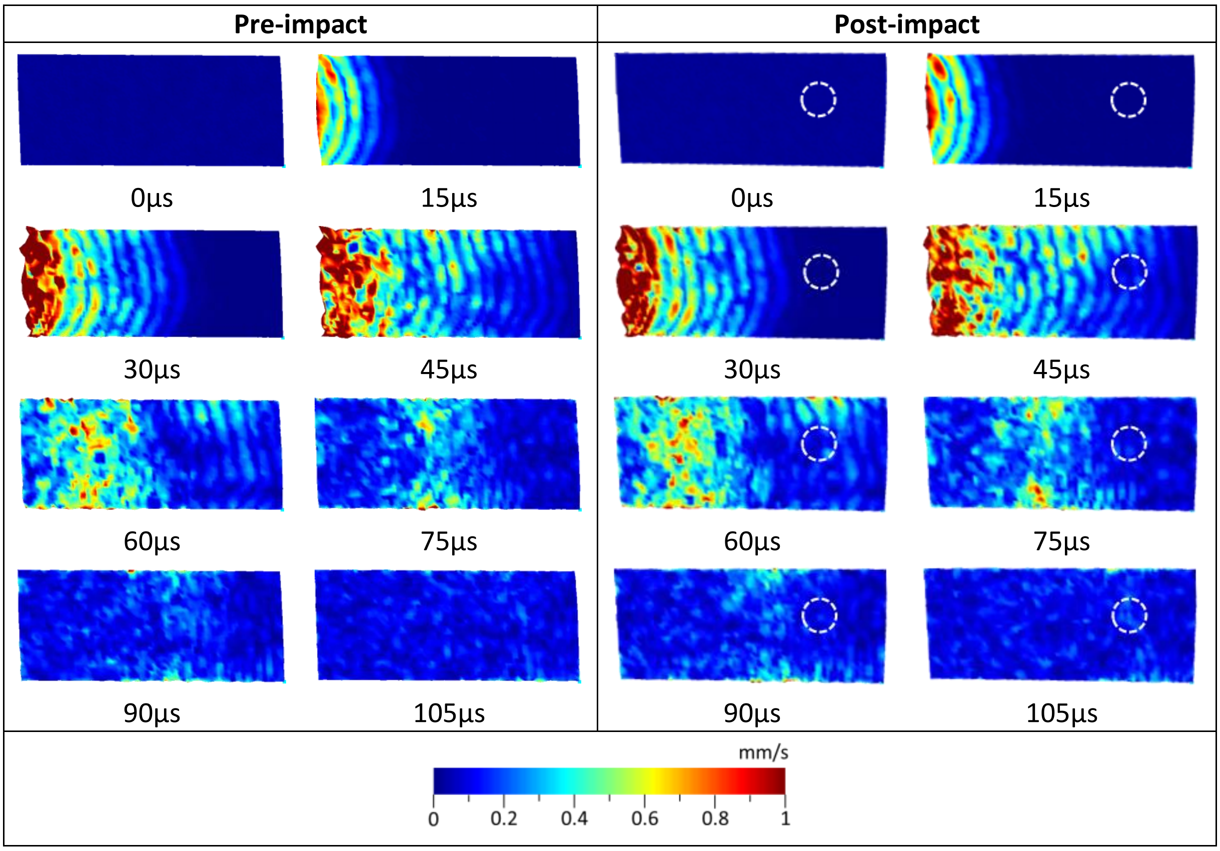

Figure 64. Resultant magnitude results of the 200kHz excitation vibrometry scan of the blade pre and post-impact

As with the results from the 100kHz excitation, the S_0 mode appears to be unaffected by the presence of the impact damage in the resultant magnitude results. Comparing the S_0 propagation in both the pre and post impact results at 45μs it is not possible to distinguish the presence of damage by visual observation alone especially as there appears to be no disruption in the wave front to the right of the impact damage as observed with the A_0 mode in Figure 63.

The effects of attenuation and dispersion of higher frequency waves, coupled with high levels of noise, results in a highly disrupted, low amplitude A_0 wave front by the time the mode reaches the impact site as shown at 90μs. As with the 100kHz results, this makes it difficult to determine whether the Lamb wave has interacted with the damage through means of visual observation alone.

To verify the Lamb wave interaction, the out-of-plane component was again isolated and plotted separately as shown in Figure 65.

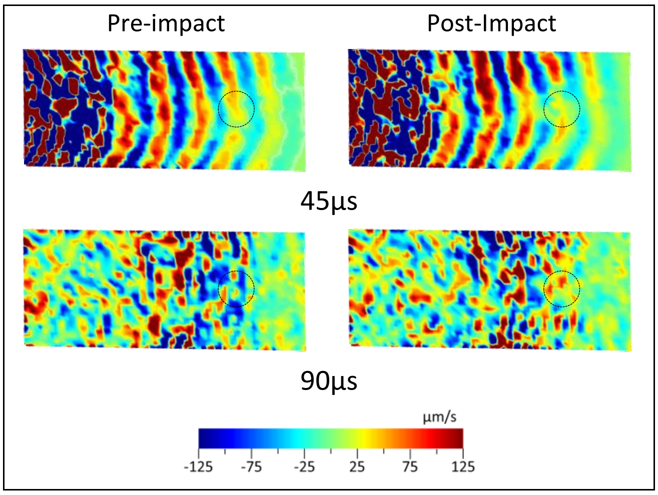

Figure 65. 200kHz excitation out-of-plane component highlighting the Lamb wave interaction with the impact damage

The results at 45µs in Figure 65 show that there is possibly some interaction with the S_0 mode with the post-impact results indicating a significantly lower amplitude than the pre-impact results due to the presence of the impact damage. This can be justified by the shorter wavelength of the 200kHz excitation S_0 mode compared to that of the 100kHz excitation. However, there appears to be no disruption of the wave front to the right of the impact site which also suggests that there is limited interaction with the impact damage. It is therefore not possible to conclusively determine the presence of the damage using the S_0 mode from the 200kHz excitation by visual observation alone.

It is difficult to determine from these results whether the A_0 mode is influenced by the presence of the damage as demonstrated at 90µs. It is apparent there is a difference in the results and it could be argued that the reduction in amplitude in the post-impact results was due to the presence of the damage. However, due to the high levels of disturbance in the wave front this is also by no means conclusive.

6.4.3. 300kHz results

The resultant magnitudes for the pre and post impact 300kHz excitation are shown Figure 66.

The increased wave velocity due to dispersion is apparent when compared to the results of the 100kHz excitation. As with the two other excitation frequencies, the S_0 mode in the resultant magnitude results appears to be mostly unaffected by the impact damage. However, by the time the S_0 mode interacts with the impact damage, the amplitude has significantly reduced.

The increased attenuation of the higher frequency excitation is apparent in this results set. The A_0 mode is measured in the area of investigation with a peak amplitude of 1mm/s. At 45μs the amplitude of the wave has significantly decreased. This decrease in amplitude with the added effects of edge reflections and scattering due to the microstructure makes it almost impossible to determine Lamb wave interaction just from studying the resultant magnitude time-domain results alone. In turn, adjusting the colour scale to study the low amplitude Lamb wave activity does not help to clarify the results.

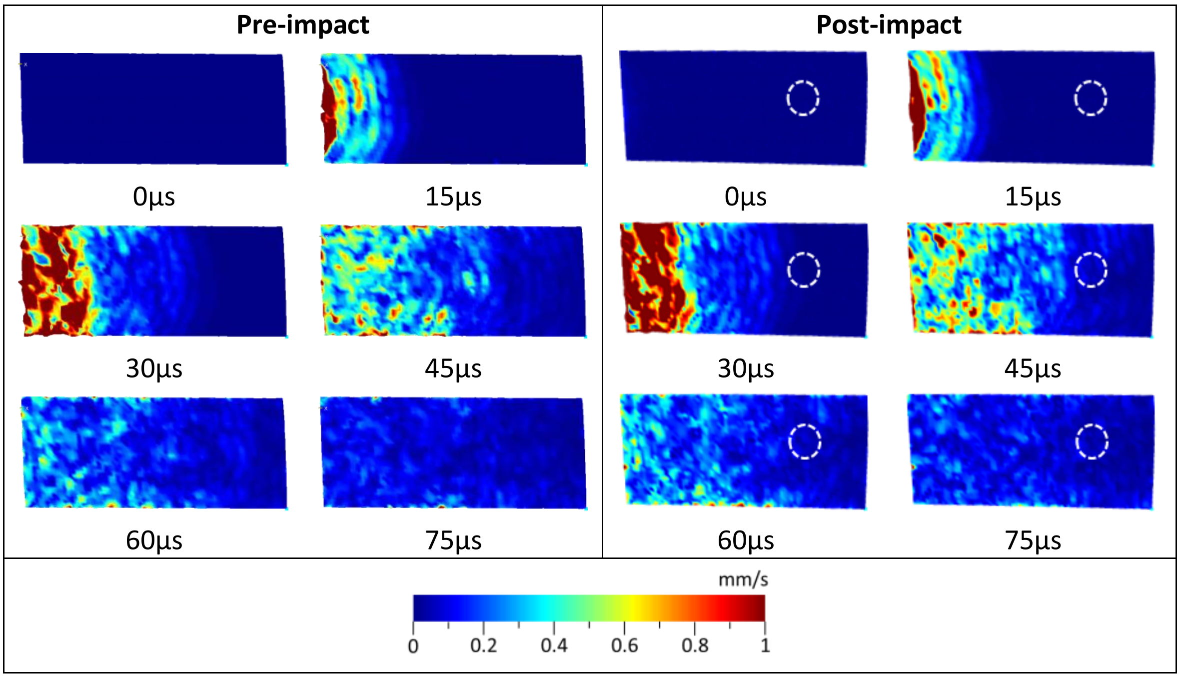

Figure 66. Resultant magnitude results of the 300kHz excitation vibrometry scan of the blade pre and post-impact

As with the results from the previous two excitation frequencies, the out-of-plane mode was isolated and is presented in Figure 67.

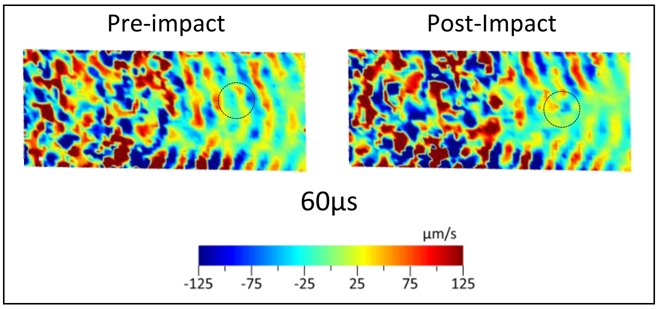

Figure 67. 300kHz excitation out-of-plane component highlighting the Lamb wave interaction with the impact damage

As with the 200kHz excitation, the S_0 mode interacts with the damage as shown at 60μs in Figure 67. This is shown in the post-impact results by a fringe of low amplitude to the right of the impact damage. However, as was also the case with the 200kHz excitation, due to the high levels of disturbance in the wave it is not possible to determine whether the A_0 mode interacts with the damage.

The clarity of the wave propagation may be improved upon by increasing the number of scan points, hence increasing the spatial resolution for the higher frequency excitations. However, for comparability between excitation frequencies and due to constraints on acquisition time this was not changed during this study.

6.5.Root-mean squared baseline subtraction

From the time domain results presented in the previous sections, it is apparent that the A_0 Lamb mode does interact with the damage although it is difficult to identify the presence of damage on the structure without carefully examining the results. It would therefore be advantageous to identify the presence of the BVID and quantify it using comparative post processing methods. A computationally inexpensive post-processing technique is baseline subtraction. Subtracting the waveforms of the out-of-plane component of the post-impact dataset from the waveforms of out-of-plane component from the pre-impact dataset identifies the region on the scan area where there is a significant change. By calculating the root-mean squared (RMS) velocity values for the resulting subtracted waveforms for each measurement point over the whole measurement period, the region of significant change in the waveform, and hence the location of the damage can be identified. The RMS baseline subtraction analysis for the out-of-plane component of the Lamb wave is presented in Figure 68. Only the out-of-plane component has been considered as it was shown to significantly interact with the damage. The impact site is denoted by the dashed circle.

For each excitation frequency the impact site is seen to be clearly identified using this technique although the peak RMS values for the 100kHz excitation are greater than those for the 200kHz and 300kHz excitations because of the lower attenuation of the lower frequency. The RMS values for the area of the plate outside the impact site are not zero (demonstrated by the threshold set on the lower end of the colour bar) because of small differences in experimental setup between the pre and post impact vibrometry scans resulting in a small phase difference which when subtracted results in low amplitude signals being produced. In addition to this, low amplitude reflections result due to Lamb wave interaction with the damage and hence cause an additional change in signal.

The size of the area influenced by the defect appears to vary depending on excitation frequency. Using the Polytec PSV software, it was possible to measure the size of the area of peak RMS. From taking four measurements across the peak (0°, 45°, 90°, 135°) for each excitation frequency the average length of the area affected by the presence of the damage was found to be 12.6mm, 7.8mm and 14.9mm, for the 100kHz, 200kHz and 300kHz results respectively. Surprisingly the average length of the area affected by the presence of the damage while reducing between 100kHz and 200kHz increases from the 200kHz excitation results to the 300kHz excitation results whereas it was expected that a reduction in wavelength should increase be more sensitivity to the impact damage. This cause of this may be the result of the smaller wavelength of the 300kHz excitation having higher fidelity and hence interacting with damage smaller aspects of the damage.

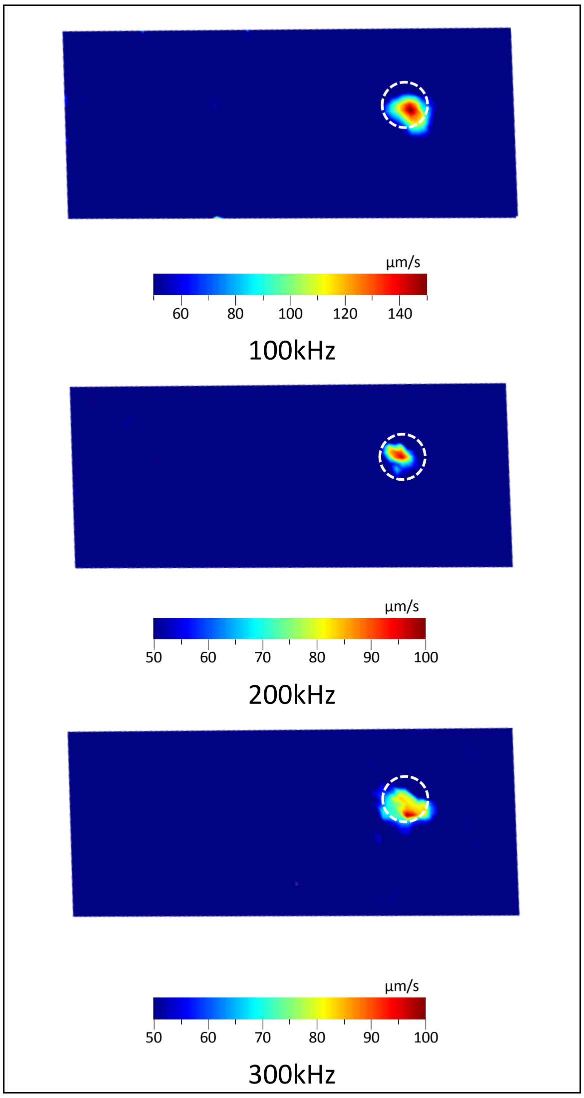

Figure 68. RMS baseline subtraction analysis of the out-of-plane component of the Lamb modes

6.6.Out-of-plane cross-correlation

Calculating the cross-correlation coefficient of two waveforms has previously been used in acousto-ultrasonic studies as method of quantitatively comparing two waveforms [106]. A value of unity for the cross-correlation coefficient indicates no change in the waveforms. By comparing the measured signals pre and post-impact an indication may be obtained of where the wave has interacted with the damage. Results from a cross-correlation analysis for the out-of-plane component of the Lamb wave are presented in Figure 69. The impact site is denoted by the dashed line.

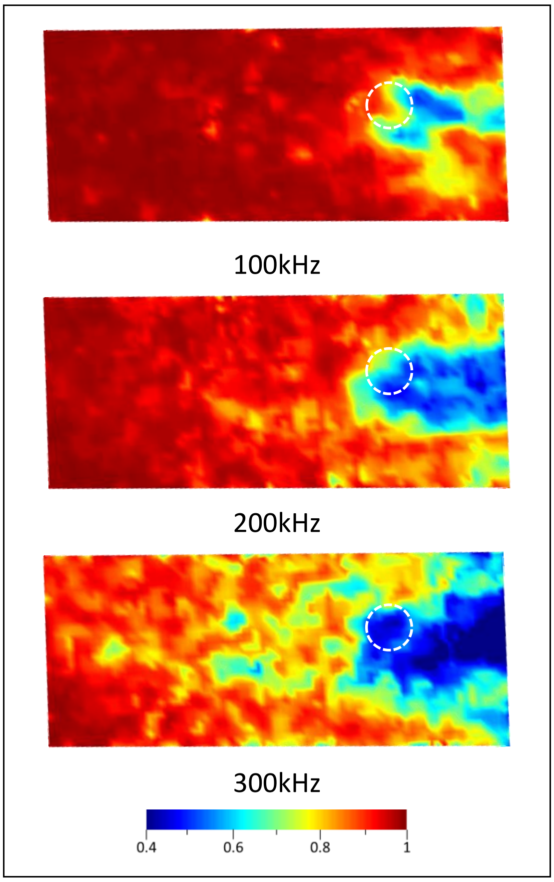

Figure 69. Out-of-plane cross-correlation coefficient results

It is evident that the Lamb wave interaction with the impact damage significantly alters the waveform when compared to the pre-impact waveforms.

The results from the 100kHz excitation show that there is little change in the waveform in-front (left hand side of Figure 69) of the impact damage. There is however a significant, localised reduction in correlation downstream (right) of the impact damage. There is an increased area of lower correlation behind the impact damage in the results from the 200kHz excitation. In addition to this, there is also a minor reduction in correlation in front of the impact damage. The 300kHz results show a further increase in the area of lower correlation behind the impact damage when compared to the 200kHz results as well as reduced correlation in front.

The increased area of lower correlation demonstrates that higher frequency Lamb waves are more sensitive to interaction with damage due to their smaller wavelength. At the higher frequencies there is also a reduction in correlation in front of the impact damage. This is most likely to be due to reflections from the damage.

Previous studies that have used the cross-correlation technique have shown less difference in signals quantified by a smaller reduction in cross-correlation coefficient [126, 233]. It is worth noting however that previous studies used sensors physically coupled to the structure that have a mass-dampening effect as well as a transfer function. In addition to this, cross-correlation coefficients have not been previously calculated at the impact site.

6.7.In-plane cross-correlation

Considering the in-plane components of the wave it is also possible to conduct a cross-correlation analysis to investigate how the in-plane components are affected by the presence of the impact damage. This is achieved by calculating the respective cross-correlation coefficients for both of the in-plane components. The resultant magnitude of the two cross-correlation coefficients is then calculated. The theoretical maximum for the cross-correlation is therefore √2 to normalise them. In order to make the results comparable to the out-of-plane results, the cross-correlation coefficients are divided through by √2. The results of this analysis are presented in Figure 70. The dashed line denotes the impact site.

It is apparent in these results that the propagation of the in-plane component of the Lamb wave is affected by the presence of the impact damage. The 100kHz results clearly indicate a difference in the two Lamb wave signals at the site of the impact damage. Comparing this with the out-of-plane results it is evident that there is less reduction in cross-correlation coefficient in this region.

Unlike for the out-of-plane results, there is a significant reduction in the in-plane cross-correlation coefficient over a much larger region of the area of investigation. This can be justified by considering the scattering of the in plane modes due to the microstructure. It was demonstrated earlier by comparing the resultant magnitude plots with the out-of-plane plots for the 100kHz excitation that a significant level of noise could be attributed to the in-plane components due to the random placement of the chopped fibres. In fibre composite materials the in-plane Lamb wave components are influenced by the fibre direction[126] therefore inhomogeneity of the fibre directions will have a more significant influence on the noise in the in-plane components than the out-of-plane.

The results from the 200kHz excitation identify a region of reduced cross-correlation coefficient surrounding the impact site. This region is larger than for the 100kHz excitation and is similar to that observed in the out-of-plane results. This can be attributed to the shorter wavelength of the higher frequency excitation. Like the 100kHz excitation, there is a region of reduced cross-correlation coefficient upstream of the impact site. This suggests that the in-plane component of the Lamb wave is partially reflected by the presence of the impact damage which is not detected by examining the time-domain plots alone.

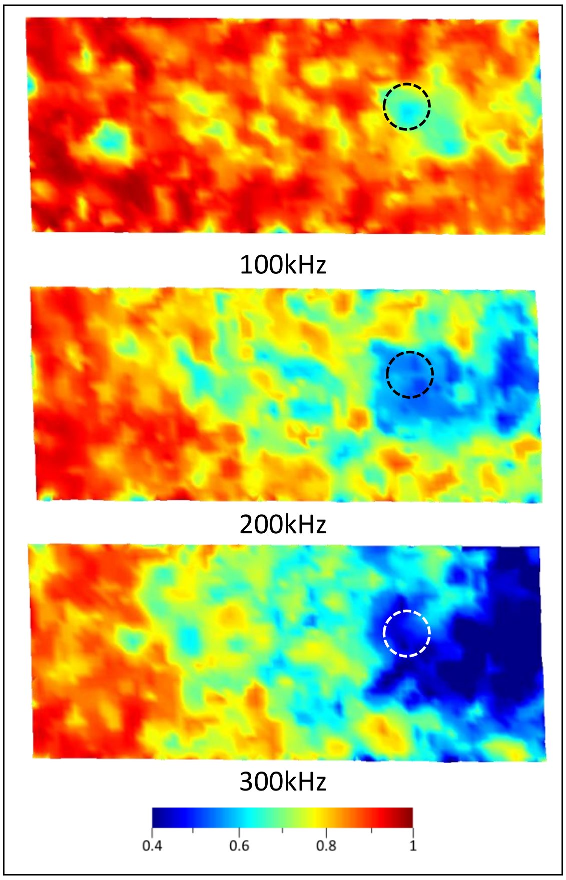
100kHz

200kHz

300kHz

Figure 70. In-plane cross-correlation coefficient results

The results from the 300kHz excitation show a large region of the area of investigation where there is a significant reduction in the cross-correlation coefficient. As for the 200kHz excitation, there is a larger area of reduced cross-correlation coefficient to the left of the impact site than is that observed for the out-of-plane results. This would suggest that more of the in-plane components were reflected by the presence of the impact damage than the out-of-plane components.

It is worth noting that this analysis does not indicate that the S_0 mode interacts with the damage as the whole signal length is considered. Though the A_0 is mostly out-of-plane due to Poisson’s ratio, it will have a small in-plane component which may be causing the reduction in correlation. It is also possible that interaction with the impact damage has caused a mode conversion resulting in the A_0 mode being converted into an S_0 mode, and hence a reduction in in-plane correlation. The results from this analysis however do demonstrate that it is possible to detect Lamb wave interaction with impact damage using in-plane methods of sensing.

6.8. Three-component magnitude cross-correlation

Considering all three components of the Lamb wave, it was possible to perform a 'three-component' cross-correlation analysis. As with the in-plane analysis, the resultant magnitude of the cross-correlation coefficients are calculated and divided through by √3 to make the results comparable. The results of the three-component cross correlation analysis are presented in Figure 71. The dashed line denotes the impact site.

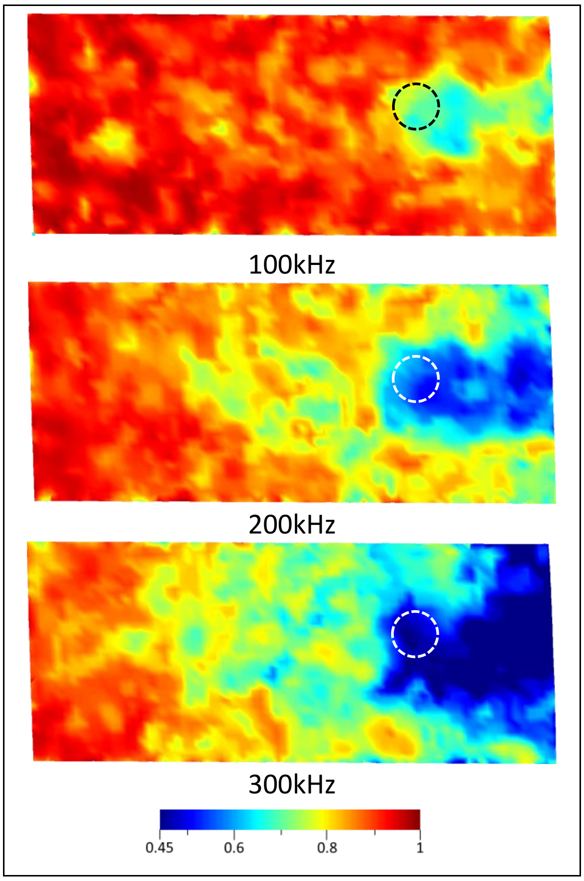

Figure 71. Three component cross-correlation coefficient results

The results from the three-component magnitude plots demonstrates that there is conformity between the in-plane and out-of-plane components as it is demonstrated that the reduction in cross-correlation coefficient surrounds the impact site.

The plots highlight the regions within the area of investigation where the waveform has been disrupted by the presence of the impact damage. This is significant for planning sensor placements to maximise the probability of damage detection. Though the higher frequency excitations are in general shown to be more interactive with the damage, Lamb wave attenuation would also have to be included. Thus, a trade-off between probability of detection and size of sensor network would be needed for the design of a sensor network.

6.9.Moving window cross-correlation

The cross-correlation plots presented in Figure 69, Figure 70 and Figure 71 consider the entire sample length of each measurement point when calculating the cross-correlation coefficients. Although this has been shown to highlight regions where the Lamb wave interacts with the damage as well as highlighting areas suitable for sensor placement, windowing the time domain signal may further improve the visualisation. By windowing the signal a higher level of sensitivity to the damage may also be achieved as effects such as edge reflections and scattering due to the microstructure will have less of an influence on the cross-correlation coefficient.

To calculate the windowed cross-correlation coefficients, the time signals for each excitation frequency for each measurement point of the vibrometry scans were considered. These signals were windowed using 15µs windows which were cross-correlated with their respective pre and post impact datasets. The length of the time window gave a sufficient period of time for the advancements of the wave front to be observed while also giving sufficient length of waveform to enable the cross-correlation analysis to be conducted. The same 0µs datum point was used as the time domain plots. In addition, two 15µs time window plots prior to this point were also plotted. Only the out-of-plane component of the wave was considered to demonstrate the technique.

6.9.1. 100kHz Results

The results for the 100kHz moving window cross-correlation coefficient plots are presented in Figure 72. In the -30µs - -15µs time window, the entire plot shows a low cross-correlation coefficient. This is due to no regular signal having arrived within the area of investigation by this point. Hence, only low amplitude random noise is present which results in low cross-correlation coefficients. This was also observed on the study on the stiffened panel (see section 4.5.1).

As the time progresses to the -15µs - 0µs an increased region of cross-correlation coefficient is observed on the left boundary of the area of investigation. This is the arrival of the first, very low amplitude S_0 wave. The amplitude of this was so low that it was not visible in the time domain plots and hence it was omitted. However, this low amplitude wave is regular and consistent within the two datasets. This regularity results in a region of high cross-correlation coefficient and demonstrates the ability of the cross-correlation technique in identifying statistical similarity even with low amplitude waves.

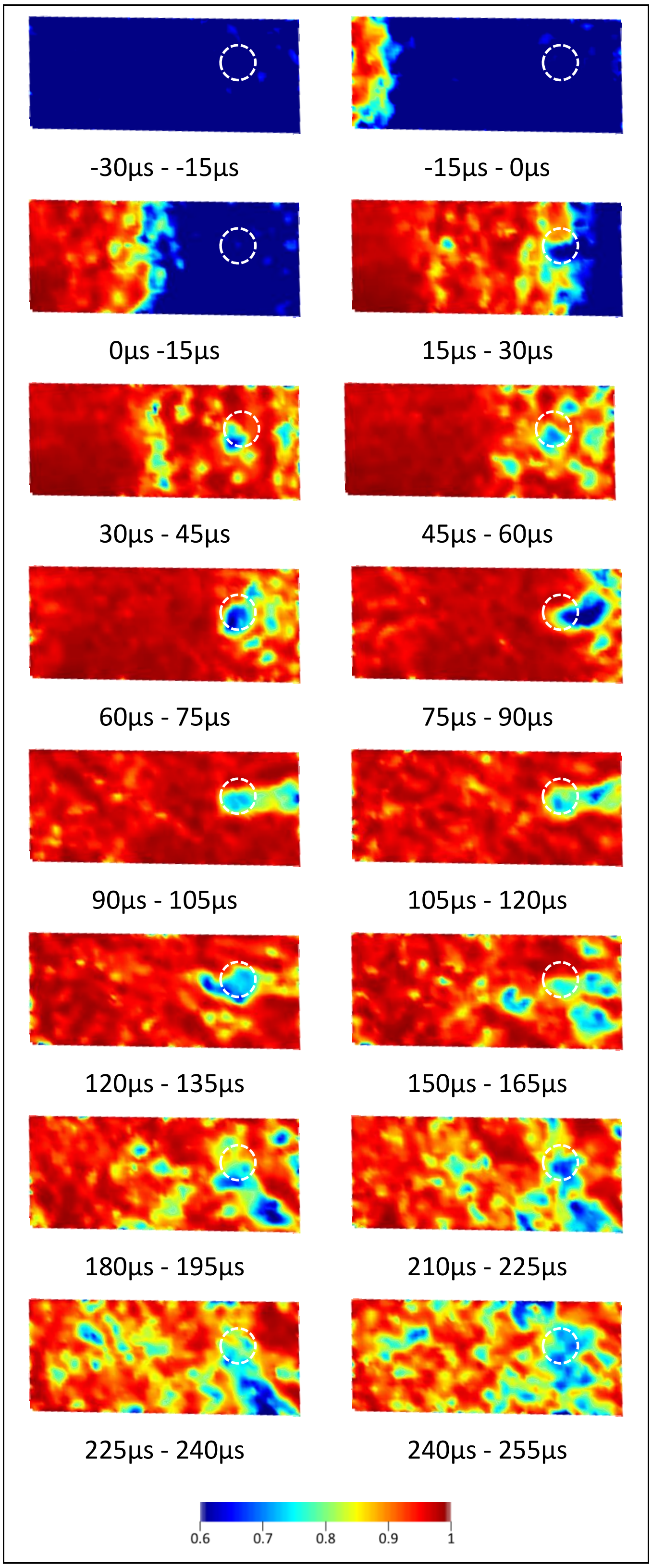

Figure 72. 100kHz out-of-plane moving window cross-correlation coefficient plots (the impact site is denoted by the white dashed line)

The 0µs - 15µs window shows the S_0 mode being sensed within the area of investigation and in the 15µs - 30µs time window, the interaction of S_0 becomes apparent. Within this window there is a significant disruption in the wave front of increased cross-correlation coefficient which can be attributed to the presence of the damage. However it is also worth noting that, as previously discussed, the S_0 mode is more prone to noise due to scattering of the Lamb wave within the microstructure. This is further exacerbated as the S_0 mode is comprised of in-plane wave components and therefore the out-of-plane amplitude of the S_0 mode is low. Because of this, and the sensitivity range of the vibrometer used, the S_0 mode is has a much lower signal-to-noise ratio (as it is closer to the noise floor). This is demonstrated by the spots of low cross-correlation coefficient on the plots of these two time windows which is particularly prominent at the front of the region of increased cross-correlation coefficient in the 0µs - 15µs time window.

The arrival of the A_0 mode is also apparent in the 0µs - 15µs time window. This is shown by a region of increased cross-correlation coefficient (dark red) to the left of the plot. This is also consistent with the time domain plot in Figure 62. The increased values of cross-correlation coefficient can be attributed to the A_0 mode being comprised of out-of-plane wave components and hence less affected by background noise.

In the 30µs - 45µs and 45µs - 60µs time windows a prominent region of low cross-correlation coefficient is observed at the impact site. This indicates that the S_0 mode of the 100kHz wave does interact with the impact damage. It could also be inferred that the spots of low cross-correlation coefficients surrounding the impact site in these plots may be a result of the wave interaction with the impact damage. However, as this is at a significant distance from the source, the wave here is subject to the effects of scattering and attenuation (hence, a reduction in amplitude leading to a lower signal-to-noise ratio). As such, this is by no means conclusive.

The 60µs - 75µs time window shows the instance just before the A_0 mode interacts with the impact damage. In this time window, low cross-correlation coefficients are observed in the region of the impact site with spots of low cross-correlation to the right of the site. The low cross-correlation coefficient to the left of the site is not present in this time window unlike in the previous window. This is likely to be due to the attenuation of the S_0 mode that was causing the low cross-correlation as well as the arrival of the more dominant, higher amplitude, out-of-plane A_0 mode.

The 75µs - 90µs, 90µs – 105µs and 105µs - 120µs time windows show the reduction in cross-correlation coefficient as a result of the Lamb wave interaction with the impact damage. In these plots it is evident that only the region directly behind the impact damage is affected with minimal areas of reduced cross-correlation coefficient elsewhere. This demonstrates that the location of sensors for detecting this type of damage in an AU system is an important consideration. This correlates well with the out-of-plane time domain plots presented in Figure 63 that show a significant difference in the propagation of the wave behind the impact site. Interestingly, there are no areas of reduced cross-correlation elsewhere within the plot that can be attributed to reflections from the damage. This indicates that the majority of the Lamb wave energy is transmitted through the impact site rather than being reflected.

As demonstrated by the time domain plots in Figure 62 the amplitude of the Lamb waves from 120µs onwards significantly reduces and a high amount of reflection and scattering of the waves is observed. This is also observed in the moving windowed cross-correlation plots from 120µs onwards. The 120µs - 135µs plot shows a region of reduced cross-correlation coefficient around the impact site although the area of reduced correlation behind this site that was observed in the previous three plots is less prominent.

From 150µs onwards, the patterns of cross-correlation coefficient become less organised and the location of the damage is less apparent. When this is compared with the time domain plots in Figure 62, it is evident that the Lamb waves have attenuated and thus the amplitudes of the waves are significantly lower. It is not possible to fully state whether the presence of damage caused these areas of reduced cross-correlation coefficient or whether they can be attributed to other causes such as scattering or random noise which has more of an influence due to the lower signal-to noise ratio as a result of the reduced amplitude.

1.1.1. 200kHz results

The 200kHz moving window cross-correlation coefficient plots are presented in Figure 73. As with the 100kHz results, the same 0µs datum point has been used as for the time domain plots and the two time windows prior the 0µs datum have been included for completeness.

As for the 100kHz results, the -30µs - -15µs time window shows a low correlation due to only random noise being present. In addition the arrival of the low amplitude S_0 mode is also plotted in the -15µs - 0µs time window.

Interaction of the S_0 mode is observed in the 15µs - 30µs time window plot. It is apparent that the front of the region of increased cross-correlation coefficient is disrupted by the presence of the damage especially when it is compared with the front plotted in the 0µs - 15µs time window which appears to less disrupted. When studying the time domain plots in Figure 64, this interaction is not easily identifiable by visual comparison alone.

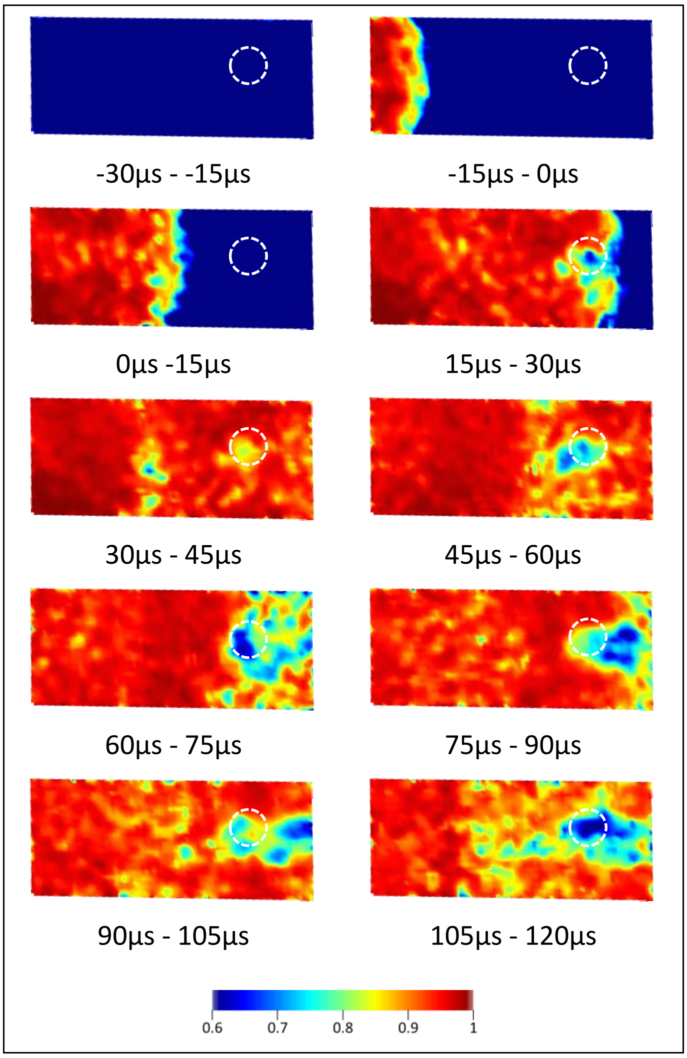

Figure 73. 200kHz out-of-plane moving window cross-correlation coefficient plots (the impact site is denoted by the white dashed line)

Considering the 30µs - 45µs time window, the reduction in the cross-correlation coefficient at the impact site is not as significant as the reduction in cross-correlation coefficient observed in the respective time window in the 100kHz results. This supports the visual comparison presented in Figure 65 that there is some interaction with the S_0 mode although it is not significant. However, the 45µs - 60µs plot shows a more significant reduction in cross-correlation coefficient at the impact site. When this is compared with the time domain plots in Figure 64 it is apparent that this is S_0 mode interaction as the A_0 is just about to arrive at the impact site by this point. However unlike the A_0 mode interaction presented in the 100kHz moving window cross-correlation plots shown in Figure 72, there is no reduction in cross-correlation coefficient to the right of the impact site although this is consistent with the 100kHz S_0 mode. It can therefore be stated that the S_0 mode is affected at the site of damage this but does not affect transmission of the wave.

The interaction with the A_0 mode is observed from the 60µs - 75µs time window onwards. In this time window, a significant reduction in cross-correlation coefficient is observed at the impact site clearly indicating that this mode interacts with the damage surrounding the impact site with are regions of low cross-correlation coefficient. This is most likely to be the result of scattering of the Lamb wave which is interacting with the propagating Lamb wave caused by the presence of the impact damage. This was not as prominent in the 100kHz moving window cross-correlation results. It is likely that the reason for this is due to the shorter wavelength of the 200kHz excitation.

During the 75µs - 90µs time window the reduction in cross-correlation coefficient is observed to the right of the impact site, in a similar way to the 100kHz results. However, the size of the region of low cross-correlation coefficient is far greater than that for the 100kHz results due to the shorter wavelength of the 200kHz excitation being more sensitive to the damage. There is also no region of low cross correlation coefficient to the left of the impact site indicating that the Lamb wave is transmitted and not reflected by its interaction with the damage. Comparing with the same respective time windows in the time domain results in Figure 66 it is evident that it is again difficult to identify this interaction by visual means alone.

A similar region of reduced cross-correlation coefficient is observed in the 90µs - 105µs window to that window of the 75µs - 90µs window with a region of reduced cross correlation coefficient to the right of the impact site. Areas with a less significant reduction in the cross-correlation coefficient are observed to the left of the impact site (yellow). This becomes more significant in the 105µs - 120µs time window. It cannot be clearly assessed whether this reduction is due to scattering from the impact damage or as a result of random noise having more influence on the low amplitude signals. Comparing these plots with the time domain plots in Figure 64 it can be inferred that the cause of this reduction in cross-correlation coefficient is likely to be the result of the scattering of the low amplitude waves which is also inhibited by the reduced signal-to-noise ratio.

6.9.2. 300kHz results

The 300kHz moving window cross-correlation coefficient plots are presented in Figure 74. As with the two previous result sets, the same 0µs datum point has been used as the time domain plots and the two time windows prior to the 0µs datum have been plotted for completeness. As observed in the 100kHz and 200kHz results the -30µ - -15µs show low cross-correlation coefficients due to random noise. An increase in coefficient is observed as the low amplitude S_0 mode enters into the area of investigation in the -15µs - 0µs time window. Likewise, a similar propagation is observed in the 0µs - 15µs time window.

Initial interaction of the S_0 mode with the impact damage is observed in the 15µs - 30µs window. A significant reduction in the front of the cross-correlation coefficient is observed at the impact site indicating the location of the damage. Some small spots of reduced cross-correlation coefficient are observed to the left of the area of investigation. Examining the respective time domain plots in Figure 67 it can be seen by visual comparison that there are some subtle differences in the time-domain waveforms plotted which is made clear by the cross-correlation plots.

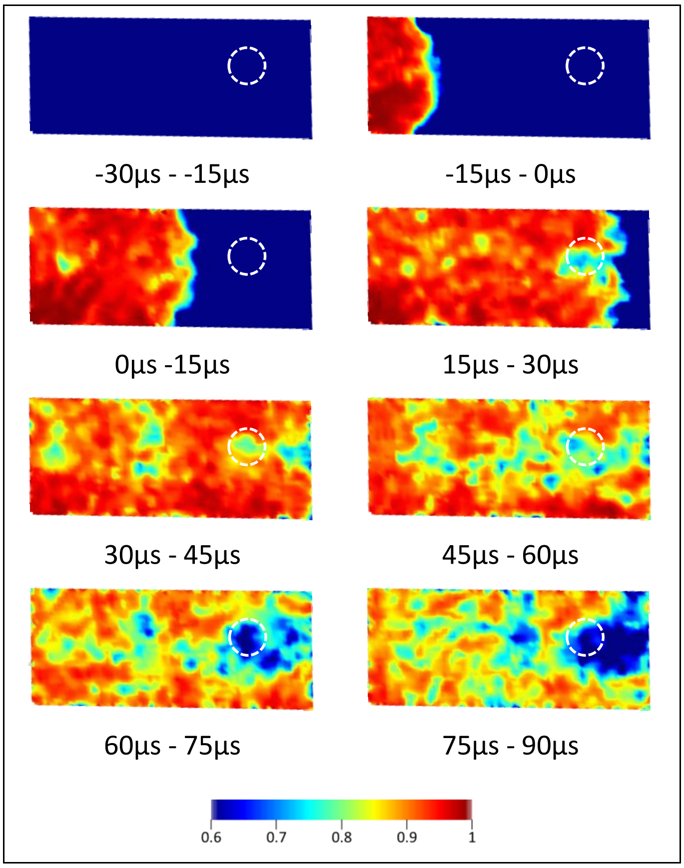

Figure 74. 300kHz out-of-plane moving window cross-correlation coefficient plots (the impact site is denoted by the white dashed line)

This reduction in the cross-correlation coefficient at the left of the area of investigation is also observed in the 30µs - 45µs time window with sporadic areas of reduced cross-correlation coefficient are also observed in the 45µs - 60µs time window. This can be attributed to two main phenomena of the Lamb wave. The higher frequency Lamb wave is more attenuative therefore the signal-to-noise ratio of the wave reduces at a more rapid rate (in the case where the noise floor is constant). The S_0 mode is considered in these time windows which is more prone to scattering due to the microstructure. This is intensified at higher frequencies where the wavelength is reduced and hence is more sensitive to the inhomogeneity of the microstructure.

Interaction with the A_0 mode is observed from 60μs – 75μs window onwards. The dominance of the A_0 mode is demonstrated by the significant reduction in the cross-correlation coefficient at the impact site. When comparing this time windowed cross-correlation plot with the respective time domain plots in Figure 66 it is evident that at this time the amplitude of the Lamb wave has decreased substantially and the affects previously discussed are influential. This is represented in the 60μs - 75μs and 75μs - 90μs cross correlation plots by the area of low cross-correlation coefficient to the left of the impact site. Nevertheless, in the 75μs - 90μs plot the most significant reduction in cross-correlation coefficient results from the presence of the impact damage. Like the other two excitation frequencies, a reduction in the coefficient is observed in the wake of the impact damage. However, for the 300kHz Lamb wave this is a much larger region. This is due to the shorter wavelength which is consistent with the cross-correlation coefficient plot for the entire sample length presented in Figure 69.

6.10. Damage measurement

To quantify the damage, a section of the turbine blade surrounding the impact site was removed to enable high precision measurements of the damage to be made. On removal of the section a crack was discovered on the internal face of the blade surface which ran lengthwise along the blade as shown in Figure 75. The length of this crack exceeded the dimensions of the section removed.

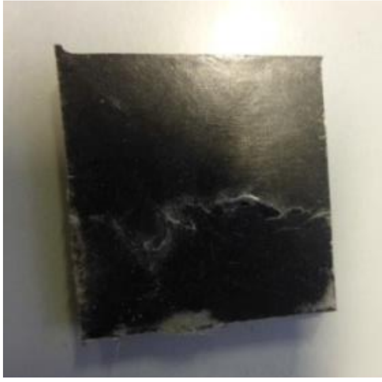

Figure 75. Resulting crack on the internal face of the turbine blade.

6.10.1. Outer surface measurement

To measure the BVID on the external face of the removed section, a Taylor-Hobson Talysurf 2 surface profilometer with a 2μm-radius stylus was used. A three-dimensional measurement was taken of a 12mm x 12mm area, with a 0.05mm y-axis spacing, a 3μm x-axis spacing and a 16nm z-axis resolution which provided sufficient measurement resolution while enabling the measurement to be conducted in a timely fashion. This allowed a 3D representation of the impact site to be produced. By extracting a 2D profile across the widest part of the impact site, the BVID was found to have depth of 40µm and an average length of 7.5mm as shown in Figure 76.

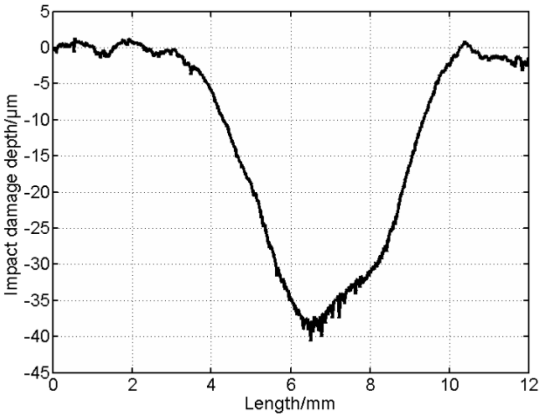

Figure 76. Surface profile of the BVID showing the length and maximum depth of the indentation created.

The depth of the impact damage on the outer face was significantly lower than 0.25mm which had been previously suggested as a quantifiable level for BVID. When inspecting the removed section it was only possible to see the damage at certain angles of viewing in well-lit conditions.

Comparing the measurement of the length of the impact site with the dimension determined from the 200kHz RMS baseline subtraction technique, there was only a 7% difference between the two demonstrating that this Lamb wave analysis technique has potential for indicating the scale of BVID. Indeed, all three excitation frequencies identified dimensions of the region of significant difference in waveform which are of similar magnitude to the damage measured.

The 3D measurement of the impacted area is presented in Figure 77.

The 3D measurement shows a clear indentation caused by the impact damage. Though the maximum depth of the indent was found to be 40µm, the 3D measurement shows that only an approximately circular area of around 2mm diameter of the indentation is of this depth. This measurement however does confirm that there was no additional damage caused by the impact on the outer surface of the blade.

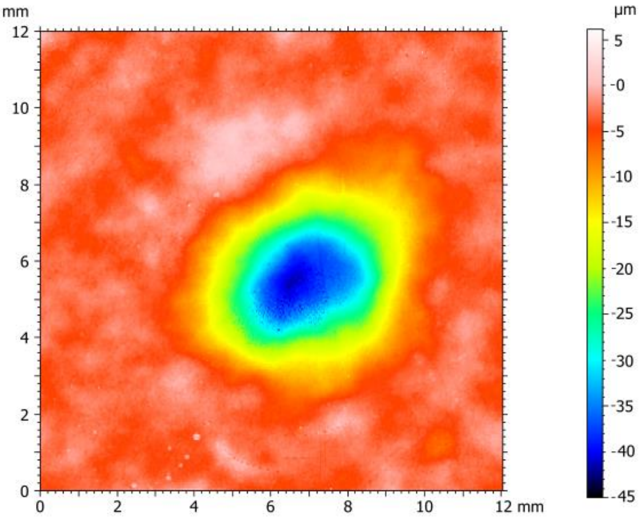

Figure 77. 3D Talysurf scan - Plan view of the BVID.

6.10.2. Inner surface measurement

Due to the surface profilometer being a contact measurement method it was not possible to use it to measure the inner face, which had a significantly higher level of damage rendering it unsuitable for stylus-based measurement. Precision measurements were made using a Polytec confocal-type white light interferometer.

A 15mm x 15mm area was measured with a 0.88µm x and y-axis resolution and a 50nm z-axis resolution. This resolution was again suitable for measuring the damage while also completing the measurement in a timely fashion. This allowed a 3D representation of the crack to be produced using a non-contact method.

The results from the white light interferometry are presented in Figure 78.

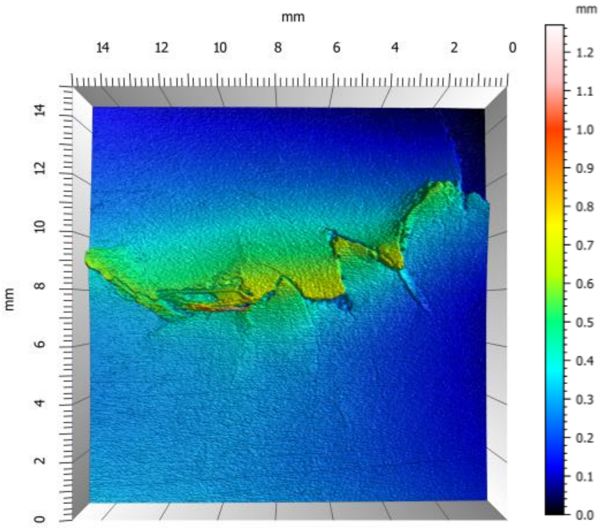

Figure 78. White light interferometry measurement of the crack on the inner face

These results show that the impact resulted in displacing material by approximately 0.9mm along the length of the crack indicated by the colour bar in Figure 78 and is photographed in Figure 75. This is significant damage which would affect the structural performance of an operational wind turbine blade.

Comparing the scale and location of the crack with the results from the 300kHz baseline subtraction it is possible to see that the larger area of increased RMS value was due to the presence of the crack, although this observation is by no means conclusive. As the crack ran in the same direction as the propagating wave, it would have had little effect on the wave. It is possible however that shorter wavelength of the 300kHz excitation did interact with the damage.

6.11. Discussion and conclusion

This chapter has demonstrated how 3D scanning laser vibrometry can be used to conduct a thorough investigation of acousto-ultrasonic induced Lamb wave interaction with impact damage on a composite turbine blade. The results from the 3D laser vibrometry clearly showed that the 100kHz excitation S_0 Lamb mode had minimal interaction with the impact however the higher excitation S_0 Lamb modes were more interactive due to the shorter wavelengths. The A_0 Lamb mode was found to interact at all frequencies with the impact damage, which is supported by previous studies. A high level of noise was observed particularly when the in-plane components were considered. This was caused by the inhomogeneity in the placement of the short chopped fibres and highlighted the challenge of monitoring structures reinforced with such fibres.

The dispersive phenomenon of Lamb wave modes was observed in the vibrometer results by the increased wave velocity of the higher frequency excitations.

An RMS baseline subtraction technique was applied to the out-of-plane component of the Lamb waves at the three excitation frequencies. This successfully produced a visual location and an estimate of the size of defect. When compared to the precise surface profilometer measurements the size of the defect was found to be within 7% of this. It is worth noting however that a threshold has to be set in order to reduce the effects of the low amplitude signals. This technique demonstrates the potential for using scanning laser vibrometry for routine inspection of structures.

A comparison of the pre-impact and post-impact measured signals was made by calculating the cross-correlation coefficient for each measurement point, allowing a visual indication of the region where the impact damage had influenced the Lamb wave. The out-of-plane component was first considered as it was shown to be more strongly influenced by the presence of the impact damage.

The cross-correlation coefficients for the in-plane components were considered with a cross-correlation coefficient being calculated for both individual in-plane components and their combined magnitude plotted. This showed an increased region of reduced correlation highlighting that it would be possible to use in-plane sensors to measure the interaction of the Lamb modes with impact damage. This would be particularly beneficial for integrated sensors. Noise on the in-plane components was attributed to scattering due to the inhomogeneity of the short chopped fibre material, which was supported by the reduction of cross-correlation coefficient over the entire area of investigation. The magnitude of the cross-correlation coefficients of all three Lamb wave components was then considered for completeness. This gave a full visual representation of the Lamb wave interaction with the impact damage.

A moving window cross-correlation technique was also applied to all excitation frequency datasets for the out-of-plane component. This gave a visual representation of how the cross-correlation coefficients at the different measurement points varied over time. It was found across all of the datasets that the presence of random noise resulted in low cross-correlation coefficients when no Lamb waves were present within the area of investigation. The moving window cross-correlation analysis also identified that a low amplitude S_0 mode was present as part of the out-of-plane component within the area of investigation prior to the 0μs datum points designated for the time domain plots. This demonstrates the sensitivity of the cross-correlation technique.

By using the moving window technique it was possible to isolate the different Lamb wave modes to investigate how they interacted with the impact damage. It was found that the presence of the impact damage affects the S_0 mode as was indicated by the full sample length cross-correlation plots. However, it appeared that the presence of the impact damage did not influence the cross-correlation coefficient in the wake. This therefore indicates that the S_0 mode alone would not be suitable for identifying the presence of impact damage on this type of structure with sensors mounted elsewhere on the structure as far as out-of-plane sensing is considered.

It was found however that the A_0 mode interacted with the impact damage which resulted in a more significant reduction in cross-correlation coefficient than the S_0 mode. It was also found that the region to the right (the wake) of the impact damage experienced a reduction in cross-correlation coefficient. This size of this region increased as the excitation frequency increased demonstrating the effect of shorter wavelengths sensitivity to damage. It appeared that minimal, if any, Lamb wave was reflected by the presence of the impact damage indicated by a region of relatively high cross-correlation coefficients to the left of it. This differs somewhat to the observations of the Lamb wave interaction with adhesive disbonds (see section 4.5). This therefore suggests a ‘pitch-echo’ method of Lamb wave sensing cannot be used for detecting this type of damage. This is an important realisation for the design of sensor networks.

The influence of noise was also observed in the moving window cross-correlation plots particularly for the higher frequencies. Although two pre-impact scans were not performed and therefore the influence of noise cannot be fully quantified, it is an important consideration for the design of sensor networks to prevent type I errors occurring. A recommendation to achieve this would be to base the detection of the Lamb wave using a thresholding technique and to only consider a small time window of the A_0 Lamb mode.

The results from the cross-correlation analyses demonstrated that higher frequencies were more sensitive than lower frequencies to impact damage, shown by significantly larger areas of low correlation. This is in agreement with previous studies [215]. Although it would be advantageous to use higher excitation frequencies for acousto-ultrasonic SHM systems, considerations of signal attenuation have to be made as has been shown in the laser vibrometry results. Therefore, any acousto-ultrasonic sensor network design should consider the placement of sensors with respect to the attenuation of the signal and the excitation frequency with respect to the minimum defect size.

The results of the cross-correlation analysis have highlighted that in a monitored area of a structure there are areas that show minimal reduction in cross-correlation coefficient and therefore would be unlikely to detect the damage in an acousto-ultrasonic system. Therefore, there is potential for using cross-correlation analysis on laser vibrometry to support the optimisation of sensor locations.

A section of the turbine blade surrounding the impact site was removed. On removal, a crack was discovered on the internal face of the blade. Precise measurements of the damage were made on both sides of the section using surface profilometry and white light interferometry. The measured damage correlated well with the results of the laser vibrometer study and the baseline subtraction RMS analysis, particularly for the 200kHz excitation where the size of the impact was found to be within 7%.

This study has presented an in-depth investigation into Lamb wave interaction with impact damage in composites for SHM applications. It has shown that even relatively low-energy impacts can result in BVID which can cause significant damage in areas which cannot be easily inspected. It has been shown that acousto-ultrasonically induced Lamb waves have great potential for monitoring the structural integrity of wind turbine blades in-service although careful consideration must be made when considering the excitation frequency due to the complexity of the Lamb wave interaction particularly in complex composite materials.

7. Virtual Delta-T mapping for improved effectiveness of acoustic emission location in aerospace structures

7.1.Introduction

The Delta-T technique developed by Baxter *et al*. [32] has been shown to provide improved AE source location in complex structures as the training technique accounts for the presence of features in the structure. The training technique was further improved by Pearson *et al.* [90] who used an AIC picker for a more accurate determination of the time of arrival of the wave (a full explanation of the technique is given in section 2.6.3). This technique has proven to produce good source location for lab based studies. However, the significant time and human input required to train the sensor network has made the Delta-T technique not viable for in-service use on large aircraft structures due to the time required to train the sensor network.

There have been numerous studies conducted to simulate AE mechanisms and their propagation using finite element analysis [127]. Examples of such work include the studies conducted by Sause and Horn [128, 129] into accurately modelling the Lamb waves excited in an AE event. Though advancing the understanding of AE characteristics, there appears not to be any published works where numerical methods have been employed to train experimental AE sensor networks for AE source location.

Techniques similar to this however are being developed for the global monitoring of aircraft structures using vibrational techniques such as those currently being developed under the VIBRATION project [234]. The goal of such research is to produce accurate modal vibration models for training and optimising real-life sensor networks though at the time of writing there are limited published works [235].

This study focuses on developing a method using LISA for the training of AE sensor networks. The objective of this is to deliver a methodology that reduces the time and man-power required to train the sensor networks whilst maintaining a high level of AE source location accuracy.

7.2.Linear location investigation

To investigate this methodology, the proposed techniques were first applied to locating damage along a line between two sensors. This was a cost and time-effective approach for testing the initial ideas. This also minimised the risk of error associated with a more complex investigation. A 3mm 6062-T6 Aluminium plate of dimensions 350mm x 350mm was used for this investigation. Details of the plate are shown in Figure 79.

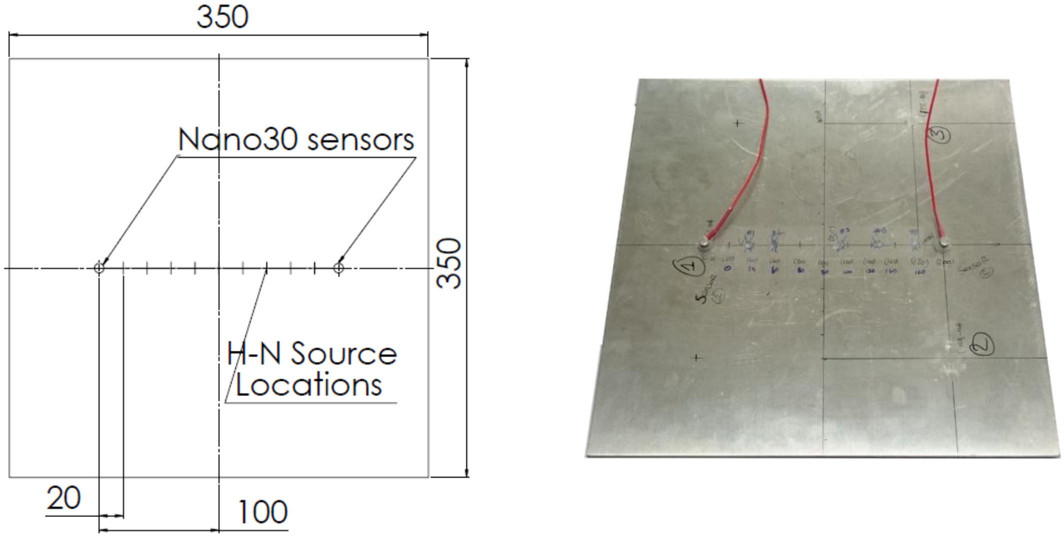

(a) (b)

Figure 79. (a) Diagram of linear investigation, (b) Aluminium plate used in the linear location experiment

7.2.1. Experimental training

Two experimental approaches were taken for the training of the sensor network. A traditional delta-t approach and a novel inverse delta-t approach. The inverse approach uses the sensors as actuators with the signal measured at the nodes of the grids. The same transmission path was used as in the traditional delta-t technique though in the opposite direction.

7.2.2. Experimental delta-t training technique

Two commercially available MGL Nano 30 sensors (operating frequency 125kHz - 750kHz) were acoustically coupled using silicone RTV (Loctite 595) along the central axis of the plate, 100mm from the centre as shown in Figure 79. The couplant was allowed to cure for a minimum of twenty four hours. Nine nodes of a linear Delta-T grid were drawn on to the plate with a spacing of 20mm.

Five H-N sources were created at each node on the Delta-T grid to ensure sufficient information was recorded to determine the arrival time of the Lamb wave.

7.2.3. Experimental inverse delta-t training technique

The Nano 30 sensors were individually excited with a 150v peak-to-peak, 200kHz Hanning windowed 5-cycle sinusoidal signal using a MGL µDISP signal generator

A Polytec PSV-500-3D-M scanning laser vibrometer was used to measure the Lamb wave signals at the nodes on the linear grid. The same setup was used as had been used in previous studies (section 4.3) and the plate was also coated with retro reflective glass spheres to improve the back scatter of light. Two sets of measurements were taken, one for each sensor excitation.

7.2.4. Modelled training

For the simulated training technique, both the traditional and inverse Delta-T techniques were investigated. A LISA model of the aluminium plate was created in the LISA environment with a global cube edge length of 0.5mm as used in the previous investigations (see Sections 4.4 and 5.7). A sample frequency of 20MHz was used as it had proven to yield suitable results in a previous study [230]. All three components of the displacement were recorded for each modelled sensor location. A sample length of 1.6ms was recorded for each measurement. As the 'sensed' signal in the model is noiseless it is not possible to use the AIC picking method on the raw signal as it causes the picker to tend to infinity. To enable the AIC picker function, a low-level Gaussian noise was added to the signal.

7.2.5. Modelled delta-t training technique

Accurately modelling H-N sources is complex and worthy of a stand-alone study. Therefore, for this investigation the H-N sources at each node were replaced by a Hanning windowed five-cycle 200kHz sinusoidal signal. The sources were modelled as point sources at the nodes on the Delta-T grid and the sensors were modelled simply as point receivers. A total of nine simulations were run; one for each nodal location.

7.2.6. Modelled inverse delta-t training technique

The sources were modelled as point sources at the locations of the Nano 30 sensors and the receivers were located at the nodal locations on the grid. Only two simulations were required to be created for this technique; one for each Nano 30 sensor. Thus, the computational simulation time was reduced by using this method when compared with that of the traditional delta-t approach.

7.2.7. Experimental AE sources

Five damage locations were randomly distributed at 15mm, 38mm, 93mm, 123mm and 151mm from the left hand sensor (in Figure 79) within the grid. The locations were determined by using a random number generator. Representative AE damage sources were artificially created by using H-N sources and recorded at the sensor locations using the same experimental setup as used for training. These artificial damage signals were used as a location benchmark for comparing the simulated training technique with the experimental training technique.

7.3.Results and discussion

The location error results for each artificial damage locations are presented in Figure 80 for the different techniques. The location error for the location of the artificial damage has been calculated for the out-plane component of the wave as this is the component primarily measured by the sensor. As the LISA model and laser vibrometer produced three channels of data for the X, Y and Z components of the wave each channel was used to locate the damage. An average of the locations based on all three wave components is presented to demonstrate the influence of in-plane modes.

It is worth noting that, from wave theory, an acceptable error margin is the diameter of one sensor [32]. In the case of a Nano 30 sensor the diameter is 8mm therefore any error less than this is acceptable. The results obtained show that both the experimental and simulated technique yielded results that were within the margin of error.

It is evident from the results presented in Figure 80 that there is a wide spread of Euclidean distance error for both techniques. For the experimental technique the lowest error of 0.27mm was observed for the artificial AE source at location one with highest source of error of 2.49mm observed at location four. This gave a difference in error of 2.22mm.

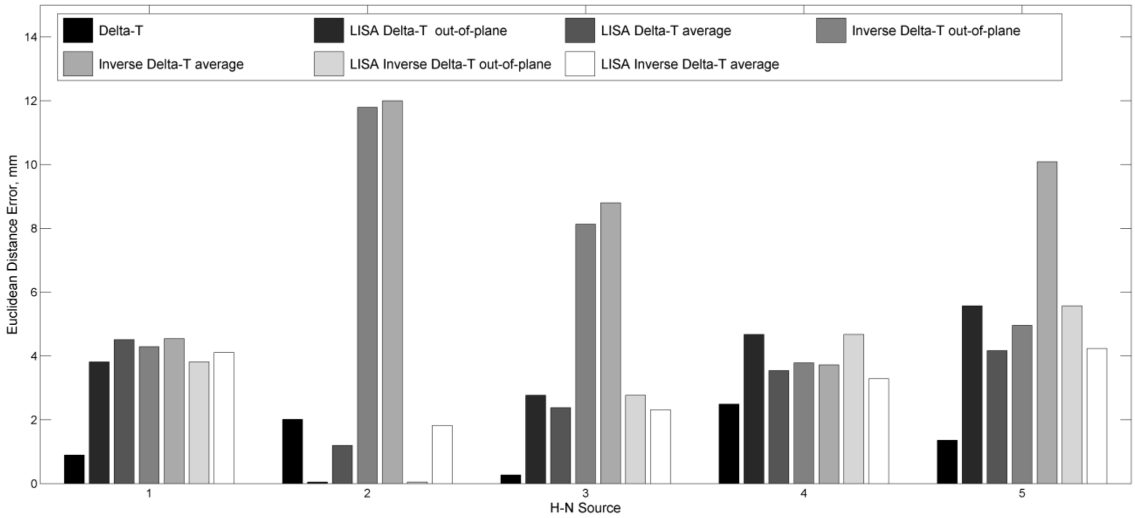

Figure 80. The Euclidian Error Distance for the location of the H-N sources using the experimental and modelled techniques

A source of error is the human error in locating the H-N sources. Creating an H-N source involves breaking a 0.5mm pencil lead at each node on the delta-t grid. This is subject to error in accurately locating the pencil lead at the centre of the node. In addition, the H-N sources that were used in this study as locations of artificial damage are also subject to the same error. Although there is no evidence to quantify this error, it is suspected that it is approximately +/- 2mm (the thickness of an ink line drawn on a structure).

Considering the results from the simulated investigation, the lowest source of error of 0.04mm and 1.20mm were observed at location two for the out-of-plane component and the three component average, respectively. The highest source of error of 5.58mm was observed at location five for the out-of-plane component and location one (4.51mm) for the three component average. This gives a difference 5.54mm for the out-of-plane component and 3.31mm for the three component average.

The high values from the experimental inverse Delta-T technique could be explained by the quality of the training data. At the sampling frequency used to measure the training data the minimum sensitivity achievable is 200mm/s which is two orders of magnitudes higher than that of the signal measured. As in previous studies the, 200 measurements were taken at every measurement points and averaged to improve the signal-to-noise ratio. Nine locations were measured for this technique. Due to measuring in this sensitivity range, when the backscattered light is low (as in the case of an area that has an insufficient coating of glass beads) the signal-to-noise ratio dramatically reduces. As a result it would be possible for the AIC picker to incorrectly determine the time of arrival of the wave and therefore calculate the incorrect Delta-T value. A solution for this would be to refine the measurement grid, identify any outlying values and fit an appropriate curve to the dataset that can be interrogated for location. This would increase the time required for data capture and processing however both of these processes are autonomous and therefore this would still have advantages over the traditional Delta-T technique.

Even when considering the highest values for the location error, the average location errors for the experimental Delta-T technique using a laser vibrometer were found to be 6.6mm and 7.8mm for the out-of-plane and three component average respectively.

Assessing the modelled data presented, all of the location errors fell below the 8mm acceptable limit. When considering the locations calculated using only the out-of-plane component of the modelled data it is evident that there is no difference in the location error for the Delta-T and the inverse Delta-T. When considering the in-plane components, there is a marginal difference in the location error. One significant result is that for artificial damage location 2 where the modelled data saw a location error less than that of the experimental Delta-T. When only the out-of-plane component was considered a location error of less than 0.1mm was achieved. On average however there were marginal differences between the location errors for the respective modelled Delta-T and inverse Delta-T. The modelled Delta-T and inverse Delta-T techniques saw an average location error across the five artificial damage locations of 3.4mm and 3.2mm for the out-of-plane and three component average, respectively.

When comparing the experimental technique with the simulation technique, it is evident that for four of the five AE source locations the experimental technique produced a significantly lower Euclidian error distance. This can primarily be attributed to the signal used to train the sensor network. The experimental training used H-N sources which were also used to represent the AE emitted during a damage event. Though there would be small differences in the waveforms produced between H-N sources, it has been proven that the source is repeatable [192, 193]. As the source is akin to that of a step input, a wide range of frequencies are excited. Due to the dispersive nature of Lamb waves, the higher frequencies will travel faster and therefore arrive at the sensors first (a dispersion curve for this plate is presented in section 4.2). This will inherently result in a more accurate location than that of the single frequency of 200kHz used for training in the simulated results.

Though the Euclidian error distance of the simulated results fell below that of the acceptable 8mm margin of error the size of the linear distance was small enough for the dispersive characteristics to not significantly influence the time of arrival at the sensors. It could be hypothesised that if this investigation were to be carried out on a larger plate with a greater distance between the sensors where there is a large difference in the wave velocity of the high frequency Lamb waves excited by the H-N source and the 200kHz sine wave excitation, the Euclidian distance error would be significantly larger. To reduce the Euclidian distance error, a source more representative to that of an H-N source would have to be modelled.

The lowest error for four of the five locations was from the traditional experimental Delta-T technique. The highest error case calculated using this technique was 2.5mm for artificial damage location four. Across the five damage locations the average location error was found to be 1.4mm. The good performance of this technique can be attributed in part to the input. An H-N source was used to train the sensor network and for the artificial damage. Therefore, the same frequency content and hence dispersive characteristics were observed. The distance between the sensors was 200mm which is a relatively small distance. In this short distance, the effects of frequency dispersion would have likely not have had such as significant influence on the Delta-T calculation than if the sensors had been spaced further apart.

7.4. Planar location investigation

The performance of the LISA models for locating the artificial damage in the linear location investigation demonstrated promising results. The LISA modelling technique showed great potential especially when considering desk based studies for design and development of aircraft components and sensor networks. A second investigation was conducted to assess the viability of using a LISA model to locate damage on a plane on a component of complex geometry using the delta-t technique.

7.4.1. Experimental delta-t training

A complex geometry fatigue specimen first used by Baxter [65] for the testing of the Delta-T technique was manufactured from 2024-T3 aluminium as shown in Figure 81. The dimensions of the plate are presented in Figure 82.

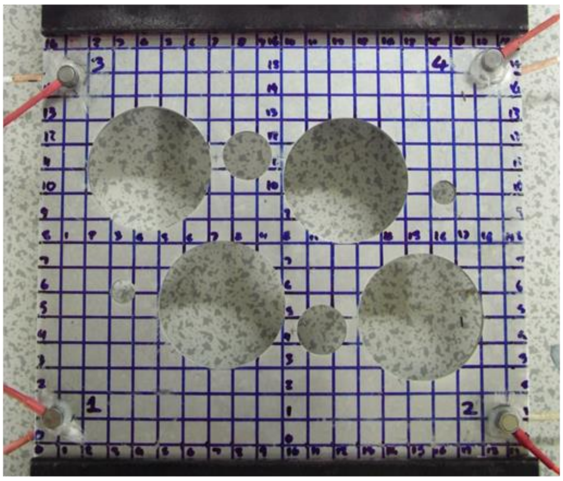

Figure 81. Aluminium fatigue specimen of complex geometry

The dimensions of the specimen were 370mm x 200mm x 3.18mm. The central 162mm section was considered only for investigation allowing the rest of the plate to be used for clamping into the load machine.

A grid with 10mm spacing was drawn on to the structure. To form an experimental comparison, a traditional Delta-T dataset was first created using H-N sources captured using the same setup as the linear location experiment.

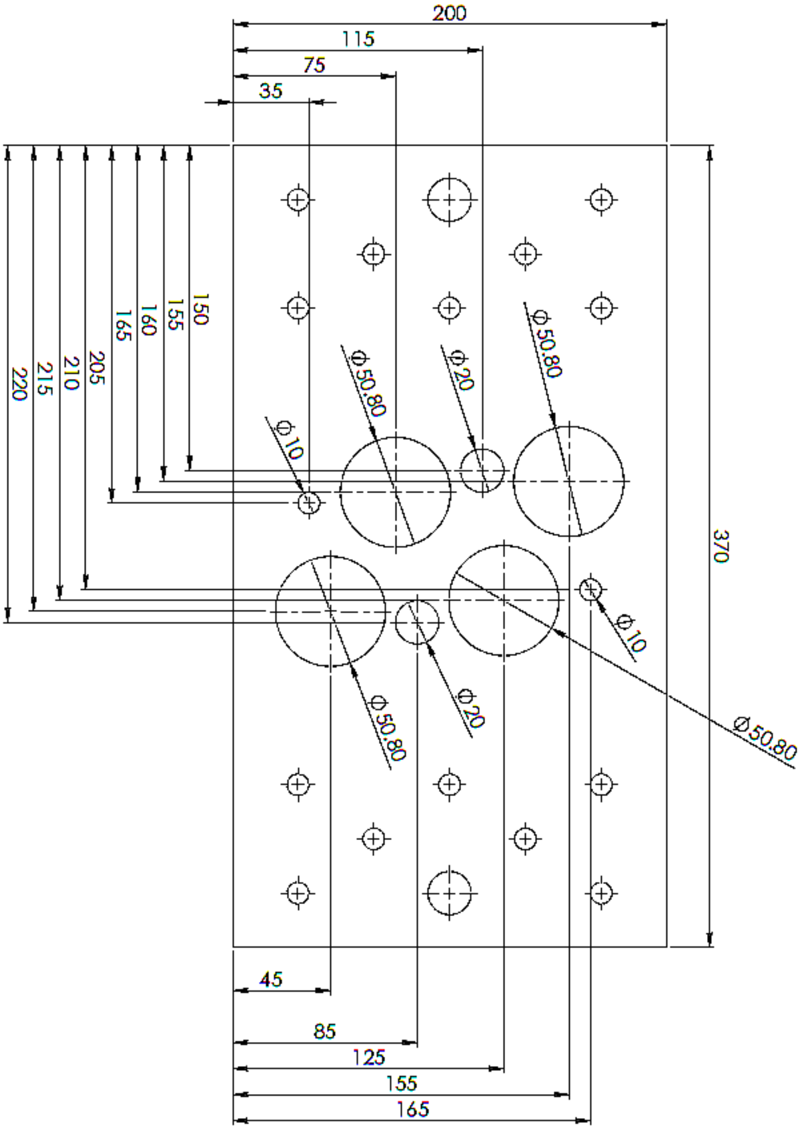

Figure 82. Dimensions of the complex geometry plate (all dimensions in mm)

Four Nano 30 sensors were acoustically coupled to the plate using silicone RTV (Loctite 595) at the corners of the area of investigation. The coordinates of the sensor locations are given in Table 3 relative to the dimensions of the plate.

Table 3. Locations of the sensors relative to the plate dimensions

Sensor Number	x-coordinate (mm)	y-coordinate (mm)
1	10	116
2	190	114
3	12	254
4	185	258

7.4.2. Modelled delta-t training

As with the linear location study, cuLISA3D was used for modelling the complex geometry plate as shown in Figure 83. For consistency, the same model parameters were used as for the linear location model. To approximate the geometry of the holes from cubes, a midpoint circle algorithm was used; an arithmetic technique commonly used for approximating circles on pixel displays. Holes which were present on the complex geometry plate which were present for the mounting of the plate into the load machine were omitted from the model for simplicity as they fell outside of the monitored area.

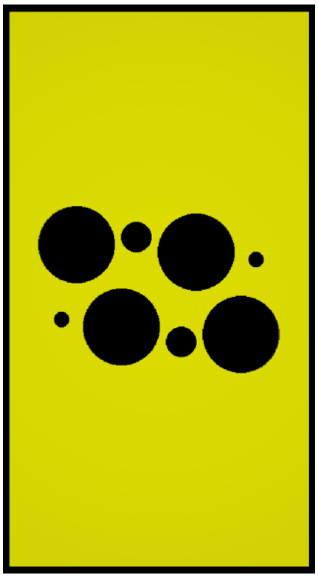

Figure 83. Complex Geometry plate modelled in cuLISA3D

As with the linear location a Hanning windowed five-cycle 200kHz sinusoidal signal was excited at respective locations to those of the nodes on the Delta-T grid used in the experimental study. The simulation was performed for each nodal location. Sensing locations were also sited to correspond to those used in the experimental setup up.

7.4.3. Experimental Acoustic Emission Sources

To test the performance of the two sensor network training techniques, two sets of AE data were produced. As with the linear investigation, H-N sources were used for the initial test which was followed by a tension-tension fatigue test in order to trial the AE source location techniques under a real loading condition.

7.4.4. H-N sources

Six H-N sources were recorded using the same setup and method as used in the linear investigation. A selection of the locations of the H-N sources were purposely off-grid to fully test the interpolative ability of the two datasets. The details of the locations relative to (0, 0) on the delta-t grid are presented in Table 4.

Table 4. Locations of the H-N sources used for testing the training data (coordinates are respective to (0, 0) on the delta-t grid)

H-N source number	x-coordinate (mm)	y-coordinate (mm)
1	20	110
2	74	114
3	100	115
4	104	44
5	126	45
6	181	50

7.4.5. Tension-tension fatigue test

The specimen was cyclically loaded in tension-tension between 0.25kN and 24kN at a rate of 2Hz in a hydraulic load machine by Pearson [90]. The load was not completely removed to reduce any AE activity as a result of slack in the system. The distribution of the load was achieved by using 5mm steel clamping plates and a 20mm pin attachment (this was omitted from the model as mentioned). The AE data was continuously recorded throughout the experiment to monitor the plate for damage. A threshold trigger was used to record the transient AE signals.

7.5.Acoustic Emission source location results and discussion

The results for both the location of the H-N sources and the resulting AE from the fatigue test using the two location techniques is presented. The widely used time-of-arrival (TOA) AE location method is also presented for location of the AE resulting from the fatigue test for comparison.

7.5.1. H-N source location

The Euclidian error distances for the H-N source locations using the two different techniques are presented in Figure 84.

The results presented show no locations for H-N sources one and six for the delta-t grid trained with the LISA data. This can be attributed in-part to the H-N sources being located at the edge of the holes. As previously discussed, the holes in the LISA model were approximated using the midpoint circle algorithm. This leaves the edges of the holes not being perfectly round unlike the holes on the plate in the experimental study. As a result, the wave propagation at the edge of the holes can be affected, influencing the delta-t location.

It is evident that other than H-N source 4, a greater error was observed when using the modelled training data for locating the sources. However, it should also be noted that the margin of error of sensor face diameter (8mm) was only exceeded when locating H-N source five using the modelled training set. This was only exceeded by approximately 5.5mm.

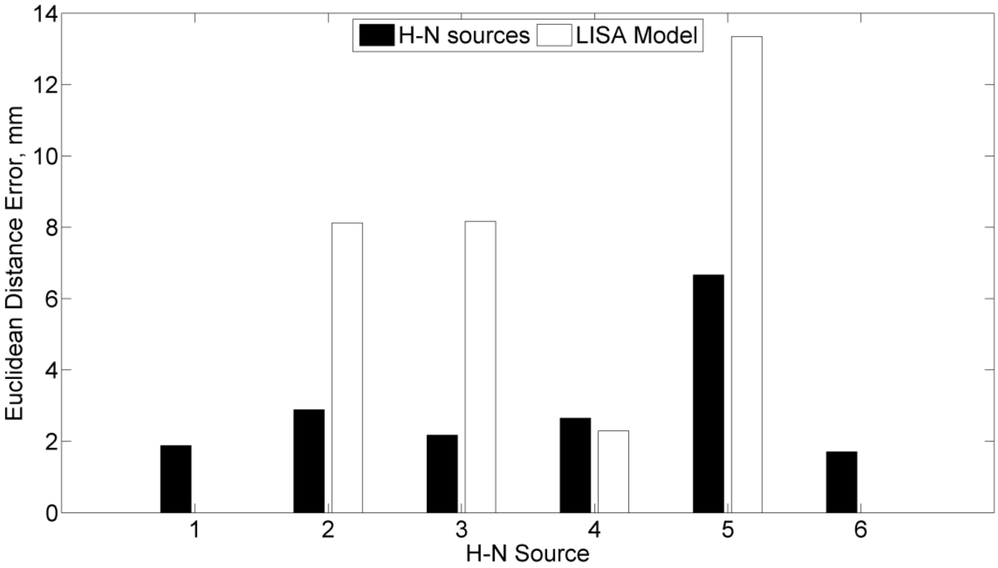

Figure 84. The Euclidian Error Distance for the location of the H-N sources using the experimental and simulated techniques

A representation of the actual H-N source locations and the error in location using the two techniques is presented in Figure 85. This plot clearly shows that the H-N sources were located at the edges of the holes which could be regarded as locations where sources of damage are likely to occur as well as being areas which are traditionally difficult to monitor.

H-N source number one which is located in the top left of the plot shows a high degree of accuracy for location using the experimental training however no location was achieved when using the modelled training. This is also true of H-N source number six (lower right of the plot). Because of this, it is not possible to make a comparison of the error of the two techniques at these locations. It can be stated that the Euclidean error distance is less than 2mm for both of these locations located with the experimentally trained delta-t which can be said to be within the margin of error associated with the experimental training method and indeed less than the 8mm sensor face diameter.

H-N sources two and three are located on the upper half of the specimen on either side of the 20mm central hole. H-N source two sits on the edge of the 20mm hole. The experimental training located the H-N source slightly to the right of the actual position with a Euclidean error distance of around 3mm as shown in Figure 84. This is an accurate location of the damage and within the margin of error. The location of the H-N source using the modelled training locates the source above and to the left of the actual location with a Euclidean error of approximately 8mm. This error is larger than the error achieved when using the experimental training however it still remains within the margin of error.

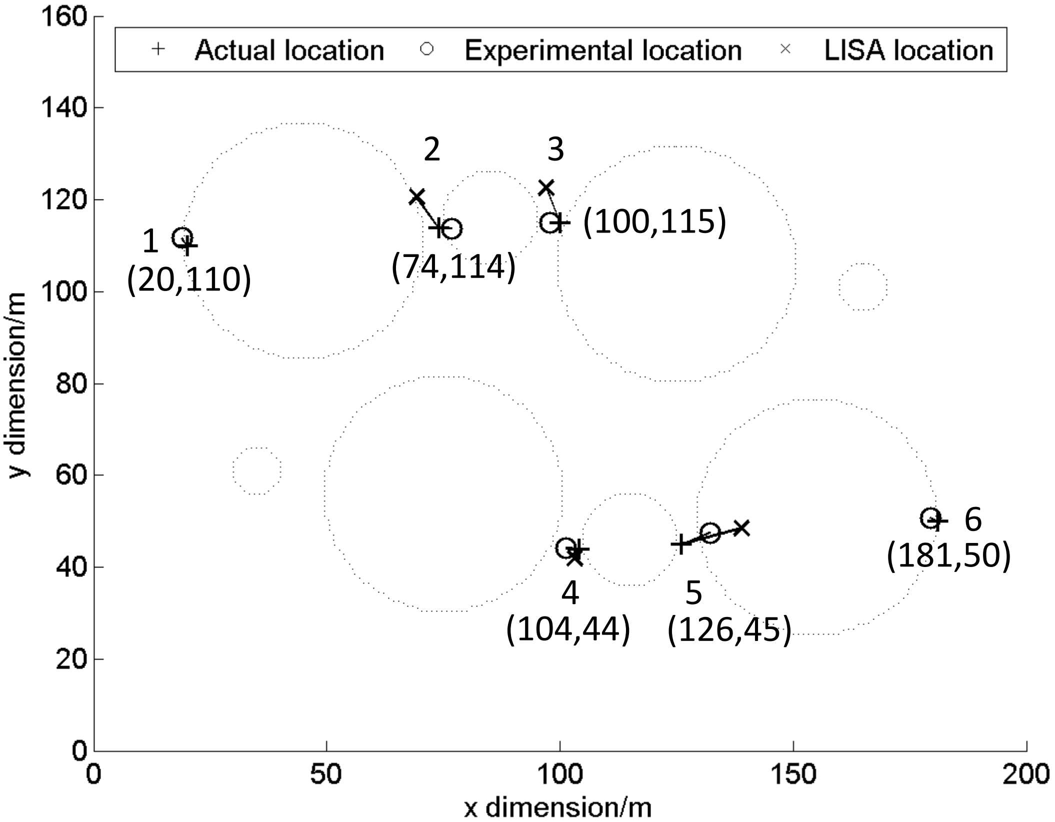

Figure 85. Error location plots for the H-N sources located using the two techniques. The numbers denote the H-N source number.

A similar level of error is exhibited by the locations of H-N source three. The experimental training locates H-N source three to the left of the actual location with a Euclidean error distance of just over 2mm. However, the modelled training locates the H-N source above and to the left of the actual location with a Euclidean error distance of approximately 8mm. This is similar to the error experienced with the location of H-N source two.

A high level of accuracy is achieved with the location of H-N source four with a Euclidean error distance for both locations techniques being less than 3mm. Interestingly, both techniques located the source to the left of the actual location.

A higher level of error is observed for H-N source five which is located to the right of the lower 20mm hole on the plot in Figure 85. Both techniques located the H-N source above and to the right of the actual location which in reality lay within the hole and therefore was not possible. This occurs because the delta-t algorithm does not identify the presence of features of the structure when it interpolates between the training locations therefore enabling AE to be located outside the physical constraints of the structure. This is a drawback to the technique. The Euclidean error for the experimental training and the modelled training was approximately 7mm and 13.5mm respectively. This error was the highest error observed for all of the H-N source locations. As shown in Figure 84, for three of the four sources successfully located using the two techniques the location error was greater when locating using the modelled training data. Therefore, it is justified that as there was a high level of error when locating the H-N source using the experimental training data that the error when locating using the modelled training data would be even higher.

Despite these errors, including those that fall outside the constraint of the structure, this is still a useful result as the technique locates the H-N sources very close to their actual locations. In the case of this occurring on an in-service structure, these results would still lead to the location of the defects which could be further localised using conventional NDT techniques, thus reducing the time needed to locate the damage.

7.6.Fatigue test Acoustic Emission locations

7.6.1. Acoustic Emission Events

The complex geometry aluminium plate was routinely inspected during the cyclic loading. At 76,000 cycles no damage was visible. However by 96,000 cycles (when the test was stopped) the presence of fatigue damage was visible as shown in Figure 86 (a). At 88,000 cycles, the total amount of AE events detected was below 100 events however this significantly rose to approximately 15,000 AE events by 96,000 cycles indicating the onset of damage.

The AE events detected during the fatigue test were recorded and the location of the AE source was located using the TOA location method as well as both the experimental and modelled delta-t training datasets which are presented in Figure 86 (b), (c) and (d) respectively. Each event was spatially binned into a 5mm x 5mm bin for clarity in presentation of results.

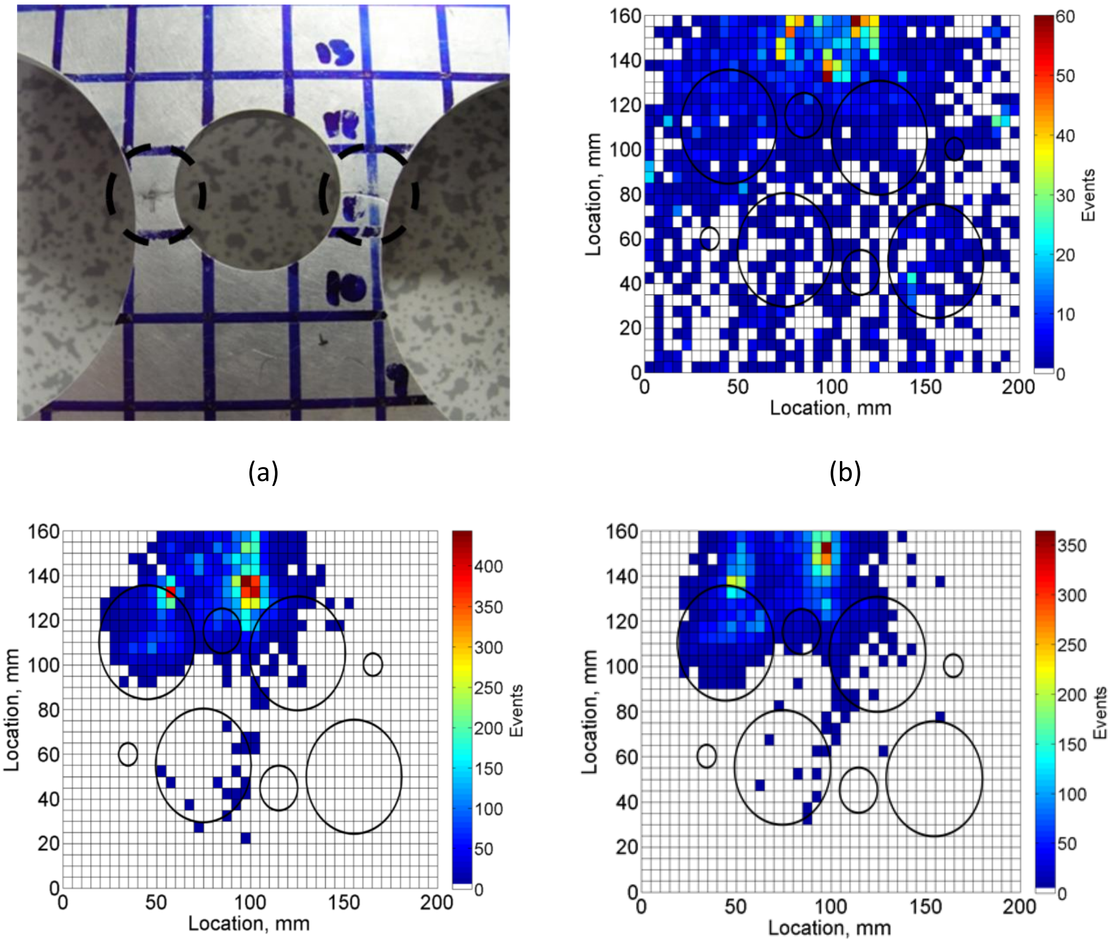

(a) (b)

(c) (d)

Figure 86. (a) Visual fatigue damage on the specimen, (b) TOA method of location, (c) Delta-T location trained with experimental data, (d) Delta-T location trained with modelled data

By studying the results of the TOA spatial binning it is apparent that AE events were located in regions all over the complex geometry aluminium plate. From these results it could be argued that there are three areas of relatively high AE at the top of the investigation area with two 5mm x 5mm bins locating approximately sixty events. Although this binning of AE events is relatively high compared with the other bins in this results plot it is worth noting that in this test around 15,000 AE events were recorded and therefore sixty events is reasonably insignificant. A few other bins saw around twenty-five AE events located with them but again this is still insignificant.

In terms of detection, it could be stated that damage from these results had occurred within the plate especially when correlated with the significant rise in AE activity after 88,000 cycles which would infer that the AE activity is not associated to background noise or rubbing at the attachment points. However, with the sporadic distribution of the AE events located with the TOA method it would be difficult to determine where on the plate the damage occurred and without the fatigue cycle-number of AE events data it would be easy to fail to determine the presence of damage. It should also be noted that although there were bins with relatively high numbers of AE events located, this did not correspond with damage observed visually.

From initial observations it is instantly apparent that the delta-t with experimentally trained data shows an improvement in performance over the TOA location method. Considering the distribution of the location of AE events, the experimentally trained delta-t method mostly groups the AE events into bins surrounding the top two 50.8mm holes which is a vast improvement on the sporadic distribution of AE event locations achieved with the TOA method. This instantly gives a much clearer indication of the presence of damage on the plate as well as its location which is likely to be contained within a 60mm x 100mm region of the plate.

When considering the number of AE events located within specific 5mm x 5mm bins the increase in location performance over the TOA method is demonstrated. Comparing the bins with the most AE events located within them, the experimentally trained delta-t method places approximately 450 AE events within one bin whereas the TOA method only bins a maximum of sixty AE events into one bin. This demonstrates a seven and a half times greater improvement in confidence. In addition, when considering the clustering of the high AE event bins, the experimentally trained delta-t technique identifies two main areas of damage which is more representative of the damage observed visually than the three areas identified with the TOA method.

Comparing the location of the high AE event bins and the damage visually observed it is apparent that there is a small error in the accuracy of the location. The damage was located within bins between the 20mm hole and the two 50.8mm holes at approximately y = 110.5mm. Considering the right side of the hole the high AE event bins were located 20mm above the observed damage. In total 2117 events were located to this cluster of bins. Averaging the Euclidean error distance clustered to this region gives an error of 19mm. This error falls outside the 8mm margin of error that was previously discussed as being acceptable. Although this is not at the site of the observed damage it is possible that these AE events may have been the result of plastic deformation occurring before the growth of the fatigue crack. However arguably, a higher than average amount of AE events were binned within the areas of the visually observed damage with around 150 events being binned at the location of the fatigue damage.

When the left side of the 20mm hole is considered the experimentally trained delta-t (conducted by Pearson [90]) locates the damage above and to the left of the its visually observed location. Unlike the right hand side of the 20mm hole, there was no indication of damage by a relatively higher amount of events being binned to location of the damage. Although it is not possible to directly determine the cause of this error in location there are a few plausible explanations. A likely cause is the change in physical geometry of the specimen. The delta-t training only considers the geometry of a healthy and intact specimen. It may have been the case that the fatigue crack grew on the right-hand side of the 20mm hole first and as a result altered the geometry of the plate and hence the propagation path of the AE. This would result in the technique falsely locating the source of the AE.

Another possible explanation is the amount of concurrent AE activity occurring on the plate. Lamb wave studies presented previously show that a reflection interacting with a transmitted wave (see section 4.5) can result in interference patterns, beam steering and the areas of high and low energy due to constructive and deconstructive interference. If AE is emitted from various locations simultaneously, it may have resulted in the propagation being disrupted and hence the arrival time. Through the use of a training technique, such as neural network, it may be possible to characterise the AE in relation to the damage mechanism and hence identify any waveforms that are not consistent (in effect been disrupted).

One other possible explanation is rapid failure of this section. This would result in a high energy, low event emission of AE. As such the hit count would be low but the energy would be higher. Although that would explain the low amount of hits where the fatigue damage was visible it does not explain the high cluster of AE hits to above and to the left of the fatigue crack. Therefore it is unlikely that this is the reason.

The delta-t locations based on the modelled data at first glance achieves a qualitatively similar distribution of locations to the experimentally trained delta-t. Like the experimentally trained delta-t location, there is a vast improvement of the location binning of AE events by the model trained delta-t technique over the TOA.

The modelled delta-t training method identified two areas where a high amount of AE event were located much like the experimentally trained delta-t, thus much more precise than the results of the TOA method. Considering the cluster of high amounts of AE events located on the right of the 20mm hole, approximately 350 AE events were located to one bin. This is around one hundred less than the experimentally trained delta-t technique but still nearly six times more than the TOA method. It is worth also noting that the experimentally trained delta-t technique produced four bins with exceptionally high AE event locations (red) whereas the model-trained delta-t method located fewer events into a four bin cluster. However, this was still higher than the neighbouring bins demonstrating a relatively high level of precision.

Considering the accuracy of the location of the damage using the modelled delta-t training data, the cluster of high number of AE events to the right of the 20mm hole was positioned much higher than the fatigue damage observed visually. However, as previously discussed, this may have been the result of the plastic deformation occurring before the onset of the crack growth. Comparing the location of this cluster with the location achieved with the experimentally trained delta-t technique, the cluster's modelled trained location is above and to the left of the experimentally trained location. Averaging the two locations of the events in the two clusters produces a Euclidean distance of 22mm. Although this distance was larger than the error distance that occurred with the location of H-N source three, the error location observed was similar as it was also above and to the left of the location achieved with experimentally trained delta-t technique.

The experimentally trained delta-t method produced a higher than average binning of locations observed at the location of the visually observed damage. A similar, but less significant bin of higher than average AE events was also observed using the modelled delta-t training at (100,125). Like the cluster of high AE events located by the modelled data the location of this bin was above the location achieved when using the experimentally trained delta-t technique. Again this was consistent results was observed locating H-N source two.

When considering the cluster of high number AE events located to the left of the 20mm hole, the modelled trained delta-t was also successful in identifying the presence of the damage in this area. Much like the high number of AE events located to the right of the 20mm hole by the model-trained delta-t, the number of AE events located within this area was less than the number of events located using the experimentally trained delta-t. The bin with the highest number of AE events located using the experimentally trained delta-t technique was approximately 325 whereas the number of AE events located to a single bin using the modelled delta-t method was around 225. This is consistent with the performance of the techniques when locating the right of the 20mm hole. Despite the lower number of AE events located within this cluster by the model-trained delta-t technique, a similar level of precision was observed to that of the experimentally trained delta-t method with the size of the clusters being consistent for both training methods.

When the accuracy is considered however, the location of the cluster produced using the modelled trained delta-t is above and to the left of the location achieved with the experimentally trained delta-t. Although the distance between the clusters using the different training techniques is not as vast as the location of the clusters to the right of the 20mm hole, this is consistent in terms of error location when compared with the location of H-N source two.

The lower number of AE events located to the respective bins using the model-trained delta-t technique can be justified by the sparser distribution of AE events when compared with the distribution of AE events achieved using experimentally the trained delta-t technique. Although the slightly sparser distribution does not significantly affect the identification of the region of damage, the additional bins with fifty or more AE events located can significantly affect the number of AE event located to the high AE event bins. Nevertheless, the number of AE events located to bins was significantly higher than what was achieved with the TOA method as well as achieving a much denser distribution.

Aside from the identification of the fatigue damage events surrounding the 20mm hole, both training techniques identified a diagonal distribution of AE events at the centre of the plate as well as a low number of events in the region surrounding the bottom 20mm hole. It is intuitive that the geometry of the plate is similar for both the top and the bottom half that the lower 20mm hole would experience some plastic deformation during the early stages of loading as this would be a region of similarly high stress concentration. As the plastic deformation progressed either side of the top 20mm hole a weak point would have been created and therefore, the plastic deformation at the bottom 20mm hole would have ceased.

Considering the more prominent diagonal distribution of AE events in the centre of the plate, it is likely that this was the result of plastic deformation that was most likely to have occurred as the plate started to fail. This is particularly likely if one side of the top 20mm hole failed first.

7.6.2. Acoustic Emission Energy

Although locating AE events presents the locations of all of the AE sources, it can mask the presence of damage as much activity can occur in structure. This may be of particular influence in cases where a high level of background noise is present such as that experienced on an aircraft in flight.

Potentially a more sensitive method of locating the presence of damage using AE is to consider the energy of the AE events sensed. The spatial binning of the AE energy for the AE events detected during the fatigue test is presented in Figure 87. An energy threshold of 7.2×10^7 aJ was applied to the spatial bins in these plots to remove the presence of low energy bins.

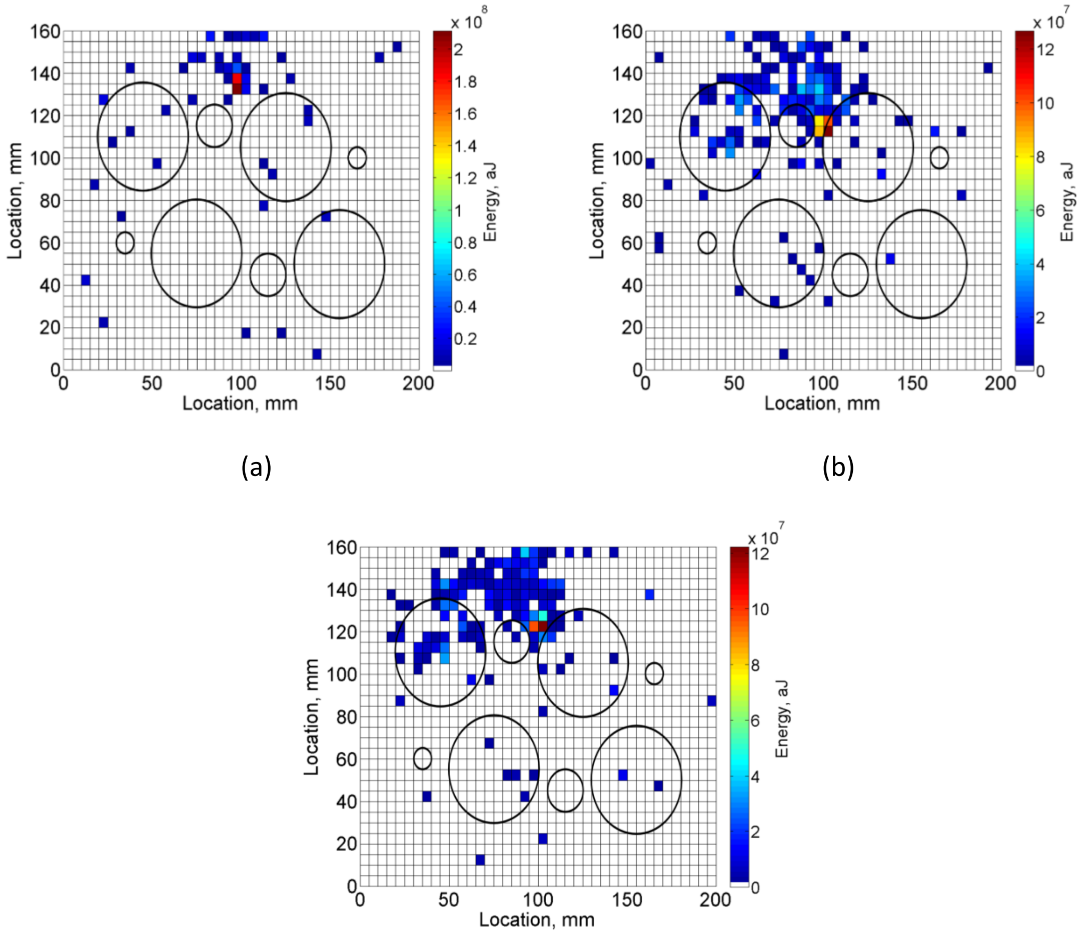

(a)

(b)

(c)

Figure 87. AE energy spatial binning for all fatigue cycles for the a) TOA method of location, (b) Delta-T location trained with experimental data, (c) Delta-T location trained with modelled data

When considering the results when using the TOA location method a small cluster of relatively high energy is observed above the right of the upper 20mm hole. The maximum energy located to one spatial bin is just over 2 x 10^8 aJ. Averaging the locations of the AE events within this bin gives a Euclidean error distance of 20.2mm from the visually observed damage. It is worth noting that the neighbouring bin above this bin also contained relatively high amounts of AE energy, albeit less that the lower bin. Although this technique appears to achieve a high level of precision, the accuracy of locating the damage is poor. Other than these two bins, there are few other bins which contain AE energy above the threshold. This could therefore be misinterpreted as only one damage event occurred on the plate.

Considering the experimentally trained delta-t it is instantly apparent that more AE events have been grouped into more spatial bins. This is an indicator of a denser location distribution of AE events and corresponds well with event plots presented in Figure 86. Firstly inspecting the highest energy spatial bins, it is apparent that a higher degree of accuracy was achieved with the experimentally trained delta-t technique than the TOA method. Four spatial bins are identified as having a relatively high energy to the right of the top 20mm hole. This corresponds well with the damage which was visually observed on the plate. It should be noted however that although an improvement in accuracy was observed with experimentally trained delta-t over the TOA method, a reduction in precision was observed as there are more high energy bins and the energy in these bins is also less. That said, if the presence of the holes is considered for the location of the AE energy so that any AE energy that is located within a hole is moved to the nearest part of the plate, the two high energy bins inside the hole would be combined with the high energy bins to their left. As such, the energy in these bins would in fact exceed the energy in the high energy bins on the TOA location plot. Either way, the improvement in the location accuracy is so significant that that slight reduction in precision is acceptable.

Unlike the TOA method of location, a group of lower energy spatial bins was located above the top 20mm hole. This corresponds well with the grouping of AE events observed in the AE event plot in Figure 86. The grouping of both AE events and AE energy within this region suggest that the previously discussed plastic deformation occurred. Interestingly, the location of the high number of AE events identified were likely to have been all of low energy. This is indicated by the number of significantly high energy AE spatial bins being located in the same respective location. Conversely, the locations of the high energy spatial bins correspond to a small amount of AE events indicating that the AE events located within this region were all of high energy which is what would be expected of AE associated with fatigue cracking.

From a simple visual comparison, it is apparent that the results from the experimentally trained delta-t and model-trained delta-t techniques correlated well. Both of the plots have a similar distribution of AE energy locations. When comparing the relatively high energy spatial bins, the location of the high energy bins using the modelled delta-t location is above the location of both the damage that was visually observed and the location achieved using the experimentally trained delta-t. Averaging the locations of the AE events within this four bin cluster gave a Euclidean error distance of 10.3mm from the damage region; and error slightly over the accepted margin of error. The energy clustered within these bins is less than what was found with the experimentally trained delta-t method. As with the events plot in Figure 86, this can be attributed to a more sparse distribution of AE events than what was achieved with the experimentally trained delta-t technique. Nevertheless, the location accuracy achieved with the model-trained delta-t was still better than that achieved with the TOA method whilst also achieving an acceptable level of precision.

Considering the other spatial bins with AE energy above the threshold located using the model-trained delta-t technique, there is a strong correlation with the experimentally trained delta-t method. A region of bins above the top 20mm hole were identified using both training techniques. This also correlates well with AE event plots and therefore suggests the presence of plastic deformation as previously discussed. The relatively low AE energy in these bins indicates that it is likely that these AE events are not the result of crack damage.

7.7.Discussion and conclusions

The linear investigation presented showed a great promise for the location of AE events created using an H-N source. This investigation demonstrated the viability of using modelled data to locate AE sources experimentally. Despite achieving promising results in this linear study it should be noted that this was conducted on a very simple isotropic plate with a very simple setup. In such a scenario, typically adequate results can be achieved using the TOA method alone.

With the experimental aspect to the linear investigation, the conventional delta-t method produced excellent location results as expected. This corresponded well to the findings previously published where the delta-t technique had been used [89, 236]. However, it should be stated that this training technique is not only time consuming (and hence expensive when applied to a commercial application) but also laborious. In addition, the creation of H-N sources can vary in amplitude particularly at different areas of the structure such as around fasteners and holes. This can result in a large amount of useless data being captured which later has to be manually sorted and discarded; hence increasing the time, cost and monotony of the operation.

Through the use of 3D scanning laser vibrometry and a novel inverse technique, an innovative training technique was developed which showed promise. Although a much larger Euclidean error distance was obtained when using this technique, the location of the H-N sources was mostly found to be within the margin of error especially when only the out-of-plane component was considered. In this investigation, point measurements were only taken using the vibrometer. This in itself has degree of error associated with it. The surface of the plate was coated with retro reflective glass beads to improve the backscatter of light. However, if the coating is insufficient or the glass beads are insufficiently mounted, noise and/or an unrepresentative signal can be measured. To reduce this effect it is recommended to use more measurement points than those normally used in a conventional delta-t setup. A smoothing or curve fitting technique could then be applied; identifying and removing the outliers. This requires no extra setup time either as the data is captured autonomously. With the capturing of more data points it may also be possible to achieve an even more accurate location of AE signals than that which is possible with a conventional delta-t approach.

Although this approach has only been explored for a linear location problem it should be possible to directly apply it to a planar location problem. This has many advantages over the conventional delta-training method in not only the time but in terms of functionality. The ability to autonomously capture delta-t data enables large errors to be mapped in a relatively short period of time; for instance an entire wing area. In addition, much like the traditional approach, the properties of the material are not required to be known for the training unlike the modelling approach. This enables complex materials and structures to be mapped without the need for prior knowledge. This is particularly advantageous for the monitoring of aging structures. Furthermore, for a structure that has already been mapped, the experimental inverse technique offers a relatively quick mapping solution for remapping after structural modification for example in the case of a repair. However, 3D scanning laser vibrometry (or for that fact even a 1D scanning system) is not a low cost experimental technique. Therefore, the initial cost of the equipment and training required may make this approach unsuitable for widespread commercial application.

The modelling approach shows great promise. The Euclidean distance error achieved with both the conventional and modelled delta-t approaches for the linear investigation fell within the margin. This was a clear indication that the technique had potential. Only the out-of-plane component for the conventional delta-t technique was considered for the mapping of the complex geometry aluminium plate. This approach was taken as the two techniques were directly comparable and the most prominent wave component sensed by the physical sensor is out-of-plane.

Generally, in the complex geometry study it was found that there was consistent location results obtained when using the model-trained delta-t technique which correlated well with the experimentally trained delta-t method. When the binned number of AE events were plotted it was found that both training techniques grouped the events to the top half of the plate particularly around and above the 20mm hole. This was a vast improvement over the TOA techniques which sparsely and sporadically distributed the locations of the AE events over the entire plate. This did not clearly identify the presence of damage with even the relatively high binning of AE events still being comparable low to the delta-t locations. This is not suitable in an in-service application as studying these plots alone could suggest that the AE is related to background noise, hence causing a type II error.

It was found however there was a larger error experienced with the model-trained delta-t method than the experimental trained delta-t technique. There are a number of reasons why this is the case. The first and most likely reason is the waveform used in the LISA model to create the training dataset. In this study a 200kHz sine wave was used in place of an H-N source for simplicity of modelling. It was also previously proven to provide representative results (see section 4.5). In reality, an H-N source is more akin to that of a step input and as such a wide frequency range is excited. Because of this, it is likely that a higher frequency was excited by the H-N source in the experimental training. As the Lamb waves are dispersive the higher frequencies will travel faster and hence arrive at the sensor sooner. This will create differences in the delta-t training data and as such result in errors in location of AE events. An improvement in the location of the AE events may be achieved by modelling a source that is more representative of an H-N source (such as that of a step input) and using that for the creation of the training dataset. It is also worth noting that the frequency content of AE emitted from the damage may also be different from that created from the H-N source and, as such, would also result in differences in arrival times.

Another source of error with the model is that the sensors were modelled as point sensors where as in reality they have a sensor face diameter of 8mm. Because of this it could be said that the wave is sensed by the sensors during the experimental training at the sensors' circumference and not at the centre point where the sensor is located in the model. This difference in sensing location would result in a difference in arrival time and hence location of an AE event. Modelling the sensor and the sensor face may improve the location. Other sensor attributes such as the effects of mass dampening and the transfer function could also be investigated. However, this is worthy of a separate study in its own right and falls outside the scope of this initial investigation.

The accuracy of the model could also be a cause for the error in source location. The accuracy of the model can be divided into two sections; the material and the geometry. Considering the material accuracy, although representative material values were used it was assumed that the material was isotropic. Although this is a reasonable assumption for a metallic material, factors such as the rolling direction of the plate may cause a very slight anisotropy. Small deviations in wave speed with respect to the propagation direction would result in small location errors. This could be remediated by conducting a very simple experimental wave speed investigation. Although it is not possible to model anisotropic materials in the commercially available LISA package at present, it has been proven to be possible [140] by other means in the LISA environment. However, this may be equally achieved by applying a correction factor to the delta-t training data.

Regarding to the geometry in the LISA model, a 0.5mm global cube edge length was used. The thickness of the plate was actually 3.18mm but due to the edge length constraint this was modelled as 3mm thick. This difference in thickness would have resulted in a difference in the characteristics of the Lamb wave propagation, in particular the dispersive characteristics. A more representative model could be created by reducing the size of the global cube edge although by doing so more GPU on-board memory is required as well as time for iteration. Similarly, the shape of the holes was approximated using a midpoint circle algorithm. This gives the edges of the circle a reasonably coarse edge which may influence the Lamb wave interaction with the hole. Although it is not possible to fully remove this problem from this type of model it is possible to reduce the effect by reducing the global cube edge length. However, the extent to which this actually affects the results is unknown and would require further study.

A common location error that was observed when using both delta-t techniques was locating AE events within the holes where it is impossible for an AE event to physically occur. This is caused by the training data not considering the geometry of the specimen in its interpolation. The interpolation is an important feature of the delta-t training dataset as it enables AE events to be located that do not occur at the locations of the H-N sources although it does mean that when a hole is present, the training data interpolates over it. If the interpolation did consider the presence of features such as hole however a higher accuracy and precision in the location of AE events may be achieved. This has not previously been considered with the experimental training technique as the geometry of the specimen is not always known and is not vital for the successful location of damage events as demonstrated in this study. However, as the geometry has to be known for the creation of the training data in the LISA environment, it could be also be used to improve the delta-t interpolation and hence the location of the AE events.

Despite the errors in location witnessed in these investigations, it can be stated that the level of accuracy and precision achieved is suitable for a real-world application. Exact location of the damage is beneficial however if the margin of error is known a local inspection area can identified by an NDT technician for further investigation. This is analogous to a medical physician using an x-ray after a patient reports pain in specific area of the body. Knowing where to investigate will assist the detection of damage and continuing maintenance operations.

The training set took approximately eighteen hours to model in the LISA environment as 357 individual models had to be created (one for each node on the delta-t grid) which took approximately three minutes to iterate. The time that it takes to iterate can be significantly reduced in a few ways. This first is to reduce the length of the samples taken as only the arrival of the wave is required and waveform features such as edge reflections are surplus to requirements. This will reduce the number of required time steps and hence reduce the time required to iterate.

The sample rate also used for the model was 20MHz. Although this showed to produce good results, reducing the sample rate will reduce the number of samples taken and hence the number of time steps required. Care would need to be taken however to ensure that the fidelity of the measured wave is not compromised.

Both of these methods would significantly reduce the time required to create a training dataset as reducing the computation time would be applicable to all 357 runs of the model. Even so, an automated solution has many advantages as time is not required from an operator and it is also less subject to human error. However, another promising method to reducing the time required to create the training dataset is the inverse delta-t method that was used for the linear investigation. Only the conventional delta-t technique was recreated in the model for the complex geometry plate so as to be directly comparable to the experimental training. If the inverse technique was adapted to be used for the complex geometry plate and proven successful, the iteration time would be able to be reduced to below twelve minutes as a model would only be required to be run for each sensor rather than each node.

The short amount of time required to create a training dataset would be highly desirable from a commercial aspect. By rapidly being able to generate delta-t training data, different network designs can be modelled and assessed in terms of their performance. This will also enable data the AE to be located using the same training data. In terms of aircraft design, as the design of the structure matures, the sensor network can be designed and modelled accordingly thus a concurrent sensor network and structure can be designed. This is projected to result in mass savings of up to 15% at component level [14]. This could be envisaged as being a key tool within the design phase of an aircraft in a similar manner to finite element models which are used for conducting stress analysis.

The ability to model delta-t training data would also enable multiple training sources to be used (such as an AE source representative of a fatigue crack for example). This could then be used to assist in characterising the damage in a similar sense to how the human nervous system can differentiate between the pain experienced from a cut and a burn for example. This could lead to a much more robust damage detection system.

Producing delta-t training data from models also has the advantage of being able to simulate AE sources within a material not just on the surface as is achieved in the experimental training. This could lead to damage such as cracks being detected and located below the surface adding an extra dimension to the delta-t location ability.

Only isotropic metallic materials have been considered in this investigation. With the increasing use of composites in aircraft structures, it would be beneficial to create a modelled delta-t training dataset however the current commercial version of LISA restricts this. As previously mentioned however, previous studies [140] have demonstrated that the LISA technique can be used for the successful modelling of composites. This would be highly advantageous whilst opening a range of possibilities for the technique presented.

Evidently, it has been shown that the TOA method of AE location has significant detrimental issues with the precision and accuracy of locating AE events. The experimentally trained delta-t location method has been shown to have a massive gain in AE event location performance. The model delta-t training set too has demonstrated that significant location performance can be achieved over the TOA method albeit to a lesser extent than the experimentally trained delta-t. Nevertheless, the potential for training AE sensor networks to locate real AE events using a computational model has clearly been demonstrated and recommendations on how the accuracy may be further improved have been discussed.

8. Optimisation of an Acoustic Emission sensor network using a Local Interaction Simulation Approach

8.1. Introduction

The optimisation of an AE sensor network is challenging for many reasons. Primarily, as the AE that is used for damage detection in structures only occurs when a damage event occurs, it is not easy to trial several different sensor networks under real loading conditions. Furthermore, although there are regions of a structure from where it is more likely for AE sources to originate (i.e. areas of high stress concentration); it is possible for damage to occur at many different regions of a structure (as in the case of impact damage). Therefore a multi-source, multi-sensor approach is required.

This approach is difficult to achieve experimentally as many sensors are required which usually is not possible due to cost constraints. Therefore for a feasible experimental investigation to be conducted, a sub-set of locations is considered, the responses from the many source locations would be recorded before removing the sensors and recoupling them to the new candidate locations and conducting the many source inputs again. However, this is not commonly feasibly due to time constraints; especially when considering the curing time of couplants.

A far more desirable solution to conducting an AE optimisation study is through the use of numerical models. This approach allows for a multi-source, multi-sensor investigation to be conducted in a relatively short period of time without the requirement for an operative or lots of expensive equipment. This too is advantageous from a sensor network design point-of-view as many sensor network designs can be considered for many different structural design solutions.

As demonstrated in the previous study (section 7), this also has the added advantage of being able to use the signals sensed in the models as training data for the location of the damage.

This study calls upon the rapid convergence ability of LISA to produce a series of models that simulate the initiation of Lamb waves from many source locations and sensed at numerous candidate sensor locations. Through using statistical techniques and the effective optimisation convergence of a GA, differing sensor networks can be assessed for performance and the best solution can be found for sensing.

8.2.AE sensor network optimisation on a flat aluminium plate

To investigate the application of the proposed methodology a sensor network was optimised for a flat, isotropic aluminium plate. This approach was taken as the results expected from this initial study were expected to be reasonably intuitive. This therefore enabled confidence to be established in the technique before trialling it on a more complex structure.

A 3mm 6062-T6 aluminium plate of dimensions 1250mm x 320mm was created within the LISA environment for the investigation. An area of investigation of 800mm x 280mm was outlined for the investigation in order to reduce effects of edges that may be detrimental.

Within the area of investigation, a 20mm x 20mm grid of candidate sensors were placed within the model totalling 615 candidate sensor locations. In regard to the placement of real sensors such as a Nano30 sensor which has a face diameter of 8mm, this would allow sensors to be placed side by side. Within the same area of investigation, locations for the representative sources were placed on a 10mm x 10mm grid as shown in Figure 88. Note that there were cases where the sources were at the same locations as the sensors.

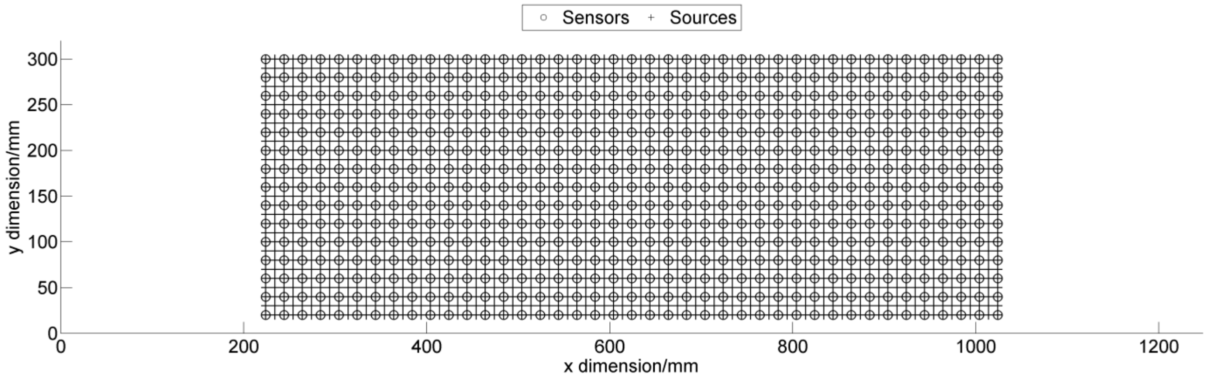

Figure 88. Candidate sensor locations and source locations for the flat plate optimisation study

As previously discussed, a source truly representative of an H-N source is challenging to model. Therefore, for this study a 200kHz five-cycle, Hann-windowed excitation was used as had been used previously (section 7.2.4). For this initial investigation, this was not deemed to be significant as this optimisation approach was going to consider the intensity of the different locations and therefore only a source that was repeatable was required.

A separate model was run for each source location at a sample rate of 20MHz for four thousand time steps (equivalent to 200µs) which was sufficient in order to ensure that that the wave was sensed at on the longest source-sensor path.

8.3.Assessing sensor location suitability

There are numerous metrics by which the suitability of a sensor network can be assessed. These include (but are not limited to) wave packet energy, peak energy and time of arrival. However, in order to make the technique relevant for use with commercially available AE systems, considerations must be made of these AE systems are triggered for the acquisition of a transient waves. This is commonly achieved by the system continually monitoring the signal from the sensors and when the amplitude of a wave crosses a threshold value, the transient wave is recorded with a pre-trigger to capture the arrival of the wave. Therefore the metric by which the sensor locations will be assessed will be based on the intensity of the peak amplitude.

Commercially available AE systems typically measure the intensity of an H-N source at the sensor at 100dB. Therefore to make this representative, the maximum responses for a source at the same location as a sensor were calculated to be equal to this and diminish as propagation distance increases. As the material is isotropic and no features are present on the structure, this will lead to a circular exponential gradient for each sensor location. Note that for this study only the out-of-plane component of the modelled Lamb wave has been considered as it is the dominant component typically sensed by commercially available sensors.

8.3.1. Time window

In order to determine the peak amplitude of the arriving wave packet a 30µs time window was taken. The starting point of the time window was determined at 12.5µs before the amplitude of the wave crossed the threshold value. The threshold level was calculated by being 40% of the maximum value of the entire waveform in similar manner to the approach used in section 5.3.4 and is visually represented in Figure 42. A global threshold value was not set as it was desirable to determine the peak amplitude response map for the entire plate. An example of a response map is presented in Figure 89.

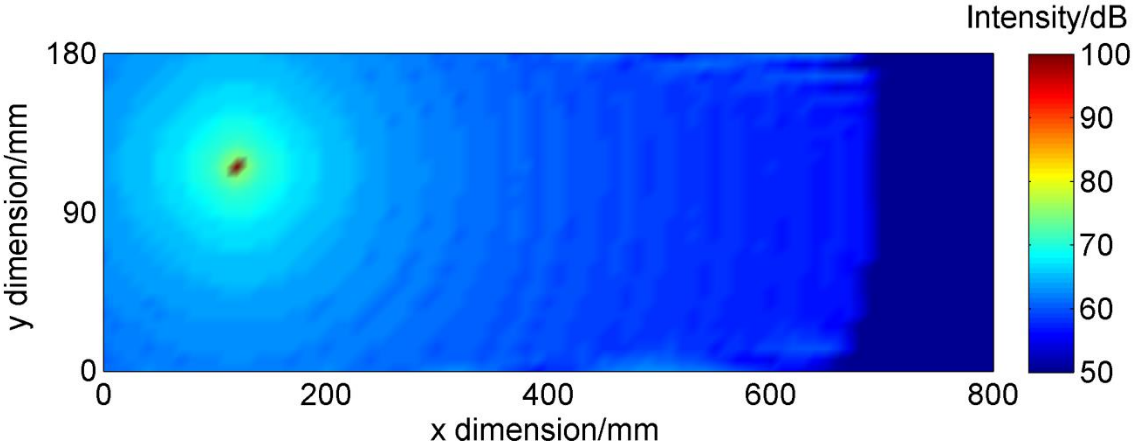

Figure 89. An example of a response map for a single sensor. The location of the sensor is denoted by the region of high intensity (red).

8.4. Optimisation problem

As with the optimisation of the AU sensor network, the number of possible different sensor network solutions is large and increases with the amount of sensors added to the network (up to half of the number of possible candidate sensors) due to the number of solutions being proportional to the binomial coefficient. This is exacerbated as it is possible to consider the same sensor network multiple times. For instance; a three sensor network could be considered as A, B, C or B, C, A or C, B, A and yet the ultimately achieve the same solution. The number of possible sensor network solutions for three, four and five sensor networks is presented in Table 5.

Table 5. Number of possible different network solutions for different network sizes.

Sensor network size	Possible number of different sensor networks
1	615
2	188805
3	38.6×10^{6}
4	5.9×10^{9}
5	7.2×10^{11}

8.4.1. Fitness functions

To assess the fitness of any given sensor network, the response maps are first considered such as the example presented in Figure 89. In the case where more than one sensor is in the network the value for from each source location received by each sensor was compared and the maximum value was taken to form a single intensity map.

This can be demonstrated by the flow chart presented in Figure 90.

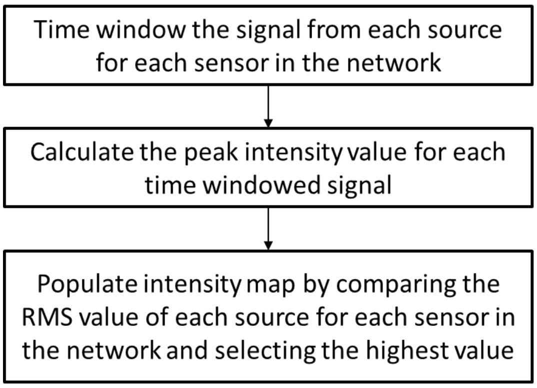

Figure 90. Flow chart for populating the intensity map

An example of two-sensor network is presented in Figure 91.

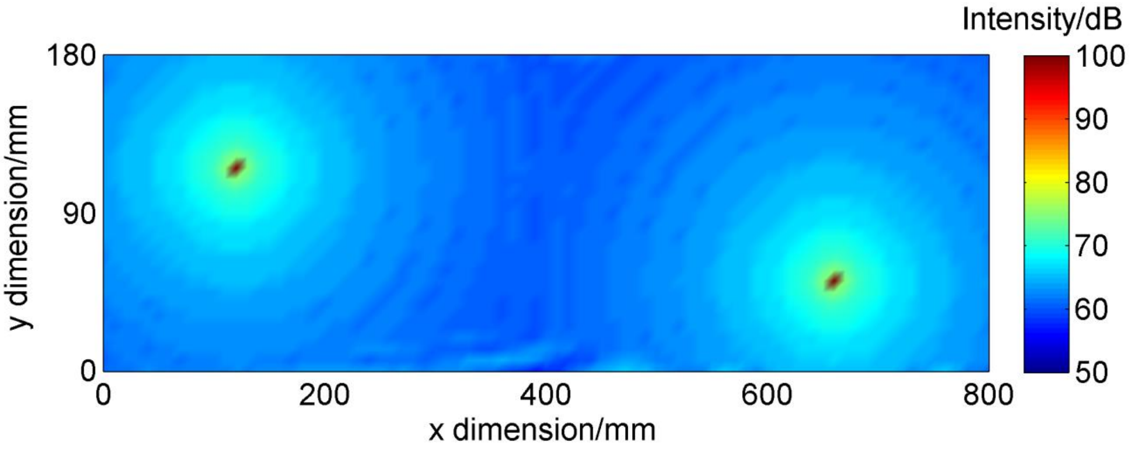

Figure 91. An example of a two sensor intensity map plot used to determine the fitness of a sensor network.

Once the intensity map for a particular candidate sensor network has been established, the fitness of the network can be established. For this investigation, the fitness was first established by the sum of the response from each source location. This can be expressed mathematically as demonstrated in Equation (29).

$$fitness = \sum_{i=1}^{N_{sources}} \begin{pmatrix} \max(x_1) \\ \vdots \\ \max(x_n) \end{pmatrix} \tag{29}$$

$$\boldsymbol{where\ x\ is\ a\ candiate\ sensor\ in\ the\ network}$$

$$\boldsymbol{N.B.} \begin{pmatrix} \mathbf{max}(\boldsymbol{x_1}) \\ \vdots \\ \mathbf{max}(\boldsymbol{x_n}) \end{pmatrix} \boldsymbol{represents\ the\ intensity\ map}$$

This approach was taken with the objective being to maximise the coverage achieved by the sensor network. This particular fitness function achieves this based on the assumption that a good coverage would result in high intensities from all sources. Therefore, it was established that this would result in the intensity plot having a higher total value.

The fitness function presented in Equation (29) is based on the assumption of reasonably even coverage. However, this could be skewed by localised areas of high intensity despite regions of extremely low intensity being present. This is something that may be highly prevalent when features are present on the structure. Therefore an alternative fitness function was also developed which sought to generate a more even spread of intensity. This fitness function used the minimum intensity value from an intensity map as the fitness. This approach was taken as it was seen that the best network solution was one that had a high minimum value. Therefore the GA sought to maximise the minimum value. This is expressed in Equation (30).

$$fitness = \ min\begin{pmatrix} \max(x_1) \\ \vdots \\ \max(x_n) \end{pmatrix} \qquad \textbf{(30)}$$

$$\boldsymbol{where\ x\ is\ a\ candiate\ sensor\ in\ the\ network}$$

$$N.B.\begin{pmatrix} \max(x_1) \\ \vdots \\ \max(x_n) \end{pmatrix} represents\ the\ intensity\ map$$

It is worth noting that for both of the fitness functions used that solutions where the same sensor location is selected for more than one candidate location (i.e. A, A, B in a three sensor network), the solution would be assessed to have a poorer fitness than a network with unique candidate locations. Therefore, the optimiser discards these solutions without the need for an additional penalty value.

8.4.2. Genetic algorithm configuration

As with the previous AU optimisation study (see section 5) a genetic algorithm was used as the optimiser for this investigation. Binary encoding was once again used with the respective binary gene referencing a particular candidate sensor. As a 10-bit binary gene was required to be used (as the number of candidate sensors ranged from 1-615), penalty values of -10,000 were assigned to the genes that that exceeded this limit. This would ensure that these solutions would be discarded by the optimiser. In the case of multi-sensor networks, the genes were placed side-by-side to form a chromosome which defined that particular candidate sensor network. For details of GA encoding the reader is referred to section 2.10.1.

The parameters of the GA previously used (see section 5.4.3) were retained for this study as they had been proven to demonstrate good results on a similar sized optimisation problem. Convergence was deemed to have been achieved when the best solution had not been improved upon for two thousand generations.

8.5.Results

The results for the two different cost functions are presented in this section for optimising the location of AE sensors on a flat aluminium plate.

8.5.1. Sum of maximum values GA convergence

The convergence of the GA for the increasing sensor network sizes are shown in Figure 92 where the sum of the maximum values was used to determine the sensor network fitness.

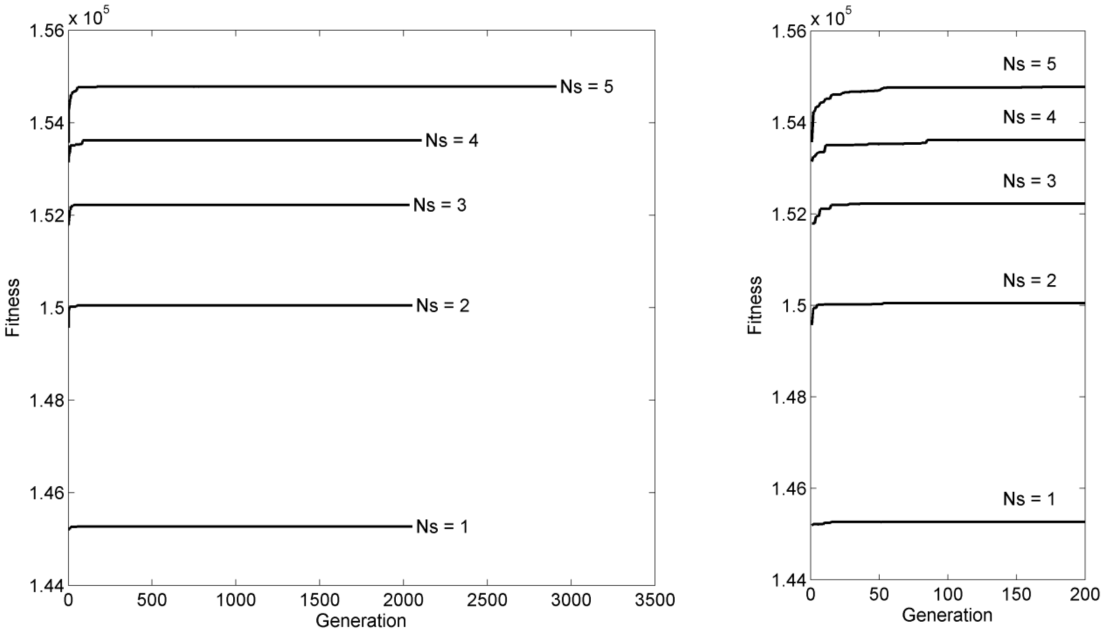

(a) (b)

Figure 92. (a) Convergence performance of the GA for increasing sensor network size (Ns) (b) the first 200 generations where convergence occurs (maximum fitness).

It is evident that the GA converged upon a solution within the first two hundred generations as presented in Figure 92b for all sensor network sizes. This demonstrates the ability of GA to rapidly converge on the optimal solution with the GA running for around 90% of all of the generations to ensure convergence. Thus, the number of generations required to ensure convergence can be rapidly reduced. This may however be attributed to the size of the initial population. The initial population size is calculated by forty times the sensor network size being optimised (see section 5.4.3). For example, the initial population for the five sensor-network is five thousand. Although this may appear to be a large initial population it is in fact 6.9 x 10^{-7}% of the entire search space. Determining this number of solutions does incur a time penalty but it does achieve a prompt convergence in terms of the number of generations required. The time taken to compute maybe improved upon by reducing the size of the initial population. However, the algorithm would possibly require to be run for a higher number of generations to ensure convergence. A technique that may remediate this however could be to employ a variable mutation rate. This would enable a wide area of the search space to be sampled during the early generations. As the generations increase, the mutation rate would reduce to enable the GA to converge on the optimal solution. This however falls outside the scope of this investigation and is worthy of a standalone study.

8.5.2. Sum of the maximum values (fitness)

The sum of the maximum values for the optimal intensity maps as the network size increases is presented in Figure 93. For this particular optimisation, this was how the fitness was assessed.

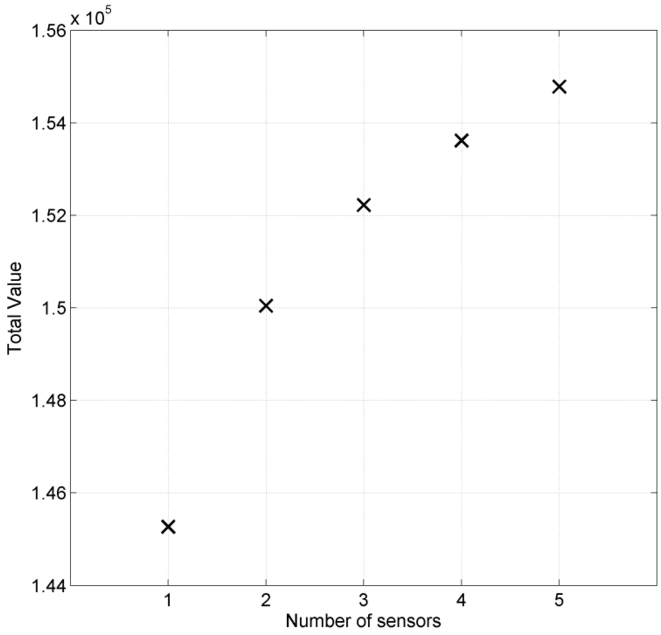

Figure 93. The sum of the maximum values of the optimal intensity map with increasing sensor network size when the objective is to maximise the total value.

As to be expected, the sum of the maximum values for the intensity maps increases as more sensors are added to the network. This is logical as with the addition of more sensors, the coverage increases and thus, the total of the intensity map will increase. It is worth noting that the best possible total value for an intensity map where all of the candidate sensor locations are used is 1.90 x 10^5 and therefore a value greater than this cannot be achieved in this study.

When considering the one-sensor network, the performance of the fitness of the sensor network is 1.46 x 10^5 which is 76.8% of that possibly achievable. Interestingly, significant increase in fitness of 2.6% is observed as the size of the sensor network increases from one-sensor to two sensors. However, as more sensors are added to the network, the rate at which the fitness increases starts to reduce. This suggests that as more sensors are added to the network, the performance gains reduce at a reducing rate. As this is the case, it would eventually be a case that as more sensors are added to the sensor network, minimal performance gains would be achieved.

The five sensor network established in this optimisation study achieved a fitness of 81.6% of the total achievable fitness. Although, this seems to be high level of fitness it has to be stated that the area of investigation is small and also simple. Nevertheless, this does demonstrate that for simplistic problem such as this, AE sensing could be used to monitor a large area while still establishing a high degree of fitness.

8.5.3. Minimum value of the optimal intensity map

Although the minimum value was not used to assess the fitness (Equation (30)) in this optimisation study, the minimum values for each sensor network are presented in Figure 94 to represent the minimum intensity value.

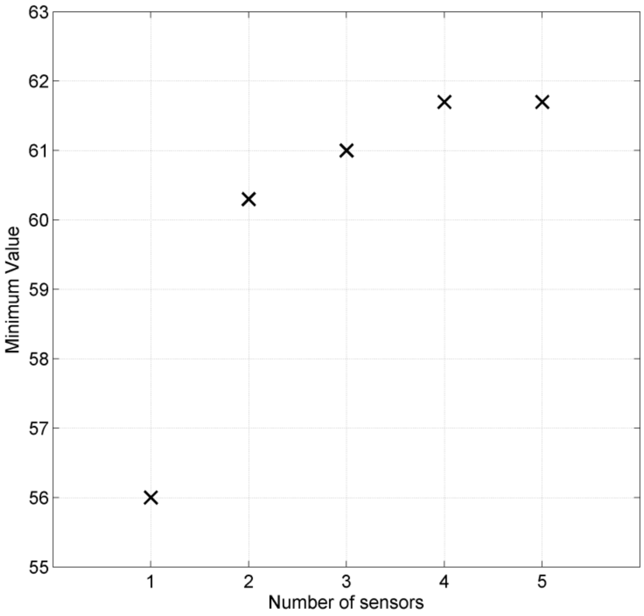

Figure 94. The minimum intensity value in the intensity map with increasing sensor network size when the objective is to maximise the sum of the maximum values (maximum fitness).

There is a similar trend with the minimum intensity value to that of the sum of the maximum values presented in Figure 93 as to be expected. A significant increase of 7% in the minimum intensity is observed as the size of the sensor network increases from a one-sensor network to a two-sensor network. As the size of the sensor network continues to increase, the rate at which minimum intensity within the area of investigation increases reduces significantly. A near-linear rate is observed as the network sixe increases from two sensors to four. This does not follow the reducing rate trend observed with the sum of the maximum values. There was also no change in minimum intensity as the size of the sensor network increased from four sensors to five. This suggests that although the sum of the maximum values was observed to increase, the spread of the responses achieved by the sensor networks was perhaps not evenly distributed.

8.5.4. Optimal location results – sum of the maximum values

The results for the locations of the sensors as the size of the sensor network increases are presented in Figure 95. When considering the one-sensor network, the optimiser places the sensor in the centre of the plate. This is logical as this is at the centre of the y and x-dimensions and the material is isotropic and the structure is simplistic. It is possible, that an anisotropic material and or a more complex structure would skew the positioning of the sensor; particularly if the structure under investigation was asymmetric. The decay of the amplitude is exponential with lower intensity values being measured from the sources further away from the sensor. This illustrates that that the region where high intensity values can be detected (70dB+) is highly local to around the sensor and that to achieve a higher level of fidelity, more sensors are required.

When a second sensor is added to the network, another logical solution is achieved. The placement of the two sensors in this network places each sensor along the midpoint of the y-dimension and centrally spaced between the x-dimension boundaries and the x-midpoint. This achieves a significantly greater coverage of the area of investigation than that of the one-sensor network.

As with the two and one-sensor networks, the three-sensor network produced by the optimiser is logical. The three sensors are spaced equidistance along the central x-axis. It is visually apparent when comparing the first three sensor networks, that that the coverage is increasing (and therefore the ability to detect AE events of a lower intensity) by the reduced regions of low intensity (dark blue).

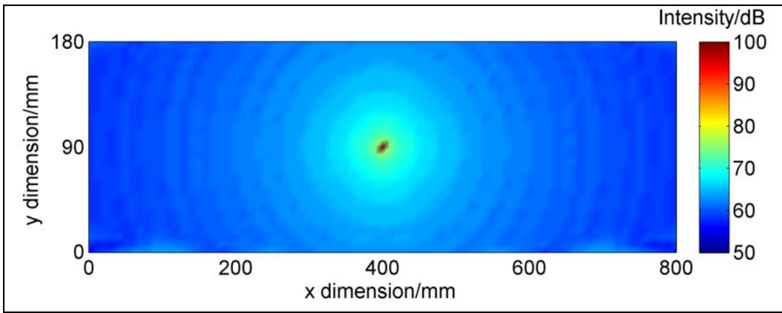

Ns = 1, minimum intensity = 56.0dB, total value = 1.45 x 10^5

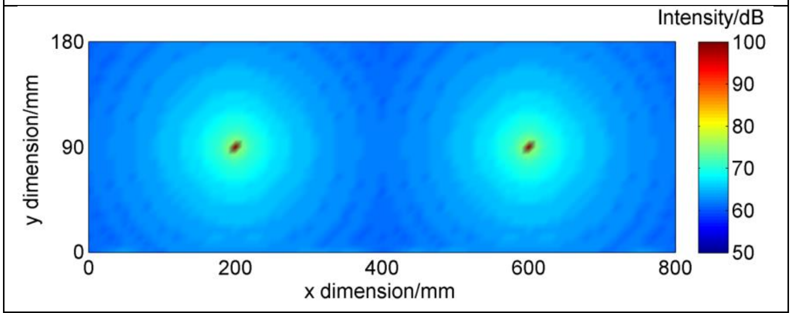

Ns = 2, minimum intensity = 60.3dB, total value = 1.50 x 10^5

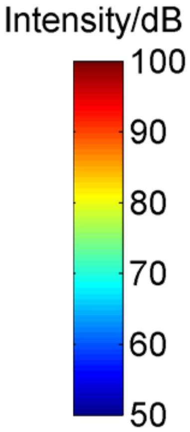

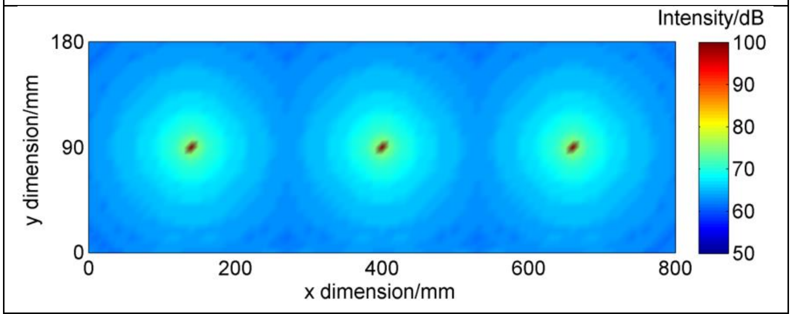

Ns = 3, minimum intensity = 61.0dB, total value = 1.52 x 10^5

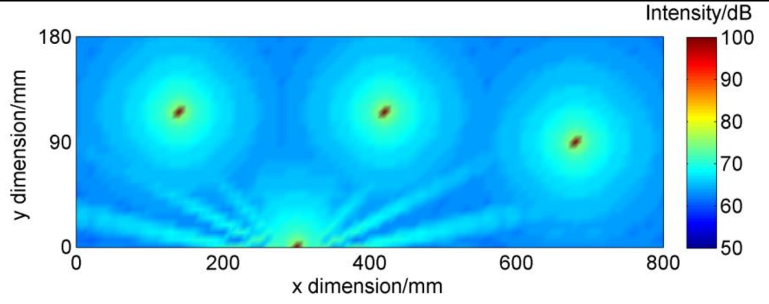

Ns = 4, minimum intensity = 61.7db, total value = 1.54 x 10^5

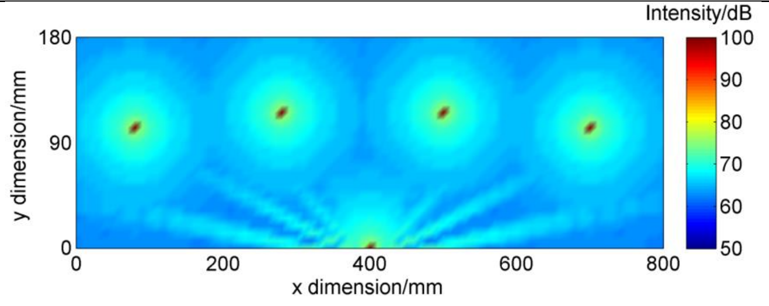

Ns = 5, minimum intensity = 61.7dB, total value = 1.55 x 10^5

Figure 95. Optimal location of sensors for increasing sensor network size (Ns) when the fitness is assessed using the sum of the maximum values (Note the locations of the sensors are at the areas of high intensity (red)).

When a four-sensor network is considered, a less logical solution is derived. However, when multiple runs (five for each sensor network size) of the GA were conducted, the GA consistently converged on this solution establishing a high level of confidence in these results. Three sensors are positioned along the length of the plate however the fourth sensor is positioned on the lower boundary of the area of investigation. It is worth noting that this is not the edge of the panel (see Figure 88). The plate in this investigation was modelled with edges and as such it appears that this has influenced the maximum value intensities achieved by this sensor location. It is likely that the effects of constructive and deconstructive interference have resulted in an interference fringe pattern. Unlike the circular decay exhibited by the other sensors in the network, this interference fringe pattern has fringes that extend with regions of high intensity. As such, this would have a significant influence on the sum of the maximum values but may also have a negative effect on maximising the coverage as the fringes are of high intensity but are localised.

Nevertheless, this would exist in a real AE setup as phenomena such as reflections would be present. Therefore, it is not unreasonable that the effect of a reflection may result in constructive interference which would possibly enable an AE system to be triggered. Interestingly, when the GA was ran multiple times, a different solution was derived with an identical fitness value which was a mirror image around a vertical centreline. This demonstrated the suitability of the solution.

A similar observation is made when a five-sensor network is considered. The optimiser places the four of the five sensors in an arc in the upper half of the plate with the fifth sensor positioned on the lower boundary. Once again, a fringe pattern is observed. This fringe pattern covers a wide area of the lower half of the plate although there are areas of relatively low intensity between the regions of high intensity giving the pattern a ‘tiger-stripe’ appearance. Again, this is not perhaps immediately obvious as it is perhaps not intuitive to consider this type of phenomena when considering the placement of sensors. Similarly, when the GA was ran multiple times, a mirrored solution was also found with the interference fringe at the top of the plate.

8.5.5. Maximising the minimum value GA convergence

As previously mentioned, a second fitness function was investigated with the objective of maximising the minimum value in the maximum intensity plot. The idea being that this would possibly be a better method of maximising coverage and eliminating solutions with areas of localised high intensity.

The results of the convergence of the GA for this fitness function are presented in Figure 96.

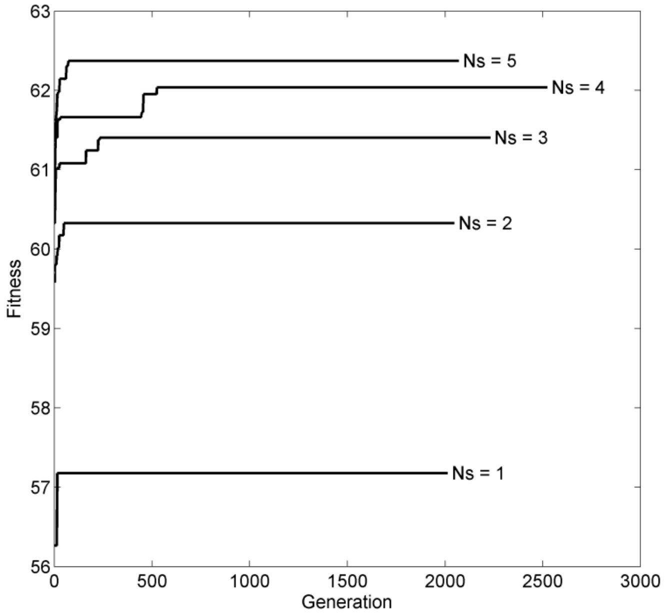

Figure 96. Convergence performance of the GA for increasing sensor network size (Ns) (maximum fitness)

Aside from the three and four-sensor networks, the GA converged rapidly on the optimal solution as observed previously with the other fitness function. The three sensor-network took more generations to converge on the optimal solution although it achieved this in less than five hundred generations. This is however not a significant cause for concern as the start position of the GA is quasi-static and therefore this higher number of generations to converge is likely to have been due to the algorithm starting in a weaker region of the search space. The four-sensor network took the most number of generations to converge on the optimal solution. Convergence was achieved in just over five hundred generations. Again this demonstrates the rapid convergence of this GA and its suitability for optimising this type of problem.

8.5.6. Minimum value of the intensity map (fitness)

The maximised minimum value of the intensity map as the size of the network increases is presented in Figure 97. As expected, the minimum value (fitness) increases as more sensors are considered. This displays a similar trend to that observed when using the first fitness function (Equation (29)). Once again, a considerable improvement in fitness is observed as the network size increases from one sensor to two sensors. This then reduces at an decreasing rate as more sensors are considered. This differs somewhat however from the trend observed with the minimum values when using the previous fitness function.

The best possible minimum value achievable is when all 615 sensors are considered. This was calculated to be 73.1dB. When considering the one-sensor network, the maximised minimum intensity value is 57.2dB which is 78.2% of what is achievable when all sensors are considered. This is a greater percentage than what was achieved when a similar metric was used to compared the first fitness function however it is still of the same order of magnitude.

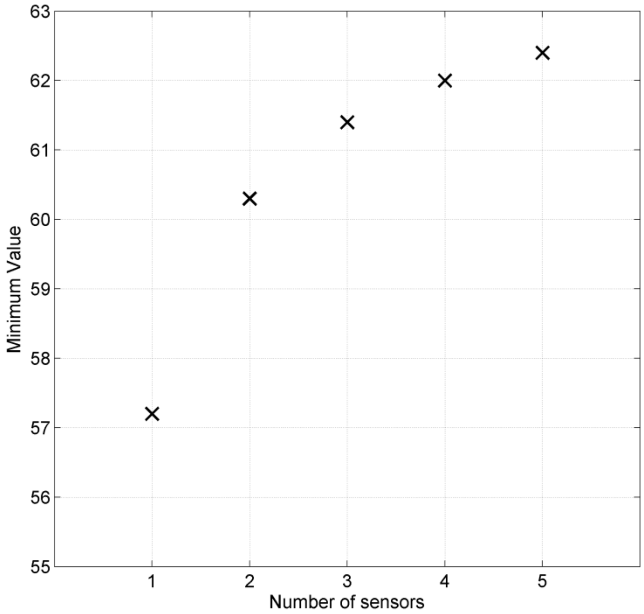

Figure 97. Minimum value of the intensity map as the network size increases (Ns) when the objective is to maximise the minimum value of the intensity map.

Unsurprisingly, the fittest solution was found with that of a five sensor network. The five sensor network achieved a fitness of 62.4dB which equates to 85.4% of what is possible when all sensors in the network are used.

For all of the sensor networks other than the two-sensor network, the maximised minimum value was greater than what was presented in Figure 94 which implies that the fitness functions do not produce identical solutions.

8.5.7. Sum of the maximum values

The sum of the maximum values is presented in Figure 98 for comparison with the first fitness function presented in Figure 93. As expected, the sum of the maximum values increases as more sensors are added to the sensor network. For all of the solutions there is marginal difference when compared to the sensor locations derived when maximising the sum of the maximum values of the intensity map is the objective.

This is interesting as this demonstrates that it is possible to still maintain a high value for the sum of maximum values with the objective of maximising the minimum value. This is not something that is necessarily achievable the other way around.

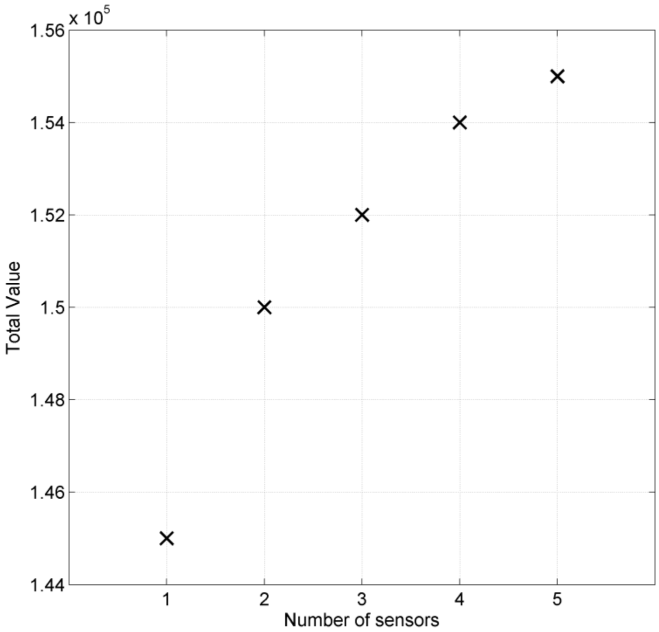

Figure 98. Sum of the maximum intensity maps for increasing sensor network size (Ns) when the objective is to maximise the minimum value of the intensity map.

8.5.8. Optimal location results – maximising the minimum value

The optimal locations for when the minimum value of the intensity map is maximised is presented in Figure 99. As with the one-sensor solution presented in Figure 95, the optimiser positions the sensor at the centre of the plate. This is, of course, logical as previously discussed however; it is worth noting that this optimiser places the sensor in the candidate location above that achieved with the previous optimiser. This is most likely due to the small interference fringes (most likely caused by reflections) along the bottom boundary.

The solution derived for the two-sensor network using this fitness assessment is identical to the previous fitness assessment. This therefore demonstrates the suitability of this this sensor network while also being respectively logical.

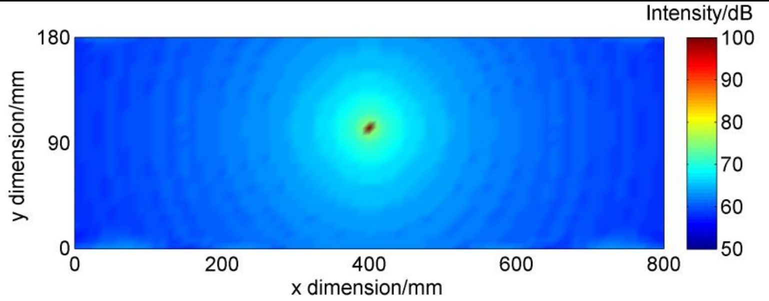

Ns = 1, minimum intensity = 57.2dB, total value = 1.45 x 10^5

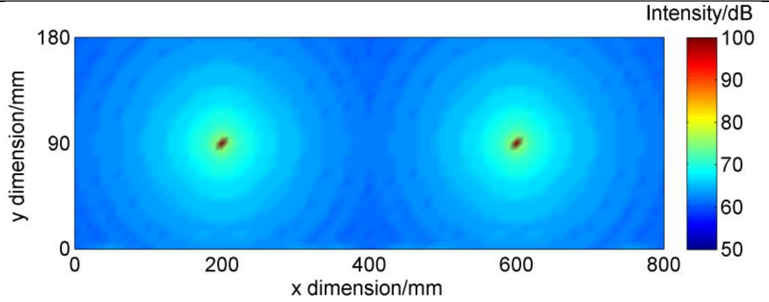

Ns = 2, minimum intensity = 60.3dB, total value = 1.50 x 10^5

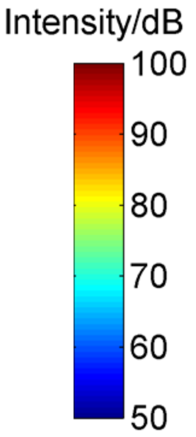

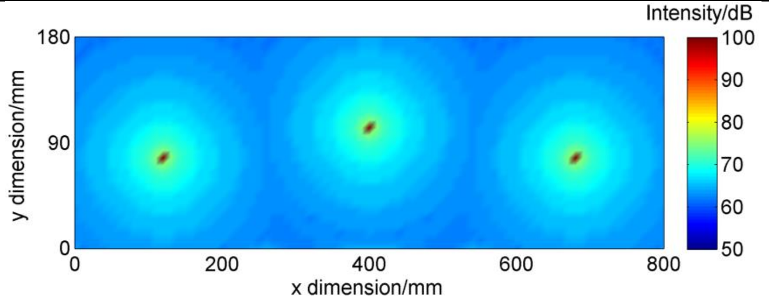

Ns = 3, minimum intensity = 61.4dB, total value = 1.52 x 10^5

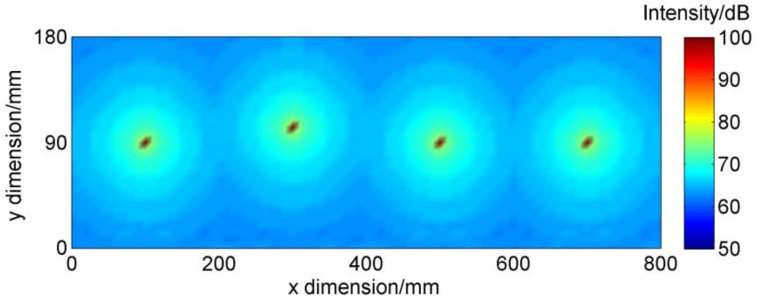

Ns = 4, minimum intensity = 62.0dB, total value = 1.54 x 10^5

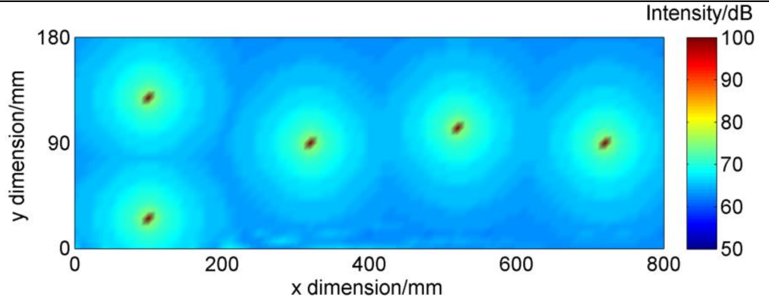

Ns = 5, minimum intensity = 62.4dB, total value = 1.55 x 10^5

Figure 99. Optimal location of sensors for increasing sensor network size (Ns) when the fitness is assessed by maximising the minimum value of the intensity map (Note the locations of the sensors are at the areas of high intensity (red)).

Significant differences in the positioning of the sensors from the previous fitness assessment method are seen from the three-sensor network onwards. The three-sensor network when maximising the minimum value of the intensity map, places the three sensors in a shallow arc with the middle sensor positioned at the above the centreline and the sensors on either side positioned below. This differs from the flat distribution observed when using the first fitness assessment method. This achieves a better coverage however as the minimum intensity value in the map is 61.4dB as opposed to 61dB achieved with the previous fitness assessment.

The four-sensor network produced by using this fitness assessment positions the sensors along the centreline of the plate with the second sensor from the left positioned slightly above the centreline. It is worth noting that by using this fitness assessment method, the optimiser does not converge on a solution that induces interference fringes in the intensity maps as previously shown in Figure 95. The minimum value in this intensity map is also greater than that achieved in Figure 95 which demonstrates that a better spread can be achieved and that the interference fringes introduce localised regions of high intensity.

The five-sensor network solution presented in Figure 99 differs dramatically to the solution achieved when maximising the sum of the intensity maps. The sensors are positioned with three of the sensors centrally on the right of the plate and the remaining two sensors located to the left above and below the centreline. As with the four-sensor solution, the sensors positions do not use the interference fringe pattern effect due to reflections as seen when the positions were determined using the maximum sum of the total values. As a result this achieves network of sensors that has a more even spread of the intensity without localised regions of high intensity.

8.6. AE sensor network optimisation on a complex geometry aluminium plate

Applying this approach to a flat plate has enabled a degree of confidence in the method to be established. However, it is not common in practice that the structure that requires monitoring is as simplistic and in which case; the placement of the sensor is perhaps not a hugely influential factor due to the ability of even a small network size to produce a suitable coverage.

To further investigate this methodology for the placement of sensors on a more complex structure a series of holes were positioned on the plate in order to affect the wave propagation in a similar manner to that of the virtual delta-t investigation (see section 7.4).

A total of fifteen 32mm holes were created at various locations on the plate as shown in Figure 100.

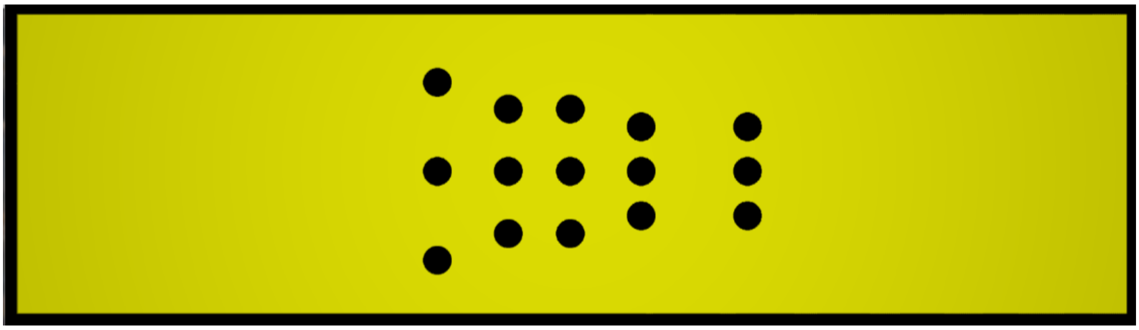

Figure 100. The complex geometry plate in the LISA environment.

For consistency, the same locations for the sensors and the sources were used as was used in the flat aluminium plate investigation. The positions of the sources and the sensors are presented in Figure 101.

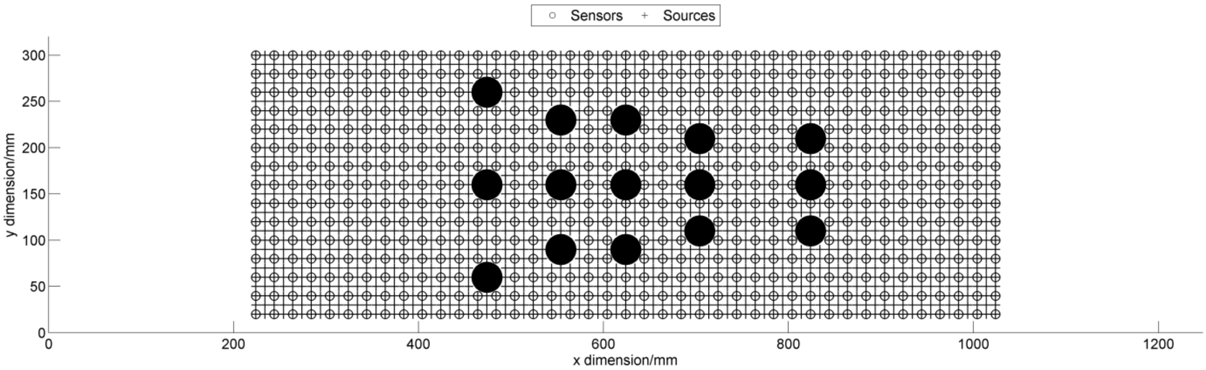

Figure 101. The location of the sources and the sensors on the complex geometry plate. The location of the holes is denoted by the black circles.

Where sources were located in a hole, the response measured at all of the sensors was set to zero in order to ensure that the optimiser would not consider sources in this region. Similarly, the sensors located within the hole were given penalty values to ensure that they were not selected by the optimiser. This resulted in 584 sensors and 2214 sources available.

Due to the presence of the holes, the longest source-sensor path required the model to be run for a 7000 time steps (which equates to 350μs). This ensured that the entirety of the first wave packet was captured along the longest source-sensor path.

All parameters of the GA were kept the same for the complex geometry plate and both fitness functions were used for assessment.

8.7.Results

The results for the complex geometry plate are presented in this section. Both fitness functions presented in Equations (29) and (30) were used for assessing the fitness and the results are presented respectively.

8.7.1. Sum of maximum values GA convergence

The convergence of the GA observed when the fitness is assessed using the sum of the maximum values is presented in Figure 102 for increasing sensor network size.

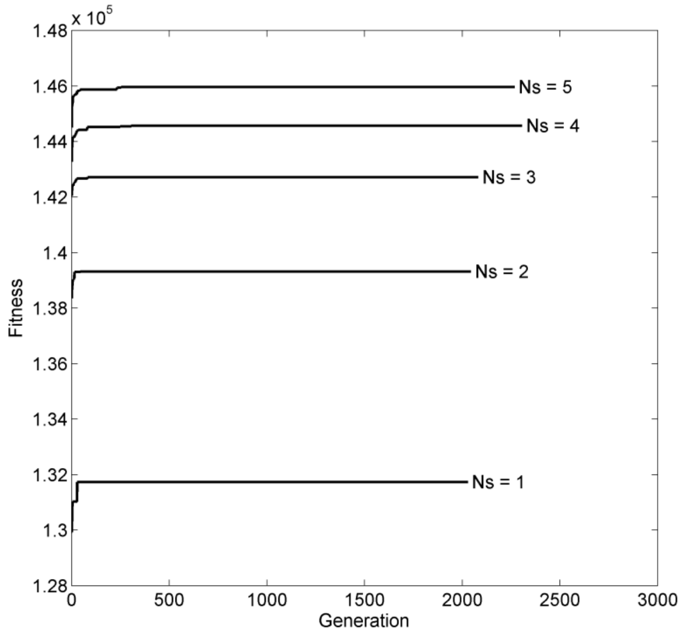

Figure 102. Convergence performance of the GA for increasing sensor network size (Ns) (maximum fitness)

It is evident that for all of the sensor network sizes, convergence occurred within the first few hundred generations. This is not too dissimilar to the convergence trend observed with the flat aluminium plate. This is of interest especially considering the additional complexity of the search space introduced with the complex geometry.

The convergence observed in this optimisation study was more rapid than what was observed when maximising the minimum value of the intensity map for the flat aluminium plate which infers that this this method of fitness assessment enables efficient convergence.

8.7.2. Sum of the maximum values (fitness)

The sum of the maximum values is presented in Figure 103 for increasing network size. For this optimisation study, this was used as the method of assessing fitness.

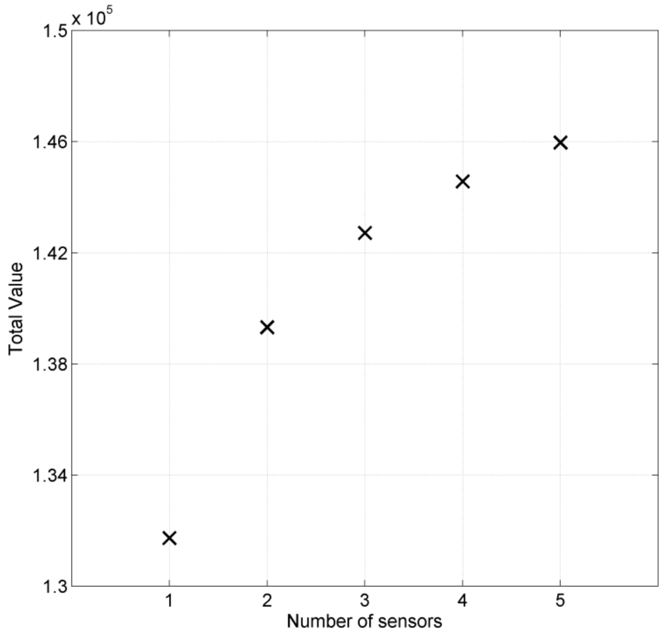

Figure 103. The sum of the maximum values of the optimal intensity map with increasing sensor network size when the objective is to maximise the total value.

As with the studies conducted on the flat aluminium plate, the sum of the maximum value increases as more sensors are added to the network. The similar trend is observed also with a reduction in the rate in which the sum of the maximum value increases as more sensors are added.

When comparing the results from the study on the flat plate, presented in Figure 93, it is evident that the sum of the maximum values is significantly lower. This can be mostly attributed to two factors; missing sources that were located within the holes and the effect of the holes on wave propagation. When considering the second factor, this is significant as when the Lamb wave interacts with a boundary (in this case the edge of the hole) some of the Lamb wave energy is transmitted along the boundary whereas some of it is reflected. This division of energy will result in lower intensities as only the first wave packet is considered and it is likely that the reflected wave packet would be not considered. Nevertheless, this immediately demonstrates that for more complex structures, a larger sensor network would be needed to maintain the required level of probability of detection.

The best possible sum of the maximum values can be achieved when all of the 584 candidate sensor locations are in use. This results in a value of 1.80 x 10^5dB. When considering the single sensor network, the network achieves a sum of the maximum values that is 72.8% of what is possible. This is lower than the 76.8% achieved on the flat plate. When the five-sensor network is considered, the percentage of the best achievable value raises to 81.1%. This is comparable to the value achieved with the flat plate of 81.6%.

8.7.3. Minimum value of the optimal intensity map

The values for the minimum values of the optimal intensity maps with increasing sensor network size are presented in Figure 104.

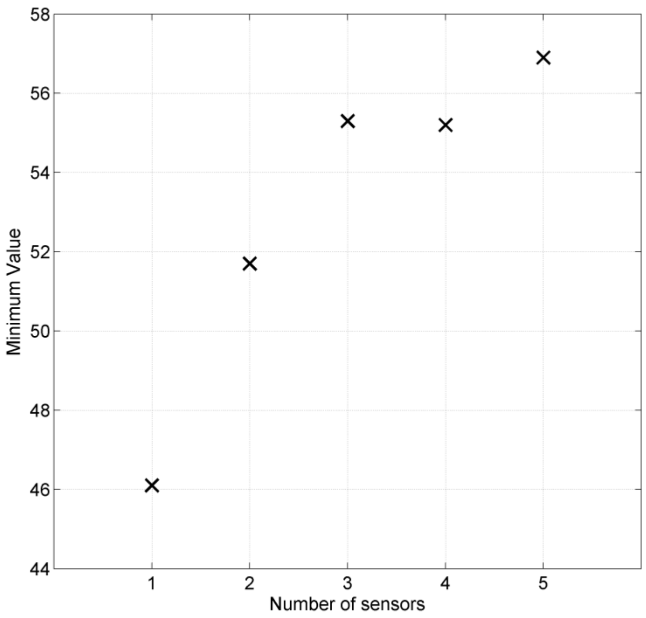

Figure 104. The minimum intensity value in the intensity map with increasing sensor network size when the objective is to maximise the sum of the maximum values.

On initial observation it is evident that, with the exception of the four-sensor network, there is a trend that the minimum intensity value increases as the size of the sensor networks increase. A high level of confidence is established in these results as the GA was run multiple times and consistently converged on the same results.

When comparting the minimum values with those of the flat plate, it is evident that the minimum values are significantly lower. This is mainly due to the reduced wave propagation caused by the presence of the holes. The minimum value obtained with the flat plate for a single sensor is greater than that of the four sensor network for the complex geometry plate. This reinforces that in order to maintain a high level of coverage; more sensors are required within the network for complex structures.

The four-sensor network showed a small reduction in the minimum value of the intensity map compared to that of the three-sensor network. Although the four-sensor network showed an increase in the value of the sum of the maximum values the reduction in the minimum value infers that the coverage is not as good. This therefore suggests that the solution for the four-sensor network contains areas of localised high intensity and not the more even spread as desired.

An interesting trend when compared with the results from the flat aluminium plate (presented in Figure 94) is that the rate of minimum value as the sensor network size increases. The rate for the flat plate reduces significantly between the two-sensor and three-sensor networks whereas for the complex geometry plate, the rate remains much higher. This is most likely due to the more significant gains in coverage to be had by adding more sensors to the sensor network for the complex geometry plate where wave propagation is significantly affected.

8.7.4. Optimal location results – sum of the maximum values

The locations of the sensors and their respective intensity maps are presented in Figure 105. Note that for the purposes of presentation, the holes are presented as squares. When considering the one-sensor network, the optimiser positions the sensor reasonably centrally on the lower boundary of the area of investigation. This solution uses the interference fringes from the boundary reflections to increase the area of high intensity. This solution does however leave regions with relatively low intensity meaning that the spread of the coverage is not greatly even. That said, it is evident that the presence of the holes does significantly affect the source-sensor transmission path. This is an inhibiting factor in maximising the coverage.

The solution derived for the two-sensor network positions the sensors with one sensor reasonably central in the region on the left of the plate where no holes are present and the other in-line with the far right set of holes on the lower boundary. The position of the sensor on the left is reasonably intuitive as a wide area is covered with minimal disruption as a result of the presence of the holes. The sensor on the right takes advantage of the reflected interference fringe. This give a reasonable coverage of the structure although it does leave an area on the top right of the plate that has minimal coverage.

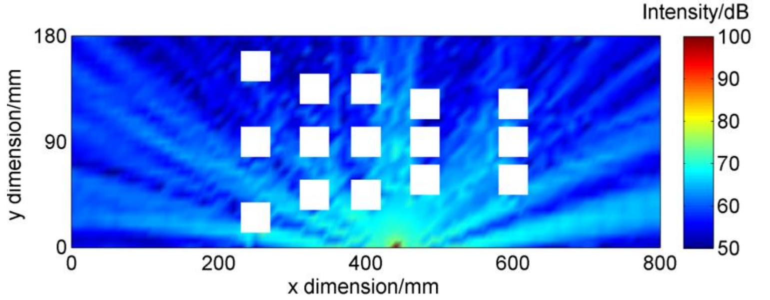

Ns = 1, minimum intensity = 46.1dB, total value = 1.31 x 10^5

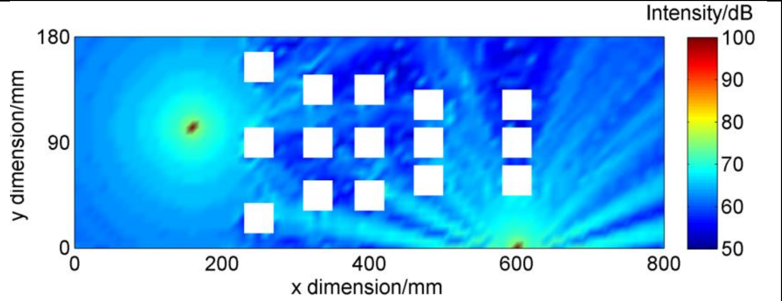

Ns = 2, minimum intensity = 51.7dB, , total value = 1.39 x 10^5

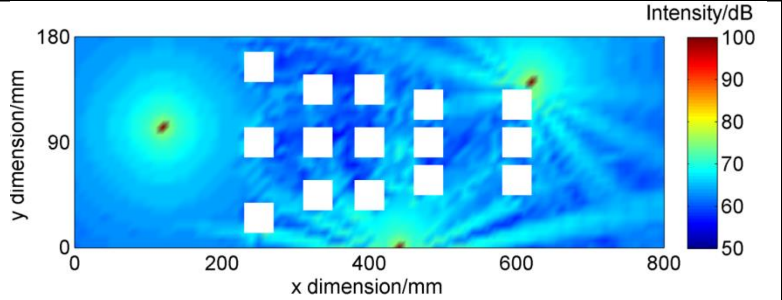

Ns = 3, minimum intensity = 55.3dB, , total value = 1.43 x 10^5

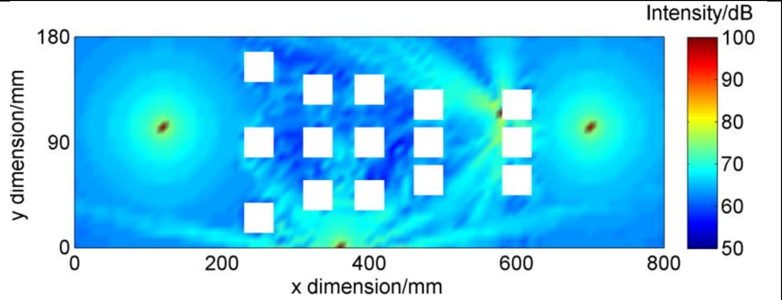

Ns = 4, minimum intensity = 55.2dB, , total value = 1.45 x 10^5

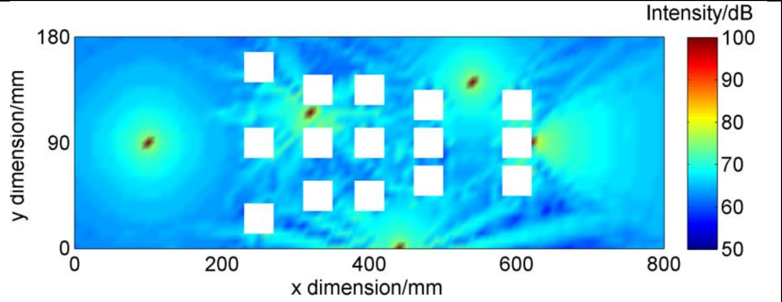

Ns = 5, minimum intensity = 56.9dB, , total value = 1.46 x 10^5

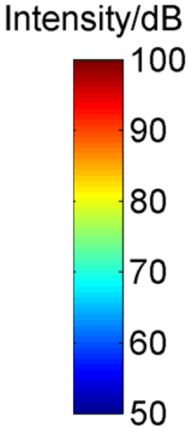

Figure 105. Optimal location of sensors for increasing sensor network size (Ns) when the fitness is assessed using the sum of the maximum values (Note the locations of the sensors are at the areas of high intensity (red)).

It is therefore hardly unsurprising that when three sensors are considered that a third sensor is position in the top right-hand region of the structure. The other two sensors are in similar places to those of the two sensor network however; their locations are different which takes into account the influence of the third sensor. Although the coverage is improved upon, there is a region within the centre of the plate that still shows relatively low intensity values.

As the fourth sensor is introduced to the network, the sensor location on the left of the structure is retained from the three-sensor network. This is logical as previously discussed; this covers a large region on the left of the structure. This same coverage has been adopted on the right of the plate by the second sensor which covers the region with no holes on the right. Again, a sensor is positioned on the lower boundary which takes advantage of the interference fringes. Similarly, a sensor is placed on the boundary of a hole which uses the interference fringes to increase coverage. This distribution, despite having a wide area of high intensity, there is a region in the central region of the holes where the coverage is still low.

The five-sensor network uses a similar distribution for at least two locations as the four-sensor network. One sensor is positioned reasonably centrally in the left-hand region where no holes are present although this position is to the left of location previously used in other networks. A sensor is also positioned on the lower boundary which again takes advantage of the interference fringes. The region to the right of the structure where no holes are present is covered by a single sensor that which is positioned on the boundary of a hole. As such this introduces a conical fringe of high intensity. Another sensor is located at the top right of the structure but unlike the sensor in the four-sensor network, this is not on the boundary of a hole. The final sensor is positioned reasonably centrally in the region with the holes. This gives a reasonably good coverage over the whole structure. That said however, the minimum intensity detectable is still lower than that of a two sensor network on the flat plate.

8.7.5. Maximising the minimum value GA convergence

The convergence of the GA when the fitness is assessed by maximising the minimum value of the intensity map is presented for the complex structure in Figure 106 for the increasing sensor network size.

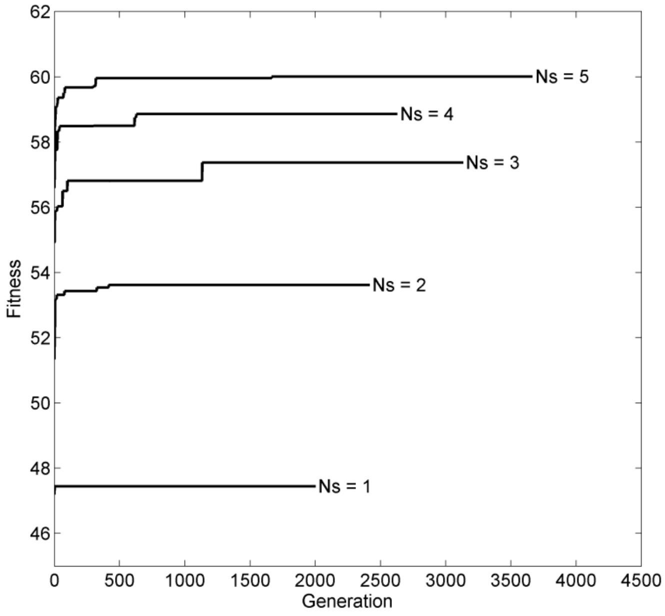

Figure 106. Convergence of the GA when the fitness is assessed by maximising the minimum value of the intensity maps for increasing sensor network sizes (Ns) (maximum fitness).

The general trends are that when more sensors are added to the sensor network, more generations were required for convergence. This is not surprising considering the increase in search space which comes with larger sensor networks. Unlike when the fitness was assessed using the sum of the maximum values, the convergence required more generations before converging on an optimal solution. Only the solution for the one-sensor network converged in less than five hundred generations. This is consistent with what was seen with the flat plate study and is most likely to be a function of how the fitness is assessed.

8.7.1. Minimum value of the intensity map (fitness)

The minimum value for the optimal sensor locations is presented in Figure 107 as the network size increases. As with all of the other fitness assessments, as more sensors are added to the sensor network the fitness increases albeit at a diminishing rate.

It is apparent that when the minimum values are compared with those in Figure 104 where the fitness was assessed using the sum of the maximum values that the minimum values for all network sizes are improved upon. This demonstrates that a better distributed coverage was achieved across the intensity map.

As with when the fitness was assessed using the sum of the maximum values, the rate at which the increments in performance decrease is less than that seen when compared with the flat plate. This again can be attributed to the presence of the holes.

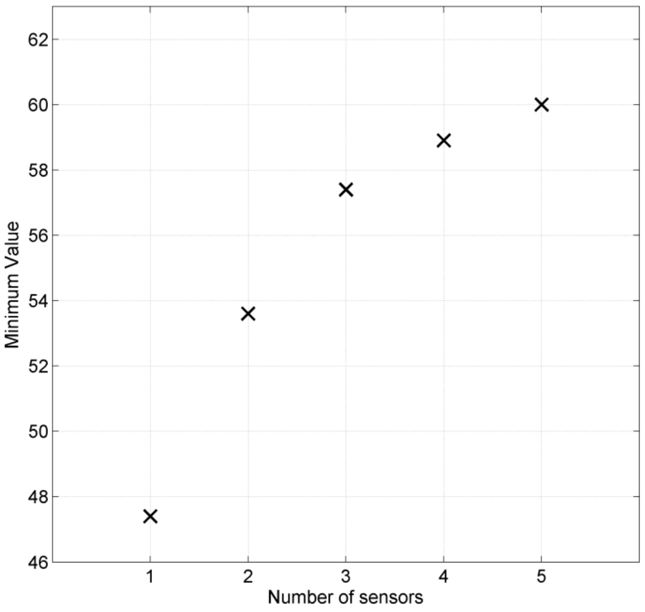

Figure 107. The minimum value of the intensity map for as the number of sensors increases (Ns).

The best maximised minimum value is achieved when all 584 sensors are used in the network. This gives a minimum value of 72.2dB. The value obtained for the single network solution gives a minimum intensity value of 47.4dB which equates to 65.7% of the best achievable value. This is greatly improved upon when the five sensor network is considered to achieve the optimal minimum value of 83.1% of best achieveable value. This is an increase of 17.4% from the one sensor solution which approximatley halves the performance gap.

8.7.2. Sum of the maximum values

The sum of the maximum values when maximising the minimum value of the intensity map is used to assess the fitness for increasing network size is presented in Figure 108. Interestingly, the sum of the maximum values is relatively consistent with what has been observed previously with the increase in performance diminishing exponentially as more sensors are added to the network.

Generally the sum of the maximum values is lower than those when this was method was used to assess the fitness. This is hardly unsurprising; however the values are not substantially less. With the addition of each sensor, the gap between the two results sets reduces until the five-sensor network where the same value is achieved. This demonstrates that different solutions have been derived; however the solutions derived from maximising the minimum cost produce solutions that still achieve reasonably high performance by this metric.

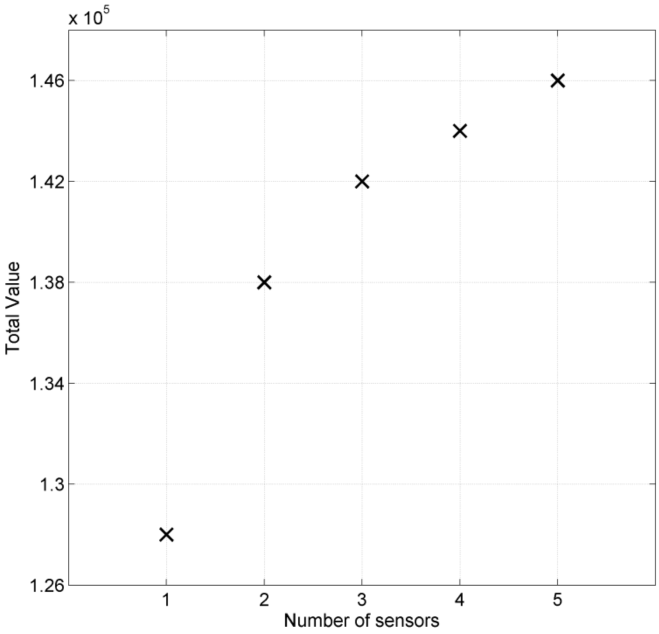

Figure 108. The sum of the maximum values when maximising the minimum value of the intensity map is used to assess the fitness for increasing network size (Ns).

8.7.1. Optimal location results – maximising the minimum value

The sensor locations (red) and the respective intensity maps are presented in Figure 109 for increasing sensor network size.

When considering the one-sensor network the optimiser positions the sensor reasonably central in the region where the holes are present. This differs somewhat to the previous fitness assessment method where the sensor was positioned on the lower boundary. Although the presence of the holes limits the wave propagation and as such, the region of high intensity is less than that observed previously, the positioning ensures that the region containing the holes has a better coverage.

The two sensor network positions one sensor in the region with the holes albeit lower and to the right of the location selected in the one sensor solution. Due to the presence of the holes, the wave propagation path is heavily affected with this sensor and as a result there are ‘shadows’ caused by the holes where the intensity is lower. The second sensor however is positioned in the top right of the structure which achieves a reasonably good coverage of the right-hand side of the structure as well as the top portion of the structure. It is apparent however that the coverage has significantly improved based on the lighter colours of the intensity map.

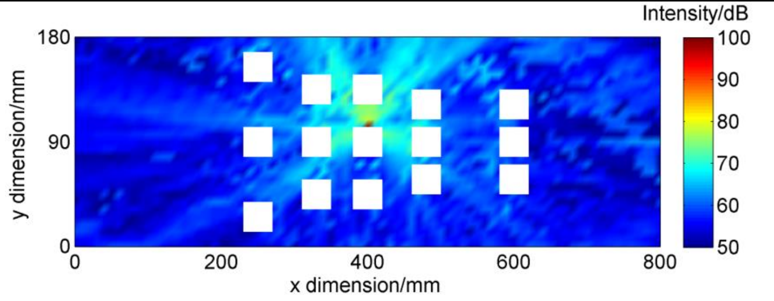

Ns = 1, minimum intensity = 47.4dB, , total value = 1.28 x 10^5

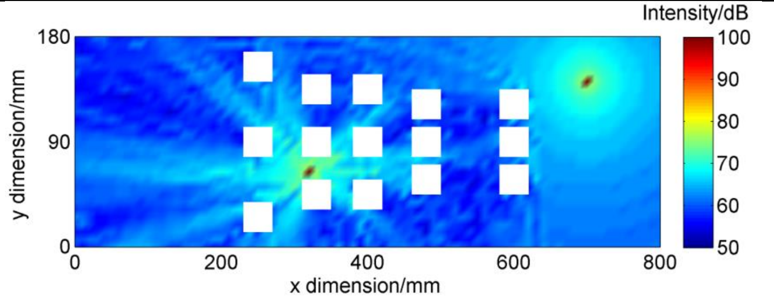

Ns = 2, minimum intensity = 53.6, total value = 1.38 x 10^5

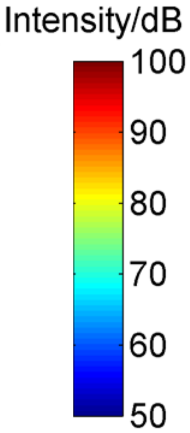

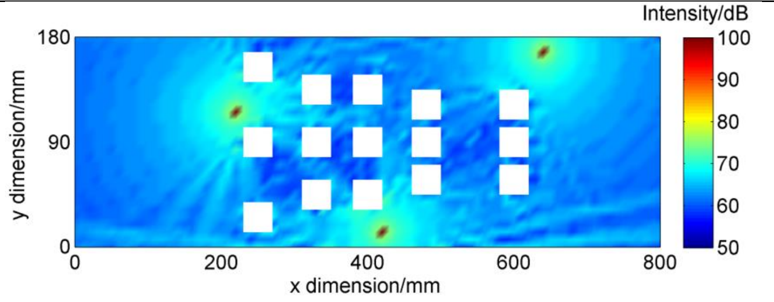

Ns = 3, minimum intensity = 57.4, total value = 1.42 x 10^5

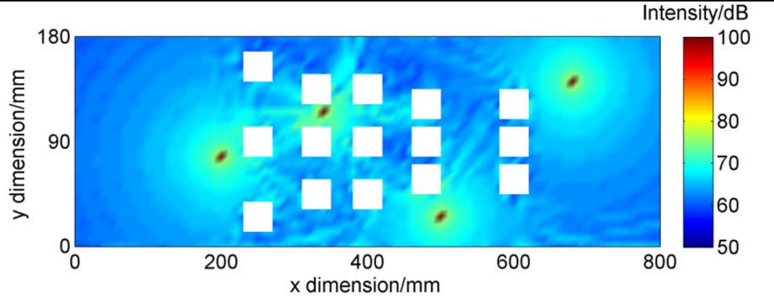

Ns = 4, minimum intensity = 58.9, total value = 1.44 x 10^5

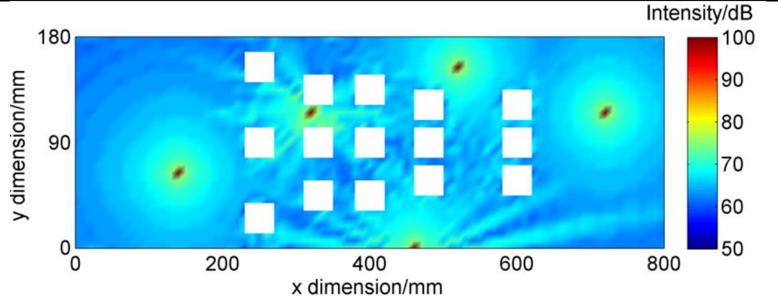

Ns = 5, minimum intensity = 60.0, total value = 1.46 x 10^5

Figure 109. Optimal location of sensors for increasing sensor network size (Ns) when the fitness is assessed by maximising the minimum value of the intensity map (Note the locations of the sensors are at the areas of high intensity (red)).

The three-sensor network demonstrates further improvements in the coverage. The first sensor is positioned between the far left holes. This enables a wide coverage of the left-hand region of the plate as well as contributing to some coverage in the region with the holes. The second sensor is positioned at the bottom of the region with the holes. This covers the bottom of the structure and the bottom of the region with the holes. The third sensor is positioned in the top right of the plate albeit in a different location to that used in the two-sensor network. This covers the right hand-side of the structure. The three sensor network starts to achieve a better coverage of the structure however; there are still regions of low intensity. These are the result of the ‘shadows’ cast by the holes on the source-sensor paths.

The four sensor network goes some way to reduce the influence of these shadows. A similar arrangement, although different, to the three-sensor network of three of the sensor is arranged by the optimiser. The fourth sensor is added reasonably centrally to the region with the holes. This reduces the effects of the shadows within the region with the holes. However, there are some areas on the outer boundaries that suffer low intensities as a result.

The five sensor network further attempts to reduce the low intensity regions caused by the presence of the holes. This is achieved by using a similar network to the four-sensor network which takes into account the influence of the fifth sensor. The fifth sensor is then positioned slightly right of the centre at the top of the structure. This enables a much more even coverage. However, it is worth noting that the minimum value detectable with this sensor network is still comparable to that of a two-sensor network on the flat plate. This highlights the influence of the holes on the source-sensor paths and indeed the coverage obtainable.

8.8.Discussion and conclusions

The results show a methodology for the placement of sensors of which two approaches were used for assessing the fitness of the solutions. As discussed previously in section 5.4.1 determining how the fitness is assessed is vital in achieving the results desired. It has been shown in this study that that of sum of the maximum values approach may be deemed a suitable approach. However, when the objective is to distribute the sensors so that an even coverage is achieved, this fitness assessment can be skewed by the presence of localised regions of high intensity.

In the case of the flat plate, this fitness assessment technique did produce some sensor network distributions that seemed logical (such as positioning the single sensor in the centre of the plate). With the larger sensor distributions, solutions were found that were influenced primarily by the presence of interference fringes. When the minimum intensity value was maximised it was found that this method was more successful in achieving a more even coverage by the sensor network. This method produced sensor network distributions that reduced the areas of localised high intensity. It could therefore be stated that this fitness assessment method is more suited for maximising the coverage of a sensor distribution than that of the sum of the maximum values. Nevertheless, the logical solutions generate confidence in the methodology, particularly for its application to more complex problems.

With the complex geometry plate the sum of the maximum intensity method of fitness assessment was significantly influenced by the interference fringes and solutions were generated that did not necessarily produce an even coverage. It could therefore be stated that this method is not well suited for evenly distributing the sensors as regions of low intensity can be ignored. Maximising the minimum intensity however produced better results which tended to have a more even coverage. Although the distribution of the sensors may not be intuitively selected by an operative based on their best judgement, based on the intensity maps it is clear that there is some logic in the positioning. However, the lack of intuitiveness in the solutions should not be taken as a sign of a poor solution. It in fact supports the need to use an optimisation technique for the placements of sensors particularly in the case of complex geometries.

It should be noted however that both of the methods of fitness assessment used are reasonably simplistic and that a more advanced statistical approach maybe better suited for the placement of the sensors. However, this too may incur a time penalty due to extra calculation in the optimisation process which may lead to achieving marginally better results. This time penalty is a worthy consideration when considering applying this technology to a design environment.

The results presented generally show a diminishing rate of fitness improvement (regardless of the fitness assessment method used) as the size of the sensor network distribution increases. This is a useful as there will be an optimal point where adding additional sensors will have a limited improvement on the performance. Of the results presented however, an optimal sensor network is not specified. In order to do this, additional information is required such as the power and computational capability available. An important consideration is the effect of the background noise as the threshold would need to be set higher than this in order to ensure that the system is not triggered by background noise and creates a type I error. As such, a sensor network should be selected so that the structure can be monitored with a suitably high fidelity.

Another consideration is the loading conditions in which the structure will operate. For this study it has been assumed that coverage is required over the entire plate. In reality, it may be the case that the probability of an AE event can be better assessed for example at areas of high stress concentration. In these instances it would be beneficial to skew the distribution of sensors to ensure that these regions have a preferential coverage. This could be conducted by using the results from a stress analysis model as an input. This may then result in sensor distributions that are better suited to the operation of the component. A similar approach could be used to ensure that less damage tolerant section of the structure are adequately covered by the optimised sensor network.

This approach has considered maximising the coverage of sensor networks. This in effect increases the probability of the network detecting an AE event. However, this may not necessarily enable the location of the AE event to be achieved where at least three sensors need to be able to detect the AE signal. A way of achieving this maybe to assess the coverage of each sensor individually. This would enable the regions to be determined in which the coverage of the individual sensors overlap and hence the region in which an AE event of specified intensity can be detected. This would require a different fitness assessment method. It is possible that the method of assessing fitness presented in section 5.4.1 could be modified to achieve this. As such, the threshold setting for the particular sensor network could be determined.

The placement of the sensors in this study has been based on a series of assumptions in the model. The first primarily is that that the actuator acts entirely out-of-plane. This is not likely to be the case in reality due to Poisson’s ratio and that there will be some in-plane component to the AE signal. The signal used is also a 200kHz sine wave which is not fully representative of an AE signal. As explained previously, this was used for simplicity to demonstrate the methodology. It is likely that the AE signal will have different frequency content and as such would have different attenuative characteristics. This would significantly influence the decay in the intensity. Therefore it would be desirable to use a source representative of an AE source, such as that of an H-N source as the input to the model.

The second assumption is based on the response of the sensors being entirely out-of-plane. Again, in practice this is not the case although each sensor type will have a different characteristic. In the case of an MFC sensor for example, the response will be mostly in-plane as well as having a degree of directionality in the response. This would be significantly influential on placement of the sensors and would be of much interest for a future study.

An aspect of this study has been the layout of the sensors and the sources. This was laid out in a grid based on Cartesian co-ordinates. However, as the decay of the intensity is radial, in this instance at least, it may be of some benefit to arrange the sensors and sources accordingly.

The placement of the sensors in this study has been conducted to achieve the optimal locations. In reality, there will be a degree of error in the placement and as well as constraints that do not make sensor placement possible (such as the requirement for extra space for packaging the sensors. Therefore it would be of benefit to not necessarily specify an exact location on the structure but rather a region where the sensor should be placed to achieve satisfactory results. Conversely, areas on the structure where placing sensors is not suitable (i.e. have a limited benefit in enabling the detection of damage) should also be highlighted.

In this study the maximum amplitude in a time window has been considered in isolation. Although every attempt has been made to capture only the maximum amplitude wave in the first wave packet, wave phenomena such as reflections can be influential as observed in the results of this study. Therefore it may be advantageous to adopt a multi-objective approach where other aspects of the wave are considered. This may include the time-of-arrival of the wave which would be of great interest where a delta-t location method is to be used and particularly useful for complex structures.

Although solutions have been presented for increasing sensor network sizes, the required solution needs to be determined by the sensor network designer for the required monitoring application. This can be assessed by a simple method such as the minimum intensity detectable or even by using a more statistical approach such as determining when the rate of fitness has dropped below a certain limit.

In summary, this study has presented a methodology using data from LISA modelling for the placement of sensors. The sensors locations have been optimised using a GA and two different methods of assessing the fitness. Although this is a simplistic study, it shows a great deal of potential for enabling optimal sensor networks to be designed in a prompt and efficient manner. Combined with methodology presented in section 7 it may also be possible to use the optimisation dataset for locating damage using the delta-t technique.

9. Conclusions and future work

The work that has been presented five studies that advance the methodologies of AE and AU sensor placement for SHM applications. The work has used experimental data which is supported with numerical reasoning. The focus of the AU studies has been primarily to maximise the probability of detection while minimising the number of sensors where the AE studies have expanded further upon this to consider damage location as well.

Through the study of the interaction of Lamb waves with adhesively bonded stiffeners and disbonds, it can be concluded that that the presence of disbond can be determined using an acousto-ultrasonic approach. This study used a novel 3D vibrometry technique to measure both the in-plane and out-of-plane responses of the Lamb waves which enabled a visual representation to be created. This allowed the understanding of Lamb wave interaction with adhesive disbonds to be advanced giving indications for sensor placements. The higher frequency excitation of the Lamb waves were shown to exhibit the highest degree of sensitivity to the damage. A LISA model was created to replicate the experimental results. The results from the model produced qualitative results that correlated well with the experimental results. Through the use of traditional ultrasonic inspection, it was found that the disbond was more complex than what had been anticipated. Through the use of a novel RMS analysis techniques, it was possible to visualise the size and the shape of the disbond which correlated well with the results from the traditional ultrasonic inspection technique.

Both the experimental and numerical approaches for the investigation of the interaction of Lamb waves with stiffeners and disbonds were adapted to form the basis of an optimisation study. The study conducted used a genetic algorithm with a novel statistically based fitness function to assess the fitness of the different sensor networks as well as the actuator-defect-sensor path. Both in-plane and out-of-plane components of the wave were considered for optimising the location of the sensors for receiving signals from five different excitation sites. It was found that the GA produced results that were not entirely intuitive due to the complex interaction of the Lamb wave with the disbond. Although the LISA model used assumptions for the adhesive and the modelling of the disbond, the sensor placement was found to be consistent with the experimental results. This demonstrated the potential for using numerical techniques for the placement of sensors on a structure.

Lamb wave interaction with impact damage on a composite wind turbine blade was investigated using 3D scanning laser vibrometry. The impact damage that was introduced to the blade was of the order of tens of microns and was established as being a barely visible impact damage; a damage type that is of particular interest for detection. Using novel root-mean squared subtraction and cross-correlation techniques enabled the size and location of the damage to be determined visually as well as highlighting regions suitable for the placement of sensors. Through the use of a newly developed windowed cross-correlation technique it was possible to visually present the interaction of the different Lamb wave modes for different frequencies. It was found that the mostly in-plane S_0 mode did not interact with the damage which demonstrated that out-of-plane sensing would be required to fully determine the presence of the this damage particularly when exciting Lamb waves using the method presented. On further inspection, the underside of the impact damage showed a crack that would have significantly affected the structural performance of the turbine blade. This study demonstrated the sensitivity of Lamb waves to BIVD as well as the importance of the sensor positioning in order to detect the presence of the damage.

AE source location using the delta-t location method was investigated using training data from a LISA model. Two studies were conducted. The first was conducted to locate H-N sources linearly on an aluminium plate. A novel experimental 'inverse' approach was also adopted for this using 3D scanning laser vibrometry. The inverse approach demonstrated many benefits over the traditional method by primarily being quicker to obtain training data while also producing meaningful results. Generally, all of the location results were contained within the acceptable margin of error. Using the LISA approach to creating the training dataset, the technique was applied to a planar location problem on a complex geometry aluminium plate subject to cyclic loading. It was found that the technique produced better location results than the TOA location method commonly used while being a less time consuming and labour intensive than the traditional experimental training method. The results using the experimentally-trained dataset were only marginally better than those achieved using the model-trained dataset demonstrating the potential of the technique. This was attributed to the excitation signal used as well as the assumptions made in the model.

The LISA modelling technique was applied to optimising sensor locations on two different aluminium plates; one flat and one with complex geometry. The approach used a genetic algorithm with two different methods of assessing fitness. This novel multi-source, multi-sensor approach was effective and efficient as well as being an approach that would be difficult to achieve experimentally. The study was successful in increasing the coverage of the plates as more sensors were added to the network. It was found also that by assessing the fitness by maximising the minimum value detectable, a reasonably even coverage was possible.

Although a large body of work has been presented in this thesis, there are many aspects of the work that can be taken forward for further study. In regards to the Lamb wave interaction with adhesively bonded stiffeners and disbonds, work should be conducted to induce a disbond under real loading conditions. It should also be noted that the optimisation study conducted only considered five excitation locations at a set distance from the stiffener. Other excitation sites should be also investigated as well as how disbonds at the edge of the panel affect sensor distribution. This is something that may be possible to achieving using the LISA technique. Other aspects should also be investigated for assessing the fitness of the sensor locations such as considering how the damage may be located as well as detected. Further investigations could also be conducted into different sizes and shapes of the disbonds (particularly, those that do not penetrate the whole width of the stiffener) as well as those at the edges of the plates. Work may also be expanded to investigate the effects in composite where the integrity of adhesive bonded stiffeners is of much interest.

With both of the optimisation studies presented for AE and AU, a form of stress mapping should be also considered when assessing the probability of a sensor distribution. This would indicate where regions of high probability of damage are likely to occur and as such regions of the structure that are of interest to be modelled can be established. This could be achieved using FEA software for simplistic structures although an experimental approach using a technique such as digital image correlation could be adopted for more complex structures. By doing this, the loading of the structure will also be considered. Similarly, a map of probability of damage occurring on a structure and it's severity could also be applied to a structure similar to that used currently in industry as another measure of sensor location suitability. Probability measures such as Bayesian statistics may be well suited to this type of problem

Within these optimisation studies only a GA has been used. GAs have many parameters which by adjustment, can yield performance gains. This is something that should be investigated as better convergence performance may be achievable as well as saving time in regards to converging on a solution. It may actually be possible to use a GA to refine the parameters of the GA used for optimisation however, this would only be of significant interest if multiple optimisation studies were to be run.

Another aspect that should be investigated is the use of different algorithms. It has been discussed that evolutionary algorithms are well suited to this type of problem. There are examples in the literature of other algorithms being used to establish optimal sensor placement and as such these should be investigated. It may be possible that algorithms such as monkey algorithms, simulated annealing or ant colony algorithms yield better performance than the GA that has been presented. It is also possible that other methods of fitness assessment may produce more desirable results. This may include considering other aspects of the waveforms such as the time-of-arrival or root-mean squared values. As such, a multi-objective approach can be adopted.

In regards to the LISA models constructed, there are many modifications that, if adopted, may improve the fidelity and accuracy of the model. The use of a smaller global cube edge length would enable features such as adhesive films to be more easily modelled. This may be possible to achieve by having different cube sizes for different areas of the model in a similar way that meshes can be refined in an FEA model. Also, the modelling of composites using LISA should be investigated. This would open a wide range of possibilities and would be highly desirable for applying the methodologies to modern composite aircraft structures.

It would be highly desirable also to model a more representative AE source which could be used as an input for the delta-t training and the AE optimisation study. The most suitable source is most likely to be that of an H-N source which is accepted as being representative of an AE source. Similarly, it may also be beneficial to use sources from damage mechanisms for training which may enable the delta-t technique to start to characterise damage as well as locate it. It is hypothesised that by using such a source, a greater degree of accuracy can be obtained when locating AE sources using the delta-t method as well as producing a more representative optimisation approach. The training source used for mapping areas of the structure should also relate to the probability of different damage mechanisms in that region of the structure.

The modelled delta-t training used in this thesis considered mapping a surface of a structure. One of the benefits of the LISA approach however is that sources can be placed inside of the material and therefore it could be possible to produce a three-dimensional delta-t map. This would enable AE sources to not only be located in a plane but also globally. In addition, the delta-t mapping technique uses a simple interpolation technique to locate damage which is also prone to locating damage in regions of a structure where it is impossible for it to exist (i.e. in the centre of a hole). It would be beneficial to add these considerations to the interpolation which may improve source location accuracy. Other interpolation methods could also be used such as using the delta-t grid to train a neural network. This may provide a better location accuracy and should be investigated.

Another interesting aspect that should be investigated is the shape and density of the delta-t training grid. Only square grids of uniform density were considered however it would be useful to quantify the improvement of locational accuracy of AE sources against the density of the delta-t grid. It would also be interesting as part of a future work study to investigate the benefits (if any) to other shaped grids such as triangular, hexagonal or even working on a polar co-ordinate system.

An inverse delta-t approach was presented in this work for the linear location study. This should be further investigated with a view to adapting it for planar locations. If successful, this could reduce the training times to under ten minutes for a problem such as the one presented in this thesis. This would be highly desirable as it would enable the delta-t training data to be created quickly enabling a rapid concurrent development of sensor networks and structures. This may also enable the delta-t maps to serve as an input for assessing the fitness of a particular sensor network in an optimisation study.

The objective of the optimisation of AE sensor locations in this thesis was to maximise the coverage of the sensor network. Although this is maximises the probability of detecting AE sources (and therefore damage), it does not necessarily allow for the sources to be detected as at least three sensors need to locate the source. This therefore would require a different measure of fitness assessment to optimise the coverage of the structure by at least three sensors. This is something that should be considered for future work. It would also be desirable to use the LISA approach for this as it the multi-source input could also be used as delta-t training data.

The techniques and methodologies developed in this work has shown huge potential for optimising both acousto-ultrasonic and acoustic emission sensor networks. The novel use of the modelling techniques to create large datasets for different geometries enables many damage scenarios to be considered which can optimised by genetic algorithms. These model datasets have proven to show a high level of validity with experimental results. In addition, the short run-times of the models makes their use viable in a commercial environment. This enables massive scope for the design of Lamb wave based damage detection sensor networks which can be created a virtual environment. In-turn, these techniques can be combined with structural stress analysis to enable a concurrent structure-sensor network design. It is predicted this reduce the mass of the structure as well as improving safety of aerospace structures - an exciting development for structural health monitoring.

References

1. Jarrett, P., *The colour Encyclopedia of Incredible Aeroplanes*. 2011, London: Dorling Kindersley.
2. London Science Museum. *Wreckage from a Comet jet*. 2015; Available from: http://www.sciencemuseum.org.uk/images/NonSSPL/10313126.aspx.
3. Swopes, B. *28 April 1988*. 2015 29/08/2015]; Available from: http://www.thisdayinaviation.com/28-april-1988/.
4. Board, N.T.S. *Aloha Airlines, Flight 243, Boeing 737-200, N73711*. 2015 29/08/2015]; Available from: http://www.ntsb.gov/investigations/accidentreports/pages/aar8903.aspx.
5. Chisholm, S., et al., *Structural Durability and Damage Tolerance in the Next Century of Commercial Aviation*, in *ICAF2015*. 2015: Helsinki, Finland. p. 571 - 602.
6. Howell, E. *Columbia Disaster: What Happened, What NASA Learned*. 2013 30/08/2015]; Available from: http://www.space.com/19436-columbia-disaster.html.
7. Smith, M.S., *NASA's Space Shuttle Columbia: Synopsis of the Report of the Columbia Accident Investigation Board*. 2003, The Library of Congress.
8. Taleb, N.N., *The Black Swan*. 2nd edition ed. 2010, London, UK: Penguin Books.
9. Airbus, *Global Market Forecast - Futures Journeys 2013 - 2032*. 2013: Blagnac Cedex, France.
10. Mahashabde, A., et al., *Assessing the environmental impacts of aircraft noise and emissions.* Progress in Aerospace Sciences, 2011. **47**(1): p. 15-52.
11. Lawrence, P., *Meeting the challenge of aviation emissions: an aircraft industry perspective.* Technology Analysis & Strategic Management, 2009. **21**(1): p. 79-92.
12. Mangalgiri, P., *Composite materials for aerospace applications.* Bulletin of Materials Science, 1999. **22**(3): p. 657-664.
13. Yang, Y., et al., *Recycling of composite materials.* Chemical Engineering and Processing: Process Intensification, 2012. **51**: p. 53-68.
14. Speckmann, H. and R. Henrich. *STRUCTURAL HEALTH MONITORING (SHM) - OVERVIEW ON AIRBUS ACTIVITIES*. in *16th WCNDT 2004 - World Conference on NDT*. 2004. Montreal, Canada.
15. Worden, K. and J.M. Dulieu-Barton, *An Overview of Intelligent Fault Detection in Systems and Structures.* Structural Health Monitoring, 2004. **3**(1): p. 85-98.
16. Lee, S., et al., *Product lifecycle management in aviation maintenance, repair and overhaul.* Computers in industry, 2008. **59**(2): p. 296-303.
17. Authority, F.A. *Chapter 8. Inspection Fundamentals*. 2008.

18. Lampe, M., M. Strassner, and E. Fleisch. *A ubiquitous computing environment for aircraft maintenance*. in *Proceedings of the 2004 ACM symposium on Applied computing*. 2004. ACM.

19. Lan, S., *Planning for Robust Airline Operations: Optimizing Aircraft Routing and Flight Times to Achieve Minimum Passenger Disruptions*, in *Department of Civil and Enviromental Engineering*. 2003, Massachusetts Institute of Technology: Massachusetts Institute of Technology. p. 123.

20. Wu, H., et al., *Methods to reduce direct maintenance costs for commercial aircraft.* Aircraft Engineering and Aerospace Technology, 2004. **79**(1): p. 15-18.

21. Barrelds, G., et al., *Health Monitoring of Aerospace Structures*. 2004.

22. Reason, J.T., *Human Error*. 1990, Cambridge, UK: Cambridge University Press.

23. Reason, J., *Human error: models and management.* Bmj, 2000. **320**(7237): p. 768-770.

24. AAIB, *Pierre Robin DR400/180, G-DELS, 22 July 1996*. 1996, Air Accident Investigation Board.

25. Speckmann, H. and H. Roesner, *Structural Health Monitoring: A Contribution to the Intelligent Aircraft Structure*, in *ECNDT 2006*. 2006: Berlin.

26. Chen, W.-C., *Some experimental investigations in the drilling of carbon fiber-reinforced plastic (CFRP) composite laminates.* International Journal of Machine Tools and Manufacture, 1997. **37**(8): p. 1097-1108.

27. Zou, Y., L. Tong, and G. Steven, *Vibration-based model-dependent damage (delamination) identification and health monitoring for composite structures—a review.* Journal of Sound and vibration, 2000. **230**(2): p. 357-378.

28. Barrelds, G., et al., *Health Monitoring for Aerospace Structures*. 2004.

29. Holford, K., et al. *Bridge Integrity Assessment by Acoustic Emission–Global Monitoring*. in *2nd International conference on identification in engineering systems*. 1999.

30. Crivelli, D., et al., *Localisation and identification of fatigue matrix cracking and delamination in a carbon fibre panel by acoustic emission.* Composites Part B: Engineering, 2015. **74**: p. 1-12.

31. Anton, S.R. and H.A. Sodano, *A review of power harvesting using piezoelectric materials (2003–2006).* Smart materials and Structures, 2007. **16**(3): p. R1.

32. Baxter, M.G., et al., *Delta T source location for acoustic emission.* Mechanical Systems and Signal Processing, 2007. **21**(3): p. 1512-1520.

33. Rossing, T.D., *Springer Handbook of Acoustics*. 2007: Springer.

34. Rienstra, S.W. and A. Hirschberg, *An introduction to acoustics.* Eindhoven University of Technology, 2003. **18**: p. 19.

35. Worden, K., *Rayleigh and Lamb waves - Basic principles.* Strain, 2001. **37**(4): p. 167-172.

36. Schmerr Jr, L.W. and S.-J. Song, *Ultrasonic Nondestructive Evaluation Systems - Models and Measurements*. 2007, New York: Springer.

37. Rose, J.L., *Ultrasonic Waves in Solid Media*. 1999, Cambridge: Cambridge University Press.

38. Rayleigh, L., *On Waves Propagated along the Plane Surface of an Elastic Solid.* Proceedings of the London Mathematical Society, 1885. **s1-17**(1): p. 4-11.

39. Megson, T.H.G., *Aircraft Structures for Engineering Students*. Third Edition ed. 1999, London: John Wiley & Sons.

40. Lamb, H., *On waves in an elastic plate.* Proceedings of the Royal Society of London. Series A, Containing papers of a mathematical and physical character, 1917: p. 114-128.

41. Raghavan, A., *Guided-wave structural health monitoring*, in *Aerospace Engineering*. 2007, University of Michigan: Michigan.

42. Rindorf, H.J. *Acoustic emission source location in theory and in practice*. Bruel and Kjaer Technical Review, 1981.

43. Eaton, M.J., *Acoustic Emission (AE) monitoring of buckling and failure in carbon fibre composite structures*, in *Institute of Materials and Manufacturing*. 2007, Cardiff University: Cardiff.

44. Rauter, N. and R. Lammering, *Numerical simulation of elastic wave propagation in isotropic media considering material and geometrical nonlinearities.* Smart Materials and Structures, 2015. **24**(4).

45. Pollock, A.A. *Classical Plate Theory in Practical AE Testing*. in *Progress in Acoustic Emission III, Proceedings of the Eighth International Acoustic Emission Symposium*. 1986. The Japanese Society for Nondestructive Testing.

46. Galán, J.M. and R. Abascal, *Numerical simulation of Lamb wave scattering in semi-infinite plates.* International Journal for Numerical Methods in Engineering, 2002. **53**(5): p. 1145-1173.

47. Alleyne, D.N.C., P, *The Interaction of Lamb Waves with Defects.* IEEE TRAiSSACTIONS ON ULTRASONICS, FERROELECTRICS, AND FREQUENCY CONTROL, 1992. **39**(3): p. 381-396.

48. Cho, Y., *Estimation of ultrasonic guided wave mode conversion in a plate with thickness variation.* Ultrasonics, Ferroelectrics, and Frequency Control, IEEE Transactions on, 2000. **47**(3): p. 591-603.

49. Lemistre, M. and D. Balageas, *Structural health monitoring system based on diffracted Lamb wave analysis by multiresolution processing.* Smart materials and structures, 2001. **10**(3): p. 504-511.

50. Han, J.-B., et al., *Mode analyses of laser-generated transient ultrasonic Lamb waveforms in a composite plate by wavelet transform.* Materials evaluation, 1999. **57**(8): p. 837-840.

51. Miller, R.K. and P. McIntire, *NDT Handbook Vol 5*. 1987: American Society for Non-destructive Testing.

52. Britian, M. *The Knockers*. 2012 [cited 2016 20/01/2016]; Available from: http://www.mysteriousbritain.co.uk/england/cornwall/folklore/the-knockers.html.

53. Hodgson, E.A.G., Z.E, *Seismic research program, rock burst problem - lakeshore mines*. 1945, Department of Mines, resources and surveys, Engineering Branch: Ottawa, Canada.

54. Hodgson, E.A., *Recent developmesnts in rock burst research at lakeshore.* Trans. Can. Inst. Mining metals, 1943. **46**: p. 313-324.

55. Obert, L.D., W, *The Microseismic Method of Predicting Rock Failure in Underground Mining, Part 2—Laboratory Experiments*. 1949, U.S. Bureau of Mines: USA.

56. Obert, L.D., W, *Microseismic Noise for the prediction of Rock Bursts - Part I. General Method*. 1945, U.S. Bureau: USA.

57. Obert, L.D., W, *Use of Subaudiable Noise for the prediction of Rock Bursts - Part II*. 1942, U.S. Bureau of Mines: USA.

58. Obert, L., *Use of Subaudiable Nosie for prediction of Rock bursts*. 1941, U.S. Bureau of Mine.

59. Kaiser, J., *Untersuchungen über das Auftreten von Geräuschen beim Zugversuch*. 1950, Technische Hochschule München.

60. Schofield, B., *Acoustic emission under applied stress*. 1963, DTIC Document.

61. Tatro, C.A., *Sonic techniques in the detection of crystal slip in metal.* Engineering Research, 1959. **1**: p. 23-28.

62. Dunegan, H., *Acoustic Emission: A Promising Technique*. 1963, Lawkence Radiation Laboratory: Livermore, CA, USA.

63. Green, A.T., C.S. Lockman, and R.K. Steele, *Acoustic Verification of Structural Integrity of Polaris Chambers.* Modern Plastics, 1964. **41**(11): p. 137-139.

64. Drouillard, T.F., *Acoustic emission: The first half century*. 1994, EG and G Rocky Flats, Inc., Golden, CO (United States). Rocky Flats Plant.

65. Baxter, M.G., *Damage Assessment by Acoustic Emission (AE) During Landing Gear Fatigue Testing*, in *Institute of Materials and Manufacture*. 2007, Cardiff University: Cardiff University.

66. Drouillard, T.F., *A History of Acoustic Emission.* Journal of Acoustic Emission, 1996. **14**(1): p. 1-34.

67. Chuang, S., *Real-Time Aircraft Structural Monitoring Using Acoustic Emission*, in *Review of Progress in Quantitative Nondestructive Evaluation*. 1987, Springer. p. 371-377.

68. Hill, E.v.K. and C.L. Rovik, *In-flight fatigue crack growth monitoring in a Cessna T-303 Crusader vertical tail.* Journal of Acoustic Emission, 2013. **31**: p. 19-36.

69. Pao, Y.-H. *Theory of acoustic emission*. in *Transactions of the... Conference of Army Mathematicians*. 1980. DTIC Document.

70. Lewis Jr, W., C. Bailey, and W. Pless, *Acoustic Emission Structure-Borne Noise Measurements on Aircraft during Flight*. 1976, DTIC Document.

71. Mizell, M. and W. Lundy Jr. *In-flight crack detection system for the C-135 lower center wing skin*. in *ISA Proc. 22nd Int. Instr. Symposium, San Diego, CA., p. 259f*. 1976.

72. Carlyle, J.M., et al., *Practical AE methodology for use on aircraft.* ASTM SPECIAL TECHNICAL PUBLICATION, 1999. **1353**: p. 191-208.

73. McBride, S., *Canadian forces in-flight acoustic emission monitoring program.* 1979.

74. Hutton, P. and J. Skorpik, *Develop the application of a digital memory acoustic emission system to aircraft flaw monitoring*. 1978, Battelle Pacific Northwest Labs., Richland, WA (USA).

75. Carlyle, J.M., *Acoustic Emission Testing of XV108, a Vickers VC-10-C1*. 1990, British Aerospace (Commercial Aircraft) Ltd.: Woodford, England.

76. Carlyle, J.M., *VC-10-C1 Acoustic Emission Testing Procedure*. 1991, Ministry of Defence: London, England.

77. Carlyle, J.M., *VC10 AE Reveiw*. 1996, Defence Research Agency: Farnborough, Hampshire, England.

78. Hoyle, M.C., et al., *A New Structural Integrity Policy for the VC10.* ASIP, 1996: p. 39.

79. Skinner, G., *Maintaining mature military air transport aircraft.* Proceedings of the Institution of Mechanical Engineers, Part G: Journal of Aerospace Engineering, 1996. **210**(2): p. 129-134.

80. Holford, K.M., et al., *Acoustic emission for monitoring aircraft structures.* Proceedings of the Institution of Mechanical Engineers, Part G: Journal of Aerospace Engineering, 2009. **223**(5): p. 525-532.

81. Hensman, J., et al., *Locating acoustic emission sources in complex structures using Gaussian processes.* Mechanical Systems and Signal Processing, 2010. **24**(1): p. 211-223.

82. Holford, K.M., *Acoustic emission - basic principles and future directions.* Strain, 2000. **36**(2): p. 51-54.

83. Dungan, H.L., *Global Flaw Location with One transducer*. 1997, Dungan Engineering Company Incoparated: Midland, TX, USA.

84. Maji, A., D. Satpathi, and T. Kratochvil, *Acoustic emission source location using lamb wave modes.* Journal of engineering mechanics, 1997. **123**(2): p. 154-161.

85. Mostafapour, A., S. Davoodi, and M. Ghareaghaji, *Acoustic emission source location in plates using wavelet analysis and cross time frequency spectrum.* Ultrasonics, 2014. **54**(8): p. 2055-2062.

86. Ziola, S.M. and M.R. Gorman, *Source location in thin plates using cross-correlation.* The Journal of the Acoustical Society of America, 1991. **90**(5): p. 2551-2556.

87. Paget, C., K. Atherton, and E. O'Brien. *Triangulation algorithm for damage location in aeronautical composite structures*. in *Proceedings of the 4th International Workshop on Structural Health Monitoring (F. Chang, ed.),(Stanford, CA, USA)*. 2003.

88. Aljets, D., et al., *Acoustic emission source location in plate-like structures using a closely arranged triangular sensor array.* Journal of Acoustic Emission, 2010. **28**: p. 85-98.

89. Eaton, M.J., R. Pullin, and K.M. Holford, *Acoustic emission source location in composite materials using Delta T Mapping.* Composites Part A: Applied Science and Manufacturing, 2012. **43**(6): p. 856-863.

90. Pearson, M., et al. *Improved Acoustic Emission Damage Source Location During Fatigue Testing of Complex Structures*. in *ICAF2015*. 2015. Helsinki, Finland: VTT Technical Research Centre of Finland Ltd.

91. Vary, A. and K. Bowles, *Ultrasonic evaluation of the strength of unidirectional graphite-polyimide composites.* 1977.

92. Vary, A. and R.F. Lark, *Correlation of fiber composite tensile strength with the ultrasonic stress wave factor.* 1978.

93. Green, A.T., *Evaluation of Composite Structures by Stress-Wave-Factor and Acoustic Emission*, in *Composite structures*. 1981, Springer. p. 450-462.

94. Williams Jr, J.H., S.S. Lee, and H. Nayeb-Hashemi, *Ultrasonic wave propagation loss factor in composite in terms of constituent properties.* Journal of Nondestructive Evaluation, 1980. **1**(3): p. 191-199.

95. Williams, J., *Ultrasonic evaluation of impact-damaged graphite fiber composite.* Materials Evaluation, 1980. **38**: p. 68-72.

96. Duke Jr, J., et al., *Characterization of composite materials by means of the ultrasonic stress wave factor*, in *Composite structures 2*. 1983, Springer. p. 53-60.

97. Tanary, S., et al., *Nondestructive evaluation of adhesively bonded joints in graphite/epoxy composites using acousto-ultrasonics.* Journal of pressure vessel technology, 1992. **114**(3): p. 344-352.

98. Fahr, A. and S. Tanary, *Acousto-Ultrasonic Evaluation of Adhesive Joints*, in *International Advances in Non-destructive testing*. 1990, Science Publishing: New York, USA. p. 231-253.

99. Fahr, A., et al., *Estimation of strength in adhesively bonded steel specimens by acousto-ultrasonic technique.* Mater. Eval., 1989. **47**(2): p. 233-240.

100. Tiwari, A., et al. *In-situ Acousto-Ultrasonic technique to monitor damage in ceramic matrix composites*. in *HITEMP 1992*. 1992.

101. Drouillard, T.F. and A. Vary, *AE literature- Acousto-ultrasonic reflections.* Journal of Acoustic Emission, 1994. **12**(1): p. 71-78.

102. Rose, J.L. and L.E. Soley, *Ultrasonic guided waves for anomaly detection in aircraft components.* Materials Evaluation, 2000. **58**(9): p. 1080-1086.

103. Rose, J., K. Rajana, and M. Hansch, *Ultrasonic guided waves for NDE of adhesively bonded structures.* The Journal of Adhesion, 1995. **50**(1): p. 71-82.

104. Rose, J., J. Barshinger, and P. Meyer. *Ultrasonic guided wave inspection of a 747 tear strap structure*. in *ASNT's 1997 Fall Conference and Quality Testing Show*. 1997.

105. Zhao, X., et al., *Active health monitoring of an aircraft wing with embedded piezoelectric sensor/actuator network: I. Defect detection, localization and growth monitoring.* Smart materials and structures, 2007. **16**(4): p. 1208.

106. Pullin, R., et al., *On the Development of a Damage Detection System using Macro-fibre Composite Sensors.* Journal of Physics: Conference Series, 2012. **382**(1): p. 012049.

107. Su, Z., L. Ye, and Y. Lu, *Guided Lamb waves for identification of damage in composite structures: A review.* Journal of Sound and Vibration, 2006. **295**(3–5): p. 753-780.

108. Polytec, *Polytec Scanning Vibrometer Theory Manual*. Vol. 9.0. Wahlbronn, Germany: Polytec Gmbh.

109. Halkon, B., *The History of Laser Vibrometry: An overview of advances in the interpretation of non-contact vibration measurements, and the effects of speckle induced noise and inherent motion cross sensitivities on the validity of particular vibration component measurement*, in *Deparment of Mechancial Engineering*. 2001, Loughborough University: Loughborough. p. 39.

110. Castellini, P., M. Martarelli, and E.P. Tomasini, *Laser Doppler Vibrometry: Development of advanced solutions answering to technology's needs.* Mechanical Systems and Signal Processing, 2006. **20**(6): p. 1265-1285.

111. Mortimer, B., et al., *The speed of sound in silk: Linking material performance to biological function.* Advanced Materials, 2014. **26**(30): p. 5179-5183.

112. Carlini, A., et al. *Valve motion measurements on motorbike cylinder heads using high-speed laser vibrometer*. in *Fifth International Conference on Vibration Measurements by Laser Techniques*. 2002. International Society for Optics and Photonics.

113. Nishizawa, O., T. Satoh, and X. Lei, *Detection of shear wave in ultrasonic range by using a laser Doppler vibrometer.* Review of scientific instruments, 1998. **69**(6): p. 2572-2573.

114. He, L. and S. Kobayashi, *Determination of Stress-Acoustic Coefficients of Rayleigh Wave by Use of Laser Doppler Velocimetry.* JSME International Journal Series A Solid Mechanics and Material Engineering, 2001. **44**(1): p. 17-22.

115. Kehlenbach, M., et al. *Numerical and experimental investigation of Lamb wave interaction with discontinuities*. in *Proceedings of the 4th international workshop on structural health monitoring*. 2003.

116. Maslov, K. and V.K. Kinra, *Scanning laser vibrometry for Lamb wave evaluation of composite tubulars.* Nondestructive Testing and Evaluation, 2000. **15**(6): p. 395-409.

117. Staszewski, W.J., et al., *Structural health monitoring using scanning laser vibrometry: I. Lamb wave sensing.* Smart Materials and Structures, 2004. **13**(2): p. 251-260.

118. Mallet, L., et al., *Structural health monitoring using scanning laser vibrometry: II. Lamb waves for damage detection.* Smart Materials and Structures, 2004. **13**(2): p. 261-269.

119. Leong, W.H., et al., *Structural health monitoring using scanning laser vibrometry: III. Lamb waves for fatigue crack detection.* Smart Materials and Structures, 2005. **14**(6): p. 1387-1395.

120. M Radzien´ ski, L.D.s., M Krawczuk, M Palacz, *Damage localisation in a stiffened plate structure using a propagating wave.* Mechanical Systems and Signal Processing, 2013. **39**(1-2): p. 388-395.

121. Sohn, H., et al., *Automated detection of delamination and disbond from wavefield images obtained using a scanning laser vibrometer.* Smart Materials and Structures, 2011. **20**(4).

122. S Olson, M.D., M Davies, E Swenson, H Sohn. *Computational Lamb Wave Model Validation Using 1D and 3D Laser Vibrometer Measurements*. in *Proceedings of SPIE, the international society of Optical Engineering*. 2010. Redondo Beach, California: SPIE.

123. Lee, J.-R., et al., *Long distance laser ultrasonic propagation imaging system for damage visualization.* Optics and Lasers in Engineering, 2011. **49**(12): p. 1361-1371.

124. Staszewski, W.J., B.C. Lee, and R. Traynor, *Fatigue crack detection in metallic structures with Lamb waves and 3D laser vibrometry.* Measurement Science and Technology, 2007. **18**(3): p. 727.

125. Schubert, L., et al., *INTERACTION OF LAMB WAVES WITH IMPACT DAMAGED CFRP'S STUDIED BY LASER-VIBROMETRY AND ACOUSTO ULTRASONIC.*

126. Grigg, S., et al., *Assessment of Damage Detection in Composite Structures Using 3D Vibrometry.* Journal of Physics: Conference Series, 2015. **628**(1): p. 012101.

127. Sengupta, S., A.K. Datta, and P. Topdar, *Structural damage localisation by acoustic emission technique: A state of the art review.* Latin American Journal of Solids and Structures, 2015. **12**(8): p. 1565-1582.

128. Sause, M. and S. Horn, *Simulation of acoustic emission in planar carbon fiber reinforced plastic specimens.* Journal of Nondestructive Evaluation, 2010. **29**(2): p. 123-142.

129. Sause, M.G. and S. Horn, *Simulation of lamb wave excitation for different elastic properties and acoustic emission source geometries.* Journal of Acoustic Emission, 2010. **28**: p. 109-121.

130. Delsanto, P.P., et al., *Connection machine simulation of ultrasonic wave propagation in materials. I: the one-dimensional case.* Wave Motion, 1992. **16**(1): p. 65-80.

131. Delsanto, P.P., et al., *Connection machine simulation of ultrasonic wave propagation in materials. II: The two-dimensional case.* Wave Motion, 1994. **20**(4): p. 295-314.

132. Delsanto, P.P., R.S. Schechter, and R.B. Mignogna, *Connection machine simulation of ultrasonic wave propagation in materials III: The three-dimensional case.* Wave Motion, 1997. **26**(4): p. 329-339.

133. Iordache, D., P.P. Delsanto, and M. Scalerandi, *Pulse distortions in the FD simulation of elastic wave propagation.* Mathematical and Computer Modelling, 1997. **25**(6): p. 31-43.

134. Ruffino, E. and P.P. Delsanto, *Problems of accuracy and reliability in 2-D LISA simulations.* Computers & Mathematics with Applications, 1999. **38**(5–6): p. 89-97.

135. Sundararaman, S. and D.E. Adams, *Accuracy and Convergence Using a Local Interaction Simulation Approach in One, Two, and Three Dimensions.* Journal of Applied Mechanics, 2009. **76**(3): p. 031008-031008.

136. Lee, B.C. and W.J. Staszewski, *Modelling of Lamb waves for damage detection in metallic structures: Part I. Wave propagation.* Smart Materials and Structures, 2003. **12**(5): p. 804.

137. Lee, B.C. and W.J. Staszewski, *Modelling of Lamb waves for damage detection in metallic structures: Part II. Wave interactions with damage.* Smart Materials and Structures, 2003. **12**(5): p. 815.

138. Lee, B.C. and W.J. Staszewski, *Sensor location studies for damage detection with Lamb waves.* Smart Materials and Structures, 2007. **16**(2): p. 399-408.

139. Paćko, P., et al., *Lamb wave propagation modelling and simulation using parallel processing architecture and graphical cards.* Smart Materials and Structures, 2012. **21**(7): p. 075001.

140. Nadella, K. and C.S. Cesnik, *Local interaction simulation approach for modeling wave propagation in composite structures.* CEAS Aeronautical Journal, 2013. **4**(1): p. 35-48.

141. Venkataraman, P., *Applied Optimization with MATLAB Programming*. 2nd ed. 2009, New Jersey: John Wiley & Sons.

142. Venter, G., *Review of optimization techniques*, in *Encyclopedia of aerospace engineering*. 2010, John Wiley and Sons.

143. Khan, S., M. Asjad, and A. Ahmad. *Review of Modern Optimization Techniques*. in *International Journal of Engineering Research and Technology*. 2015. ESRSA Publications.

144. Turing, A.M., *Computing machinery and intelligence.* Mind, 1950: p. 433-460.

145. Holland, J.H., *Adaptation in natural and artificial systems: An introductory analysis with applications to biology, control, and artificial intelligence*. 1975, Oxford, England: U Michigan Press. viii, 183.

146. Weinstein, D., *Herbert Spencer*, in *Stanford Encyclopedia of Philiosophy*. 2012, Stanford University: Stanford, USA.

147. Haupt, R.L. and S.E. Haupt, *Practical Genetic Algorithms*. 1998, Canada: John Wiley & Sons.

148. Clarke, A. and J.C. Miles, *Strategic Fire and Rescue Service decision making using evolutionary algorithms.* Advances in Engineering Software, 2012. **50**(1): p. 29-36.

149. Mitchell, M., *An Introduction to Genetic Algorithms*. 1st Edition ed. 1998, Cambridge, Massachusetts: The MIT Press.

150. Carlyle, J.M., *In-flight acoustic emission research.* 1981.

151. Kammer, D.C. *Sensor placement for on-orbit modal identification and correlation of large space structures*. in *American Control Conference*. 1990. San Diego, CA, USA.

152. Smith, M.S., *NASA'S SPACE STATION PROGRAM: EVOLUTION AND CURRENT STATUS*. 2001, Congressional Research Service: Washington, D.C, USA.

153. Kammer, D.C., *Effects of noise on sensor placement for on-orbit modal identification of large space structures.* Journal of Dynamic Systems, Measurement and Control, Transactions of the ASME, 1992. **114**(3): p. 436-443.

154. Yeo, L.S., W; Kammer, D, *Sensor placement for on-orbit modal identification via a Genetic Algorithm.* American Institute of Aeronautics and Astronautics Journal, 1993. **31**(10): p. 1922-1928.

155. Han, J.H. and I. Lee, *Optimal placement of piezoelectric sensors and actuators for vibration control of a composite plate using genetic algorithms.* Smart Materials and Structures, 1999. **8**(2): p. 257-267.

156. Manson, G. and K. Worden, *Sensor optimisation for a damage location problem.* Proceedings of the International Modal Analysis Conference - IMAC, 2001. **2**: p. 1226-1233.

157. Staszewski, W.J. and K. Worden. *An overview of optimal sensor location methods for damage detection*. in *Proceedings of SPIE - The International Society for Optical Engineering*. 2001.

158. Worden, K. and A.P. Burrows, *Optimal sensor placement for fault detection.* Engineering Structures, 2001. **23**(8): p. 885-901.

159. Guo, H.Y., et al., *Optimal placement of sensors for structural health monitoring using improved genetic algorithms.* Smart Materials and Structures, 2004. **13**(3): p. 528-534.

160. Overton, G. and K. Worden, *Sensor optimisation using an ant colony methapor.* Strain, 2004. **40**(2): p. 59-65.

161. Gao, H. and J.L. Rose. *Ultrasonic sensor placement optimization in structural health monitoring using evolutionary strategy*. in *Smart Structures and Materials 2006: Sensors and Smart Structures Technologies for Civil, Mechanical, and Aerospace Systems*. 2006. San Diego, CA, USA.

162. Zhang, J., K. Worden, and W.J. Staszewski. *Sensor optimisation using an immune system metaphor*. in *Conference Proceedings of the Society for Experimental Mechanics Series*. 2008.

163. Das, S., A. Chattopadhyay, and Z. Xu, *Acoustic based structural health monitoring for composites using optimal sensor placement: analysis and experiments.* Journal of Reinforced Plastics and Composites, 2009. **28**(1): p. 83-97.

164. Laiho, J., A. Wacker, and T. Novosad, *Radio network planning and optimisation for UMTS*. 2006: John Wiley & Sons.

165. Flynn, E.B. and M.D. Todd, *A Bayesian approach to optimal sensor placement for structural health monitoring with application to active sensing.* Mechanical Systems and Signal Processing, 2010. **24**(4): p. 891-903.

166. Flynn, E.B. and M.D. Todd, *Optimal placement of piezoelectric actuators and sensors for detecting damage in plate structures.* Journal of Intelligent Material Systems and Structures, 2010. **21**(3): p. 265-274.

167. Markmiller, J.F.C. and F.K. Chang, *Sensor network optimization for a passive sensing impact detection technique.* Structural Health Monitoring, 2010. **9**(1): p. 25-39.

168. R Guratzsch, S.M., *Structural Health Monitoring Sensor Placement Optimization Under Uncertainty.* AIAA Journal, 2010. **48**(7): p. 1281-1289.

169. Huyer, W. and A. Neumaier, *SNOBFIT--stable noisy optimization by branch and fit.* ACM Transactions on Mathematical Software (TOMS), 2008. **35**(2): p. 9.

170. Ting-Hua, Y., L. Hong-Nan, and Z. Xu-Dong, *A modified monkey algorithm for optimal sensor placement in structural health monitoring.* Smart Materials and Structures, 2012. **21**(10): p. 105033.

171. Zhao, R.-q. and W.-s. Tang, *Monkey algorithm for global numerical optimization.* Journal of Uncertain Systems, 2008. **2**(3): p. 165-176.

172. Dongyue, G., et al., *Design of a sensor network for structural health monitoring of a full-scale composite horizontal tail.* Smart Materials and Structures, 2014. **23**(5): p. 055011.

173. De Stefano, M., et al., *Optimum Sensor Placement for Impact Location Using Trilateration.* Strain, 2014: p. n/a-n/a.

174. Worden, K. and W.J. Staszewski, *Impact location and quantification on a composite panel using neural networks and a genetic algorithm.* Strain, 2000. **36**(2): p. 61-70.

175. Zitzler, E., M. Laumanns, and L. Thiele, *SPEA2: Improving the strength Pareto evolutionary algorithm*. 2001, Eidgenössische Technische Hochschule Zürich (ETH), Institut für Technische Informatik und Kommunikationsnetze (TIK) Zürich, Switzerland.

176. EASA, *Certification Specifications and Acceptable Means of Compliance for Large Aeroplanes CS-25*. 2016, EASA.

177. Gaitonde, M., *PROBABILISTIC JUSTIFICATION OF COMPOSITE AIRFRAME IN-SERVICE INSPECTIONS*, in *20th International Conference on Composite Materials*. 2015: Copenhagen.

178. Oxford English Dictionary. *transducer, n.* 1986 [cited 2016 03/02/2016]; Available from: http://www.oed.com/view/Entry/204675?redirectedFrom=transducer#eid.

179. Yan, T. and P.J. Theobald, B.E, *A conical piezoelectric transducer with integral sensor as a self-calibrating acoustic emission energy source.* Ultrasonics, 2004. **42**.

180. Theobald, P. and A. Thompson, *Towards a calibrated reference source for in-situ calibration of acoustic emission measurement systems*. 2005, National Physics Laboratory: Teddington, UK.

181. Physical Acoustics Corp. *NANO30 - 150-750 KHZ MINIATURE AE SENSOR WITH INTEGRAL COAXIAL CABLE*. 2016 [cited 2016 05/02/2016]; Available from: http://www.physicalacoustics.com/by-product/nano30-150-750-khz-miniature-ae-sensor-with-integral-coaxial-cable/.

182. ASTM, *Standard Guide for Mounting Piezoelectric Acoustic Emission Sensors*. 2012, ASTM Interational: West Conshohocken, PA, USA. p. 3.

183. Dugmore, K., D. Jonson, and M. Walker, *A comparison of signal consistency of common ultrasonic couplants used in the inspection of composite structures.* Composite structures, 2002. **58**(4): p. 601-603.

184. Colombo, S., et al., *Frequency response of different couplant materials for mounting transducers.* NDT & E International, 2005. **38**(3): p. 187-193.

185. Beck, P., *Quantitative damage assessment of concrete structures using Acoustic Emission*. 2004, Cardiff University.

186. Hensman, J.J., et al. *On the reproducibility of transducer coupling for acoustic emission testing*. in *Advanced Materials Research*. 2006. Trans Tech Publ.

187. Vallen, H., *AE testing fundamentals, equipment, applications.* Journal of Nondestructive Testing(Germany), 2002. **7**(9): p. 1-30.

188. MISTRAS Group Ltd., *ARB-1410: Arbitrary Waveform Generator Board and WaveGen1410 Software*. 2009: Princton, NJ, USA.

189. Polytec Gmbh. *PSV-500-3D-V Scanning Vibrometer VHF*. 2016 [cited 2016 01/02/2016].

190. MISTRAS Group Ltd., *PCI-2 The New AE Research tool*. 2009: Princeton, NJ, USA.

191. MISTRAS Group Ltd., *Express-8: An eight channel acoustic emission board and system*. 2015: Princeton, NJ, USA.

192. Hsu, N.N. and F.R. Breckenridge, *CHARACTERIZATION AND CALIBRATION OF ACOUSTIC EMISSION SENSORS.* Materials Evaluation, 1981. **39**(1): p. 60-68.

193. ASTM, *Standard Guide for Determining the Reproducibility of Acoustic Emission Sensor Response*. 1999, ASTM: West Conshohocken, PA, USA. p. 1 - 9.

194. Nivesrangsan, P., J. Steel, and R. Reuben, *AE mapping of engines for spatially located time series.* Mechanical Systems and Signal Processing, 2005. **19**(5): p. 1034-1054.

195. AGH - University of Science and Technology, *cuLISA3D Theory and User Information v0.8.4*. 2011, AGH – University of Science and Technology, Faculty of Mechanical Engineering and Robotics, Department of Robotics and Mechatronics: Poland. p. 1-6.

196. Packo, P., T. Uhl, and W.J. Staszewski, *Generalized semi-analytical finite difference method for dispersion curves calculation and numerical dispersion analysis for Lamb waves.* The Journal of the Acoustical Society of America, 2014. **136**(3): p. 993-1002.

197. Madenci, E., et al., *Analysis of composite laminates with multiple fasteners.* International journal of solids and structures, 1998. **35**(15): p. 1793-1811.

198. Krishnamoorthy, A., S.R. Boopathy, and K. Palanikumar, *Delamination analysis in drilling of CFRP composites using response surface methodology.* Journal of Composite Materials, 2009. **43**(24): p. 2885-2902.

199. Bhowmik, S., et al., *Durability of adhesive bonding of titanium in radiation and aerospace environments.* International Journal of Adhesion and Adhesives, 2006. **26**(6): p. 400-405.

200. Arenas, J.M., et al., *Considerations for the industrial application of structural adhesive joints in the aluminium-composite material bonding.* Composites Part B: Engineering, 2013. **44**(1): p. 417-423.

201. Davis, M. and D. Bond, *Principles and practices of adhesive bonded structural joints and repairs.* International journal of adhesion and adhesives, 1999. **19**(2): p. 91-105.

202. Higgins, A., *Adhesive bonding of aircraft structures.* International Journal of Adhesion and Adhesives, 2000. **20**(5): p. 367-376.

203. Petrie, E.M., *Adhesives for the assembly of aircraft structures and components: Decades of performance improvement, with the new applications of the horizon.* Metal Finishing, 2008. **106**(2): p. 26-31.

204. Wang, X., et al., *Tool wear of coated drills in drilling CFRP.* Journal of Manufacturing Processes, 2013. **15**(1): p. 87-95.

205. N Quaegebeur, P.M., P Masson, M Castaings, *Methodology for optimal configuration in structural health monitoring of composite bonded joints.* Smart Materials and Structures, 2012. **21**(10): p. 11.

206. Sargent, J.P., *Durability studies for aerospace applications using peel and wedge tests.* International Journal of Adhesion and Adhesives, 2005. **25**(3): p. 247-256.

207. Digby, R.P. and D.E. Packham, *Pretreatment of aluminium: topography, surface chemistry and adhesive bond durability.* International Journal of Adhesion and Adhesives, 1995. **15**(2): p. 61-71.

208. Bossi, R. and M.J. Piehl, *BONDING PRIMARY AIRCRAFT STRUCTURE: THE ISSUES.* Manufacturing Engineering, 2011. **146**(3): p. 101-102,104-109.

209. Weitzenböck, J.R. and D. McGeorge, *The designer's dilemma: How to deal with the uncertainty about the long-term performance of adhesively bonded joints.* Proceedings of the Institution of Mechanical Engineers Part M: Journal of Engineering for the Maritime Environment, 2004. **218**(4): p. 273-276.

210. Meeks, C., E. Greenhalgh, and B.G. Falzon, *Stiffener debonding mechanisms in post-buckled CFRP aerospace panels.* Composites Part A: Applied Science and Manufacturing, 2005. **36**(7): p. 934-946.

211. Brotherhood, C.J., B.W. Drinkwater, and S. Dixon, *The detectability of kissing bonds in adhesive joints using ultrasonic techniques.* Ultrasonics, 2003. **41**(7): p. 521-529.

212. Huntsman;, *Advanced Materials - Araldite 420 A/B*. 2009, Huntsman Advanced Materials: Basel, Switzerland.

213. Reusser, R.S., et al., *Reflection and transmission of guided ultrasonic plate waves by vertical stiffeners.* The Journal of the Acoustical Society of America, 2014. **136**(1): p. 170-182.

214. Marks, R., et al., *Using genetic algorithms to optimize an active sensor network on a stiffened aerospace panel with 3D scanning laser vibrometry data.* Journal of Physics: Conference Series, 2015. **628**(1): p. 012116.

215. NASA;, *ULTRASONIC TESTING OF AEROSPACE MATERIALS.* Preferred Reliabilty Practices, 1998. **PT-TE-1422**: p. 1-6.

216. Eaton, M.J., R. Pullin, and K.M. Holford, *Towards improved damage location using acoustic emission.* Proceedings of the Institution of Mechanical Engineers, Part C: Journal of Mechanical Engineering Science, 2012. **226**(9): p. 2141-2153.

217. Sheppard, J., et al., *Lamb Waves for Non-destructive Evaluation of Composite Wing Section*, in *2008 IMAC-XXVI: Conference & Exposition on Structural Dynamics*. 2008, SEM.

218. Kim, H., et al., *Impact Damage Formation on Composite Aircraft Structures.* 2012.

219. International Air Transport Association, *Ground Damage Prevention Programme Targets 10% Cost Reduction*, in *Industry Times*. 2005.

220. The Boeing Company, *Foreign Object Damage,*, in *Aero*. 1998, The Boeing Company: Seattle, USA.

221. Kim, H., *Impact Damage Formation on Composite Aircraft Structures.* 2012.

222. Davies, G.A.O. and X. Zhang, *Impact damage prediction in carbon composite structures.* International Journal of Impact Engineering, 1995. **16**(1): p. 149-170.

223. Gunn III, L.C., *Operational Experience with Health Monitoring on the Delta II Program*, in *2nd International workshop on Structural Health Monitoring*, F.K. Chang, Editor. 2001, CRC Press: Florida.

224. Marsh, G. *The challenge of wind turbine blade repair*. 2011 [cited 2015 17th July]; Available from: http://www.renewableenergyfocus.com/view/21860/the-challenge-of-wind-turbine-blade-repair/.

225. Kusiak, A. and W. Li, *The prediction and diagnosis of wind turbine faults.* Renewable Energy, 2011. **36**(1): p. 16-23.

226. Sørensen, B.F., et al., *Improved design of large wind turbine blade of fibre composites based on studies of scale effects (Phase 1). Summary report*. 2004.

227. Norris, G. and M. Wagner, *Boeing 787 Dreamliner*. 1 ed. Vol. 1. 2008, MI, USA: Zenith Press. 160.

228. McGowan, D.M. and D.R. Ambur, *Damage-Tolerance Characteristics of Composite Fuselage Sandwich Structures With Thick Facesheets.* 1997.

229. Technical Wind Services. *Wind Turbine Blade Services*. 2015 [cited 2015 17th July]; Available from: http://www.technicalwindservices.com/wind-turbine-blade-repair.php.

230. Marks, R., et al., *Sensor location studies for damage detection in Aerospace Structures using 3D scanning Laser Vibrometry*, in *ICAF 2015*, A. Siljander, Editor. 2015, International Committee of Aeronautical Fatigue: Helsinki, Finland. p. 808-818.

231. Pan, Y., L. Iorga, and A.A. Pelegri, *Analysis of 3D random chopped fiber reinforced composites using FEM and random sequential adsorption.* Computational Materials Science, 2008. **43**(3): p. 450-461.

232. Rokhlin, S., et al., *Nondestructive sizing and localization of internal microcracks in fatigue samples.* NDT & E International, 2007. **40**(6): p. 462-470.

233. Pearson, M.R., et al. *Impact damage detection and assessment in composite panels using macro fibre composites transducers*. in *Journal of Physics: Conference Series*. 2011. IOP Publishing.

234. VIBRATION. *The Vibration Project*. 2015 [cited 2016 12/01/2016]; Available from: http://www.fp7-vibration.eu/.

235. VAMVOUDAKIS-STEFANOU, K.J. and S.D. FASSOIS. *Vibration-Based Damage Detection for a Population of Like Structures via a Multiple Model Framework*. in *Proceedings of the 6th International Symposium on NDT in Aerospace (Madrid, Spain 2014)*.

236. Al-Jumaili, S.K., et al., *Acoustic emission source location in complex structures using full automatic delta T mapping technique.* Mechanical Systems and Signal Processing.